Electrochemical Oxygen Sensor Development for Liquid Sodium

By:

Billy K. Nollet

A dissertation submitted in partial fulfillment of the requirements for the degree of

Doctor of Philosophy

(Nuclear Engineering & Engineering Physics)

University of Wisconsin - Madison

2013

Date of final oral examination: July 20, 2013

The dissertation is approved by the following members of the Final Oral Committee:

Todd R. Allen, Professor, NEEP
Mark H. Anderson, Research Professor, NEEP
Dane Morgan, Associate Professor, MSE
Michael L. Corradini, Professor, NEEP
Kumar Sridharan, Research Professor, NEEP

Executive Summary

Safe operation of a sodium-cooled fast reactor (SFR) requires in-depth understanding of the corrosion implications of liquid sodium coolant on reactor materials. Dissolved oxygen concentration is of particular importance in characterizing sodium attack, so an accurate means of measuring and controlling oxygen is crucial. There is significant room for improvement in current oxygen sensing technology, so extensive research has been conducted at the University of Wisconsin-Madison to address this issue. Experimental facilities and electrochemical oxygen sensors have been developed, tested, and analyzed. This research is discussed in detail in this report.

The oxygen sensors tested in this research were developed using a yttria stabilized zirconia (YSZ) electrolyte whereas many of the past research in this field was conducted with yttria doped thoria (YDT or YST) electrolytes. Thorium, an alpha emitter, is expensive and increasingly difficult to acquire, so motivation to switch to a new material exists. YSZ is commonly used as the electrolyte for solid oxide fuel cells, and ample data is available for high temperature ionic conduction of this material.

While some work has been done with YSZ in oxygen sensors (the automotive field, for example, uses YSZ O_2 sensors), research on YSZ sensors in sodium is limited. A thorough study of YSZ-based electrochemical oxygen sensors must include detailed corrosion testing and analysis of YSZ in liquid sodium, careful oxygen sensor development and testing, and finally, a comprehensive analysis of the acquired sensor data.

The research presented in this report describes the design and development of an electrochemical oxygen sensor for use in sodium using a YSZ electrolyte through the previously-mentioned steps. The designed sensors were subjected to a series of hypotheses which advance common understanding of oxygen sensor signal. These results were used in conjunction with past research to form reliable conclusions.

Acknowledgments

Financial support for this project was provided by the U.S. Nuclear Regulatory Commission's Nuclear Education Fellowship and the U.S. Department of Energy.

I would like to thank Dr. Mark Anderson for his consistent availability and willingness to provide insight for this research, Paul Brooks for his sound advice on practical aspects of the project, and Mike Hvasta for his support, guidance, and friendship since my first day of graduate school. Additionally, I would like to thank Dr. Todd Allen, Dr. Kumar Sridharan, Dr. Dane Morgan, and Dr. Mike Corradini for their assistance with various aspects of this work. I would additionally like to acknowledge Sam Briggs for his repeated assistance with materials science analysis.

I would also like to thank my parents, sisters, Karen, and Bryce for their love and support throughout my life. Finally, I would like to thank my multitude of friends and family who are always a phone call away, no matter what hour of night I happen to be walking home from work.

Contents

List of Figures

List of Tables

Part I

Theory & Background

Chapter 1

Introduction & Motivation

This chapter is a summary of the literature review that was conducted to provide context and direction for this project. The purpose of this chapter is to explain the motivation behind this research as well and provide fundamental background information. A detailed description of the benefits and challenges to Generation IV rectors is presented. In particular, the Sodium Fast Reactor (SFR) is analyzed and the important areas of necessary research presented.

It is concluded that liquid sodium oxygen concentration is a key measurement for both safe operation of a sodium cooling system and conducting a meaningful and accurate corrosion study. The importance of an effective oxygen meter is established, and therefore, the motivation for this research project is presented.

Chapter 1 Contents

Contents

1.1 Generation IV Reactors

Generation IV reactors are designed to help meet increasing global energy needs. In general, the next generation of reactors will be engineered to meet the following general goals[1].

Sustainability

Generation IV reactors will need to provide long-term energy and efficient fuel utilization. Nuclear waste production will be decreased and long term storage of used fuel will accordingly be shortened.

Economics

Generation IV reactors need to have a substantial cost advantage over other energy production methods. Similarly, the financial risk associated with building and running a Generation IV reactor needs to be on par with other energy production projects.

Safety & Security

Generation IV reactors must operate safely and reliably. Further, reactor core damage must be of very low likelihood. Finally, Generation IV reactors must prove to be an undesirable means for weapon material acquisition (theft).

The six Generation IV systems are tabulated below:

- Gas-Cooled Fast Reactor
- Lead-Cooled Fast Reactor
- Molten Salt Reactor System
- Sodium-Cooled Fast Reactor
- Supercritical-Water-Cooled Reactor
- Very-High-Temperature Reactor

1.1.1 Sustainability of Fuel Cycles

The Generation IV International Forum's Fuel Cycle Crosscut Group (FCCG) analyzed the waste and resource use of a once-through fuel cycle. Their findings were that the limiting factor for nuclear energy using the once-through cycle is storage space for spent fuel (repository space)[2]. See figure 1.1.

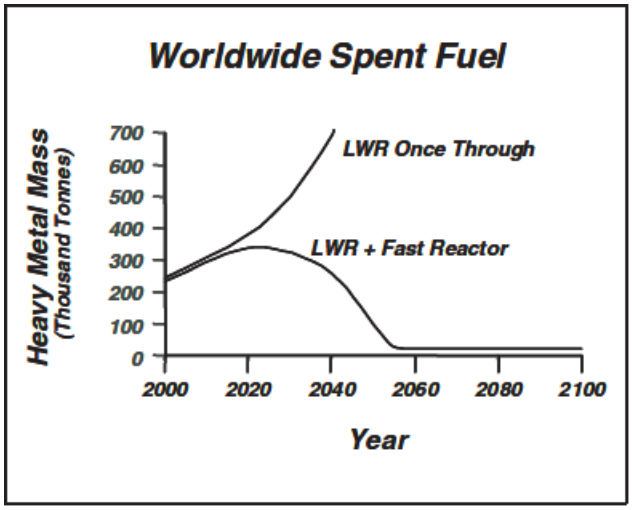

Figure 1.1: The once-through fuel cycle produces far more spent fuel than would the introduction of fast reactors[1].

According to the FCCG's findings, accumulation of spent fuel using the once-through cycle would result in the need of a new repository in the US in only a few decades. Global uranium supply, barring advances in mining/extraction techniques, becomes the long term limiting factor. In figure 1.2, the dashed line labeled "speculative resources" indicates the estimated global uranium supply based on the aforementioned assumption. Notice that the once-through data rises high above the estimated supply line by 2060, but through fast reactor introduction the uranium requirement is greatly reduced[1].

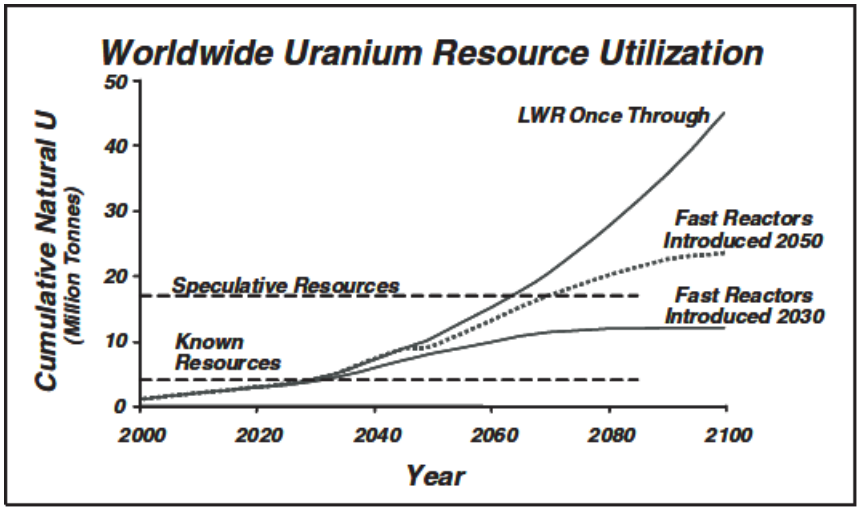

Figure 1.2: Fast reactors offer a possible solution to the natural uranium supply problem[1].

1.2 Sodium Fast Reactors (SFRs)

Sodium Fast Reactors are one of the proposed Generation IV nuclear energy systems mentioned above. While the other options are all being investigated to some extent, this project is concerned with the SFR; as such, it is the only reactor that will be discussed in detail in this report.

Fast neutron fission reactions have a higher neutron yield than thermal neutron fission; the resulting surplus neutrons can be used to breed fuel or transmutate fission products. This reactor system offers a closed fuel cycle and has high potential for actinide management.

Core outlet temperatures are typically 530-550[C][3] and plant size is variable from modular reactors (100s [MWe]) to large reactors (1500-1700[MWe])[1]. Since the operating temperature is much lower than the boiling temperature of liquid sodium (883[C])[4], these reactors don't need to be pressurized[5]. A secondary sodium loop will be installed to act as a non-radioactive buffer between the radioactive sodium running through the reactor core, and the steam generator.

Of the six Generation IV reactor systems listed above, the SFR is the most technologically developed[6]; they have been built and operated in many countries already. However, several

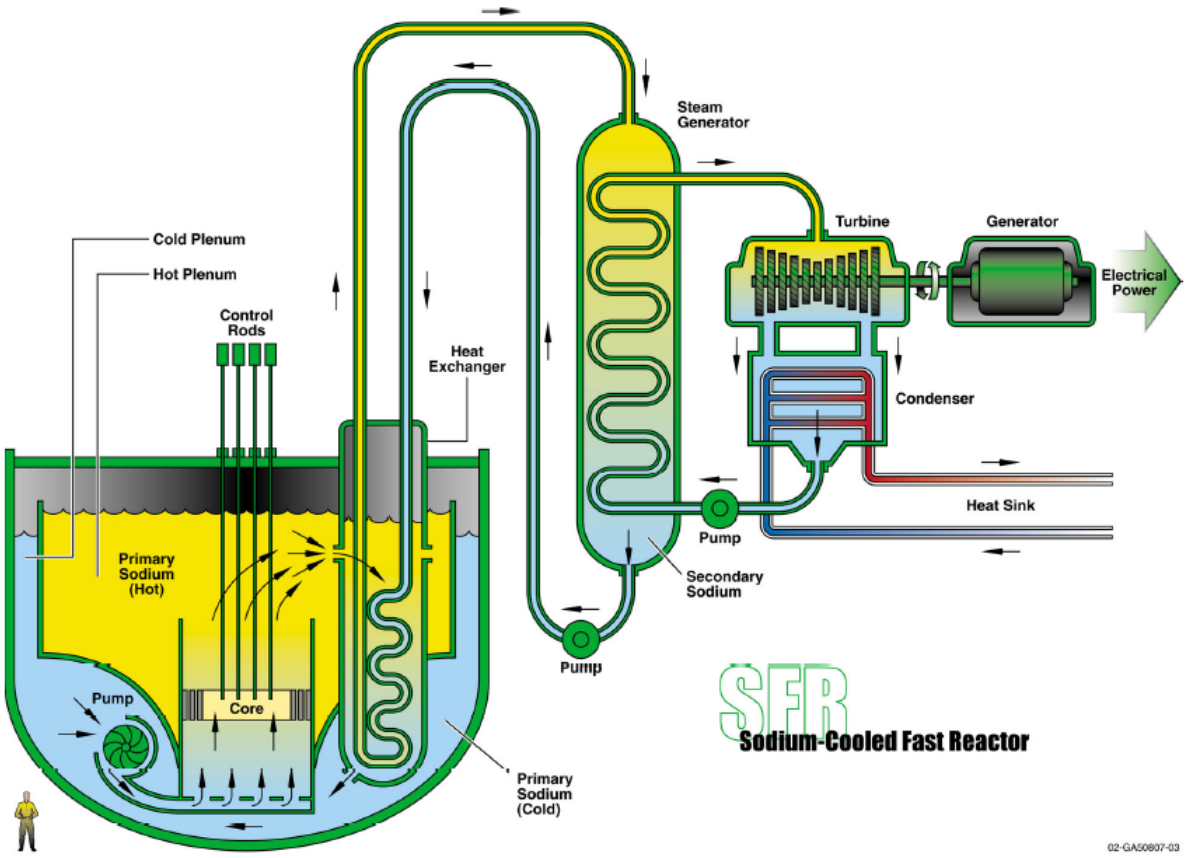

Figure 1.3: A basic diagram of a Sodium Fast Reactor System[1]

technological gaps need to be addressed, and the safety of a sodium coolant system hinges on total understanding of sodium interactions. Of the issues facing SFRs, sodium corrosion is the focus of this paper.

1.2.1 Corrosion Implications on SFR

Two potential hazards associated with using liquid sodium are its extreme chemical reactivity and high level of induced radioactivity in ^{24}Na. As discussed above, the cooling system of an SFR is divided into two sodium loops. The primary sodium loop pumps sodium through the core, removing energy from the fuel and control rod assemblies. This sodium is easily activated and sees the bulk of the reactor power. The secondary coolant loop then serves as a buffer loop to transport energy from the radioactive primary sodium to the steam

generator (the reactor's main heat exchanger). The steam generator transfers energy from the secondary sodium to water, causing it to boil and consequently create steam that turns a turbine. Given the hazardous reaction of sodium and water, proper engineering of the sodium loops is critical to reactor safety.

High temperature liquid sodium flowing from the hot section of the aforementioned primary loop slowly dissolves the constituent elements of the system's stainless steel (chromium, iron, and nickel). These solutes are then transported and deposited to the cooler sections of the loop. This results in a thinning of the cladding wall, and diminishing cladding ability to withstand fission gas pressure and fuel-cladding contact. As cladding walls become thinner, tangential stresses on these walls and, consequently, creep rate increase. Since cladding is the thinnest component of a reactor coolant system, it is most susceptible to wastage or thinning. In addition, since the cladding sees high neutron flux, it is susceptible to high radiation damage, and many consequent metallurgic effects. These effects make failure an even higher probability and highlight the importance of resistance to sodium corrosion.

As a result of the inherent danger associated with using high temperature liquid sodium and water in the same vicinity, cautious engineering and prerequisite research is of the highest importance. It is paramount to understand the causes and effects of liquid metal corrosion, as well as methods to deter corrosive effects. Obviously with the depletion of metal from some system locations and accumulation of metals in other locations, thinning of containment components and flow restrictions from solute deposits must be understood and accounted for in design and construction.

1.3 Liquid Metal Corrosion

Corrosion is described by Evans[7] as the "destruction of metal by chemical or electrochemical action." In short, corrosion can be defined as the transfer of electrons. This definition is inadequate, however, when considering liquid metal corrosion, which involves the solubility of a solid metal in a liquid metal since no net transfer of electrons is required for this phenomenon to occur. Liquid metal corrosion "depends on the solution rate and extent of solubility of the solid metal in the liquid metal"[8]. A variety of corrosion mechanisms occur as the system moves towards equilibrium. These mechanisms are discussed in detail after a brief description of key variables to consider when analyzing liquid metal corrosion.

Temperature

Both solubility and diffusion rate increases with temperature; thus temperature is one of the most important variables in liquid metal corrosion. Moreover, temperature gradients in a liquid metal lead to temperature gradient mass transfer, where differences in solubility between the hot and cold sections of the liquid metal lead to the diffusion of dissolved metal from high to low concentrations.

Surface Area/Volume Ratio

In a closed system with no cold trap, the ratio of exposed surface area to the volume of liquid metal available will dictate the amount of corrosion experienced. The exposed solid metal will corrode sufficiently to saturate the liquid metal; thus, the amount of corrosion will increase with the ratio of surface area to volume of coolant.

Flow Properties

In a dynamic test loop the liquid metal flow velocity has an important effect. The thickness of the viscous sub-layer decreases as the Reynolds number increases, thereby decreasing the diffusion length of metal atoms passing from hot to cold loop sections.

1.3.1 Examples of Liquid Metal Corrosion

Liquid metal attack has been observed in several mechanisms which will be categorized accordingly[9]:

- simple-solution
- alloying between liquid and solid metal
- intergranular penetration
- impurity reactions
- temperature & concentration-gradient mass transfer (dissimilar metal mass transfer)

Simple-Solution Type Attack

Phase diagrams of liquid-metal/solid-metal interactions are available, and describe the solubility of a solid metal into a liquid metal. So the eventual extent of damage done to a solid metal can be determined knowing the ratio of exposed surface area to system volume. However, these phase diagrams do not describe the *rate* of this attack. The rate of attack is dictated by a number of variables, including the presence of impurities[8]. It is also important to note that McKisson and Eichelberger, in their summary of solubility data[10], found reproducibility of this data difficult to attain; they concluded that the source of difficulty is primarily due to impurity interaction.

An example of this effect was detailed by Swisher[11]. His research with iron in liquid potassium showed that the solubility of iron is a function of oxygen concentration. Furthermore, nitrogen has been known to increase the solubility of many metals in liquid lithium[12].

Alloying Between Liquid & Solid Metal

This phenomenon occurs only when there is some solubility of the liquid metal *in* the solid metal. The result is considerable amounts of liquid metal dissolved into the solid metal, forming an inter-metallic compound[8]. For example, sodium penetrates solid copper and forms an intermetallic compound at the grain boundaries which is much harder than copper.

Intergranular Penetration

A very serious type of molten metal corrosion is intergranular penetration, which occurs when one constituent of a metal alloy (like stainless steel) is selectively removed from that alloy. For example, 800[C] lead, like liquid sodium, has been known to remove nickel from austenitic stainless steels[8]. In thermal convection loops, this corrosion effect is responsible for the removal from nickel from a hot section, and the deposition of that nickel in a cold zone.

This corrosion mechanism can similarly be attributed to impurities. However, in this case, the impurities of interest are in the solid metal rather than a contaminant in the liquid metal. For example, oxygen contaminated niobium has been known to be penetrated by lithium[13]. Further, Hoffman found lithium guilty of intergranular penetration of carbon-contaminated iron[14].

Temperature & Concentration-Gradient Mass Transfer

This effect will not be observed in isothermal static tests. This corrosion mechanism is driven by variation in solubility of the solid metal in the liquid metal, which is a function of temperature. Various metals were tested in lithium and this effect was demonstrated[15]. Figure 1.4 was compiled using DeStefano's data, and shows the variation in solubility as a function of temperature.

As a result from these variations in solubility, metal will be dissolved from the solid wall into solution in the hot section, whose high temperature allows a certain concentration of said metal. The dissolved metal will then be deposited in the cold section, whose decreased temperature limits the amount of solute allowed in the liquid metal.

Impurity Reactions

Impurity presence in liquid metals (oxygen, nitrogen, carbon, etc.) can have a dramatic effect on the attack rate; as discussed in each of the mechanisms detailed above, impurity

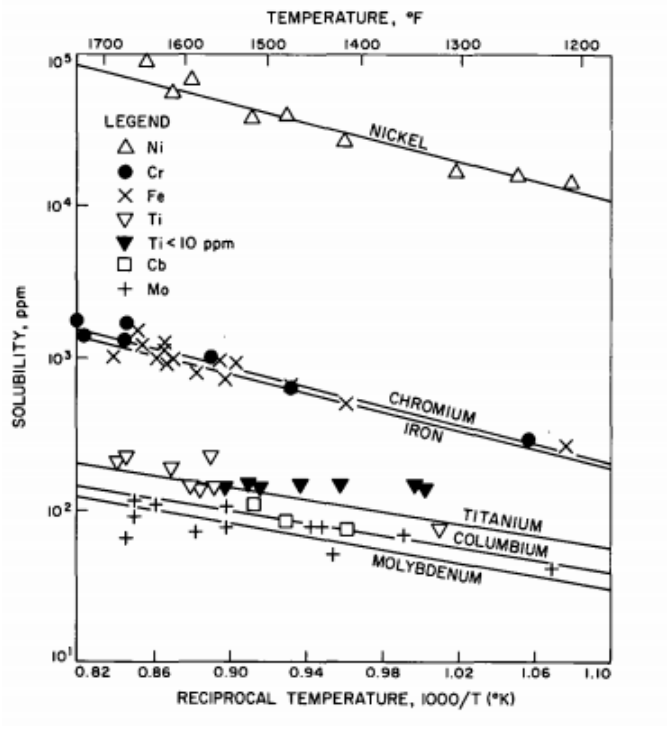

Figure 1.4: Solubility of some metals in Lithium. Data from DeStefano[15]. Figure from Phillips[16]

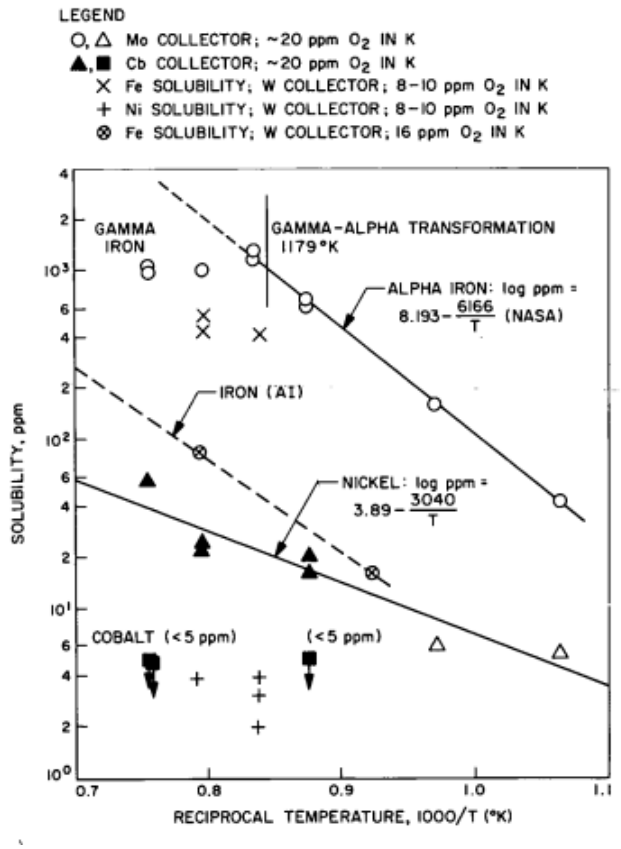

Figure 1.5: Solubility of iron, nockel, and cobalt in potassium. Data from references [10][11][17][18]. Figure from Phillips[16].

concentration has an accelerating effect in each case[16]. Figure 1.6 shows an explicit example of the effect oxygen dissolved in liquid sodium can have on the corrosion of a stainless steel system[19][20].

Olander has compiled multiple experiments in figure 1.7. Olander concluded that oxygen concentration in liquid sodium is a critical quantity to understand in order to predict corrosion behavior of liquid sodium[21]. However, as will be discussed in the following chapter, oxygen concentration is a difficult measurement to take regardless of the method employed. The remainder of this report is dedicated to the design of an effective oxygen sensor for liquid sodium.

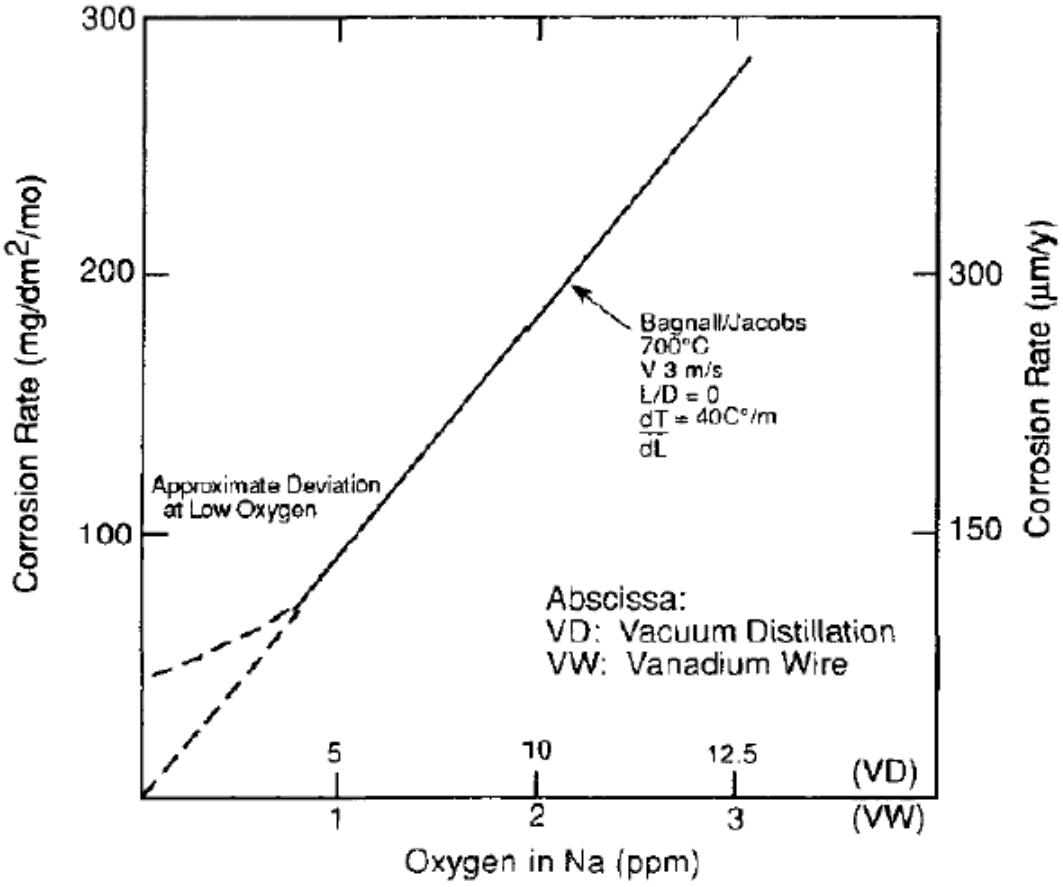

Figure 1.6: This plot shows the effect of oxygen dissolved in liquid sodium on the corrosion rate of 316SS[19][20].

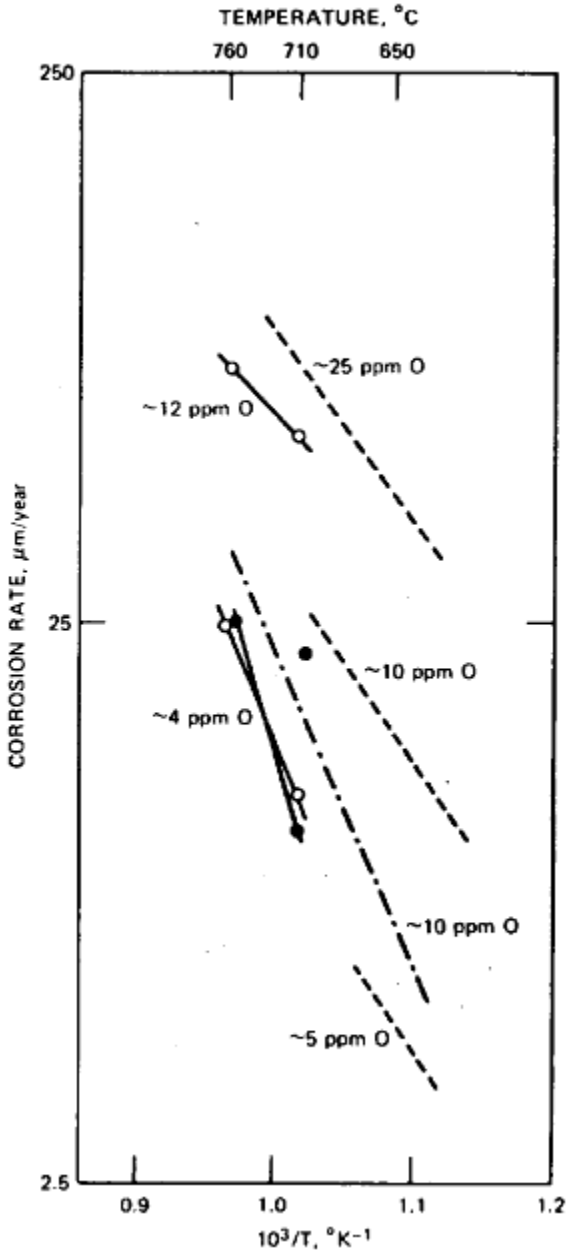

Figure 1.7: This figure was compiled by Olander, showing a combination of multiple experiments all showing increasing corrosion rate with increasing oxygen concentration[21].

1.4 Summary of Chapter 1

This section has discussed the background and motivation behind development of Generation IV nuclear reactors. Specifically, the Sodium Fast Reactor (SFR) was discussed as one of the most technologically feasible fast reactor designs. Specific issues associated with a molten sodium coolant were discussed, including a general overview of liquid metal corrosion mechanisms. Of the corrosion mechanisms discussed, oxygen impurity concentration was consistently found to have a significant impact on the corrosion rate of key reactor components as seen in figures 1.6 and 1.7.

Since oxygen concentration is a key parameter in predicting corrosion behavior of reactor materials, it is important to have an accurate measurement method for oxygen in sodium. The research presented in this document is motivated by this necessity. The goal of this project is to document the design, manufacturing, testing, and optimization of an affordable oxygen sensor for liquid sodium.

Chapter 1 Bibliography

[1] A technology roadmap for generation iv nuclear energy systems. Technical Report GIF-002-00, U.S. DOE, December 2002.

[2] Report of the fuel cycle crosscut group. In *Generation-IV Roadmap*. DOE, March 2001.

[3] Shoji Kotake Masakazu Ichimiya, Tomoyasu Mizuno. A next generation sodium cooled fast reactor concept and its r & d program. Technical report, Japan Atomic Energy Agency, May 2007.

[4] Gammon Ebbing. *General Chemistry*. Charles Hartford, 9 edition, 2011.

[5] M. Köhler. Engineering and design of fast reactors. Technical report, The Royal Society, 1990.

[6] T.H. Fanning, editor. *Sodium as a Fast Reactor Coolant*, Topical Seminar on Sodium Fast Reactors. Argonne National Lab, May 2007.

[7] U.R. Evans. *An Outline of Corrosion Mechanisms, Including Electrochemical Theory*. Wiley, 1948. p. 3 of Corrosion Handbook.

[8] W.D. Manly. Fundamentals of liquid-metal corrosion. Technical report, Oak Ridge National Laboratory, July 1958.

[9] A. Brasunas. Interim report on static liquid metal corrosion. Technical report, Oak Ridge National Laboratory, 1954. USAEC Report ORNL-1647.

[10] McKisson & Eicheloberger. Solubility and diffusion studies of ultra pure transition elements in ultra pure alkali metals. Technical report, Atomics International Summary, April 1965. presented at AEC-NASA Liquid Metals Information Meeting.

[11] J.H. Swisher. Solubility of iron, nickel, and cobalt in liquid potassium and effect of oxygen getting agents on iron solubility. Technical report, Lewis Research Center, March 1965. NASA TN D-2734.

[12] M.S. Freed & K.J. Kelly. Corrosion of columbium base and other structural alloys in high-temperature lithium. Technical report, Pratt and Whitney Aircraft Canel Div. of United Aircraft Corp., June 1961. PWAC-355.

[13] G.M. Ault. A decade of progress in refractory metals. Technical report, National Aeronautics and Space Administration, June 1965. NASA TM X-52135.

[14] E.E. Hoffman. Corrosion of materials by lithium at elevated temperatures. Technical report, Oak Ridge National Laboratory, October 1960. ORNL-2924.

[15] J.R. DeStefano. Corrosion of refractory metals by lithium. Technical report, Oak Ridge National Laboratory, March 1964. ORNL-3551.

[16] Wayne Phillips. Effects of alkali metal gettering agents on stainless steel corrosion. Technical report, Jet Propulsion Laboratory, April 1968. Technical Report 32-1239.

[17] W.S. Ginnel & R.J. Teitel. Solubility of transition metals in molten potassium. Technical report, Doublass Aircraft Company, April 1965.

[18] W.S. Ginnel & R.J. Teitel. Determination of solubility of several transition metals in molten potassium. Technical report, Trans. Am. Nucl. Soc., November 1965. pp393-394.

[19] *Factors that Affect Corrosion in Sodium*, Proceedings of the Second International Conference on Liquid Metal Technology in Energy Production, Richland, WA, April 1980. A. R. Keeton and C. Bagnall.

[20] R. Baboian, editor. *Corrosion Tests and Standards Manual*. ASTM, 2005.

[21] Donald R. Olander. *Fundamental Aspects of Nuclear Reactor Fuel Elements*. Technical Information Center, Springfield, VA, March 1985. TID-26711-P1.

Chapter 2

Oxygen Measurement & Control with the Plugging Meter & Cold Trap

This chapter describes two of the most common instruments used for oxygen measurement and control in liquid sodium systems. The plugging meter (PM) is an instrument which identifies the saturation temperature of the liquid sodium flowing through it. The saturation temperature can then be compared to solubility correlations from literature. The cold trap (CT) is a continuous filtering system which cools the sodium just below the saturation temperature, causing the oxygen impurity to precipitate out of solution. The cleaned, cooled sodium can then be returned to the loop and brought back to operating temperature, leaving the impurity in the CT. The temperature of the CT can then be correlated to the oxygen concentration using the same correlations as the plugging meter, assuming there are no other sources of impurity, and assuming the entire system is at equilibrium. Both systems are described in detail below.

The PM was used to take oxygen measurements during oxygen sensor tests. The CT, while it does indicate the oxygen concentration, was used primarily as a filter for the sensor experiments.

Chapter 2 Contents

Contents

2.1 Variables Used in this Chapter

Variable	Physical Meaning
c	Dissolved oxygen concentration [ppm]
T_{sat}	Saturation temperature [K]
ΔT	Temperature change [K]

2.2 The Plugging Meter

The solubility of oxygen in sodium is a function of temperature[1]. The plugging meter (PM) is an instrument which cools the molten sodium down to the saturation temperature (which is also a function of O_2 concentration), and the oxygen begins to precipitate out of solution.

Figure 2.1 is a diagram of a simple PM. The hot sodium is pumped through a heat exchanger which pulls out the power necessary to cool the sodium; the cold sodium is then forced through a plugging orifice (Figure 2.2). The plugging orifice is an obstructing body in the sodium path which forces the molten metal through small holes. These holes become plugged by the oxygen impurity when the sodium drops below the saturation temperature and the flowrate drops off as a result. When the electromagnetic flowmeter (Figure 2.1) indicates a drop in flow-rate, the user knows that the saturation temperature has been reached.

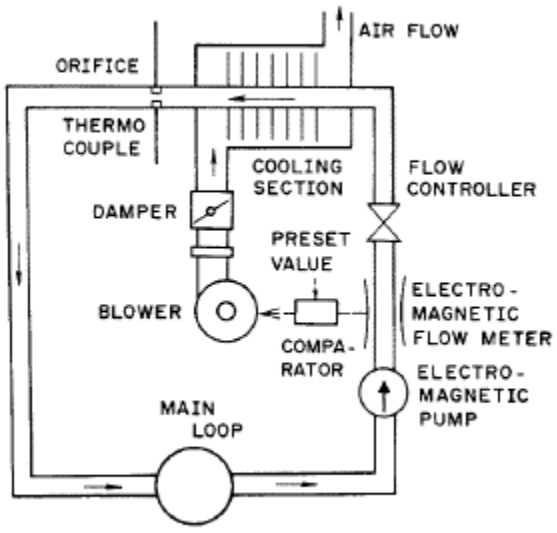

Figure 2.1: One configuration for a plugging meter and associated components[2]

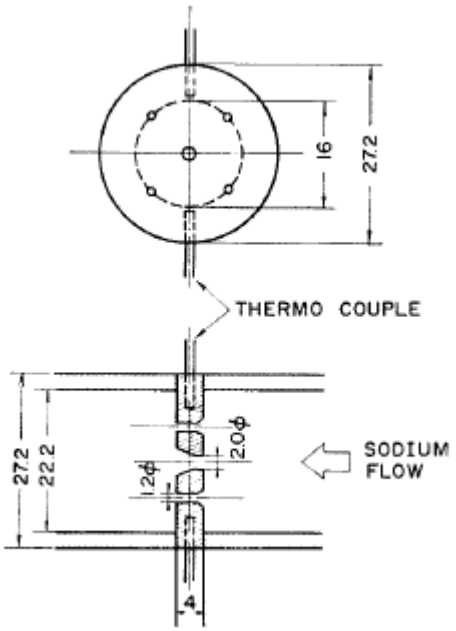

Figure 2.2: An example plugging orifice shown both in cross section and in the sodium flow path[2]

The value for the saturation temperature can then be correlated to an oxygen concentra-

tion according to past research; the popularly accepted Noden correlation, listed in equation 6.2, relates the saturation temperature, T_{sat} to the oxygen concentration, c[3]. This correlation has been verified in other experiments [4] (see Chapter 3 for a detailed review of past solubility research [5]).

$$c\left(T_{sat}\right) = 10^{\left(6.1579 - \frac{2384.2}{T_{sat}}\right)} \tag{2.1}$$

The plugging meter is a conceptually very simple solution to the oxygen measurement problem. It's also an attractive solution because it does not require any 'contaminants' into the loop; all the components of the PM can either be made of stainless steel (loop materials), or won't come into contact with sodium. In a harsh environment such as molten sodium, it is best practice to avoid the introduction of outside materials when possible (anything introduced to the loop has the potential to react with the sodium and contribute contaminants to the coolant).

2.2.1 Plugging Meter Limitations

The PM inherently becomes harder to use as the impurity concentration decreases[6]. For example, as the O_2 level decreases, the saturation temperature for that concentration approaches the freezing temperature of the sodium. Furthermore, as the saturation temperature decreases, the necessary power removal goes up because the sodium must be cooled to a lower temperature (so the necessary ΔT of sodium through the heat exchanger increases), and the amount of time required to reach the desired final temperature increases. The time per measurement has been shown to exceed 30 minutes for very clean sodium[7]. A continuous measurement technique would be preferred to these delayed measurements.

Perhaps the biggest problem with the PM is that it is a non-discriminatory technique. There is no guarantee that the impurities that plug the orifice are actually oxygen compounds[8]; this still could cause the orifice to plug slightly before the *oxygen* saturation temperature[9].

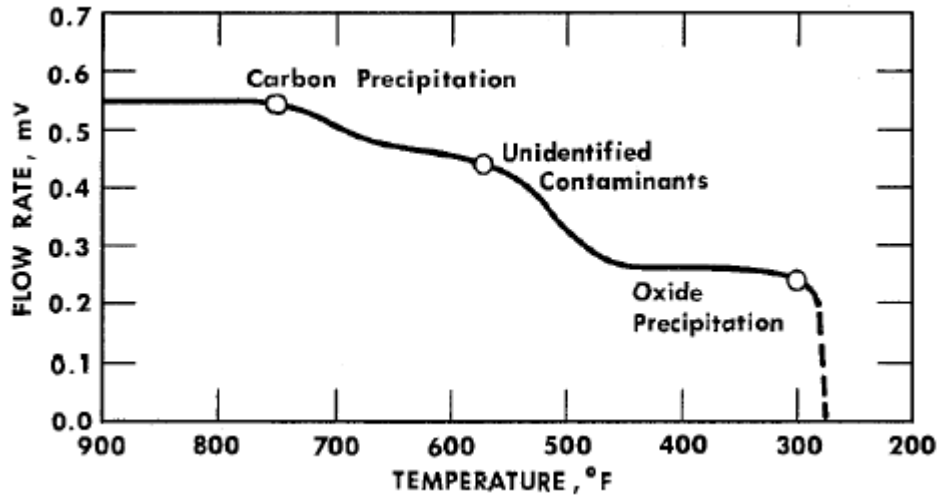

Figure 2.3: The plugging meter is non-discriminatory, and does not discern between various sodium contaminants[9].

This effect is shown in figure 2.2.1.

Plugging orifice selection can also be an issue. Different plugging orifices are optimum for different oxygen concentration ranges. The volume of the plugging holes must be much smaller than the total volume of impurity in the system[10][11]. Since plugging orifices are an integral part of the construction of the PM, swapping them out is not trivial, so a single plugging orifice is usually chosen for a given PM. Thus, the plugging meter's most effective range is set during loop construction, a constraint which the galvanic cell oxygen sensor does not share.

A practicality issue arose with the PM during experiments at UW-Madison. It is difficult to determine from data the precise temperature at which the orifice was plugged. This problem is discussed in detail in Chapter 5.

2.3 The Cold Trap

The cold Trap (CT) filters oxygen impurities out of liquid sodium (typically Na_2O or NaOH) [12] to reduce corrosion effects. It has been shown that sodium systems maintained at operating conditions (around 1[ppm] dissolved oxygen concentration) exhibit equal or less corrosion than light water reactor cooling systems[13, 14]. In the experiments described in this report, the cold trap was used to control the oxygen concentration in the system, so that the oxygen sensors could be calibrated. PM measurements were used to verify proper functioning of the CT.

Cold traps are typically installed in a small parallel loop to the main sodium system. A constant supply of sodium is pushed through a heat exchanger. Reducing the temperature of liquid sodium forces oxygen impurities to precipitate out of solution. In contrast to a PM, CT operation relies on this temperature being held constant. The impurities are collected on all surface area in the CT, and the cleaned, cooled sodium is returned to the bulk flow[15, 16].

Cold traps can either be forced or natural circulation. Natural circulation cold traps offer limited user control[17]. It is difficult to control the flow-rate, and thus the rate of filtration of the sodium. In addition, natural circulation traps function at a low flow-rate, making plug detection difficult to detect. If the CT is plugged, then the operator will not know that sodium purification has stopped without plugging tests or other oxygen measurement methods. Even with these issues, however, the natural circulation cold trap has been used to successfully control oxygen concentration in sodium[18].

Forced circulation cold traps operate by directing a small portion of the bulk sodium through the chilling unit. The impurity is similarly collected on either the walls or on stainless steel shavings sealed in the CT, then the sodium is returned to the hot flowing bulk sodium (see figure 2.3).

Due to the substantial power removal needed to cool sodium, the portion of bulk flow that is pushed through the CT is small. The time-rate change in oxygen concentration as a result of CT operation has been studied, and the sodium purity asymptotically approaches

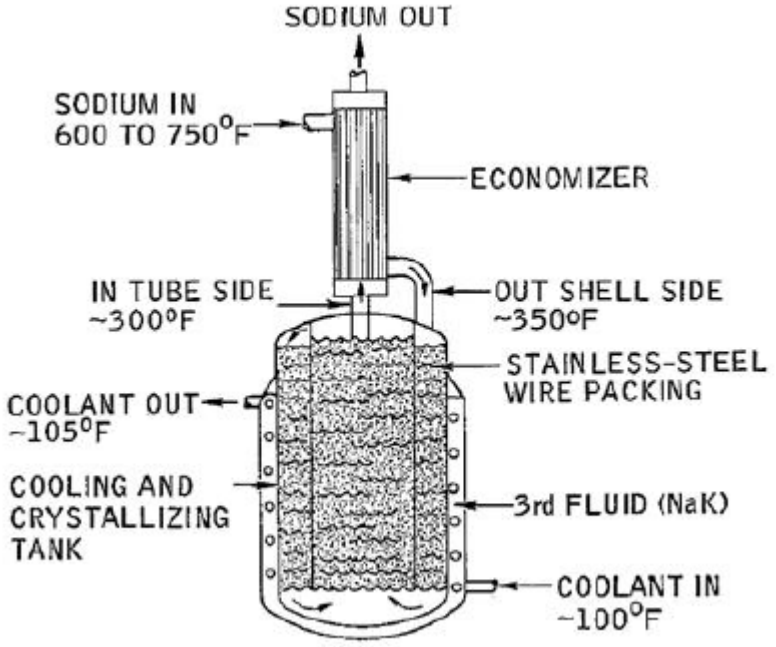

Figure 2.4: A forced circulation cold trap continuously filters a small percentage of the bulk sodium flow [19].

the saturation concentration dictated by CT temperature[18, 20, 21].

The CT used for the experiments discussed in this research report is a forced flow CT. Details for this instrument are given in Chapter 4, and data from this instrument are shown in Chapter 5.

Chapter 2 Bibliography

[1] V.J. Rutkauskas. Determination of the solubility of oxygen in sodium by vacuum distillation. Technical report, Los Alamos Scientific Laboratory, July 1968.

[2] Sudima Kotani Yamamoto, Murase. Measurement of impurity concentration in sodium by automatic plugging indicator. Technical report, Atomic Energy Research Laboratory, Hitachi Ltd., 1977.

[3] J. D. Noden. A general equation for the solubility of oxygen in liquid sodium. *Journal of the British Nuclear Energy Society*, 12(1):57–62, 1973.

[4] D.L. Smith. Monitoring and measurement of oxygen concentrations in liquid sodium. Technical report, International Conference on Liquid Metal Technology in Energy Production, 1976.

[5] K.T. Claxton. Review of solubility data for the liquid sodium-oxygen system. Technical report, United Kingdom Atomic Energy Authority, April 1965. AERE-R-4897.

[6] J. R. Gwyther et al. Developments in plugging meters and cold traps for LMFBRs. Second International Conference on Liquid Metal Technology in Energy Production, Richland, April 20-24 1980.

[7] K. Furukawa et al. Liquid sodium technology development (1). *Journal of Nuclear Science and Technology*, 3(12):501–515, 1966.

[8] K.A. Davis. Liquid metal in-line impurity measuring instruments (sodium) state-of-the-art study. Technical report, Liquid Metal Engineering Center, 1968.

[9] J. W. Mausteller, F. Teppers, and S. J. Rodgers. *Alkali Metal Handling and Systems Operating Techniques*. Gordon and Breach, 1967.

[10] D. Feron. Plugging indicator - measurement of low impurity concentrations at a constant orifice temperature. In H. U. Borgstedt, editor, *Material Behavior and Physical Chemistry in Liquid Metal Systems*, pages 89–96. Plenum Press, 1982.

[11] J. B. Pearson, T. J. Godfroy, R. S. Reid, and K. A. Polzin. NaK plugging meter design for the feasibility test loops. Number 8288 in Proceedings of ICAPP '08, Anaheim, CA, June 8-12 2008. NASA Marshall Space Flight Center.

[12] K.R. Kim et al. Theoretical analysis on the sodium purification for cold trap design and performance. *Journal of Industrial and Engineering Chemistry*, (4(2):113-121), June 1998.

[13] C.K. Mathews. Liquid sodium - the heat transport medium in fast breeder reactors. *Bulletin of Material Science*, 16(6):476–489, 1993.

[14] R.D. Kale and M. Rajan. Developments in sodium technology. *Current Science*, 86(5):668–675, March 2004.

[15] R.K. Steunenberg and L. Burris. From test tube to pilot plant: A 50 year history of the chemical technology division at argonne national laboratory. Technical report, Argonne National Laboratory, August 2000.

[16] F. Zhao and X. Ren. Optimal performance analysis of a sodium cold trap. *Nuclear Engineering and Design*, (239:490-494), 2009.

[17] S.L. Walters E.F. Batutis, S.J. Rodgers and J.W. Mausteller. Removal of na2o from a sodium system using natural circulation cold traps. Technical Report TR-22, Mine Safety Appliances Company, Callery, PA, 1953.

[18] C.B. Jackson. Liquid metals handbook: Sodium-nak supplement. U.S. Atomic Energy Commission, 1955.

[19] O.J. Foust, editor. *Sodium-NaK Engineering Handbook*, volume 5. Liquid Metal Engineering Center, 1979.

[20] C.C. Addison. *The Chemistry of the Liquid Alkali Metals.* John Wiley & Sons, 1984.

[21] V.I. Subbotin P.L. Kirillov, F.A. Kozlov and N.M. Turchin. Removal of oxides from sodium and tests for the oxide content. *Atomnaya Energiya*, 7(1):30–36, January 1960. English translation.

Chapter 3

Electrochemical Oxygen Sensor: Theory & Background

An extensive literature review in the field of sodium reactors and instrumentation yielded research that dated back to the 1950's. A large number of research papers were produced following the commissioning of the Sodium Reactor Experiment (SRE) in 1957. However, as Light Water Reactors (LWR's) and Boiling Water Reactors (BWR's) became more popular, sodium research dwindled and expertise on the subject faded. Thus, many of the papers cited in this chapter are several decades old. While more modern data would have helped the design process for the UW sodium loops, there was still ample information available from which to launch this project.

This chapter focuses on the electrochemical oxygen sensor. This instrument has theoretical advantages over the plugging meter and cold trap discussed in the previous chapter. A detailed description of the fundamental theory is described in this chapter along with a review of past work in this area. Past shortcomings and areas of improvement are also presented. A brief overview of current research on these sensors around the world is also included to establish the international importance of oxygen detection in liquid sodium.

Chapter 3 Contents

Contents

3.1 Variables Used in this Chapter

Variable	Physical Meaning
c	Dissolved oxygen concentration [ppm]
μ	Chemical potential [J]
F	Faraday constant [C/mol]
t_{ion}	Coefficient of ionic conductivity [-]
E	Sensor voltage [V]
ΔG^o	Change in Gibbs energy [J]
E_o	Standard electrode potential [V]
R	Universal gas constant [J/mok K]
γ	Activity coefficient
γ_o	Activity coefficient at saturation conditions
c_o	Dissolved oxygen concentration at saturation [ppm]
T	Temperature [K]
σ	Electrical conductivity [Ω m]
n	Number of oxygen ions[-]
K	Equilibrium constant [-]
P_{O_2}	Oxygen partial pressure [ATM]

3.2 Theory of Operation

The galvanic cell oxygen sensor is an on-line instrument that offers continuous measurement of thermodynamic activity of the oxygen in sodium (in contrast to the plugging meter which can only be sampled at time intervals dictated by system conditions as described in the previous chapter). The cell generates a voltage that is dependent on the ratio of the oxygen activity in sodium (c)to that of some reference electrode. Unlike the plugging meter (PM), the galvanic cell is selective to oxygen, so only a change in *oxygen* concentration will result in a change in voltage. A basic oxygen sensor design is shown in figure 3.1[1].

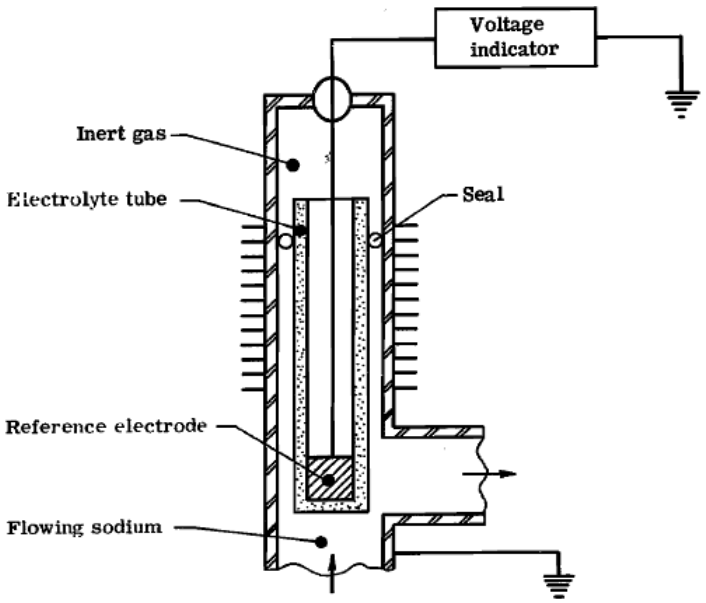

Figure 3.1: A simple schematic of an electrochemical O_2 sensor by Minushkin and Kolodney[1]

An electrochemical cell is constructed by enclosing a reference electrode of known oxygen partial pressure in a solid electrolyte and submerging the assembly in liquid sodium. The reference electrode can be constructed using air and a catalyst metal, but for initial discussion a metal-metal oxide reference electrode is assumed. Reference electrode theory is discussed in detail in section 3.2.2. The cell can be described as:

$$\text{Na, } \text{Na}_2\text{O(D)} \text{ || Solid Electrolyte || Me, } \text{Me}_2O \tag{3.1}$$

The reference electrode, defined as (Me, Me_2O) above, is a metal-metal oxide sealed at equilibrium with the gas head-space above. The oxygen partial pressure of this electrode is now strictly a function of temperature. (Na, Na_2O(D)) is sodium oxide dissolved in liquid sodium, and this metal-metal oxide acts as the second electrode. If Me_2O is less stable than Na_2O, then oxygen will transfer from right to left in the cell described above. This reaction can be described as:

$$2\text{Na} + \text{Me}_2\text{O} \rightarrow \text{Na}_2\text{O(D)} + 2\text{Me} \tag{3.2}$$

This reaction will generate an EMF, E, defined by:

$$E = \frac{1}{2F} \int_{\mu_R}^{\mu_L} t_{ion}\, d\mu \tag{3.3}$$

μ_L and μ_R are the chemical potentials of the left and right sides of the reaction in equation 3.2 above. F is the faraday constant. t_{ion} is the coefficient of ionic conductivity of the electrolyte material (defined as the ionic conductivity divided by the total conductivity, see section 3.2.3) and is defined to be unity for an ionic conductor. Equation 3.3 then becomes a measure of free-energy change in the reaction labeled equation 3.2. So equation 3.3 becomes:

$$E = -\frac{\Delta G^o}{2F} \tag{3.4}$$

The above relation becomes the Nernst equation after substituting for the free energy of reaction:

$$E = E_o - \frac{RT}{2F} \ln \left(\frac{[\text{Me}]^2 \, [\text{Na}_2\text{O(D)}]}{[\text{Na}]^2 \, [\text{Me}_2\text{O}]} \right) \tag{3.5}$$

The quantities in brackets are the activities of the respective species in the system. E_o is the standard electrode potential of the cell and is a function of cell operating temperature[2]:

$$E_o = \frac{\Delta G^o\left(\mathrm{Me_2O}\right) - \Delta G^o\left(\mathrm{Na_2O}\right)}{2F} \tag{3.6}$$

ΔG^o is the standard free energy of formation of the oxides at operating temperature. Note that for a platinum-oxygen reference system (or sometimes palladium), the metal acts as a catalyst, not a reactant, so no platinum is actually consumed during operation. In this case, the standard cell potential simplifies to:

$$E_o(\text{catalyst}) = -\frac{\Delta G^o(\mathrm{Na_2O})}{2F} \tag{3.7}$$

For all metal-metal oxide reference systems, both liquid and powder, equation 3.6 describes the system chemistry. Platinum-air and other catalyst-gas reference systems are described by equation 3.7.

The activity of Me and Me_2O is unity and since the oxygen concentration of sodium is very low, Raoult's law can be implemented and the activity of sodium becomes unity, $[\mathrm{Na}] = 1$. The Nernst equation for this galvanic cell is simplified to[1][3]:

$$E = E_o - \frac{RT}{2F} \ln\left[\mathrm{Na_2O(D)}\right] \tag{3.8}$$

Equation 3.8 is a relationship between cell voltage, temperature, and oxygen activity in sodium. The activity of sodium oxide dissolved in sodium is related to concentration via the activity coefficient, γ, by the equation $[\mathrm{Na_2O(D)}] = \gamma c$. At saturation concentration, c_o, the activity of sodium oxide is unity, so $[\mathrm{Na_2O(D)}] = \gamma_o c_o = 1$. Finally, at low concentrations seen in sodium, γ is roughly constant ($\gamma \approx \gamma_o$). These substitutions can be made to equation 3.8 and the following relationship between oxygen and sensor voltage can be acquired:

$$E = E_o - \frac{RT}{2F} \ln\left(\frac{c}{c_o}\right) \tag{3.9}$$

It should be noted that c_o is a function of temperature, $c_o\,(T)$, as discussed in detail in the following section.

3.2.1 Oxygen concentration at saturation (c_o)

There is some inconsistency in solubility relationships from published data. Noden assembled a thorough collection of solubility measurements and determined a best fit through all of the data, which is shown in figure 7.8. All of the cold trap and plugging measurements quoted in this paper were calculated from the Noden correlation[4]:

$$\log_{10}\left[c_o(T)\right] = 6.1579 - \frac{2384.2}{T} \tag{3.10}$$

T in the Noden correlation is temperature in kelvin. This relationship describes the logarithmic dependence of oxygen concentration on temperature. The trend in figure 7.8 is clear, however, the variability in the individual measurements is substantial. Thus, errors in the solubility curve will propagate through to errors in expected sensor performance. This possible source of discrepancy will be analyzed later in this report.

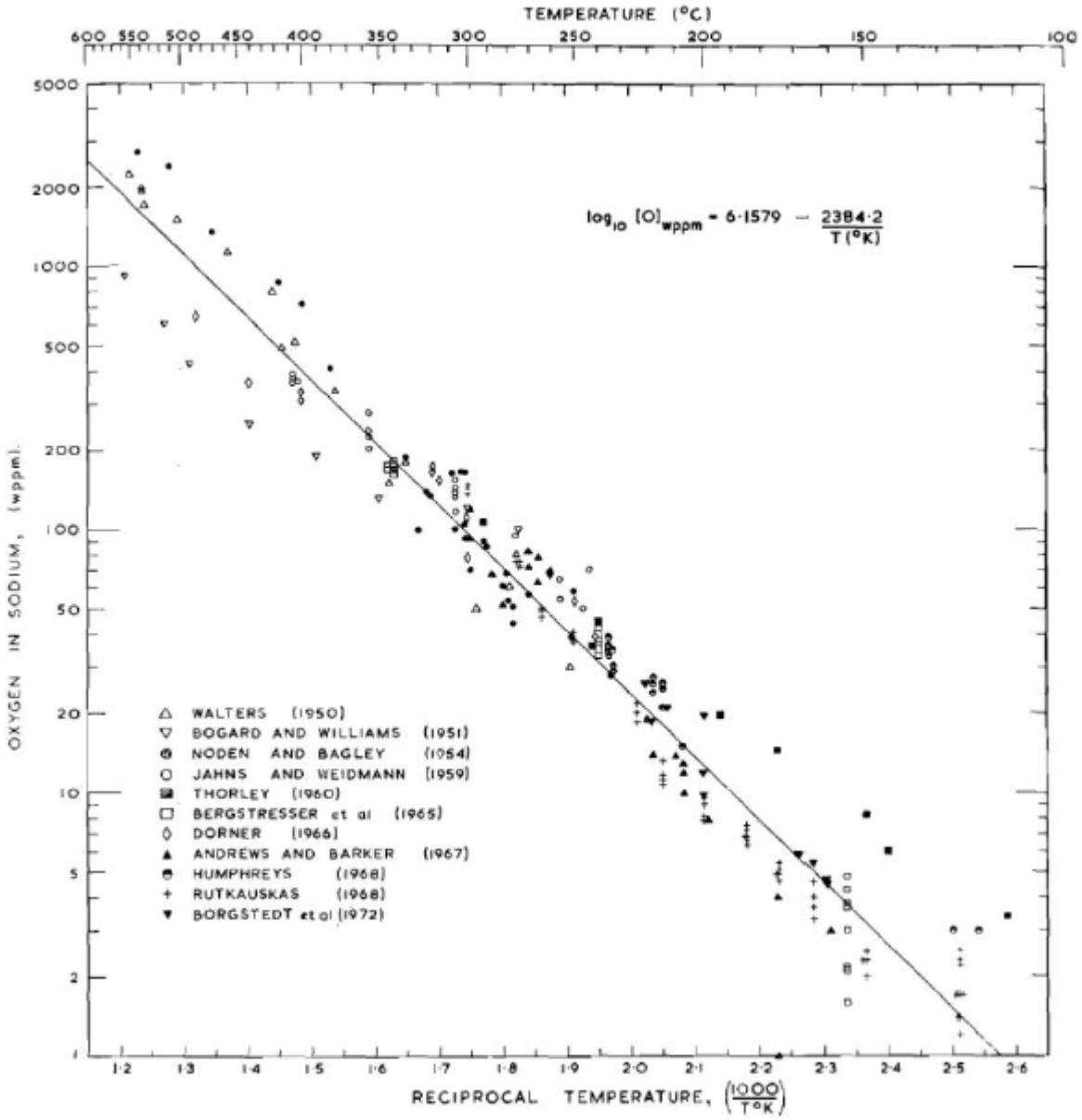

Figure 3.2: Oxygen solubility data assembled by Noden[4]from [5, 6, 7, 8, 9, 10, 11, 12, 13]

3.2.2 Reference electrode

Two different reference systems were used in this research. Engineering considerations for these reference electrodes are described below.

The reference electrode must produce and maintain a predictable voltage over the lifetime of the sensor. If the reference signal is unstable then changes in sensor signal cannot be attributed to changes in oxygen in sodium. The reference electrode must also be compatible with the solid electrolyte and reach equilibrium quickly. The automotive industry uses air in contact with a porous metallic catalyst (usually platinum or palladium [14]) for a reference electrode. Air similarly works with sodium, however, the difference in oxygen pressure on either side of the electrolyte would be large, and the sensor would have to have access to fresh air constantly. It is desirable for both sides of the electrolyte to be close in oxygen partial pressure. Some of the results presented in this paper were achieved using an air-catalyst reference system.

Using a metal-metal oxide in a sealed environment ensures the oxygen pressure would be constant at a given temperature. Sodium-sodium oxide is perhaps the most obvious choice for a reference electrode since it oxidizes quickly and would be very nearly the same concentration as the liquid sodium which is being measured. In addition, at any operating temperature, sodium is a liquid, and a good electrical connectivity is ensured with the electrolyte (many liquid reference systems have been tested, not only for sodium but for lead-bismuth as well[15]). However, sodium is not inert and it will attack the electrolyte. Many sensors have been made using a metal-metal oxide powder as the reference electrode[16]. For example, iron-iron oxide would maintain a low partial pressure; however, the complexity of various oxides that would form at low temperature would make predicting the reference voltage difficult. Nickel and copper both form simple oxides with low oxygen pressures. In addition, they are metal deficient semi-conductors which means that they create metal vacancies as they oxidize, allowing metal ions to diffuse through the oxide and thereby speeding up the oxidation process. Thus, these metals could absorb and maintain oxygen pressure in

the reference chamber and do so quickly. The rate of oxidation could be considered as a measure of how quickly the metal would respond to changes in temperature and oxygen pressure. It has been shown that copper has a faster oxidation coefficient than nickel at the temperatures these sensors will be tested at (320[C]) [17]. While many different metals could work as a reference electrode, copper was chosen as the reference electrode for the experiments presented in this report for the reasons described above.

3.2.3 Solid electrolyte

Zirconia (ZrO_2), when doped with a small weight percentage of yttria (Y_2O_3), becomes an ionic conductor. The added yttrium ions (3+) replace the zirconium ions (4+) in the lattice. In order to preserve charge neutrality, for every two yttrium ions introduced into the ceramic, one oxygen vacancy (2−) is introduced. Similar effects are seen with calcia stabilized zirconia (CSZ) and yttria stabilized thoria (YST). The diagram shown in figure 3.3[1] illustrates the introduction of oxygen vacancies in the electrolyte.

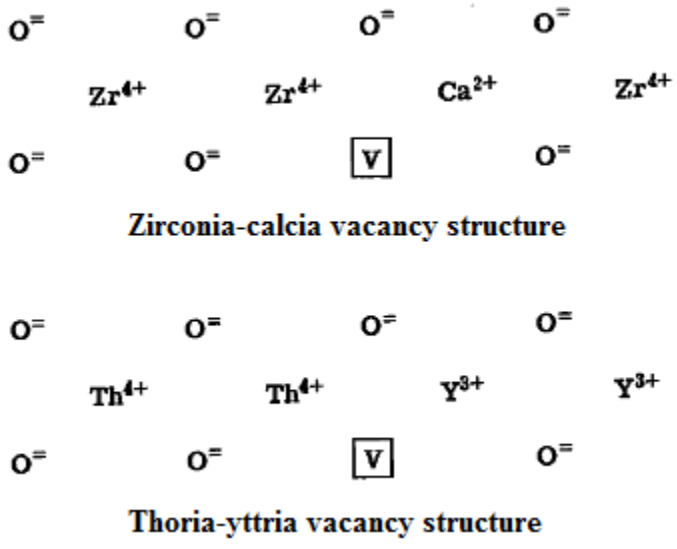

Figure 3.3: Oxygen vacancies are introduced into the lattice of the electrolyte in order to maintain charge neutrality after the addition of dopant ions[1].

By increasing the concentration of vacancies, the ionic conductivity increases until the

vacancies begin to interact with one-another. When the vacancies begin to interact and form clusters, the structure of the material begins to change, and ionic conductivity shuts down. The peak ionic conductivity in YSZ has been observed around eight weight-percent yttria [18].

The coefficient of ionic conductivity, t_{ion}, describes the ratio of ionic conductivity of a material to its electronic conductivity, and is defined in equation 3.11, where σ refers to the conductivity of the respective species:

$$t_{ion} = \frac{\sigma_{ion}}{\sigma_{ion} + \sigma_{electron}} \tag{3.11}$$

In order to derive equation 3.9, t_{ion} was assumed to be near unity, meaning that the electronic contribution to the total conductivity is negligible. Diversions from stoichiometry in the ceramic will induce some electronic conductivity, thereby causing the generated emf to be less than predicted by theory.

Chemical effects of deviating from stoichiometry

When the number of oxygen ions and number of metal ions are equal (accounting for vacancies), the electrolyte is stoichiometric. However, a change in oxygen partial pressure can cause a departure from stoichiometry within the ceramic. For example, if one mol of a material of initial composition MeO is subjected to a region of low oxygen pressure, then oxygen will leave the ceramic. If some number, n oxygen ions (O^{2-}) escape from the electrolyte, then $n/2$ molecules of oxygen gas are formed (O_2) and n oxygen vacancies (V_o) are introduced into the lattice. The result of this oxygen departure is the ejection of $2n$ electrons from the electrolyte. These electrons (negatively charged) are pushed into the electrolyte conduction band and therefore contribute to the *electronic* conduction of the electrolyte ($\sigma_{electron}$). This reaction can be written as:

$$6.02\times10^{23}\times\mathrm{MeO}-n\times O^{2-}\rightarrow(6.02\times10^{23}-n)\times\mathrm{MeO}+\frac{n}{2}\times\mathrm{O}_2+n\times V_o+2n\times e^- \quad (3.12)$$

Assuming the number of ions ejected is small compared to the amount of MeO present (for this example, $6.02\times10^{23}\gg n$), equation 3.12 can be simplified to:

$$O^{2-}=\frac{1}{2}O_2+V_o+2e^- \quad (3.13)$$

The equilibrium constant, K, for equation 3.13 is:

$$K=\frac{P_{O_2}^{1/2}\left[V_o\right]\left[e^-\right]^2}{\left[O^{2-}\right]} \quad (3.14)$$

If the oxygen vacancy concentration is fixed by the dopant concentration (yttria, calcia, etc), then the activity of the vacancies will be unity.

$$K=\frac{P_{O_2}^{1/2}\left[e^-\right]^2}{\left[O^{2-}\right]} \quad (3.15)$$

Now, if there are no other sources of electrons in the lattice, then:

$$\left[V_o\right]=1/2\left[e^-\right] \quad (3.16)$$

This relationship can be plugged into equation 3.15, and re-arranged for the electron activity.

$$\left[e^-\right]=\frac{\left[O^{2-}\right]^{1/2}K^{1/2}}{P_{O_2}^{1/4}} \quad (3.17)$$

Electronic conductivity is proportional to the concentration of electrons in the conduction band of the electrolyte. According to equation 3.17, electronic conductivity is inversely related to oxygen pressure. So decreasing the P_{O_2} above the electrolyte will increase the

electronic conductivity, reducing the coefficient of ionic conductivity, t_{ion}.

In the event that the electrolyte is placed in a high P_{O_2} environment, then oxygen gas will be pushed into the ceramic. Oxygen gas will interact with the vacancies in the electrolyte to produce oxygen ions (molecular oxygen can not occupy the vacancies, so the ions must be "produced"). In order to preserve charge neutrality, electron holes will be introduced to the product side of the reaction as well (the mathematical equivalent would be adding electrons to the reactant side of the reaction equation). The relationship corresponding to equation 3.13 is:

$$\frac{1}{2}O_2 + V_o = O^{2-} + 2e^+ \tag{3.18}$$

In the equation above, e^+ represents an electron hole, not a positron. An electron hole is a mathematical construct which is the absence of an electron. The electron hole activity can be determined in the same manner that the electron activity was determined above, in terms of the equilibrium coefficient, K:

$$\left[e^+\right] = \frac{P_{O_2}^{1/4}}{K^{1/2}\left[O^{2-}\right]^{1/2}} \tag{3.19}$$

So the increase in P_{O_2} over the electrolyte increases the electron hole activity in the conduction band, and therefore also induces some electronic conductivity.

Thus, any deviation in stoichiometry will result in an increase in electronic conductivity in the electrolyte, whether the electrolyte is subject to an increase or decrease in oxygen P_{O_2}. t_{ion} for zirconia electrolytes has been shown to be near unity for oxygen pressures between one and 10^{-15}[ATM] ($t_{ion} > 0.99$ for 10^{-15}[ATM] $\leq P_{O_2} \leq$ 1[ATM]) [19, 20, 21, 22]. If the oxygen pressure of the reference electrode is held in this range, then no deviations from stoichiometry are expected in the YSZ. However, oxygen saturated sodium at 320[C] has a oxygen pressure of 10^{-60}[ATM][23], and is even lower for unsaturated sodium. Zirconia electrolytes have been studied at 1000[C] at pressures down to 10^{-40}[ATM], and were found

to lose 0.6% of their oxygen in these conditions[24]. While data has not been found at oxygen sensor operating conditions, it is probable that some oxygen is still depleted from the ceramic, which could cause electronic conductivity. By comparison, thoria electrolytes have been found to be better ionic conductors, and lose only 0.05% of their oxygen when equilibrated at 1000[C], and 10^{-40}[ATM][25].

3.3 Expected Sensor Signal

The first term in equation 3.9 is E_o, the standard electrode potential. This quantity can be determined from thermodynamic data bases for the gibbs energy of formation of the constituents of the electrode (according to equations 3.6 and 3.7. These values were calculated using *HSC 7 Chemistry* software from Outec Research. These values are also available in literature from Barin and Knacke[26, 27].

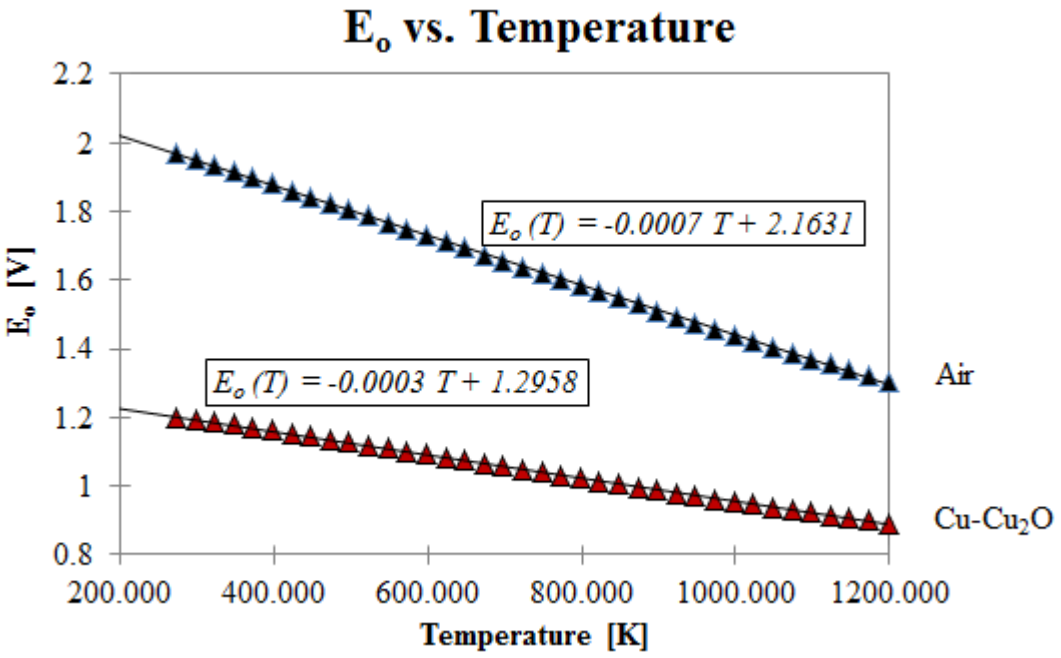

Figure 3.4: The standard electrode potentials for air and copper-copper oxide reference electrodes calculated according to equations 3.7 and 3.6

The noden correlation was used to determine the oxygen concentration at saturation,

which was given in equation 5.1. Now all the terms in equation 3.9 are defined, and if the sensor is operated at 320[C], the following functions of oxygen concention, c, are found. These equations are plotted in figure 6.2.

For copper-copper oxide:

$$E(c) = 1.249 - 0.0256 \ln(c) \tag{3.20}$$

For air:

$$E(c) = 1.879 - 0.0256 \ln(c) \tag{3.21}$$

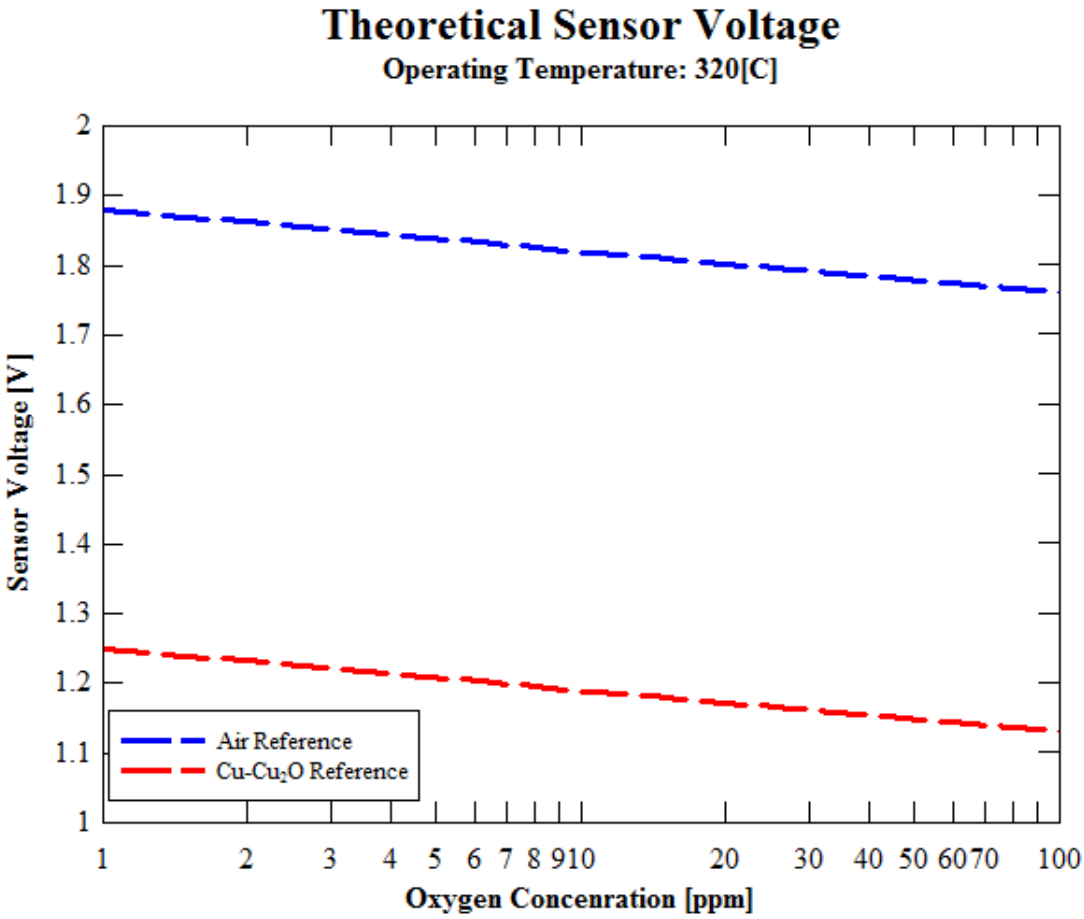

Figure 3.5: Theoretical voltage output for both types of sensors used in this research.

It is important to note that changing the reference electrode does not effect the theoretical

slope of the oxygen sensor. Mathematically, changing the reference system only changes E_o and c_o. Neither of these are multiplied by the logarithm term in equation 3.9 (implementing the law of logarithms moves the $\ln(c_o)$ term out with the E_o term). A closer analysis of effects on the signal slope will be presented in the *Oxygen Sensor Results and Analysis* chapter of this report.

3.4 Past Sensor Research

The greatest problem facing the galvanic cell oxygen sensor is the compatibility of the porous ceramic barrier with liquid sodium. Since sodium oxide is more chemically stable than most other oxides, the oxide of the conductive ceramic will preferentially move into sodium solution, thus corroding away the critical outer ceramic layer. Historically the best material for an outer conductive layer has been yttria stabilized thoria (YST)[28].

The compatibility of various ceramics with liquid sodium not only depends on the chemical composition, but has been found to be strongly linked to the method of fabrication. For example, zirconia bricks were completely disintegrated in a test in which high fired zirconia crucibles survived with weight loss of only 0.2%[29]. Indeed, some materials have been found to see little attack (thoria) or no attack (beryllia) from sodium[28]. However, the list of candidate materials shrinks considerably when the ionic conductivity at operating temperature is required. The past work discussed below was done with the best materials available, which were zirconia and thoria based electrolytes.

The vast majority of past oxygen sensor research has been conducted with YST electrolytes[1, 3, 28, 30, 31, 32, 33]. Examples of these sensors are shown in figures 3.6, 3.7 and 3.8.

Many of these authors report research on calcium-stabilized zirconia as well, but this material typically yielded poor compatibility with sodium, so development moved forward with YST instead.

While the sensors have been inconsistent in voltage output, they consistently generate

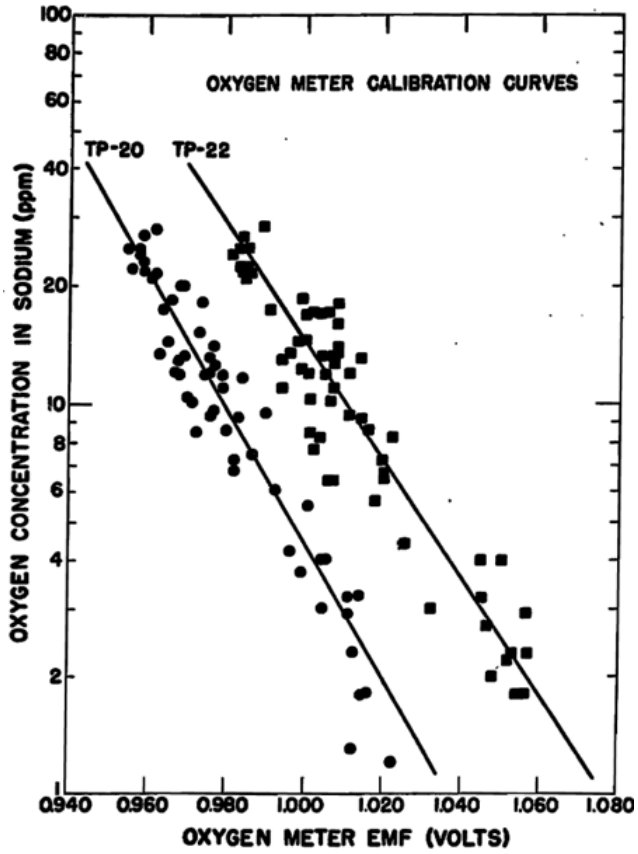

Figure 3.6: This data was collected by McPheeters[33]. Two identical sensors are shown to illustrate the inconsistency from sensor-to-sensor.

a voltage which is less than predicted by theory. The slope of the generated signal has considerable variability (cell-to-cell variation was found to be *greater* than 10% [30]), but is close to the theoretical slope. The causes of these differences have not been conclusively determined. Many of the authors suggest in closing arguments that the signal deviations are attributable to imperfect ionic conductivity[1] and errors in the solubility correlation[31]. Other hypotheses were that the reference electrode made poor contact with the electrolyte, and these authors suggested a liquid reference electrode. However, liquid reference electrodes have been tried since, and the generated signal is still under expectations[15, 31].

While the data presented above gives a strong report that the sensors do not agree with theory, past research has not been able to explain why. Thoria sensors typically lasted over 1000[hr], so each sensor could simply be calibrated against a cold trap, then used as

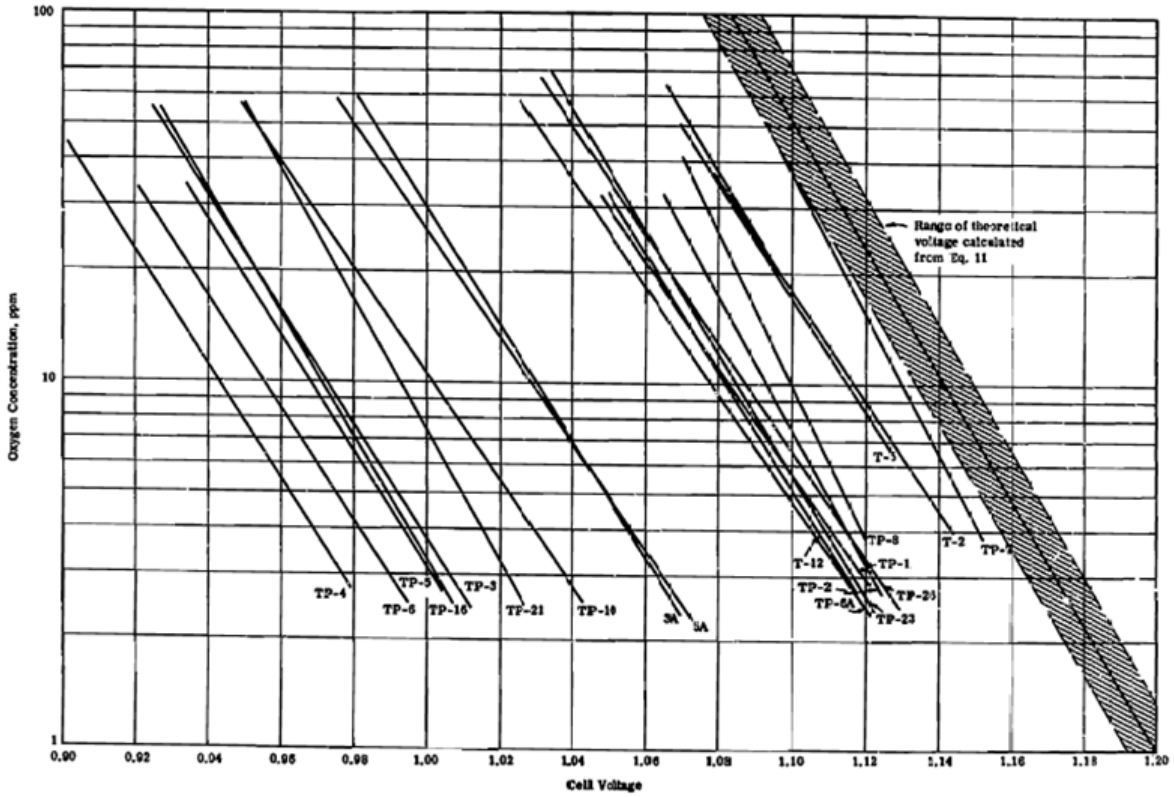

Figure 3.7: Minushkin put together the most through compilation of data[1], but his data always under-predicted theory, and had a range of slope outputs. Not only is the voltage inconsistent, but the slope of the signal seems to vary from sensor-to-sensor.

a continuous oxygen monitor for the remainder of its lifetime. However, with a growing preference to move away from reliance on actinides in the United States, a sensor of an alternative material is desired. Since zirconia-based electrolytes are less stable in sodium than thoria, these sensors will need to be cost effective as short-term, disposable sensors. Thus, the need to calibrate before use would ideally be phased out of the design process.

A closer look at sensor deviations from theory will be taken later in the analysis section of this report.

Supplemental corrosion research has been conducted, and the summary of results is available in Chapter 5, *Ceramic Corrosion in Liquid Sodium.*

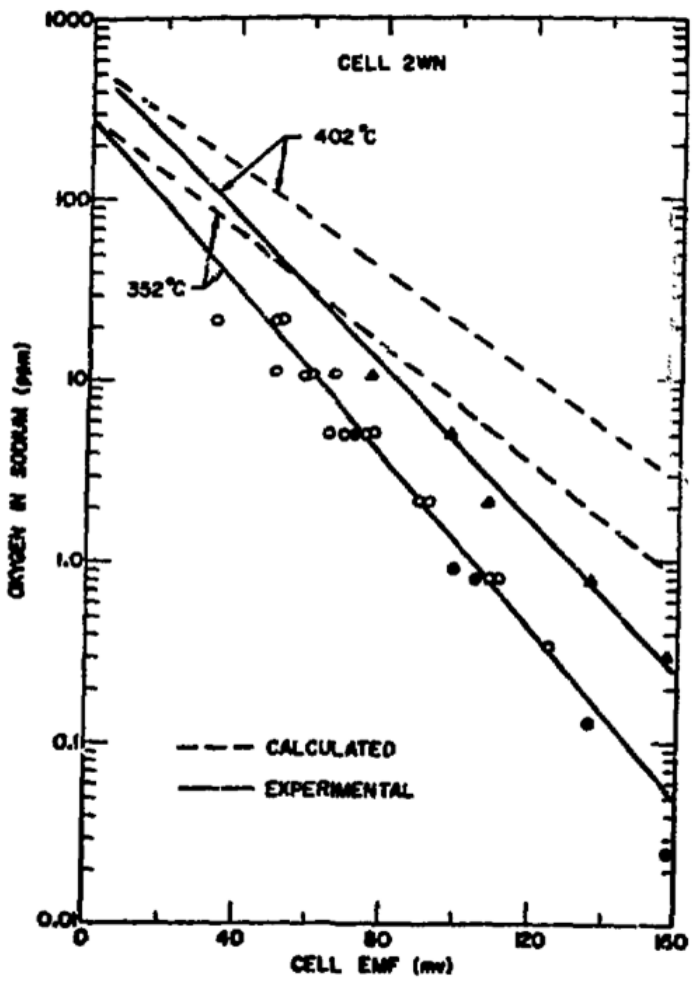

Figure 3.8: Smith's data exhibited similar behavior to previous work[31]. He investigated a sodium-sodium oxide reference electrode.

3.5 Current Sensor Research

Several research groups around the world are currently working on developing an electrochemical oxygen sensor. Zirconia, thoria, and ceria based electrolytes are under investigation in France, India, and South Korea, as well as the zirconia sensors discussed in this report.

The Atomic Energy and Alternative Energies Commission (CEA) in France has two research groups independently working on developing a liquid sodium oxygen sensor. One research group at CEA Cadarache, lead by Christian Latge, is developing a yttria stabilized thoria (YST) electrolyte sensor based off the British Harwell sensors from the 1980s[34, 35,

36]. The Harwell sensors were used in the French sodium fast reactor, Superphoenix, but have since become unavailable. Latge's group is working on re-producing this technology, but does not currently have any data or publications available[37]. Development has been slow for these sensors because of the precautions necessary for working with radioactive materials.

The second French oxygen sensor research group is at CEA Saclay, headed by Jean-Louis Courouau[38]. This group is focusing on developing an oxygen sensor using a non-thoria electrolyte. They have begun testing on a variety of different ceramics with indium reference electrodes. However, they do not have any published sensor data yet, and their unpublished results show high corrosive attack of the various electrolyte materials. CEA-Saclay has a ceramics division on-site, and are accumulating a substantial variety of various materials and sintering recipes to test in sodium[39].

South Korea's Ulsan National Institute of Science and Technology (UNIST) is working on non-thoria sensors as well, and the lead researcher's name is Sang Hun Shin. His most recent publications are focused on ceramic corrosion and ionic conductivity assessments of YSZ and gadolinia doped ceria (GDC). Static and flowing sodium test facilities have been developed, but oxygen sensor development is ongoing[40].

India is developing a YST sensor. Preliminary publications state that a sodium-compatible YST electrolyte has been developed, and is currently being investigated as a sensor electrolyte[41]. More modern data has not been found, however (past 2011).

After an exhaustive online search, and confirming with colleagues at CEA and Argonne National Lab (ANL), it does not appear that oxygen sensor development is currently taking place in Japan. Unpublished work seems to have been done in Russia in recent years based on work done for lead-bismuth alloys, but they do not appear to have results yet[37, 39, 42].

In summary, the only currently functioning non-thoria oxygen sensors in the world are the YSZ sensors discussed in this report. The French and South Koreans are currently developing similar sensors. Thoria sensors, while current data suggests they are a better long-term solution to the oxygen sensor problem, are slow to develop due to the radioactivity

of the material.

3.6 Summary of Chapter 3

The galvanic cell was described from fundamental electrochemical principles. The fundamental physical and chemical phenomena at each component of the cell were described in detail. This instrument offers continuous measurement without the low-concentration limitations of the plugging meter.

Past oxygen sensor work has been described, and common issues associated with sensor development have been listed. Past researchers have proposed possible explanations for signal deviations from theory, and these ideas have been described. If a short lifetime sensor is to be made of YSZ and useful in sodium application, an improved understanding of the sensor signal is needed.

The goal of this research is not only to demonstrate that YSZ can be used to produce a sensor which gives a signal of the correct functional form, but also to help narrow the gap in understanding of actual sensor signal from theory. While a comprehensive understanding of experimental deviations from theory may be unrealistic given the complex nature of electrochemical and thermodynamic processes, and given the struggles of past researchers in this field, this report describes a hypothesis-testing method which successfully advances oxygen sensor theory closer to experimental data.

Chapter 3 Bibliography

[1] B. Minushkin & M. Kolodney. Development of a continuous electrochemical meter for oxygen in sodium. Technical report, United Nuclear Corporation, 1967.

[2] J. McKee B. Minushkin, editor. *Development of Electrochemical Methods for Oxygen Monitoring and Removal in Sodium*. United Nuclear Corporation, April 1965.

[3] H. Steinmetz. Development of a continuous meter for oxyggen in sodium. Technical report, United Nuclear Corporation, White Plains, New York, January 1963.

[4] J. D. Noden. A general equation for the solubility of oxygen in liquid sodium. *Journal of the British Nuclear Energy Society*, 12(1):57–62, 1973.

[5] S.L. Walters. Effect of adding oxygen to sodium flowing in a stainless-steel system. Technical Report NP-1955, Mining Safety Appliances, 1950.

[6] A.D. Bogard and D.D. Williams. Solubility of sodium monoxide and sodium hydroxide in metallic sodium. Technical Report NRL-3865, Naval Research Laboratory, 1951.

[7] J.D. Noden and K.Q. Bagley. Solubility of oxygen in sodium and nak alloy. Technical Note 80, United Kingdom Atomic Energy Association (UKAEA), 1954.

[8] W. Jahns and G. Weidmann. The determination of low oxygen concentrations in sodium. Technical Report 1:189-190, Nucleonick, 1959.

[9] K.S. Bergstresser et al. Determination of trace amounts of oxygen added to metallic sodium. Technical Report LA-3343, Los Alamos Scientific Laboratory, 1965.

[10] S. Dorner. Solubility of oxygen in sodium. Technical Report EURFNR-179P, English Translation of Projekt Schneller Bruter Report, 1966.

[11] R.C. Andrews and K.R. Barker. Effect of high temperature sodium on the mechanical properties of candidate alloys for the lmfbr program. Technical Report MSA R67-207, Mining Safety Appliances, 1967.

[12] V.J. Rutkauskas. Determination of the solubility of oxygen in sodium by vacuum distillation. Technical report, Los Alamos Scientific Laboratory, July 1968.

[13] J.R. Humphreys. Argonne national laboratory reactor development program progress reports. Technical Report ANL-7518 & ANL-7460, Argonne National Laboratory, 1968.

[14] J.K. Norskov. Origin of the overpotential for oxygen reduction at a fuel-cell cathode. *Physical Chemistry Journal*, September 2004.

[15] Ning Li T.W. Darling. Oxygen concentration measurement in liquid pb-bi eutectic. Technical report, Los Alamos National Laboratory, January 2001.

[16] B. Minushkin. *Electrochemical Oxygen Meter Operating Manual*. United Nuclear Corporation, White Plains, New York, August 1965.

[17] O. Kubaschewshi and B.E. Hopkins. *Oxidation of Metals and Alloys*. Butterworth and Co., 2nd edition, 1953.

[18] Gunter Borchardt Robert A. Jackson Martin Kilo, Christos Argirusis. Oxygen diffusion in yttria stabilized zirconia - experimental results and molecular dynamics calculations. In *International Bunsen Discussion Meeting*, volume 78, October 2002.

[19] W.D. Kingery et. al. Oxygen ion mobility in cubic $zr_{0.85}$ $ca_{0.15}$ $o_{1.859}$. *Journal of the American Ceramic Society*, (42:393), 1959.

[20] Kaleui Kiukkola and Carl Wagner. Measurements on galvanic cells involving solid electrolytes. *Journal of the Electrochemical Society*, (104:379), 1957.

[21] B.C.H. Steele and C.B. Alcock. Factors influencing the performance of solid electrolytes in high temperature thermodynamic measurements. In *AIME Annual Meeting*, New York City, February 1964.

[22] D.W. Stricker and W.G. Carlson. Ionic conductivity of cubic solid solutions in the system cao-y2o3-zro2. *Journal of the American Cermaic Society*, (47:122), March 1964.

[23] R. Swalin. *Thermodynamics of Solids*. Number Chap. 7, p. 84. John Wiley and Sons, New York, 1962.

[24] H. Schmalzried. Uber zirkondioxyd als elektrolyt fur elektrochemische utersuchungen bei hoheren temperaturen. *Zeitschreift fur Electrochemie*, (66:572), 1962.

[25] R.A. Rapp. Personal communication. Technical report, Ohio State University, May 1964.

[26] I. Barin. *Thermochemical Data of Pure Substances*. VCH Verlags Gesellschaft, Weinheim, 1989.

[27] I. Barin & O. Knacke. Thermochemical properties of inorganic substances. Technical report, Springer, NY, 1973.

[28] O.J. Foust, editor. *Sodium-NaK Engineering Handbook*, volume 5. Liquid Metal Engineering Center, 1979.

[29] Kumar Blomquist Leibowitz Sowa Pavlik Baker Fink, Heiberger. Interactions of refractory materials with sodium. Technical report, Argonne National Laboratory, 1976.

[30] B. Minushkin. The liquid metal oxygen meter. Technical report, United Nuclear Corporation, White Plains, New York, 1965. p.272-273.

[31] D.L. Smith. Monitoring and measurement of oxygen concentrations in liquid sodium. Technical report, International Conference on Liquid Metal Technology in Energy Production, 1976.

[32] J. Burda M. Fresl D. Jakes, J. Kral. Development of electrochemical oxygen meter for liquid sodium. In *Solid State Ionics 13*, pages 165–173, North-Holland, Amsterdam, 1984. Nuclear Research Institute, Czechoslovakia.

[33] Charles C. McPheeters and James M. Williams. A comparison of three methods of oxygen concentration measurement in sodium. Technical Report La-DC-7743, Los Alamos Scientific Laboratory, December 1966.

[34] R.C. Asher et al. The harwell oxygen meters and harwell carbon meter. Technical report, British Nuclear Engergy Society, 1984.

[35] M.R. Hobdell and C.A. Smith. Electrochemical techniquies for monitoring dissolved carbon, hydrogen, and oxygen in liquid sodium. *Journal of Nuclear Materials*, (110):125–139, 1982. Berkeley Nuclear Laboratories, United Kingdom.

[36] R.G. Taylor and R. Thompson. Testing and performance of electrolytic oxygen meters for use in liquid sodium. *Journal of Nuclear Materials*, 1983.

[37] C. Latge. In-person conversation. Fast Reactor Conference, FR13, March 2013.

[38] J. Courouau et al., editor. *Corrosion by oxidation and carburization in liquid sodium at 550[C] of austenitic steels for sodium fast reactors*, Paris, France, March 2013. IAEA, Fast Reactor Conference - FR13. CEA Saclay, France.

[39] J. Courouau. In-person conversation and email correspondence. Fast Reactor Conference, FR13, March-June 2013.

[40] S.H. Shin et al. Development of electrochemical oxygen sensor and experimental system for materials compatibility test for ultra-long cycle fast reactor. In *FR13*, Paris, France, March 2013. UNIST, IAEA.

[41] R. Ganesan et al. Development of sensors for on-line monitoring of nonmetallic impurities in liquid sodium. *Nuclear Science & Technology*, 48(4):483–489, 2011.

[42] C. Grandy. In-person conversation and email correspondence. Department Manager, Nuclear Engineering Division, Argonne National Laboratory, June 2013.

Part II

Experiment, Results, & Analysis

Chapter 4

Experiment Design & Construction

Two sodium loop experiments and one static corrosion test facility have been constructed at UW-Madison. A high flow corrosion test loop has been running off site at UW's Stoughton facility, and a smaller oxygen sensor test loop has been running in a glovebox on campus. A brief overview of both systems and detailed descriptions of the most relevant components are given in this chapter.

Chapter 4 Contents

Contents

4.1 Variables Used in this Chapter

Variable	Physical Meaning
Φ_B	Magnetic flux [V s]
t	time[s]
ε	Electromotive force (EMF)[V]
$\vec{F}$	Force [N]
l	Length [m]
$\vec{I}$	Current [A]
$\vec{B}$	Magnetic field [T]
$\dot{m_c}$	Mass flow rate of coolant [g/s]
C_{p_c}	Specific heat capacity of coolant [cal/g-K]
T_{c_f}	Final temperature of coolant [K]
T_{c_i}	Initial temperature of coolant [K]
$\dot{m_{Na}}$	Mass flow rate of sodium [g/s]
$C_{p_{Na}}$	Specific heat capacity of sodium [cal/g-K]
T_{Na_f}	Final temperature of sodium [K]
T_{Na_i}	Initial temperature of sodium [K]
$\vec{v}$	Velocity vector [m/s]
q	Charge [C]
V	Voltage [V]
Q	Volumetric flow rate [m^3/s]
d	Inner diameter [m]
k_1, k_2, k_3	Correction factors [-]
D	Outer diameter [m]
ρ	Resistivity [Ω m]

4.2 Glovebox Sodium Loop

The glovebox sodium loop has been constructed entirely of 316 stainless steel (316SS). All permanent connections were welded, and removable connections use either Swagelok or VCR fittings. Copper crush rings inside both VCR fittings were found to leak due to differences in thermal expansion with the surrounding 316SS hardware. A 316SS washer was substituted in both VCR fittings, and the leaking problem has not resurfaced. The total loop volume is ≈ 0.2 gallons. This loop is contained in a glovebox, and an inert atmosphere is maintained for safety and fine oxygen control.

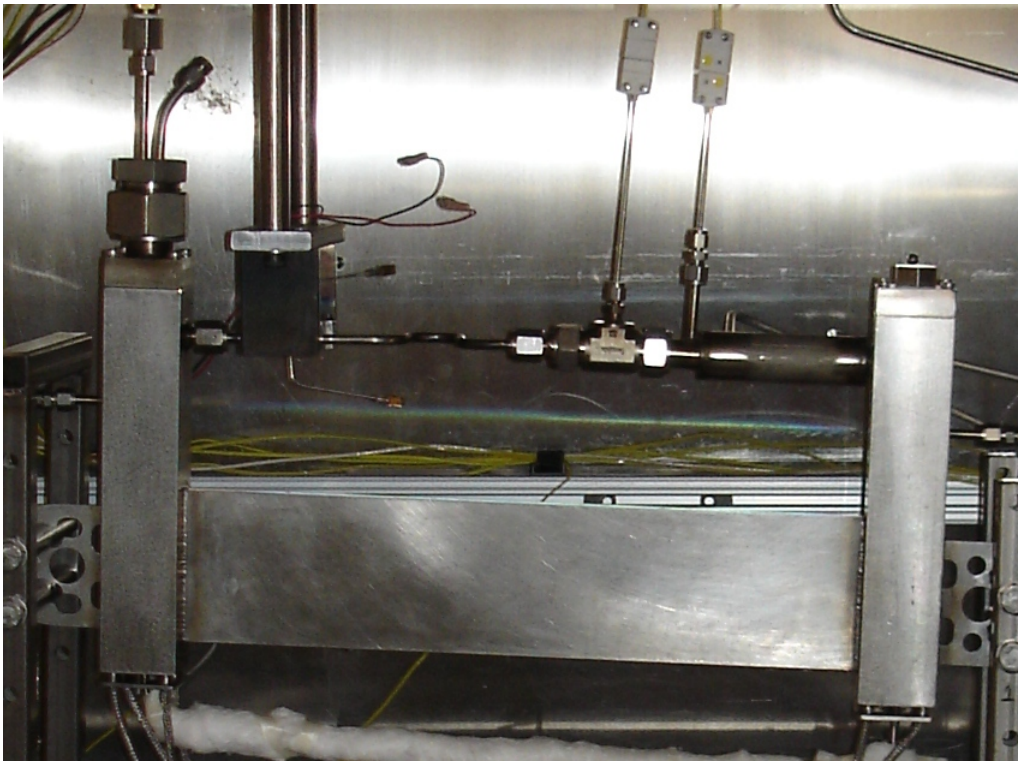

Figure 4.1: The glovebox sodium loop is made of 316 stainless steel, welded construction, and uses both Swagelok and VCR fittings. Total loop sodium capacity is ≈ 0.2 gallons.

4.2.1 Flat Linear Induction Pumps

The electrically conductive sodium is moved through the system using an electromagnetic induction pump. This enables the sodium to be pumped without any moving parts in contact with the liquid metal. The sodium channel was cut such that the sodium would fill a flat channel (see the bottom section of figure 4.1). A Flat Linear Induction Pump (FLIP) was then secured to each side of the sodium channel (see figure 4.2).

Figure 4.2: This figure shows one of the FLIPs before it was mounted to the loop. Notice the large wire coils responsible for the traveling magnetic field, which induces the eddy currents in the liquid sodium.

The FLIPs used for the UW gloveobx sodium loop were made by Dr. Steve Kuznetzoff.

FLIP Theory

The FLIP works on the principle of Faraday's Law of Induction[1]; a time-rate-change in magnetic flux ϕ_B through a conductive loop *induces* an electromotive force, ε in that loop

according to the following equation:

$$\frac{\partial \Phi_B}{\partial t} = -\varepsilon \tag{4.1}$$

The negative sign in equation 4.1 is a result of Lenz's law, which states that the induced current must act to oppose the direction of increasing flux. For this engineering application, the physics is not as significant as the result: by operating with a poly-phase current through the coils seen in figure 4.2, eddy currents are induced in the liquid sodium (I). These currents then act as a current carrying wire (of length, l) does in the presence of a magnetic field (B); they experience a force (F) according to the Lorentz Force Law:

$$\vec{F} = l\left(\vec{I} \times \vec{B}\right) \tag{4.2}$$

It should be noted that the Lorentz Force Law is usually seen in terms of a charge, q moving with velocity, $\vec{v}$. The equivalent is shown above for a collection of moving charges making up a current, $\vec{I}$.

On these basic principles of electromagnetism, the FLIP is able to provide the pressure necessary to push the liquid sodium through the sodium loop. In order to engineer this system, a deeper understanding of the physics is required, however. According to equation 4.2 above, the amount of force available to pump sodium is dependent on the strength of the induced current, and the magnetic field strength[2]. The magnetic field strength depends both on the current through the FLIP coils and the distance of separation between the two FLIPs. The coils of wire shown in the FLIP construction in figure 4.2 generate magnetic fields through these coils.

As the distance between the FLIPs decreases, the equivalent magnetic field increases[1]. However, as the FLIPs move closer to the hot sodium duct, they experience a greater incident heat flux that must be removed in order to avoid overheating.

The resin on the FLIP coils, which is the most susceptible component to heat damage, is

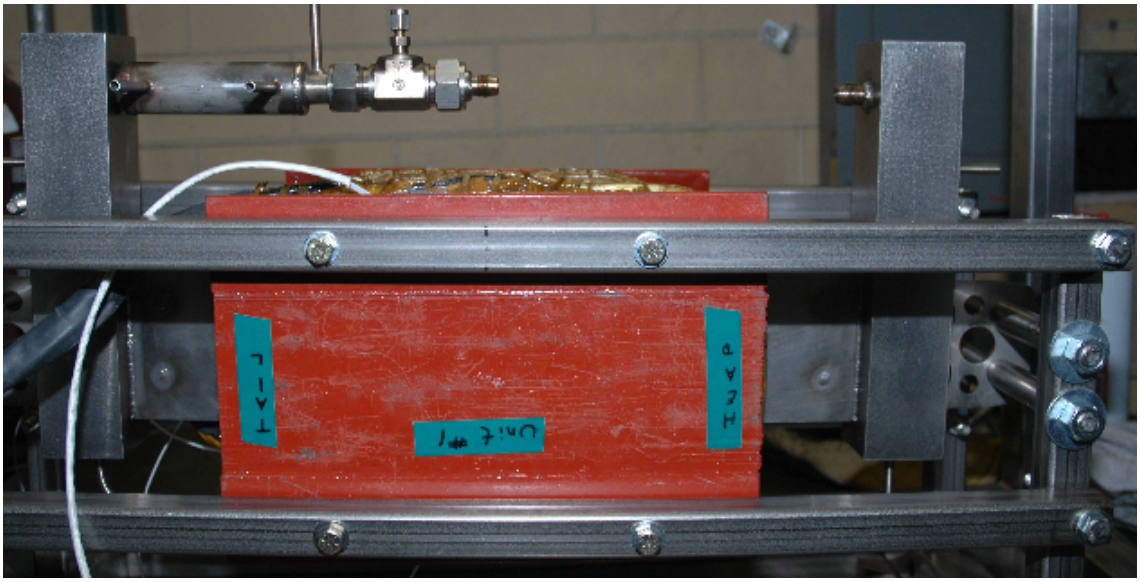

Figure 4.3: One of the two FLIPs before it was mounted to the loop. Notice they are on either side of the thin sodium channel. For the sake of a clear photo, the loop was un-insulated.

rated to 140[C]. In an effort to simplify construction and operation, the decision was made not to actively cool the FLIPs; as a result, the loop must be thermally insulated and the FLIPs must be spaced to adequately dissipate the incident heat on the FLIPs. Spacing the FLIPS further apart results in decreasing the magnetic flux in the sodium path, which therefore decreases the pumping efficiency (lowering the flow-rate of sodium). Thus, the FLIPs can not be spaced so far apart that adequate flow-rate can not be achieved for successful plugging events. Note that the photo presented in figure 4.3 was taken without insulation in place in order to clearly show the FLIPs mounted to the sodium duct.

4.2.2 Plugging Meter

The plugging meter in the glovebox sodium loop was constructed using a simple tube-in-tube counter-flow heat exchanger in series with a plugging orifice in a 1/2-inch stainless steel tube. The plugging orifice was secured in a 1/2-inch Swagelok fitting that connects the heat exchanger to a T-section as seen in figure 4.4.

The heat exchanger gas was chosen to be compressed air for ease of access. The inlet gas

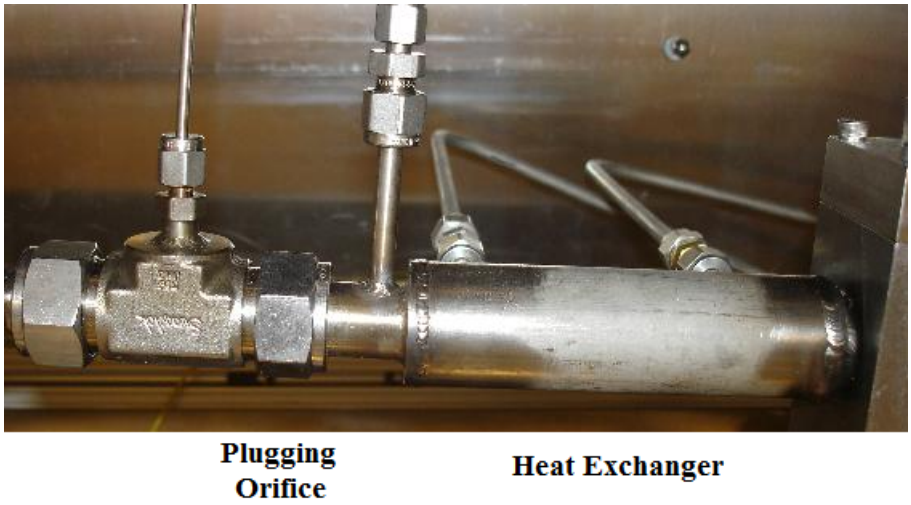

Figure 4.4: The plugging meter is made of a tube-in-tube heat exchanger followed by a plugging orifice, which is pressed in the Swagelok fitting that connects the heat exchanger to the T-fitting. Notice the two thermocouples mounted on either side of the plugging orifice.

is at 90[psi] and is plumbed through a flowmeter enroute to the heat exchanger. Thus, with a flowrate measurement of the coolant gas ($\dot{m}_c$), along with initial and final temperature measurements of both coolant and sodium (T_{c_i}, T_{c_f}, T_{Na_i}, T_{Na_f}) an energy balance was used to determine the sodium flowrate through the heat exchanger($\dot{m_{Na}}$).

$$\dot{m}_c \, C_{p_c} \left(T_{c_f} - T_{c_i}\right) = \dot{m}_{Na} \, C_{p_{Na}} \left(T_{Na_f} - T_{Na_i}\right) \tag{4.3}$$

$$\dot{m}_{Na} = \dot{m}_c \, \frac{C_{p_c}}{C_{p_{Na}}} \left(\frac{T_{c_f} - T_{c_i}}{T_{Na_f} - T_{Na_i}}\right) \tag{4.4}$$

This flowrate calculation was used to calibrate the flowrate measured by the electromagnetic flowmeter.

The size of the holes in the plugging orifice determine the minimum measurable oxygen concentration. The orifice installed in the glovebox loop (shown in figure 4.5) had six plugging holes and one flow-hole. The six plugging holes are 0.052" in diameter and are hexagonally spaced about a centered, 0.125" diameter flow-hole. The intention for this design was that while the plugging holes became obstructed with impurity, causing the drop in flowrate that indicates O_2 saturation, the large hole in the middle of the orifice will continue to allow flow.

The flow-hole helps prevent the orifice from completely clogging during a plugging test, and following a plugging test the flow-hole allows quicker clearing of the plugging holes.

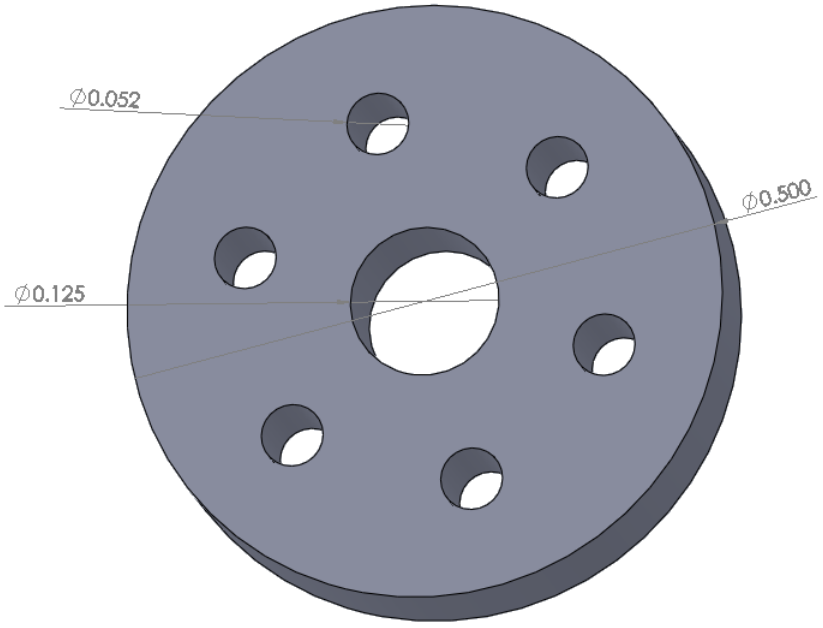

Figure 4.5: The plugging orifice shown above has two different plugging holes, the large hole is designed to never plug completely, and allow flowing sodium to quickly unplug the small holes after a plugging test.

In the event that the plugging orifice becomes completely plugged with impurities, the melting temperature of these oxides is too high to melt away with heater wire (in excess of 1130[C] for Na_2O). To un-plug the orifice in this scenario requires disassembling the loop and manually clearing the oxide with a push rod or sharp point. The large flow-hole helps prevent this occurrence.

Two thermocouples were installed in the plugging meter, one on either side of the plugging orifice. Since accurate plugging measurements depend on an accurate measurement of the saturation temperature, the temperature of the sodium *at the orifice* is desired. However, when the heat exchanger is turned off, a rush of hot sodium hits the first thermocouple from the vertical riser in the main loop. The temperature on the back side of the orifice, in contrast, rises at a much slower rate due to the choked flow through the orifice. As a result,

it was concluded that the "plugging temperature" would be taken as the temperature of the second thermocouple at the moment when the flowrate begins to increase on the back side of the plugging orifice. As a result, the temperature measurements are taken from about one inch away from the plugging orifice. Data and analysis that lead to this decision is presented in the chapter 5, *Plugging Meter Results & Analysis*.

4.2.3 Electromagnetic Flowmeter

Because liquid sodium is a electrically conductive metal, a flowmeter can be engineered using the principles of the Lorentz Force Law discussed above. As charged particles, q, move through a magnetic field, $\vec{B}$, with velocity, $\vec{v}$, they experience a force, $\vec{F}$. Equation 4.2 can be re-written to represent this specific scenario:

$$\vec{F} = q \left(\vec{v} \times \vec{B}\right) \tag{4.5}$$

So if the magnetic field is set up perpendicular to the sodium flow, the positive and negative charges in the sodium will experience a force orthogonal to these two directions in opposite directions. The result is a potential difference on opposing walls of the sodium tube.

Ideally, this system would consist of a uniform magnetic field perpendicular to the flow-path of liquid sodium. This set-up would generate the following voltage across the sodium duct[1]:

$$V = \frac{4BQ}{\pi d} \tag{4.6}$$

In equation 4.6, above, B is the magnitude of the magnetic field across the duct, d is the inner diameter of a circular sodium duct, and Q is the volumetric flowrate through the duct.

In effort to generate a uniform magnetic field, two NdFeB magnets were used, one on either side of the sodium duct (see figure 4.6).

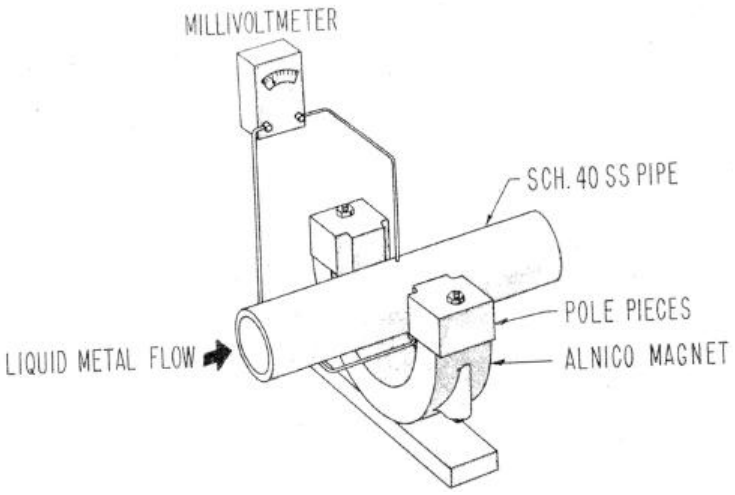

Figure 4.6: A schematic of the electromagnetic flowmeter showing many of the key components[3].

Correction Factors for Flowmeter Theory

Non-ideal effects cause deviations between theoretical predictions (equation 4.6) and actual output. These effects are discussed in detail by Hvasta[1], but are summarized here. The actual generated voltage is equation 4.6 with three correction factors (k_1, k_2, k_3) multiplied in:

$$V = k_1 k_2 k_3 \frac{4BQ}{\pi d} \tag{4.7}$$

As charges move under magnetic force into the wall, their velocity relative to the magnetic field drops to zero, and the charges are then free to recombine with oppositely charged particles on the opposite side of the wall (through the conductive sodium duct). This diminishing effect is taken into account with a material defined constant, k_1, which is derived by Gray and Astley[4].

$$k_1 = \frac{2d/D}{1 + (d/D)^2 + \left(\frac{\rho_{Na}}{\rho_{wall}}\right)(1 - (d/D)^2)} \tag{4.8}$$

The resistivity of sodium (ρ_{Na}) as a function of temperature has been studied in depth by

Freedman [5] and Epstein [6] and is listed in equation 4.9. NIST has modeled the resistivity of 316SS (ρ_{wall}) with equation 4.10[7]. These two equations are valid in the temperature range: 110[C] $\leq$ T $\leq$ 650[C].

$$\rho_{Na} = (2.381 \times 10^{-13})T^2 + (2.706 \times 10^{-10})T + (6.512 \times 10^{-8}) \tag{4.9}$$

$$\rho_{wall} = (-2.424 \times 10^{-13})T^2 + (6.521 \times 10^{-10})T + (8.152 \times 10^{-7}) \tag{4.10}$$

The second correction factor, k_2 is needed to describe the non-infinite nature of any real magnetic field. Charge recombination occurs as the entrance and exit of the flowmeter where the magnetic field is weakest. Again, Gray and Astley show k_2 is a function of the ratio of the length of the flowmeter over the inner diameter of the flowmeter tube (l/d)[4]. Upon examination of the bahavior of k_2 (equation 4.11, figure 4.7) it is clear that for $l/d > 2.5$, $k_2 \approx 1$.

$$k_2 = -0.0047\left(\frac{l}{d}\right)^4 + 0.0647\left(\frac{l}{d}\right)^3 - 0.3342\left(\frac{l}{d}\right)^2 + 0.7729\left(\frac{l}{d}\right) + 0.3172 \tag{4.11}$$

The third correction factor deals with variations of rare-earth magnet performance under increasing temperatures. k_3 for the magnets used in this experiment was analyzed by Kim and Doose[8]. These magnets have a maximum operating temperature of about 80[C]; beyond this temperature, the magnets will not revert back to initial performance even after cooling.

$$k_3 = \exp((-1.1 \times 10^{-3}) \times (T - 20)) \tag{4.12}$$

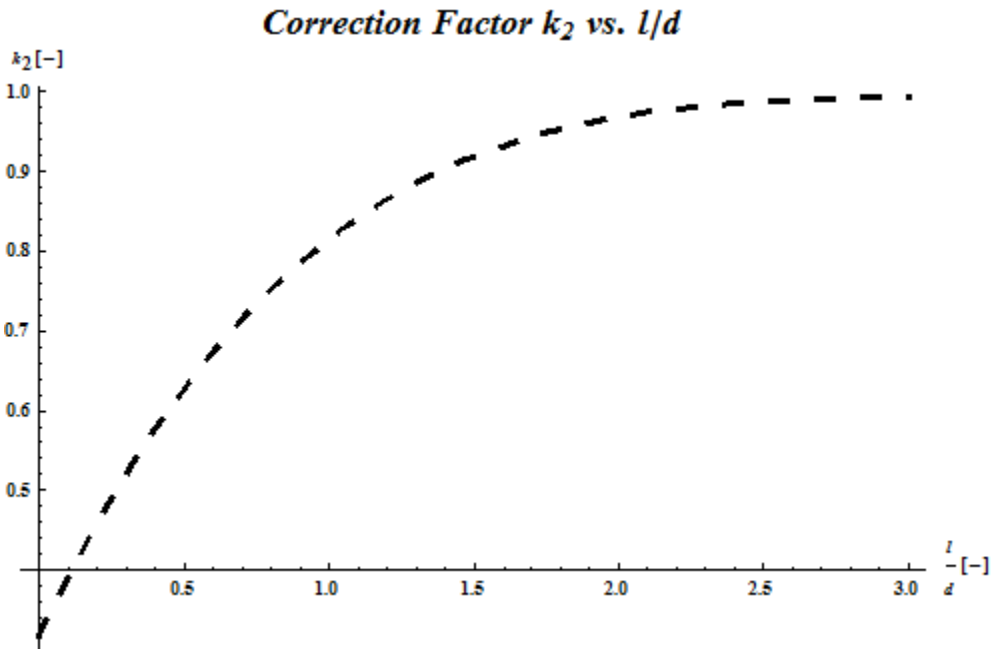

Figure 4.7: This figure shows the behavior of equation 4.11, the second correction factor for electromagnetic flowmeter theory.

4.2.4 Galvanic Cell Test Section

The galvanic cell test section was designed to accept a variety of oxygen sensor designs. A vertical mount in the riser section of the sodium loop was chosen because this section remains at constant temperature even during plugging tests. Also, it was desired to have the O_2 sensor in close proximity to the plugging meter for consistent concentration measurements. Figure 4.8 displays the O_2 sensor mounted in the loop, with the plugging meter heat exchanger immediately following the galvanic cell test section.

For ceramic crucibles being secured directly into the test section, a modified Swagelock fitting is used, in which a custom ferrel is machined to squeeze a graphite crush-ring between the loop fitting and the ceramic.

As discussed in the background section, the galvanic cell generates a voltage dependent on the ratio of oxygen activity in some reference gas to that of the liquid sodium. For a platinum-air reference, the sensor must have access to air in order to function. For this apparatus, which is enclosed in an inert environment (glovebox atmosphere) an outside gas

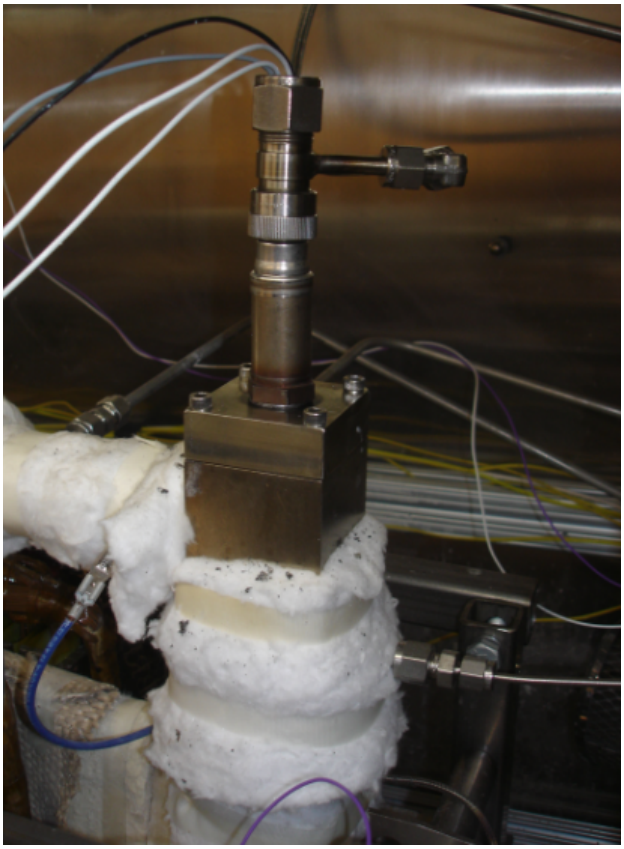

Figure 4.8: This figure displays a galvanic cell oxygen sensor plugged into the top of the riser section of the loop. This section of the loop remains at constant temperature even during plugging tests. The plugging meter is immediately downstream of this test-section.

line was connected from the outside environment (the air surrounding the glovebox) to the back of the sensor. An emergency gate valve was installed at the outside of the glovebox in the event of sodium corroding through the sensor. This valve would then serve to cut off additional outside oxygen from the sensor (this valve is not shown in figure 4.8, but the rest of the assembly is). A small, controllable air chamber is then maintained on the back of the O_2 sensor as a reference gas. For metal-metal oxide reference electrodes, the sensor is sealed gas-tight to allow the reference chamber head space to reach an equilibrium partial pressure of oxygen.

4.2.5 Instrumentation & Data Acquisition for the Glovebox Loop

Aside from the custom-engineered components discussed above (flowmeter, plugging meter, etc), the only other inputs present in the glovebox sodium loop are K-type thermocouples. These thermocouples are wired to a National Instruments data acquisition board (NI-DAQ) through a thermocouple input card(NI#9213). The oxygen sensor, was measured using a NI #9205 input card with an input impedance of 50 $[M\Omega]$. A high input impedance is necessary to limit the current through the galvanic cell (see Chapter 3). A LabVIEW program was then written to read and display these temperature and voltage measurements. See figure 4.9 for a screen shot of the front panel of the sodium loop data acquisition system.

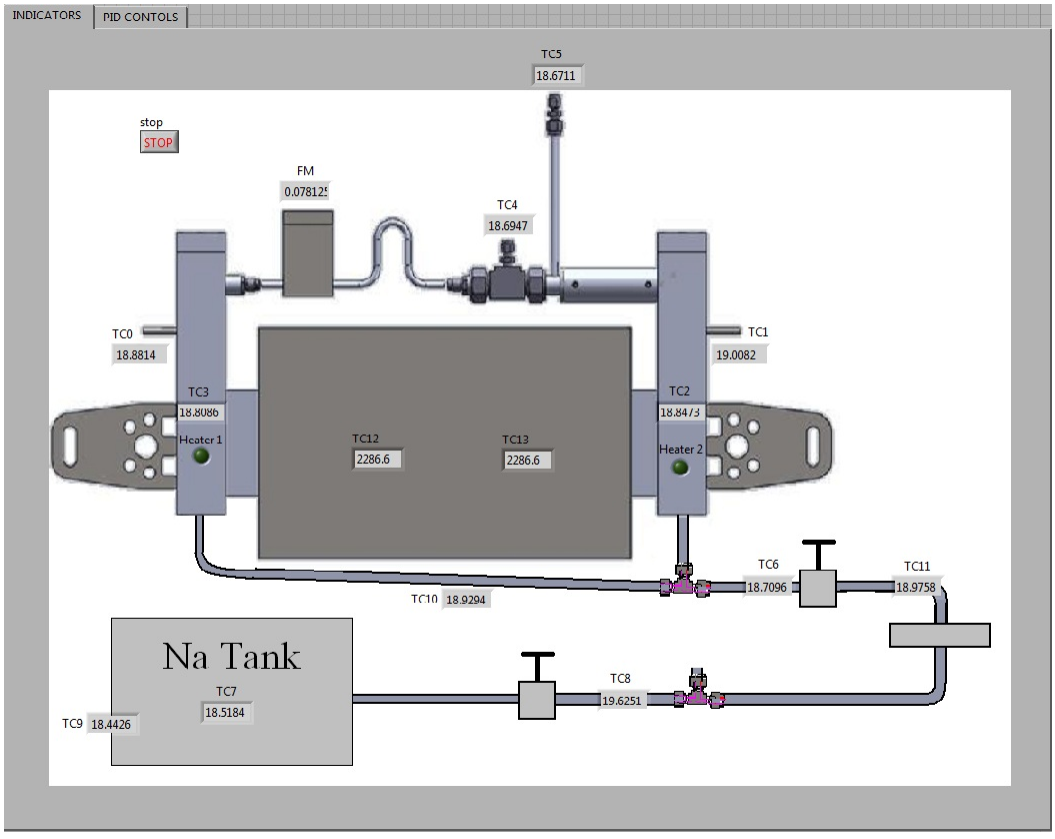

Figure 4.9: This figure is a screen shot of the LabVIEW program written to control liquid sodium experiments in the glovebox loop for this project.

LabVIEW tasks were written both to acquire signals from the thermocouples as well as send output signals to the heater relays. 2[kW] of heater power were installed in AC heaters in each vertical arm of the loop. A PID controller was programmed to manage these heaters with an outgoing digital signal (from a NI#9472 card). All fill lines connecting the sodium drainage/storage tank to the loop were wrapped in NiChrome wire and connected to DC power supplies. These DC power supplies are also controlled by LabVIEW using PIDs.

The LabVIEW PID controllers are set to hold the loop at a specified temperature. The PIDs automatically adapt how long to leave the heaters on/off. Control results using this technique have been very good; temperature control is usually within one degree Celsius of the target temperature, and easily held constant even over days of running. Depending on how hot the liquid sodium is compared to the target loop temperature, the loop will usually reach a near uniform temperature within fifteen minutes. The exception to this fifteen minute estimate is when the loop is filled with cold sodium, then heated up to high temperature once flowing. This technique, the reasons for which are discussed in Chapter 5, can postpone steady state operation by up to half an hour.

The top section of the loop, which contains the plugging meter, heat exchanger, and electromagnetic flowmeter, does not have a PID controlled heater system. Rather, it is trace heated using a manually controlled DC power supply. This operation is usually just at start-up; once plugging tests have commenced, this section can not be heated (doing so would drastically effect plugging results and inhibit the temperature drop necessary for reaching saturation temperature). As such, these heaters are strictly used for preheating and to help the system reach equilibrium temperature, then they are turned off for the duration of the run.

4.3 Static Corrosion Test Facility

The static corrosion test facility consists of six furnaces mounted in a glovebox (under an inert, nitrogen atmosphere). The furnaces can maintain liquid sodium at 600[C] using the same PID controllers written for the loop's AC heaters. The corrosion samples are then suspended in constant temperature static sodium for the duration of the test. A K-type thermocouple is then submerged into the sodium; this data is then read and recorded using the same data acquisition system and LabVIEW program described above.

The furnaces consist of a one-gallon stainless steel can, with a single, 3" diameter stainless steel crucible 5" tall inside. The crucible is insulated with a combination of Microtherm, Kaowool, Pyrogel, and Pourable-microtherm insulation. See figure 4.10.

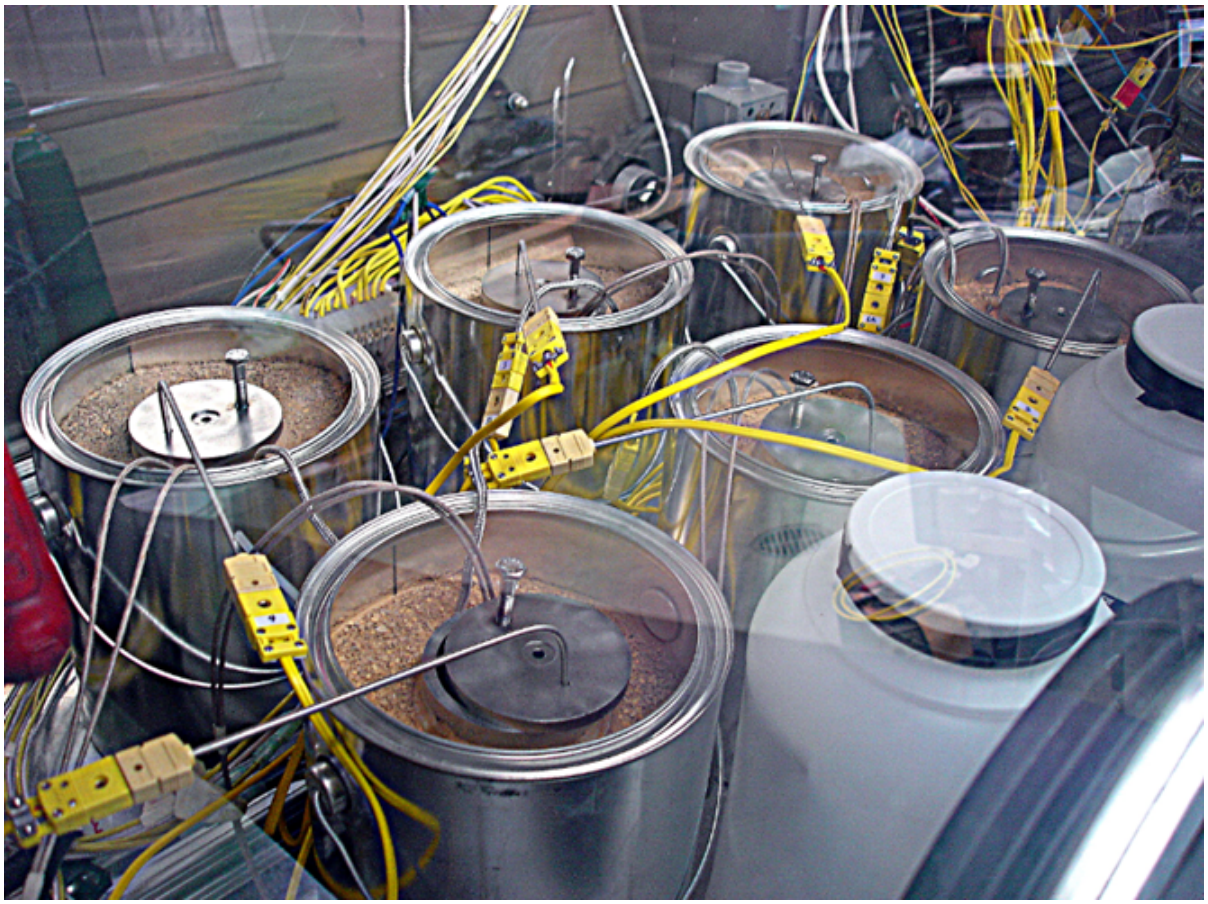

Figure 4.10: The six static corrosion test furnaces in the UW-Madison glovebox sodium test facility can heat sodium and samples up to 600[C].

4.4 Stoughton Sodium Corrosion Loop

A large-volume, high-flow sodium loop has been constructed at an off-site laboratory in Stoughton, WI. This facility was developed primarily for dynamic corrosion testing of materials at high sodium velocities. This loop stands roughly six feet tall and 8 feet wide, with a sodium capacity of 1.5 gallons. The system was designed to subject corrosion samples to reactor conditions: 550[C] liquid sodium at less than 5[ppm] dissolved oxygen concentration, flowing at 10[m/s] for experiments in excess of 500[hr]. The basic layout of the sodium loop is shown in figure 4.11.

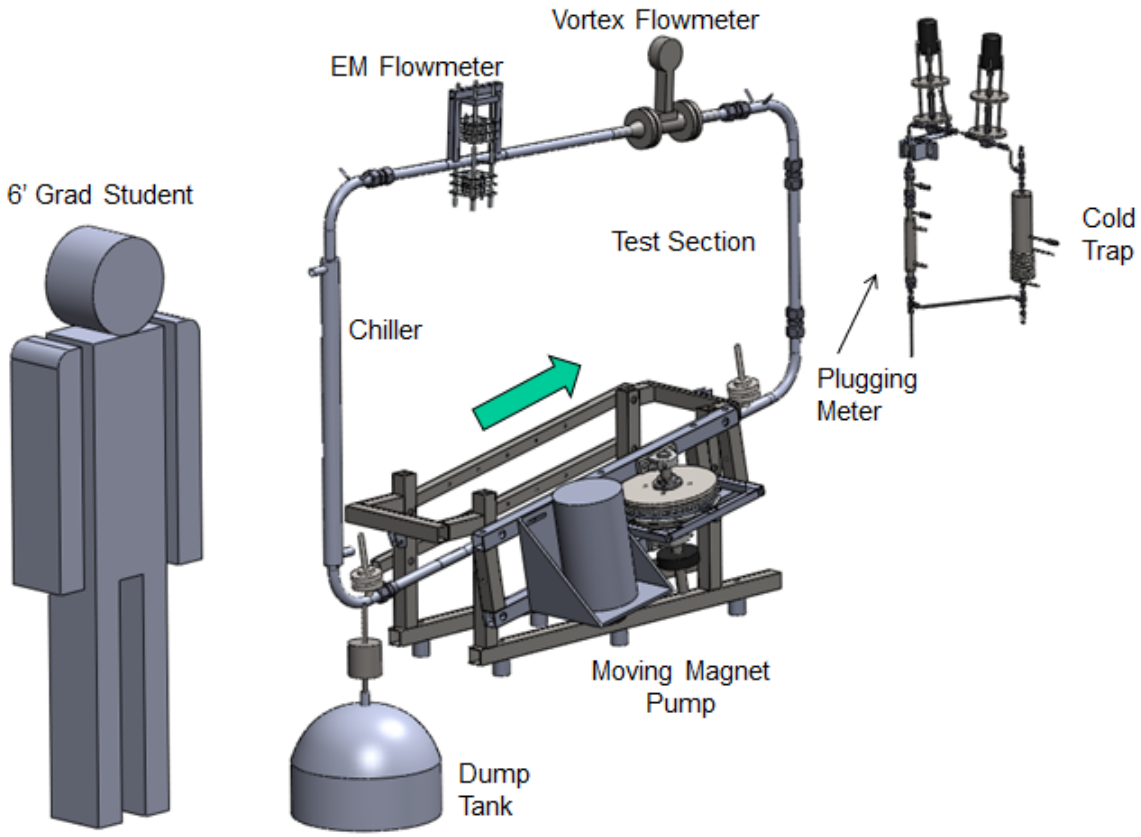

Figure 4.11: The Stoughton sodium loop can push sodium in excess of 30 gallons per minute at temperatures in excess of 550[C]. This schematic is from Hvasta[9].

This dynamic corrosion loop was also used to test oxygen sensors, and it uses many similar components described for the glovebox sodium loop. The flow-meters and plugging

meter, are nearly identical to those on the glovebox loop. While the loop originally used a flat linear induction pump (FLIP) to establish flow, it has since been fitted with a moving magnet pump (MMP). The MMP is still an induction pump, but uses rotating magnets rather than alternating current in fixed coils to establish a time-changing magnetic flux through the sodium. This pump was designed and built by Mike Hvasta[9].

The Stoughton sodium loop originally used a vortex flowmeter to calibrate the electromagnetic (EM) flowmeter. Data for the calibration of the vortex shedder and the EM flowmeter are shown in figure 4.12.

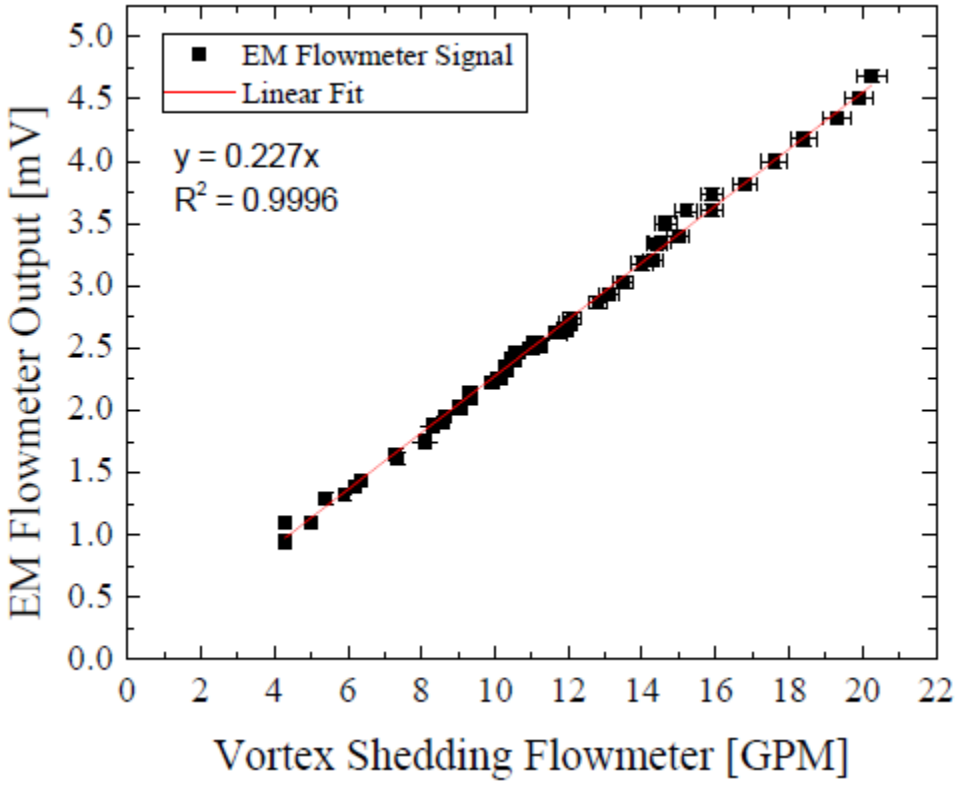

Figure 4.12: The vortex flowmeter was used to calibrate the electromagnetic flowmeter at low temperatures[9]. The vortex shedder was then removed due to its low temperature limit.

The vortex flowmeter was limited to an operating temperature of 400[C]. Thus, once the EM flowmeter was calibrated, the vortex flowmeter was removed from the system, and an oxygen sensor test section was put in its place.

A diagnostic loop and the oxygen sensor test section were also designed into the Stoughton sodium loop. These components are described in more detail below.

4.4.1 Diagnostic Loop

The dynamic corrosion test section in the Stoughton sodium loop causes a flow restriction which creates a pressure drop across the test section. A side diagnostic loop was mounted with the entrance on the high pressure side of the test section, and the return on the low pressure side. The pressure drop across the corrosion test section, therefore, drives sodium flow through the diagnostic loop. This side-loop includes a plugging meter (PM) and cold trap (CT) in parallel. A motorized stepper valve is mounted in each branch of the diagnostic loop, so the flow through either side can be regulated consistently. A schematic of the diagnostic loop is shown in figure 4.13.

The PM for the Stoughton sodium loop is nearly identical to the PM for the glovebox sodium loop described in section 4.2.2. The CT is wrapped in 1//4" cooling coils which are connected to a megawatt heat exchanger. Coolant flows through the CT at $\approx$ 12[gal/hr]. During operation, no heaters are activated on the CT, so the temperature is dictated by the flow-rate of hot sodium into the cooled CT section. Thus, the automated valves shown in figure 4.13 indirectly control the oxygen concentration in the bulk sodium.

4.4.2 Oxygen Sensor Test Section

Once calibration of the EM flowmeter was completed, the vortex flowmeter was removed, and a full-diameter tube (1.25" OD) was mounted in its place. This tube contained three oxygen sensor mounts so sensors could me tested simultaneously. Images of this test section with sensors installed are shown in Chapter 7.

A heater zone was dedicated to this test section so the sensors could be slowly heated in order to reduce thermal shock. After a slow pre-heating process, liquid sodium was then slowly pushed into the loop.

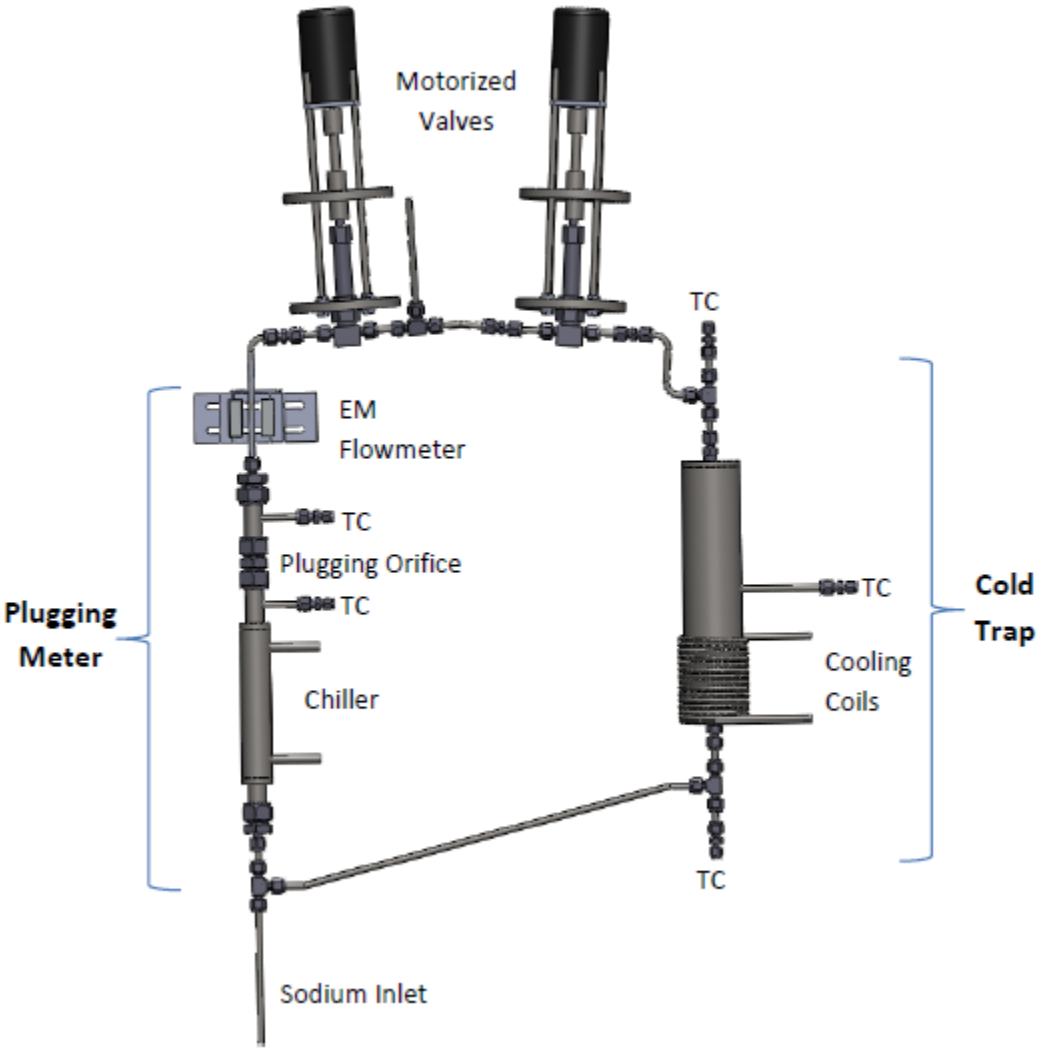

Figure 4.13: The diagnostic loop contains a PM and a CT in parallel. Flow is driven through this loop by a pressure drop created over the ddynamic corrosion test section[9].

4.4.3 Instrumentation & Data Acquisition for the Stoughton Loop

The Stoughton sodium loop interfaced to a computer through a SCXI chassis (rather than an NI-DAQ as used for the glovebox sodium loop). Otherwise, most of the hardware and controls were identical to that of the glovebox sodium loop. Of particular importance to this research was the hardware used in voltage measurements for the oxygen sensors.

As discussed in Chapter 3, it is extremely important to limit the current drawn by the oxygen sensor with either a high impedance multimeter or electrometer. The oxygen

sensors connect directly to BNC connectors which connect to an SCB-68 breakout box which connects using a ribbon cable to an NI 6280 PCI card in the data acquisition computer. This is an 18 bit input with $> 10[G\Omega]$ input impedance. This hardware should limit a 1[V] signal to 0.1[nA].

4.5 Summary of Chapter 4

This chapter described the design parameters and construction of the sodium test facilities used for this research. This description included a low-flow liquid sodium loop for testing oxygen detection methods, specifically the galvanic cell and plugging meter, under varying oxygen conditions. This loop required that materials, pump requirements, and flow detection be engineered appropriately. Instrumentation (hardware and software) requirements were defined according to experiment needs. Specific sections were included on each of the major components of the loop, each of which included the theory and references to support design decisions. A static corrosion test facility was also described. This six-furnace facility allows for parallel testing of a variety of materials in different environments. Finally, a brief overview of a larger sodium loop at an off-site lab was given. This research project was conducted using these facilities.

Chapter 4 Bibliography

[1] M. G. Hvasta. *Designing and Optimizing a Moving Magnet Pump for Liquid Sodium Systems.* PhD thesis, University of Wisconsin-Madison, 2012.

[2] David Griffiths. *Introduction to Electrodynamics.* Prentice Hall, 3 edition, 1999.

[3] R.N. Lyon et al. *Liquid Metals Handbook.* Atomic Energy Commission, 1950.

[4] W.C. Gray and E.R. Astley. Liquid metal magnetic flowmeters. *Journal of the Instrument Society of America*, June 1954.

[5] J. F. Freedman and W. D. Robertson. Electrical resistivity of liquid sodium, liquid lithium, and dilute liquid sodium solutions. *Journal of Chemical Physics*, 34(3):769–780, March 1961.

[6] C. B. Jackson. *Liquid Metals Handbook: Sodium (NaK) Supplement.* The U.S. Atomic Energy Commision, 1955.

[7] J. G. Hust and P. J. Giarratano. Standard reference material 798: Electrical resistivity-austenitic stainless steel. Technical report, NIST, 1975.

[8] S. H. Kim and C. Doose. Temperature compensation of NdFeB permanent magnets. Technical report, Advanced Photon Source, Argonne National Laboratory, 1998.

[9] M.G. Hvasta. *Designing & Optimizing a Moving Magnet Pump for Liquid Sodium Systems.* PhD thesis, University of Wisconsin-Madison, 1500 Engineering Dr, Madison, WI 53706, May 2013.

Chapter 5

Plugging Meter - Results & Analysis

In this chapter the shortcomings and benefits of a Plugging Meter (PM) are discussed. Results from plugging experiments conducted in both sodium loops (which were detailed in chapter 4) are included. This chapter aims to provide a detailed discussion of how to operate both a PM and a cold trap (CT) and interpret the acquired data.

Examples of raw data are presented and the difference between a conclusive plugging event an an inconclusive event will be demonstrated. Error propagation of acquired data will be conducted and the sources of these uncertainties will be addressed.

A comparison of PM data to CT readings will also be discussed. Agreement between the PM and CT is important to verify the accuracy of the user's plugging technique. The accuracy of oxygen sensor tests described in chapter 7 hinges entirely on the accuracy of the PM.

Chapter 5 Contents

Contents

5.1 Variables Used in this Chapter

Variable	Physical Meaning
C	Oxygen concentration [wppm]
T_{sat}	Saturation temperature [K]
ΔC	Uncertainty in oxygen concentration [wppm]
ΔT_{sat}	Uncertainty in saturation temperature [K]

5.2 Plugging Meter Operation

As discussed in Chapter 3, the solubility of oxygen in sodium is a function of temperature[1]. Therefore the sodium reservoir which stores the sodium for the loop can have varying oxygen concentration (in solution) depending on its temperature. If the sodium is cold, just barely above the melting temperature, then the saturation limit for oxygen is extremely low and the reservoir acts as a cold trap. As the sodium temperature increases, impurity (Na_2O) from the walls of the tank dissolves into solution and the oxygen concentration increases. This effect continues as long as there is adequate impurity on the walls of the tank.

The impurity level of the sodium loop can therefore be controlled by adjusting the temperature of the sodium tank before the loop is filled. This simple principle allows for easy variability of sodium conditions to test the plugging meter (and other oxygen sensors). It should be noted that this technique is not used to *measure* the oxygen concentration, for cold spots, initial impurity, and other variables can affect the sodium oxygen concentration in the loop. The fill temperature is simply adjusted to change the amount of impurity available in the loop.

The loop must be run long enough to become isothermal. Additionally, fill lines and overhead lines must be kept higher than the loop operating temperature in order to ensure that no cold trapping is going on elsewhere in the loop. A cold finger will slowly filter oxygen and other impurities from the loop, until that section becomes saturated at its temperature[2][3][4].

5.2.1 Data Acquisition & Interpretation

Interpretation of acquired data will now be demonstrated. Figure 5.1 shows the location of two thermocouples (TCs) in the plugging meter. Each TC is in the bulk sodium flow, one immediately before, and one immediately after the plugging orifice. The location of the chilling unit is also shown in figure 5.1. The significance of the chilling unit location will

be discussed later. A detailed description of the sodium loop construction is presented in Chapter 3.

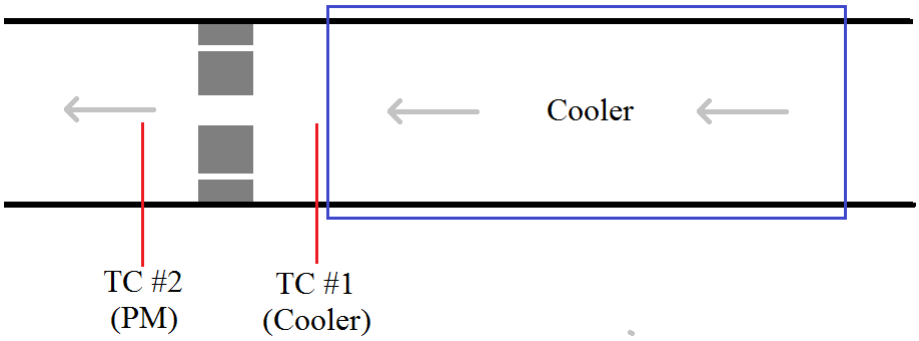

Figure 5.1: The layout of the main components of the plugging meter: chilling unit, plugging orifice, and thermocouples. The flow-meter, which is not shown, must be mounted in series with these components.

The thermocouples shown in figure 5.1 see different temperature gradients during a plugging test because of the restricted flow through the plugging orifice which separates them. Figure 5.2 shows the sodium temperature at three different locations during a plugging test. Notice that the temperature at the entrance to the plugging meter is relatively constant, at near 350[C] for this test.

The thermocouples before and after the plugging orifice (labeled TC#1 and TC#2 in figure 5.1) report significantly different temperatures during a plugging test. The thermocouple immediately following the heat exchanger notices a sharp drop in temperature when the heat exchanger is activated. This cooled sodium is then funneled through the orifice slowly, which results in a delayed effect at the downstream thermocouple. When the heat exchanger is deactivated, the first thermocouple is quicker to respond, with a sharp increase in temperature as hot sodium from the inlet (still at 350[C]) pushes through the orifice. The hot sodium has to move through the plugging orifice before the second thermocouple responds.

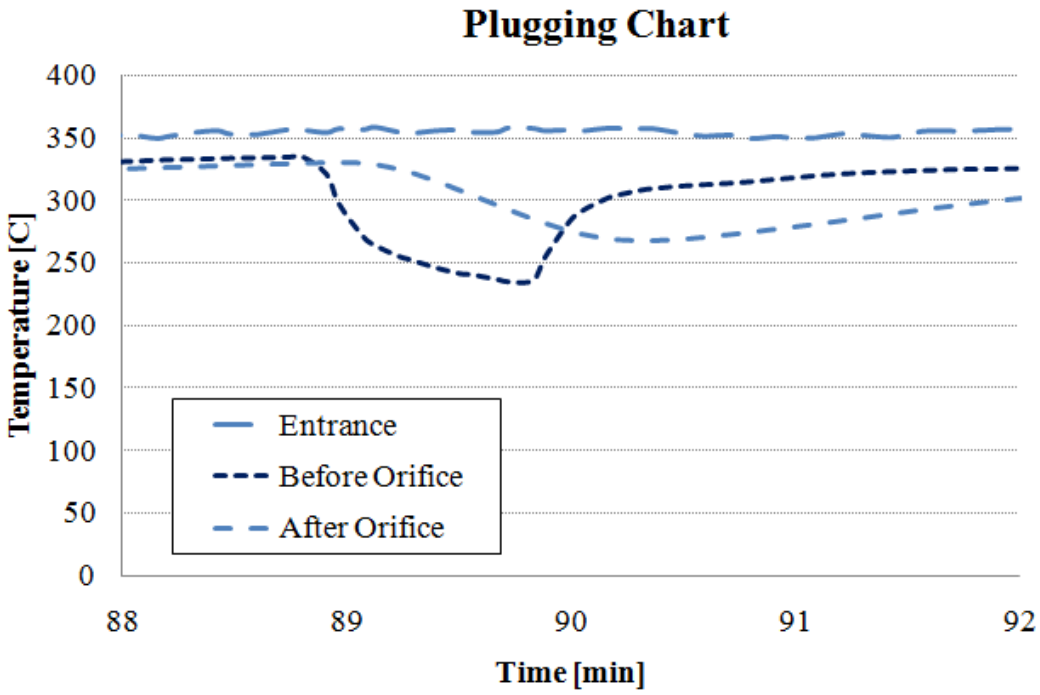

Figure 5.2: Sample of temperature data taken during a plugging test. Inlet temperature is constant, while the temperature gradient across the plugging orifice is large due to restricted flow.

Figure 5.3 shows the same data as figure 5.2, but also includes flow-meter data which is critical to plugging meter analysis. As the sodium temperature at the orifice decreases below the oxygen saturation temperature, T_{sat}, sodium oxide precipitates out of solution and begins to plug the orifice, restricting the flow-rate.

Measuring T_{sat} is done by cooling the sodium down past the temperature at which the flow-rate begins to drop, then switching off the heat exchanger and allowing the sodium to slowly climb back to equilibrium temperature as it flows through the orifice. The flow-rate should not climb immediately after the heat exchanger is turned off. If the sodium is below the saturation temperature then the plug will not begin to dissolve, so the flow-rate should remain low for a notable amount of time following deactivation of the heat exchanger (sometimes in excess of thirty seconds). The flow-rate will begin to climb as soon as T_{sat} is reached. The result of this process is a clearly defined minimum in flow-rate (see figure 5.3).

T_{sat} is the temperature of the sodium *moving through the orifice* at that moment.

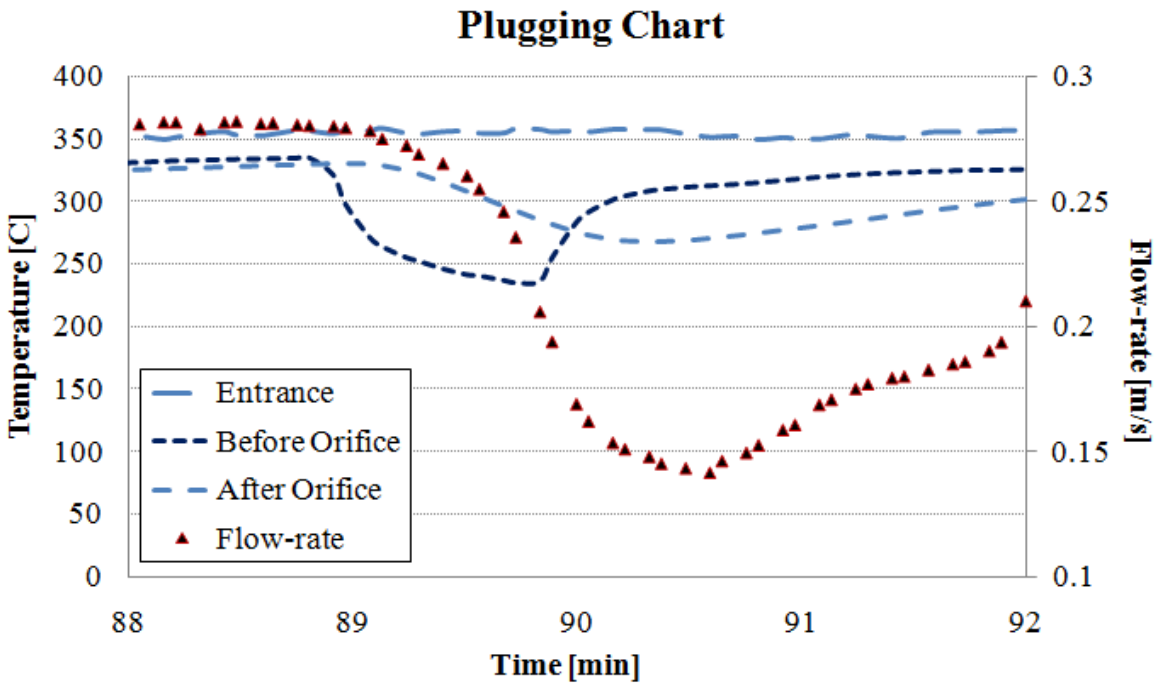

Figure 5.3: Flow-rate data for the same data set shown in figure 5.2. This plot shows all the information necessary to detect a plugging event.

A problem arises when trying to determine the exact sodium temperature at the orifice. In both the UW Glovebox Sodium Loop as well as the Stoughton Sodium Loop, the two available temperatures are immediately before and after the orifice. However, the temperature between the two is unknown (at the orifice). For calculations made in this report, the temperature on the downstream side of the orifice were taken as the saturation temperature. It was decided that the rapid temperature changes due to the heat exchanger made the upstream thermocouple poorly represent the conditions inside of the orifice. If the upstream thermocouple were used, then all the recorded saturation temperatures would be too high. In contrast, the downstream thermocouple sees a significantly delayed effect, like the sodium in the orifice. It was confirmed that the recorded saturation temperatures at the downstream thermocouple more accurately represent the data acquired with the cold trap[5]. For all tests, the same method was taken, so the consistency of the operating procedure should

ensure the results are repeatable.

The Difference between a Conclusive & an Inconclusive Plugging Event

Inconclusive plugging events occur when the flow-rate begins to climb immediately after the heat exchanger is turned off. These simultaneous events leave the user unable to resolve the exact moment of saturation, and therefore unable to back out a saturation temperature. Notice in figure 5.4, there is very little time between the climb in the temperature just before the orifice, and the climb in flow-rate.

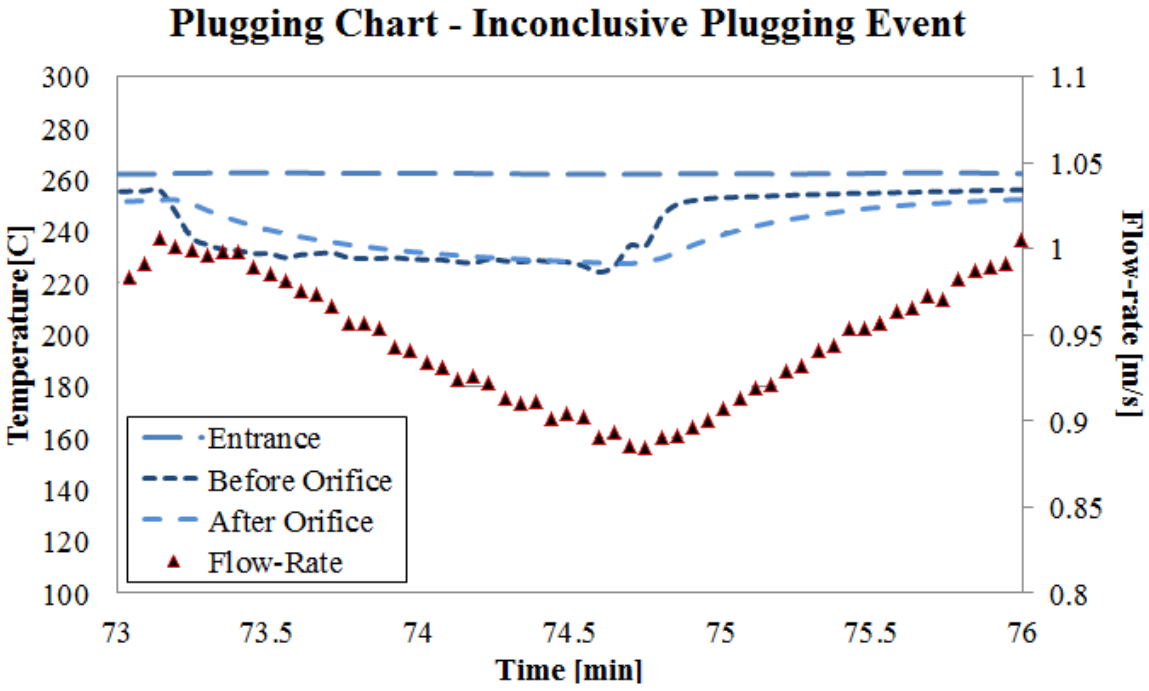

Figure 5.4: This data set shows an example of an inconclusive plugging event. Notice the flow-rate did not continue to drop after the heat exchanger was deactivated, indicating that the sodium was still above the saturation temperature.

In contrast, when the sodium is brought well below the saturation temperature, plugging will continue, and the flow-rate will fall until the saturation temperature is approached, and the result is a deceleration in plugging followed by a brief period of saturation equilibrium (no plugging or unplugging). The brief equilibrium between plugging and unplugging is

indicated by a zero-change in flow-rate (a minimum). This equilibrium is followed by a the climb in flow-rate.

Figure 5.5 is an example of a plugging event with much more distinction between the end of heat exchanger operation (indicated by the sharp rise in temperature before the orifice), and the increase in flow-rate. At a glance figures 5.4 and 5.5 appear very similar. However, these subtle differences translate to a plugging test that results in a confident oxygen measurement, and one that does not.

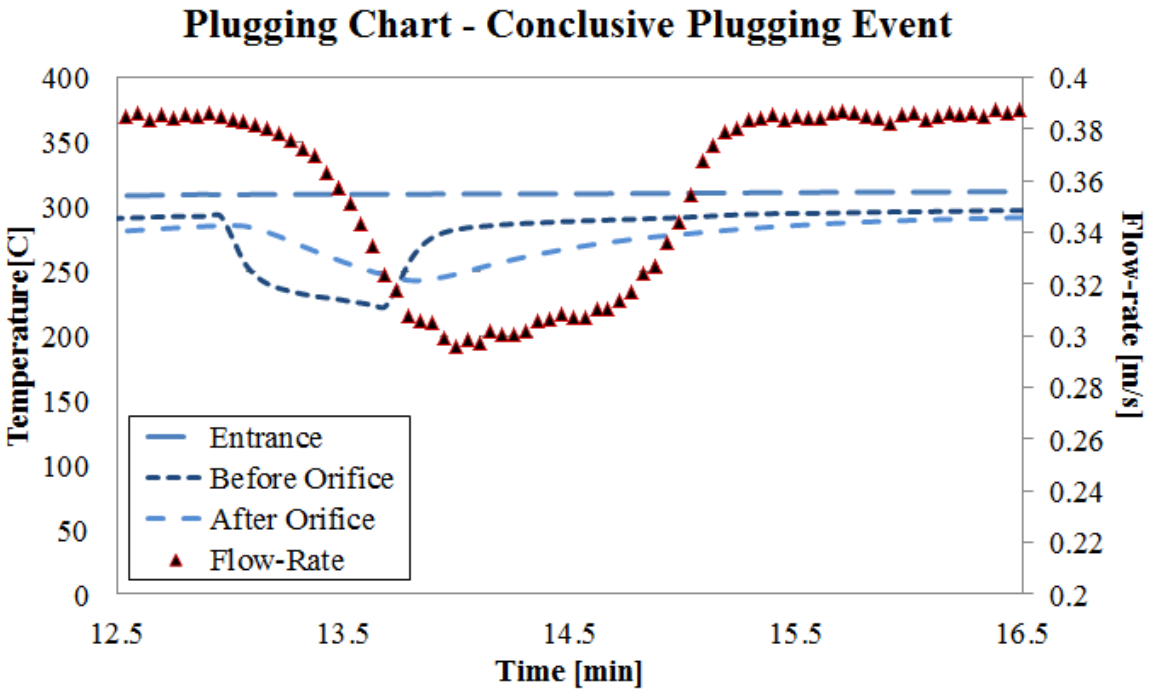

Figure 5.5: This data set shows an example of a conclusive plugging event. The moment of oxygen saturation is clearly defined. This data set was taken in identical conditions to that of figure 5.4 aside from a slower inlet flow-velocity.

If the heat exchanger is turned off prematurely, then the flow-rate will begin climbing immediately, and one can not be certain that the sodium was cooled to a low enough temperature to be saturated. Dropping below the saturation temperature and allowing the system to restore flow when the sodium rises to the appropriate temperature creates a sharply resolved moment of saturation, as seen in figure 5.3.

5.3 Plugging Meter Data Analysis

The layout of the plugging meter has been discussed, and arguments made which defend the user's selection of which thermocouples to base concentration calculations on. The difference between a conclusive and an inconclusive plugging events has also been presented. This section focuses on how the acquired saturation temperatures were used to determine the oxygen concentration in liquid sodium, and the error analysis applied to these measurements and calculations.

5.3.1 Series Averaging

As discussed in Chapter 2, the Noden Correlation is a popularly accepted relationship between dissolved oxygen concentration, (C) and saturation temperature, T_{sat}.

$$C(T_{sat}) = 10^{\left(6.1579 - \frac{2384.2}{T_{sat}}\right)} \tag{5.1}$$

This correlation translates the saturation temperature into the concentration of oxygen dissolved in sodium.

Multiple plugging tests are typically run in succession, and the oxygen concentrations from these tests are averaged. Checking repeatability in the plugging events demonstrates the magnitude of variation between measurements, and helps the user define the uncertainty of the instrument. After the heat exchanger has been deactivated, the system temperatures are allowed to return to equilibrium. This usually only takes a few minutes, and then the next plugging event can begin. Figure 5.6 shows an example of a series of plugging events, from which, an average oxygen concentration can be determined, and a standard deviation of these sequential measurements can also be calculated.

The uncertainty in each measurement is primarily due to the uncertainty in determining the moment of saturation, an uncertainty in time. During this range of time, the temperature at the orifice will vary. Typically, for a good plugging event in the UW Glovebox

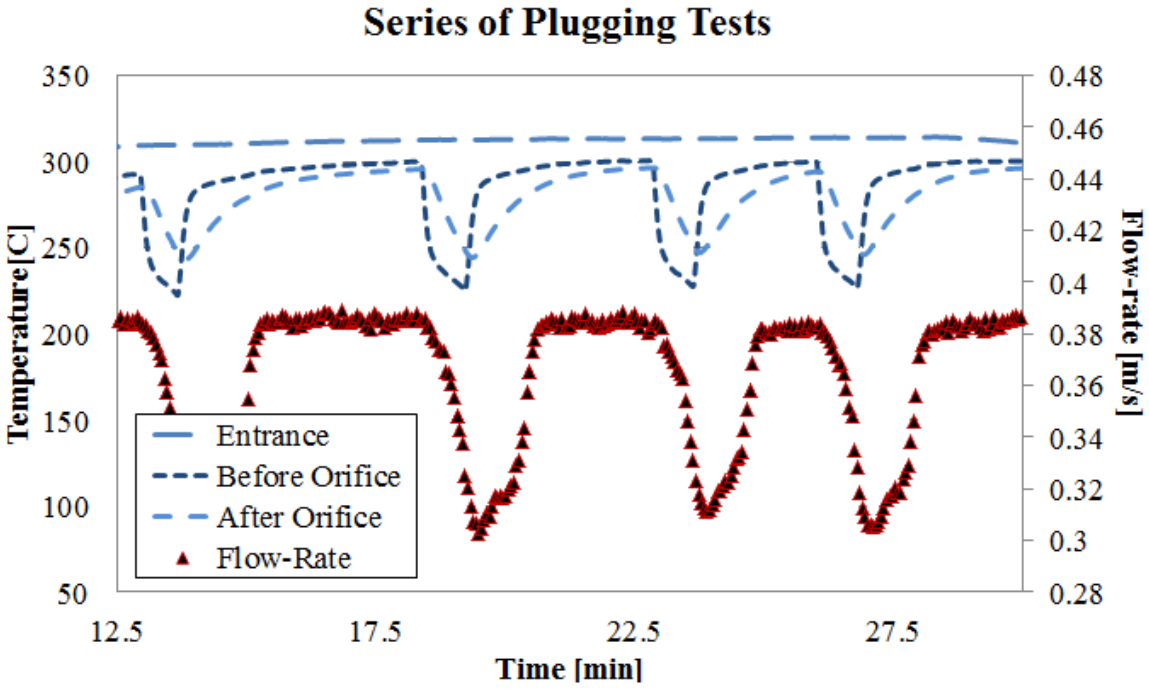

Figure 5.6: This data set shows part of a series of plugging measurements. Several measurements are taken back-to-back to investigate the consistency within the measurement. Typically, four or five sequential measurements are taken.

Sodium Loop, an uncertainty in time is as good as ±3[s] (as concentrations get lower, this uncertainty tends to increase sometimes close to ±10[s]). To evaluate the uncertainty in saturation temperature from this time, the temperature behind the orifice is simply inspected at the appropriate time before and after the estimated moment of saturation. This provides the total range of uncertainty which surrounds the saturation temperature. The magnitude of this uncertainty depends on the sharpness of the flow-rate minimum, which is a function of the flow-rate, system temperature, and how low the concentration is. With the uncertainty in saturation temperature determined, the uncertainty in oxygen concentration can be calculated using standard error propagation techniques (equation 5.2).

$$\Delta C = \sqrt{\left(\frac{\partial C}{\partial T_{sat}}\right)^2 \Delta T_{sat}^2} \tag{5.2}$$

Table 5.1 shows the results from carrying out this analysis on each of five measurements in

a series of plugging tests. The uncertainty in the time of each minimum flow-rate was ±3[s], which was used to determine the uncertainty in T_{sat} by recording the temperature 3 seconds before and after the estimated moment of saturation. The average oxygen concentration was then calculated, along with the average uncertainty.

Measurement #	T_{sat}[C]	ΔT_{sat}[C]	C[**ppm**]	ΔC [**ppm**]
1	249.57	2.125	39.2	1.97
2	247.74	2.029	37.5	1.90
3	247.54	2.119	37.3	1.89
4	250.99	2.201	40.5	2.03
5	249.51	2.129	39.0	1.97

Table 5.1: Results for one series of plugging tests. These data points, along with the average concentrations and uncertainties, are plotted in figure 5.7.

The data shown in figure 5.7 is typical for oxygen concentrations in excess of 20[ppm]. Each of the sequential measurements fell within error of the average concentration. Below 20[ppm] plugging the orifice becomes difficult, and the uncertainties tend to increase.

Adjusted technique in Stoughton Sodium Loop

Plugging events at low oxygen concentrations require variable coolant flow-rate in order to achieve low uncertainty. In this case, the sodium temperature is dropped until the flow-rate begins to drop. At this point the coolant flow-rate should be slowly increased, keeping the temperature gradient across the plugging orifice as small as possible. The result is a very gradual increase in temperature, and a more accurate identification of the moment of saturation.

The larger Stoughton Sodium Loop inclded a parallel diagnostic loop which had both a plugging meter and a cold trap (see chapter 4). The plugging meter on this system had

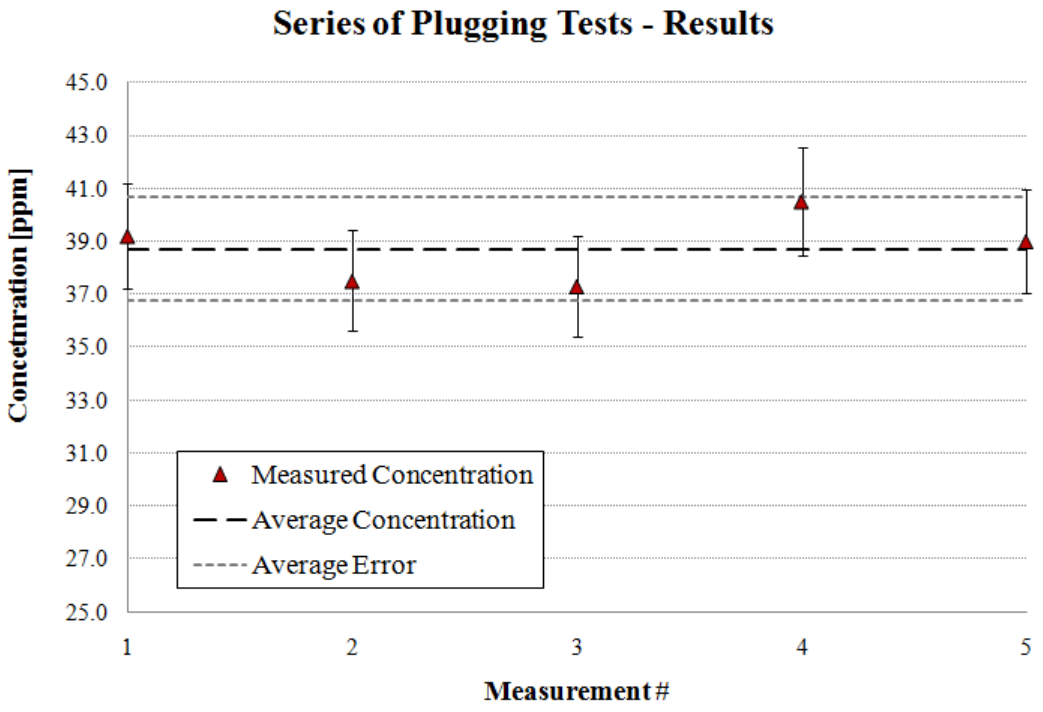

Figure 5.7: The results of the plugging tests shown in table 5.1. Each measurement falls within error of the average concentration. These results are typical for a well-conducted plugging test.

variable-flowrate coolant control, which enabled this gradual temperature increase. As a result, plugging events were recorded even below 10[ppm] while maintaining respectable uncertainty. See section 7.21.

5.3.2 Comparison of PM and CT

The glovebox sodium loop uses a flat linear induction pump (FLIP) to develop the pressure necessary to operate the plugging meter and pump sodium around the loop. Due to FLIP inefficiency and glovebox restrictions, cooling the pump is a problem. Hence, the temperature continues to rise and approach the limit set by the FLIP coils (which can not exceed 140[C] without damaging the pump. Since the operation of a cold trap to control loop impurity requires the system run for many hours before reaching a steady state impurity level, cold trap operation in the glovebox sodium loop is not practical.

In contrast, the Stoughton Sodium Loop uses an air-cooled moving magnet pump, which has had no overheating problems and can be run continuously. The cold trap in this system is described in chapter 2 and chapter 4.

A series of plugging tests were taken at varying cold trap temperatures in order to verify PM measurements. It was found that if the plugging technique outlined above was followed, then agreement between the plugging meter and cold trap was excellent (indeed perfect within error). Hvasta found the same conclusion with this same experimental facility[5].

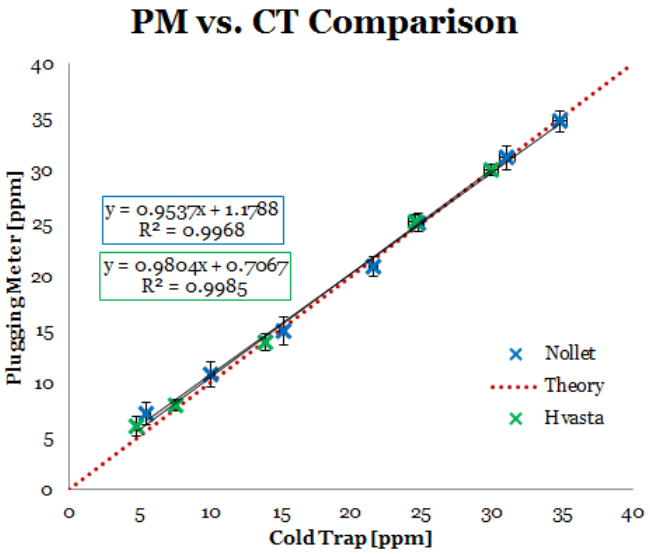

Figure 5.8: The cold trap and plugging meter agree with one-another within error. Two different data sets, individually taken, are shown in this figure. The data in green was taken by Hvasta[5].

Consistency between Hvasta's experiments and those conducted for this research provide further verification of this plugging meter technique. Uncertainties in both dimensions are included in figure 5.8, but are very small compared to the size of the point markers.

5.4 Conclusions

The Stoughton Loop has a side diagnostic loop with metering valves that allow the user to have fine control of sodium flow-rate through both a plugging meter and a cold trap. The addition of a cold trap to the system allowed the user to bench-mark plugging results against another instrument, which will provide insight to the accuracy of the described plugging meter operating technique. Fine control over the flow-rate into the plugging meter also allowed the user to measure oxygen below 10[ppm].

The successful confirmation of PM and CT data helps solidify the oxygen measurements taken during the oxygen sensor tests discussed in chapter 7. Any user beginning to work with a sodium loop should reproduce the experiment plotted in figure 5.8 in order to verify the accuracy of his/her plugging technique.

While the results in this chapter do not necessarily contribute new science to the field of sodium fast reactors technology, the accuracy of these plugging measurements rival the best measurements published in literature[5, 6]. Furthermore, the significance of the scientific contributions argued in chapter 7 directly depends on the accuracy of these plugging tests.

Chapter 5 Bibliography

[1] V.J. Rutkauskas. Determination of the solubility of oxygen in sodium by vacuum distillation. Technical report, Los Alamos Scientific Laboratory, July 1968.

[2] R. D. Kale and M. Rajan. Developments in sodium technology. *Current Science*, 86(5):668–675, March 2004.

[3] F. Zhao and X. Ren. Optimal performance analysis of a sodium cold trap. *Nuclear Engineering and Design*, 239:490–494, 2009.

[4] R. K. Steunenberg and L. Burris. From test tube to pilot plant: A 50 year history of the chemical technology division at Argonne National Laboratory. Technical report, Argonne National Laboratory, August 2000.

[5] M.G. Hvasta. *Designing and Optimizing a Moving Magnet Pump for Liquid Sodium Systems.* PhD thesis, University of Wisconsin-Madison, 1500 Engineering Dr, Madison, WI, 53706, May 2013.

[6] Charles C. McPheeters and James M. Williams. A comparison of three methods of oxygen concentration measurement in sodium. Technical Report La-DC-7743, Los Alamos Scientific Laboratory, December 1966.

Chapter 6

Ceramic Corrosion in Liquid Sodium - Results & Analysis

As discussed in Chapter 1 of this report, oxygen concentration in liquid sodium is a critical quantity when analyzing the corrosion behavior of the molten sodium. Thus, designing an effective, affordable oxygen sensor is desirable for any liquid sodium system. Since the primary issue with the liquid sodium oxygen sensor has been corrosion and cracking of the ceramic electrolyte, investigation of ceramic corrosion must be thorough. This chapter focuses on the corrosion of ceramics in liquid sodium.

Discussion of the thermodynamics and mechanisms of sodium attack on ceramics follow in this chapter, along with past and present electrolyte corrosion experiments conducted for this research. This work focuses on common zirconia ionic conducting electrolytes for application in oxygen sensor technology, however additional experiments are discussed on various other ceramics.

Chapter 6 Contents

Contents

6.1 Variables Used in this Chapter

Variable	Physical Meaning
ΔG_R	Gibbs energy of reaction [kJ/mol]
ΔG_f^o	Gibbs free energy of formation [kJ/mol]
T	Temperature [C]
c	Dissolved oxygen concentration [ppm]
ρ	Density [kg/m^3]
A	Surface area [m^3]

6.2 Chemistry and Thermodynamic Considerations

Alkali metals easily shed the single s-orbital electron in their outer shell, but removal of the remaining electrons is much more difficult. Thus, sodium almost exclusively forms a singly charged ion and compounds with nearly all anions.

Investigating the stability of ceramics in liquid sodium requires understanding the equilibrium thermodynamics of all of the elements involved. Beginning with a pure liquid metal, assume the following general reaction of a ceramic oxide in liquid sodium:

$$aMO + bNa \rightarrow cNa_2O + dM \tag{6.1}$$

MO is the metal-oxide ceramic of interest (yttria, zirconia, thoria, etc.), M is the free metal from that ceramic, and (a,b, c, d) are the balancing constants. The standard free energy of reaction for the above reaction is defined as:

$$\Delta G_R = \left(\sum \Delta G_f^o\right)_{products} - \left(\sum \Delta G_f^o\right)_{reactants} \tag{6.2}$$

So the chemical reaction is driven by the ΔG_R values. For $\Delta G_R > 0$, the reaction will not occur. For $\Delta G_R = 0$, the reaction is at equilibrium, and for $\Delta G_R < 0$, the reaction should move forward spontaneously. Thus, the largest positive values for ΔG_R are the most stable ceramics in liquid sodium. Accordingly, the most *negative* values for ΔG_f are expected to be most resistant to corrosion in liquid sodium. Figure 6.1 is a stability diagram showing ΔG_f for many oxide and nitrogen ceramics as a function of temperature[1].

Oxygen solubility in liquid sodium is temperature dependent and it has been shown that the stability of ceramics in liquid sodium would be affected by the presence of oxygen in solution[2]. A stability diagram for a system with oxygen dissolved in sodium is overlaid in figure 6.1, where the respective dashed lines show the chemical potentials of oxygen in sodium. Three oxygen concentrations are shown: 10^{-3}, 1, 10^3[ppm]. Re-inspecting figure 6.1, any ceramic with a more negative free energy of formation is stable at said temperature.

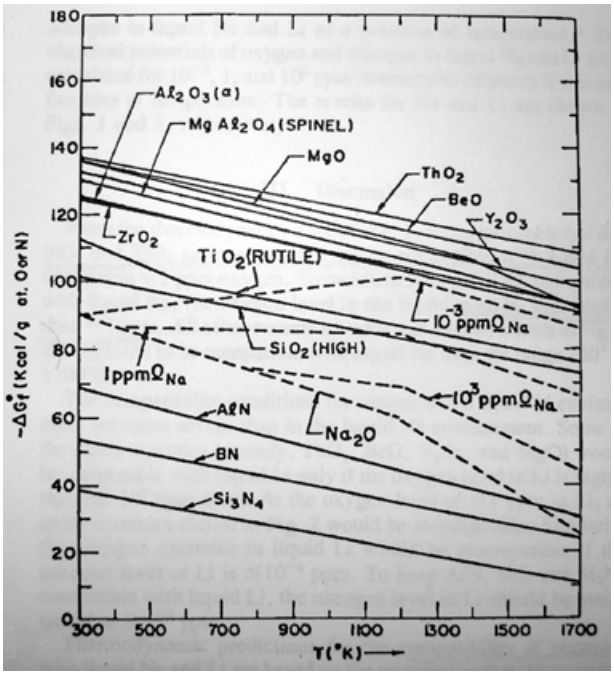

Figure 6.1: This figure shows many oxide and nitrogen compound ceramics Gibbs free energy of formation in liquid sodium at varying temperatures. Thoria and Beryllia are among the most stable according to thermodynamic theory [1].

For example, all of the oxide ceramics are stable in sodium with greater than one part-per-million oxygen in solution. However, TiO_2 and SiO_2 are not stable at concentrations less than one part-per-million. Thermodynamic theory predicts that thoria and beryllia are the most stable oxide ceramics in liquid sodium according to figure 6.1.

The described thermodynamics predictions are valid only for pure ceramics. Impurities may substantially modify free energies of formation, consequently changing their stability in liquid sodium. The kinetics of the problem has also been ignored by assuming that the surface reactions happen quickly, which may not be the case in a real system.

In order to understand a more complete picture of sodium corrosion of ceramics, corrosion mechanism must be studied. Qualitatively, liquid metal embrittlement[3] and grain boundary attack[4] have been observed. From oxygen sensor literature for liquid sodium systems, thermal cracking has been quoted as the primary cause of electrolyte failure for yttria-doped thoria(YDT)[5] sensors.

6.2.1 Yttria Stabilized Zirconia (YSZ)

YSZ is commonly used as a solid electrolyte in automotive oxygen sensors as well as in solid oxide fuel cells (SOFC)[6]. Research has also been performed on zirconia based electrolytes for sodium oxygen sensor application, but the rate of sodium attack has been repeatedly shown to be too high for a long term oxygen sensor[7, 8, 9]. However, the high ionic conductivity of YSZ and the motivation to reduce reliance on actinide metals like thorium provides reason to investigate YSZ sensors as short-term instruments.

One key difference between zirconia and thoria is the spontaneous formation of sodium-zirconate in the presence of dissolved oxygen impurity in the sodium:

$$Na_2O + ZrO_2 \rightarrow Na_2ZrO_3 \tag{6.3}$$

$$\Delta G_R = -171[\text{kJ/mol}] \qquad @320[C]$$

The negative ΔG_R means that this reaction will move forward spontaneously at 320[C]. Sodium with high concentration of oxygen will corrode zirconium-based ceramics faster than sodium of low oxygen concentration. It should be noted that this reaction occurs in addition to the general sodium oxidation reaction listed in equation 6.1. It is therefore expected that oxygen concentration affects corrosion rate of zirconia containing ceramics. An analogous spontaneous reaction has not been found for Y_2O_3 or thoria.

6.3 Static Corrosion Testing of Ceramics

In an effort to obtain a comprehensive database summarizing liquid sodium corrosion on ceramics, a diverse series of tests were conducted. The materials tested were chosen to either verify past experiments or to test possible sensor materials for liquid sodium compatibility. Specifically for oxygen sensor engineering, properties including porosity, hardness (machinability), resistance to thermal shock, and thermal expansion have to be assessed in order to

design an effective sensor. The materials tested in sodium were chosen in order to provide a range of each of these properties.

A static corrosion test facility was constructed in an inert glovebox environment on the UW-Madison campus. This facility can heat static liquid sodium to 600[C] with samples suspended from above. The liquid sodium is contained in a 316SS crucible (316SS corrosion in liquid sodium is minor, and this material interaction is well documented in previous research) and the samples are suspended using stainless steel wire from a lid that sits atop the furnace. Furnace temperature is maintained using a PID controller programmed in LabVIEW, and temperature measurements are taken using two thermocouples, both submerged directly in the sodium. This facility contains six identical furnaces with the above specifications. Power for each furnace heater is fed through a thermal switch to prevent overheating in the event of a LabVIEW crash. Details of the facility are provided in Chapter 4. It should be noted that, in order to minimize thermal shock, the samples are submerged in 100[C] sodium and the bath is then slowly brought to operating temperature (thermal shock can cause cracking of the electrolyte).

6.3.1 Operating Static Tests in Oxygen-saturated Sodium

A key limitation of working with high temperature liquid sodium is the difficulty to prevent oxidation of materials in contact with the sodium. These furnaces do not have a cold trap, and they are open to the glovebox atmosphere. Any oxygen present in the glovebox is continuously oxidized into the sodium until the sodium becomes saturated. After only dozens of hours of operation the sodium develops an oxide surface-crust, even when the glovebox was maintained below 2[ppm]. *Thus, for all of the static tests documented in this report, the sodium was assumed to be saturated with oxygen at its operating temperature.* These experiments, therefore, cannot control oxygen independently of temperature. High temperature tests occur at higher oxygen concentrations than low temperature tests. Examples of the respective oxygen concentrations are shown in Table 6.1.

Table 6.1: Oxygen concentrations of various static sodium temperatures

Temperature [C]	Concentration [ppm]	Temperature [C]	Concentration [ppm]
150	2.13	300	116.4
160	3.03	310	141.3
170	4.25	320	170.3
180	5.86	330	204.7
190	7.98	340	243.1
200	10.7	350	287.9

The values given in Table 6.1 were calculated using the Noden correlation, which was discussed in Chapter 2 and Chapter 3. The logarithmic dependence of oxygen concentration on temperature dictates that small changes in temperature have a more dramatic effect on oxygen concentration at low temperatures than at high temperatures. Figure 6.2 graphically shows this behavior.

While being able to vary oxygen at constant temperature would be optimal, given the experimental apparatus available, this could not be done. However, as shown in figure 6.2 and Table 6.1, substantial differences in oxygen could be achieved with minimal temperature change as long as the tests were conducted at higher temperatures. This data could then be extrapolated to low oxygen concentrations. Improvements for experiments of this type are discussed in Chapter 8.

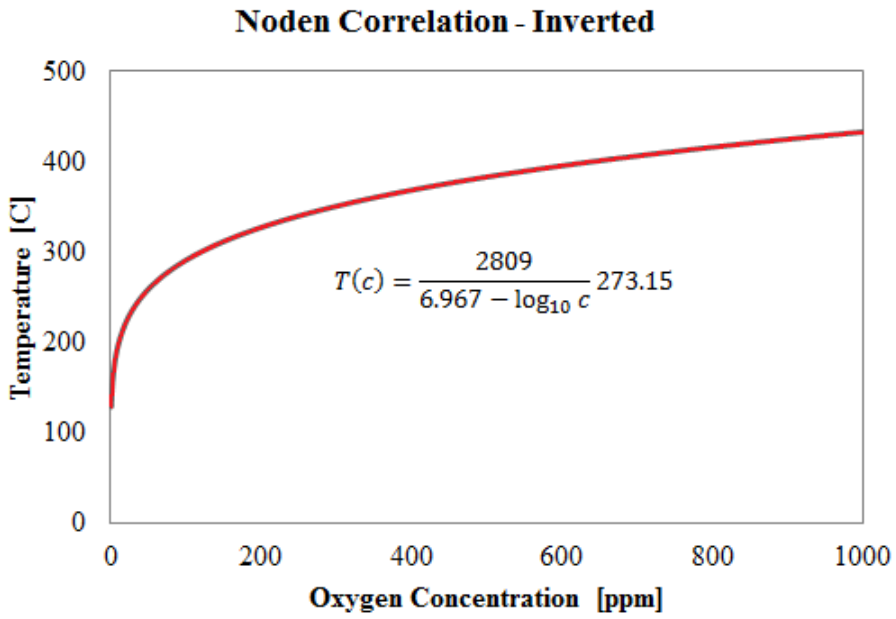

Figure 6.2: Inverting the Noden correlation shows how for a relatively constant high temperature, oxygen concentration changes substantially. In contrast, at low temperature, very large changes in temperature have a small effect on concentration.

6.4 Sintered YSZ

Preliminary testing of YSZ began with a small, low density substrate. This initial sample, a 0.3174[g] substrate of 7% YSZ (7% yttria by weight), was totally disintegrated in 355[C] liquid sodium after 105[hr] of static testing. The sodium bath was put through a sieve looking for chunks of YSZ, but only debris powder was found. While a high attack rate was expected from past work, the magnitude of this attack was intriguing. Follow-up experiments with high purity sintered YSZ crucibles obtained from McDanel functioned in 400[C] sodium for tens of hours as prototype oxygen sensors without failure. Thus, an extensive test matrix was conducted with these crucibles.

6.4.1 Sintered YSZ from McDanel

These cylinders were 10.5 wt. % yttria stabilized zirconia. Each cylinder was 0.375" outside diameter, and 0.250" inside diameter, with a height of 0.250". The total surface area of each cylinder was calculated and recorded, along with the initial mass. After sodium exposure for 50[hr], the samples were cleaned in an ultrasonic ethanol bath (to clean the sodium from the surface), then soaked in acetone, then left to air dry. The samples were then re-measured for mass. The change in sample mass was normalized by the initial surface area measurement. The results of sixteen of these tests are plotted in figure 6.3.

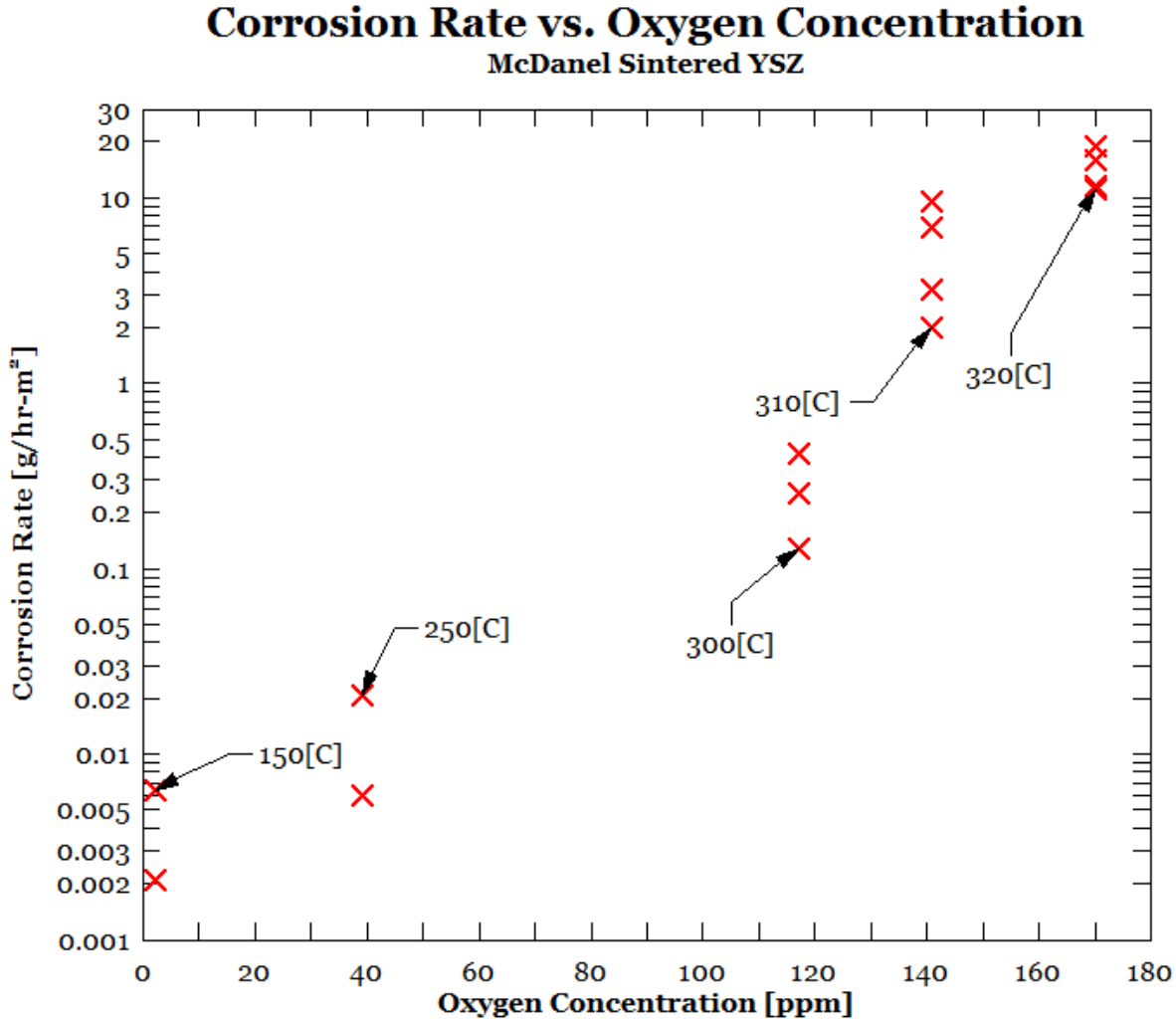

Figure 6.3: Corrosion rate (normalized by surface area) of sintered YSZ cylinders from McDanel. The oxygen concentration is linked to temperature.

Notice that by increasing from 300[C] to 320[C], nearly a 50% increase in oxygen concentration is achieved. While independent control of oxygen and temperature would be optimum, this experiment suggests that the attack rate of the McDanel YSZ samples increases with temperature, which agrees with the theory outlined in section 6.2.

EDS line-scans through the cross-section of the McDanel samples indicated no sodium penetration or change in stoichiometry. The corrosion mechanism seems to be even dissolution of all materials. While the formation of sodium zirconate is expected, it likely dissolves into the sodium immediately. The path of the EDS line-scan is shown in figure 6.4, and the data from the scan is shown in figure 6.5.

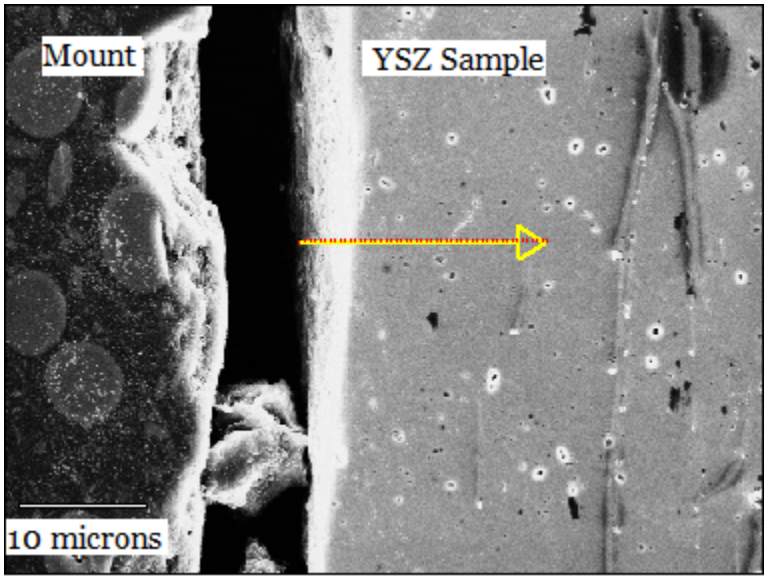

Figure 6.4: EDS line-scan of a McDanel YSZ cylinder after sodium testing at 320[C] for 50[hr]. No sodium penetration or change in stoichiometry was detected. The only corrosion mechanism appears to be dissolution.

It should be noted that the oxygen sensors tested in this research were made using this McDanel YSZ electrolyte, so the corrosion rates shown in figure 6.3 should be representative of how the sensors would behave in sodium at these conditions. However, the sodium loops have never been run higher than $\approx$ 60[ppm] dissolved oxygen, and the operating temperature is typically 320-350[C]. So the corrosion rates shown in figure 6.3 are certainly high estimates

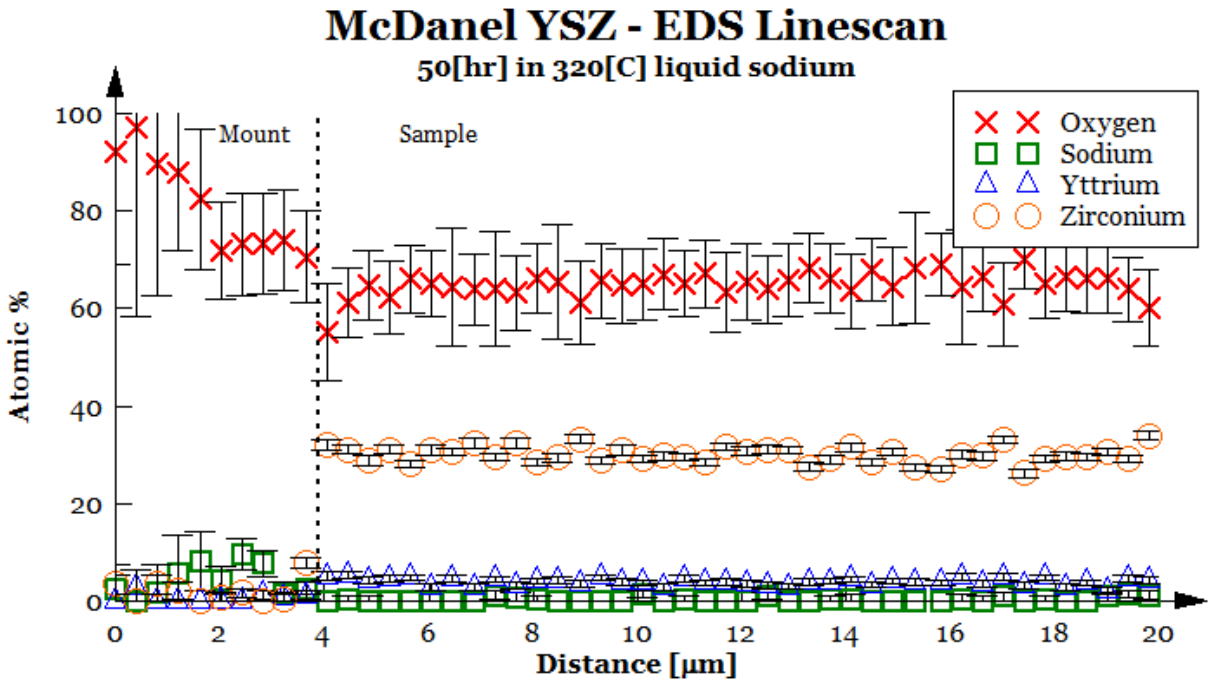

Figure 6.5: EDS line-scan of a McDanel YSZ cylinder after sodium testing at 320[C] for 50[hr]. No sodium penetration or change in stoichiometry was detected. All constituents of the material appear to be dissolving at the same rate. *A zoomed in version of this plot is included in Appendix D which shows specifically the sodium concentration.*

for what can be expected on the oxygen sensors.

6.4.2 Sintered YSZ from Friatec

Friatec AG is a German materials engineering company which specializes in corrosion-resistant materials. They donated some of their blend of YSZ to UW-Madison for sodium testing. The resulting corrosion rate was much smaller in comparison to the McDanel YSZ, as shown in figure 6.6.

While the mass-loss-rate of McDanel sensors was substantial after only fifty hours, the Friatec samples a very slight *gain* in mass after this same amount of time (and longer). It has been found that more resilient materials to sodium attack sometimes gain more mass from sodium penetration than they lose from material-corrosion (as shown with Al_2O_3 later in this report).

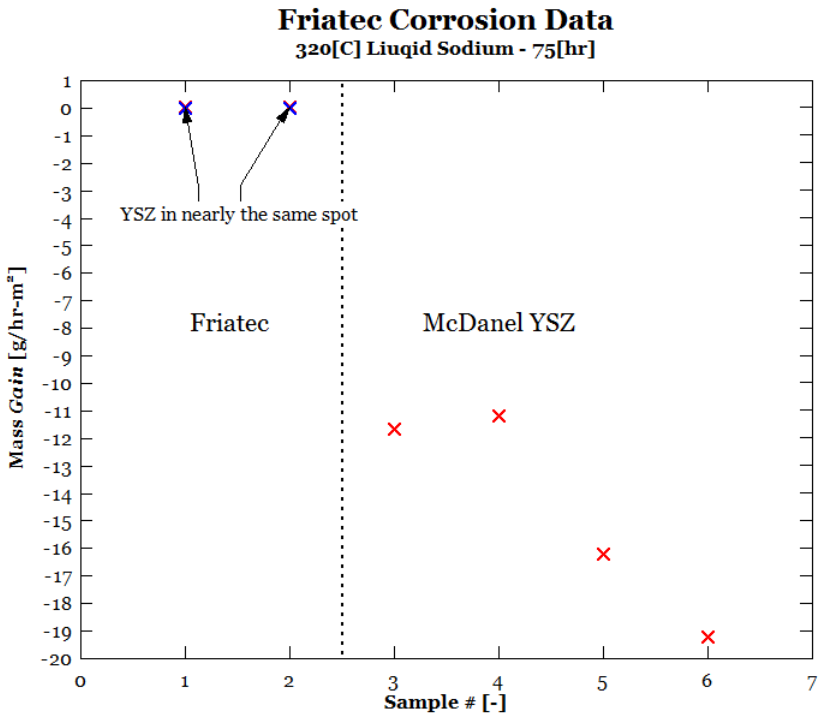

Figure 6.6: After 75 hours in 320[C] sodium the McDanel YSZ had significant mass-loss rates. In contrast, the Friatec YSZ has actually gained mass. EDS line-scans confirm the slight mass-gain is a result of sodium penetration into the ceramic.

EDS line-scan across the cross-section of a Friatec YSZ sample would reveal very little stoichiometry change, and only 0.5 atomic % sodium throughout the sample (figure 6.7). Moreover, there was not an increase in sodium concentration near the edge of the sample. This suggests that very little sodium could have penetrated into the sample, and the sample's resistance to sodium attack appears excellent.

Friatec ceramics were not found until after this research was completed, so the sensors were developed using McDanel YSZ. EDS measurements of the unexposed Friatec YSZ revealed a Y_2O_3 concentration of 10% by weight, which is the exact same yttrium amount as the McDanel YSZ. It is not known how the two companies sinter the respective ceramics, but slight *changes in the sintering process have been found to have a significant effect on resistance to sodium attack*[10]. Friatec has been helpful in providing samples for testing, and has expressed interest in further research cooperation[11]. Further studies on the effectiveness

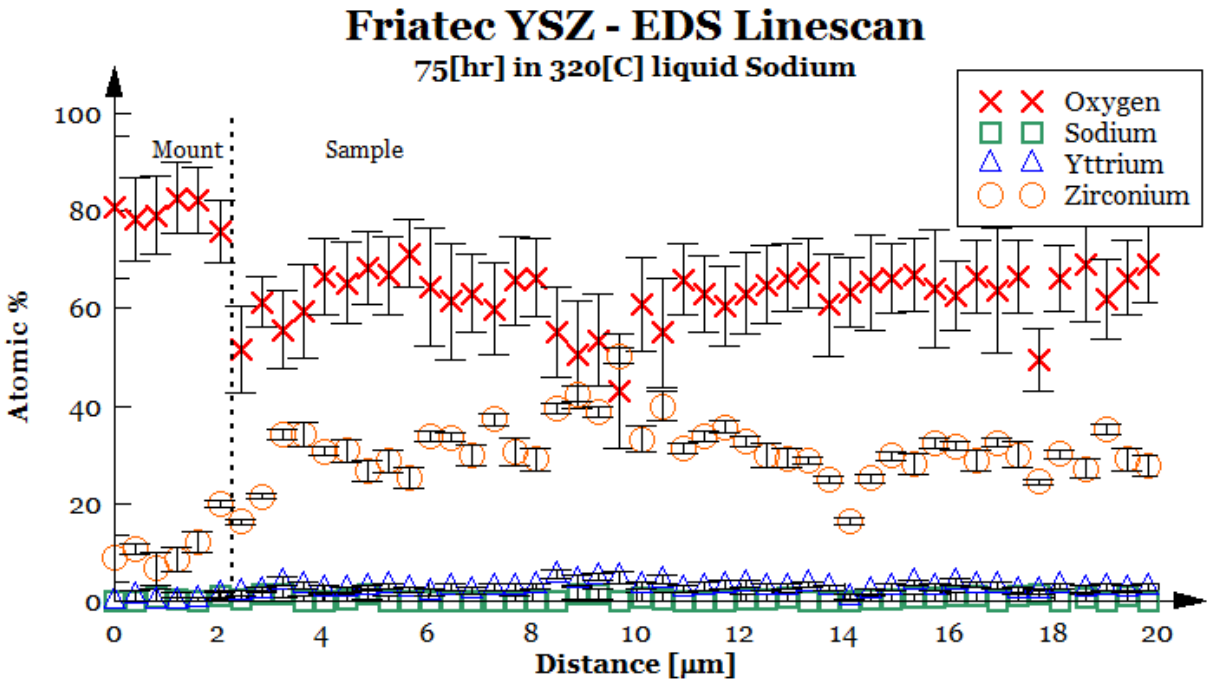

Figure 6.7: Very little total sodium was detected throughout the sample. Moreover, there was no apparent change in composition of the sample near the surface, indicating little sodium attack or penetration. Mass-loss data in figure 6.6 indicates that the Friatec YSZ is more resistant to sodium attack than McDanel YSZ. *A zoomed in version of this plot is included in Appendix D which shows specifically the sodium concentration.*

of various sintering recipes and differences in microstructure is suggested for future research in Chapter 8.

6.5 Other ceramic substrates

Alumina (Al_2O_3) shows similar stability in liquid sodium as zirconia (according to figure 6.1), however, when a substrate of sintered alumina was tested in the same conditions (355[C] for 105[hr]), the alumina showed less than 0.01% mass-loss. This alumina came from CoorsTek, and was used as a preliminary test to direct future research.

A follow-up test matrix was carried out on CoorsTek aluminum oxide, investigating mass-loss and surface-loss over time exposed to liquid sodium. Beryllium oxide (donated by American Beryllia Inc.) was tested in parallel, since according to literature[7] it behaves well

in liquid sodium. Extreme caution was taken, however, due to the health hazards associated with handling beryllium oxide. Both materials performed well, totaling less than 1% mass-loss after 490[hr] in 315[C] liquid sodium. All mass measurements were taken with 7 digits of precision, and averaged over 5 readings, re-zeroing the scale after each reading. The mass measurements were then normalized by the product ρA (density times surface area), which gives a thickness loss in microns. Both of these samples were near full listed density, with minimum porosity.

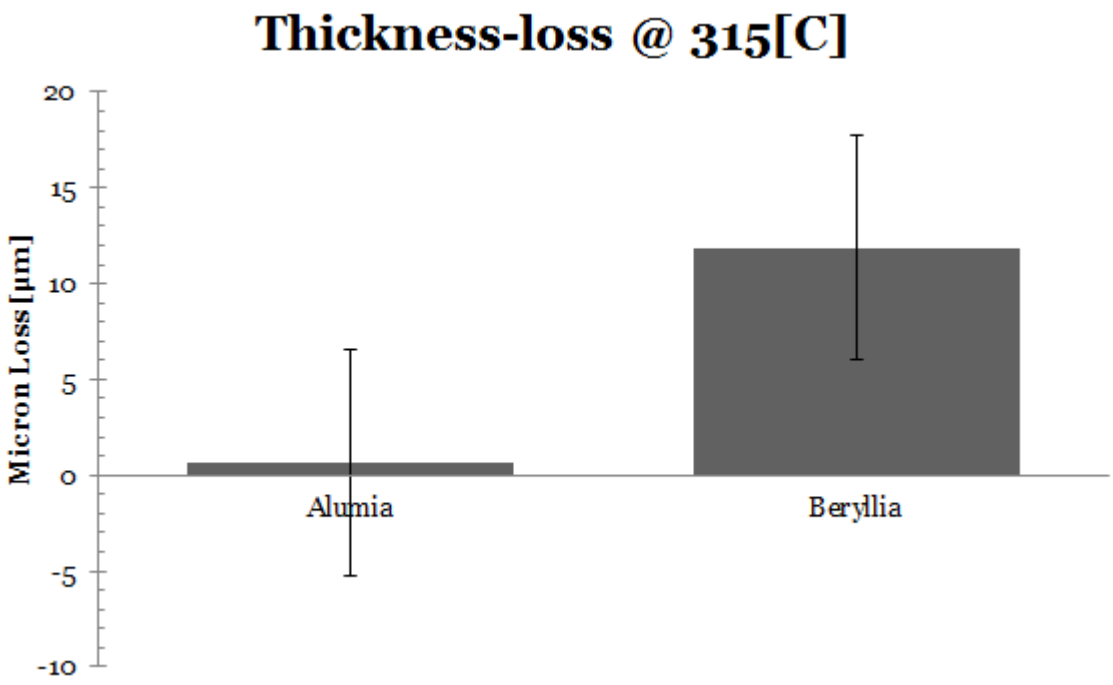

Figure 6.8: This figure shows the surface-loss of the two samples, BeO and Al_2O_3. No detectable loss was found for the alumina sample, and BeO showed minimal attack.

The test was interrupted for mass measurement every $\approx$ 100[hr]. The samples were removed and cooled at room temperature in the glovebox environment. The samples were then cleaned with the same basic cleaning process described for YSZ using ethanol, acetone, and the ultrasonic bath. These measurements were taken (summarized in figure 6.8) and the process was repeated.

The acquired data had substantial variability between 100[hr] tests. The mass of each

sample increased and decreased seemingly chaotically. The data shown in figure 6.8 is the averaged mass-loss data after 490[hr] in liquid sodium. The error bars were estimated from the variability in the 100[hr] measurements. These considerable error bars are larger than the total measurement in the case of the alumina mass-loss. This suggests that *no measureable damage* was detected in this case, and very little damaged in the beryllia. It is thought that there was some inconsistency in sample cleaning, and measurement taking. While systematically, the process was very consistent, there could have been random errors, such as ambient humidity during the drying phase that changed the mass of the sample.

The irregularities of the measurements aside, the conclusion from this experiment was that both materials performed very well in liquid sodium at low temperature. Neither is a particularly strong ionic conductor, so use as a primary electrolyte material is doubtful. However, both alumina and beryllia could be used as structural components if need be (at least at low temperatures). Follow-up experiments with alumina from another manufacturer will be shown which give contradicting data, suggesting that manufacturing technique is as important as the material itself.

A 400[C] follow-up test was conducted with fired alumina (from McDanel) and bisque alumina. In addition, MACOR and Boron Nitride (BN) were tested simultaneously. MACOR is a machinable glass ceramic composed mostly of silica; the exact composition of MACOR is given in Appendix C. MACOR and bisque alumina were of particular interest as machinable ceramics; machining an electrolyte for a sensor out of sintered YSZ or full-fired alumina is much more difficult.

The bisque alumina did not survive the ultrasonic bath. The sample was greatly fragmented and warped upon removal from sodium, then promptly fell apart during cleaning. Bisque alumina is the same elemental composition as full-fired alumina, the only difference being it has not been heated to maximum sintering temperature, so it has lower density. Chemically, this sample should have done well according to figure 1. However, clearly another corrosion mechanism occurred on the low-density material. The alternative mechanism

Figure 6.9: This figure shows full-fired McDanel alumina after only 100[hr] in 390[C] liquid sodium. The length of each square in the grid shown is 1/4".

for the attack is not yet known. Graphite-sodium interactions have been known to exhibit intercalation, where the sodium embeds itself within graphite and can cause damage even though graphite should be stable in sodium[12]. Research is ongoing into this mechanism, however, since the attack found in alumina occurred at a very low temperature compared to the graphite intercalation.

The full-fired McDanel alumina sample experienced extreme cracking, warping, and fragmentation as shown in figure 6.9. The sample did survive the ultrasonic bath but it crumbled while trying to take mass measurements. This is again likely attributed to thermal shock, grain boundary attack, or possibly intercalation. Neither of these samples were able to be measured for mass-loss.

Two different alumina samples with similar material composition from different manufacturers experienced significantly different sodium attack. The dependence on manufacturing technique has been observed in past sodium experiments[10]. More evidence of this dependence will be shown in the YSZ sections of this chapter.

In contrast to the two alumina samples, the BN and MACOR survived the first 100[hr] well so mass and thickness measurements were taken. The experiment carried out for 300[hr]

of data. See figure 6.10 for the results of these tests. Neither sample saw significant attack. In addition to mass measurements, the thickness of each sample was measured with a micrometer at each 100[hr] step. All measurements are the average of 10 individual measurements, for both thickness and mass. The percent-changes of the sample mass and thickness are shown in table 6.2.

Table 6.2: Summary of the data displayed in figure 6.10.

Sample	% Mass Change	% Thickness Change
MACOR	+0.362%	+0.903%
Boron Nitride	−0.459%	+0.440%

Figure 6.10 shows the details of the BN-MACOR experiment. The mass of each sample remained fairly constant throughout the test. The magnitude of the observed swelling and mass-change was less than 1% for both samples.

To investigate this swelling, energy dispersive x-ray spectroscopy (EDS) line scans were done across the surfaces to see if sodium diffused into the surface of the sample, causing swelling. Figure 6.11 shows an EDS line scan across the Boron Nitride. Some sodium penetration was found.

In addition, EDS line-scans of the MACOR ceramic also showed some sodium penetration at the surface, but still very little diffusion into the sample (figure 6.12). This small penetration does explain the slight mass increase and swelling seen in the MACOR sample.

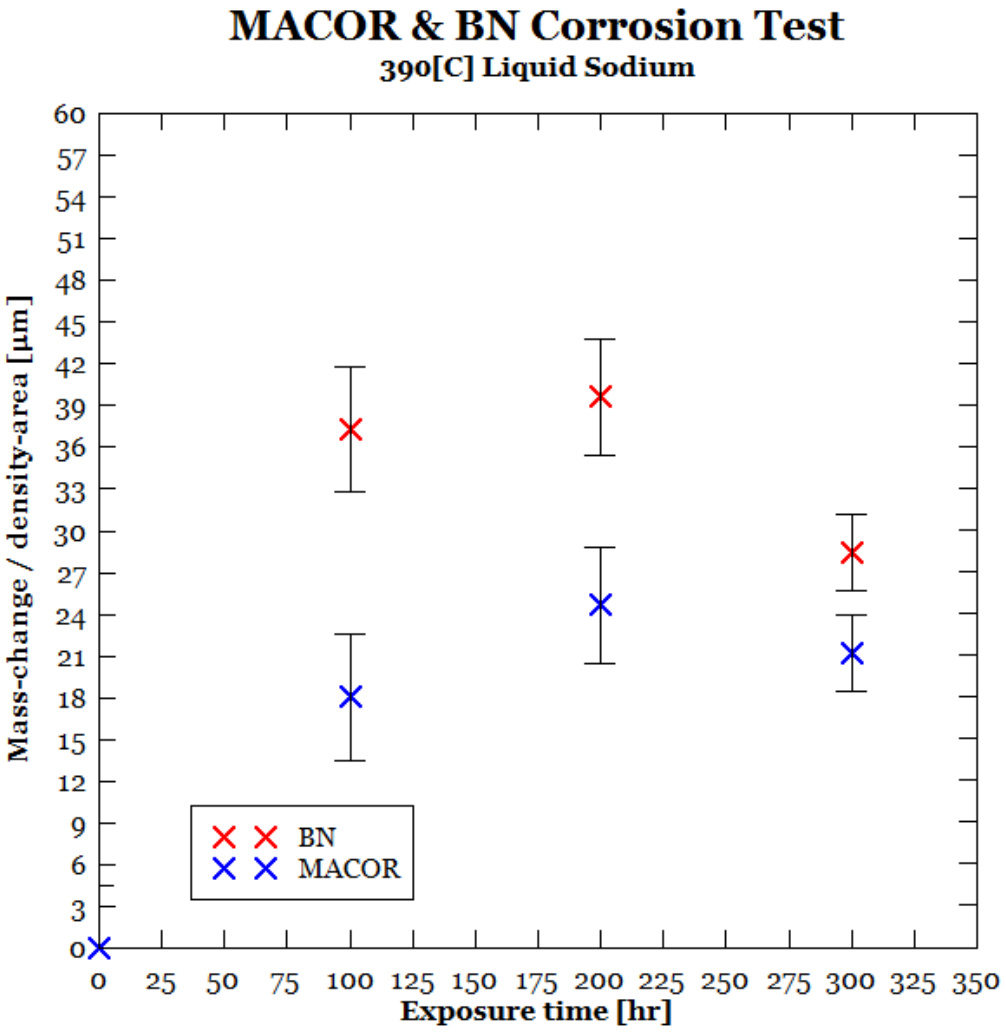

Figure 6.10: Both BN and MACOR showed slight swelling and increase in overall mass throughout static testing at 390[C]. The y-axis was determined by dividing the mass-increase measurement by the density and surface area of the samples.

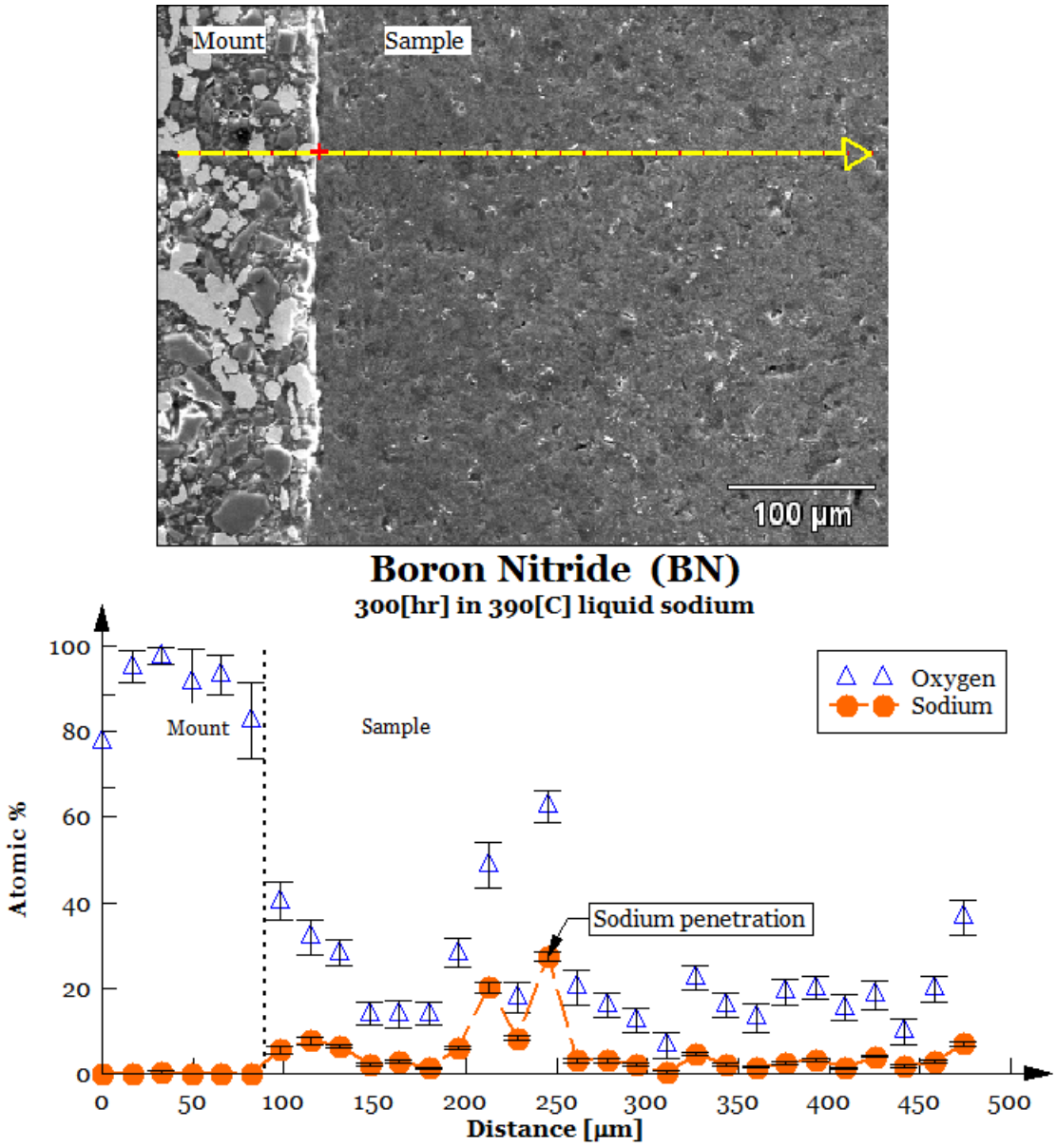

Figure 6.11: This figure shows one of three line scans conducted that show some sodium penetration through the ceramic. This penetration is most likely the cause of sample swelling. Exposure: 300[hr] at 390[C].

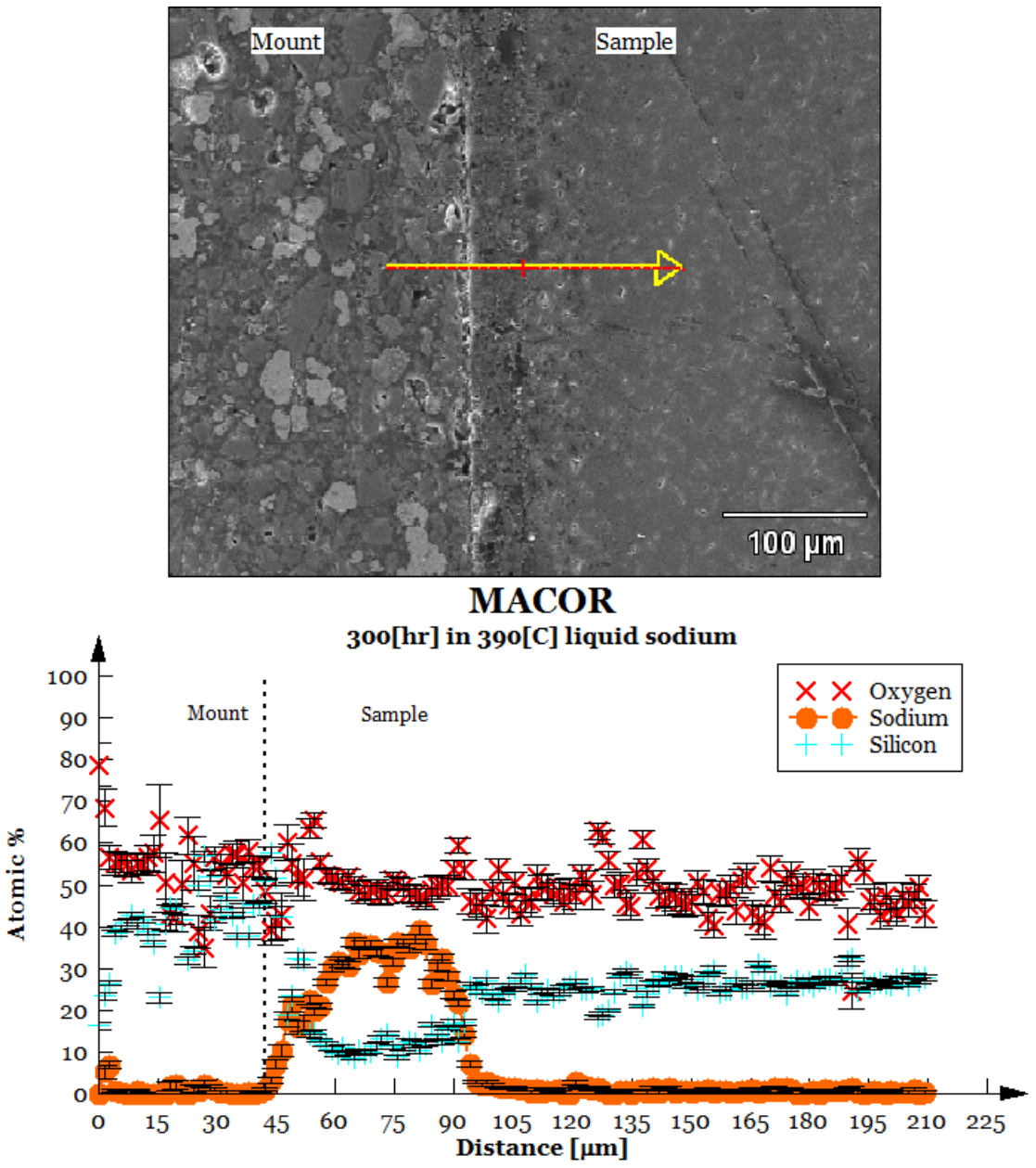

Figure 6.12: This figure shows some sodium penetration through the MACOR ceramic and the beginnings of a degraded layer in the first 50[μm]. Exposure: 300[hr] at 390[C].

MgO from Friatec

Two sintered MgO samples were donated by Friatec for testing in sodium. The samples were flat washers with an outer diameter of 0.669[in]. The inner diameters of the samples were different, one at 0.283[in] and the other at 0.350[in]. The washers were 0.10[in] thick each. These samples were submerged for 75[hr] at 320[C] and no sodium attack was observed. This is consistent with past research[7]. The results of this experiment are shown in table 6.3.

Table 6.3: Friatec MgO showed no sodium attack. Slight mass-increase was detected from sodium leaching into the sample.

Sample	Initial Mass [g]	Final Mass [g]	Difference [g]	Area [m^2]	**Rate** [g/m^2-hr]
MgO-1	$2.6329 \pm (2.28 \times 10^{-6})$	$2.3364 \pm (4.69 \times 10^{-6})$	9×10^{-6}	536×10^{-6}	+0.0163
MgO-2	$2.3358 \pm (3.03 \times 10^{-6})$	$2.6335 \pm (2.19 \times 10^{-6})$	7×10^{-6}	502×10^{-6}	+0.0129

EDS line-scans confirmed that the MgO experienced little sodium penetration, and the images showed no visual cracking or increase in porosity near the surface. The EDS results are shown in figure 6.13. The line-scan confirmed no significant change in chemical composition occurred at the surface of the ceramic.

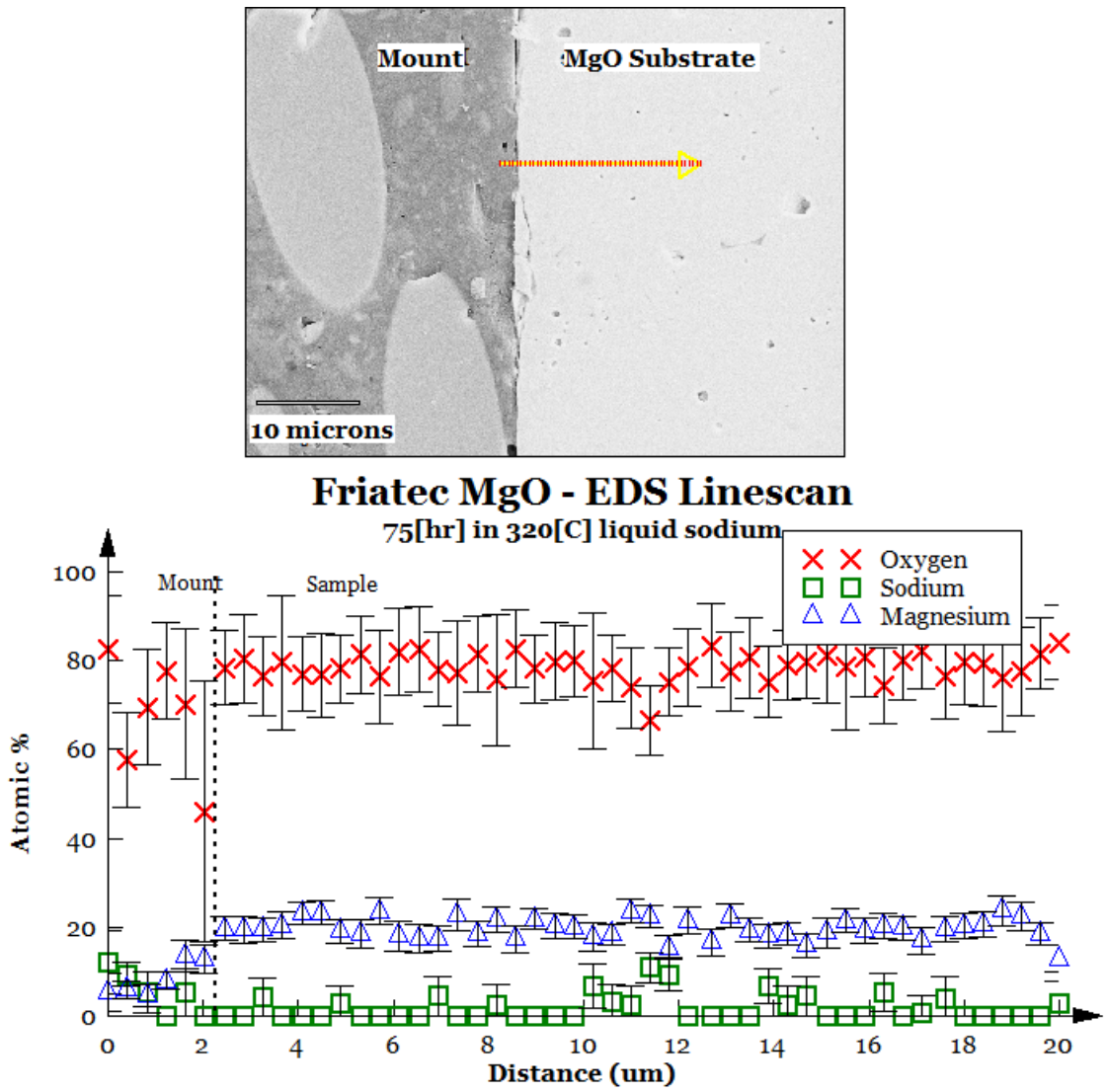

Figure 6.13: MgO experienced very little sodium attack. EDS line-scans indicated very little sodium penetration and no observable change in stoichiometry at the interface.

6.6 Thermal Spray Coatings

Thermal spray ceramics potentially offer attractive contributions to oxygen sensor electrolyte technology. Sintered electrolytes like YSZ and YST are too dense for common machining tools. Thus, manufacturing certain geometries is difficult or unreasonable. Thermal sprayed material can be applied to a variety of base materials, and can even span gaps. If thermal sprayed electrolyte material is found to survive liquid sodium then it could feasibly be used as the oxygen sensing electrolyte for sensors. The following sections of this report discuss a variety of thermal sprayed coating tests.

Thermal Spray Technologies Inc., a company located in Sun Prairie, WI, has sprayed the yttria and YSZ coatings used in this research. The company sprayed a variety of coating materials, densities, and thicknesses onto various substrates and these samples were tested in static sodium. The yttria concentration was varied in YSZ in order to study the effect of yttria dopant concentration on sodium attack. As discussed in section 6.2, yttria is among the most stable oxides in liquid sodium, and YSZ should become more resistant to sodium attack with increasing yttria content.

Three different substrate materials were prepared for thermal spray coatings: 416SS, alumina, and MACOR. 416SS was chosen as the best candidate steel for thermal spray, since the coefficient of thermal expansion (CTE) is closer to that of zirconia than many other metallic alloys (like 316 austenitic stainless steel). MACOR is a machinable glass ceramic composed primarily of alumina, silica, and magnesium oxide, and has a CTE closer to zirconia than stainless steel. Alumina was also tested since its CTE is extremely close to zirconia. However, the difficulty of machining alumina or forming complex geometries makes it a non-ideal base material for an oxygen sensor. Table 6.4 lists the CTEs for relevant materials. Large differences in CTE between the coating and substrate material can lead to coating delamination.

Table 6.4: Coefficients of thermal expansion for the materials discussed in this section

Material:	CTE [1/C]
416SS	11.0×10^{-6}
MACOR	9.3×10^{-6}
Y_2O_3	8.1×10^{-6}
Al_2O_3	8.0×10^{-6}
YSZ	7.5×10^{-6}

6.6.1 Thermal spray coatings on 416SS

A test with pure yttria coatings on 416SS substrates has been completed for 200[hr] at 300[C]. The samples were removed, cleaned, measured, and inspected after each 25[hr] in sodium. Two different coatings were tested: one less porous than the other. First observations showed the samples holding up well, but starting to fragment and shed debris as exposure duration increases. See figures 6.14 and 6.15.

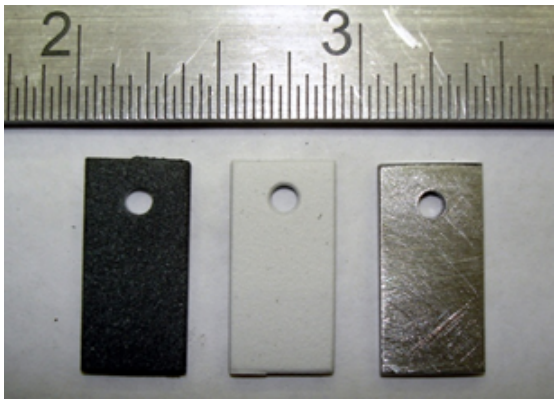

Figure 6.14: From left to right: dense, porous, and uncoated 416SS substrates (Y_2O_3 coatings) **before** exposure to liquid sodium

Figure 6.15: 416SS substrates **after** 200[hr] in liquid sodium. Testing stopped after coating began to flake from surface.

The porous coating held up best in sodium. While the surface was discolored, it did not

experience flaking or cracking. EDS scans revealed that the coating has slight separation from the surface of the steel, possibly due to differences in thermal expansion between 416SS and the yttria (figure 6.18). Some cross sections showed sodium deposited between the coating and the steel, but upon further inspection of the entire substrate, it appeared that sodium did not diffuse through the ceramic, but rather, made its way through cracks at the edge of the coating to get to the surface of the steel.

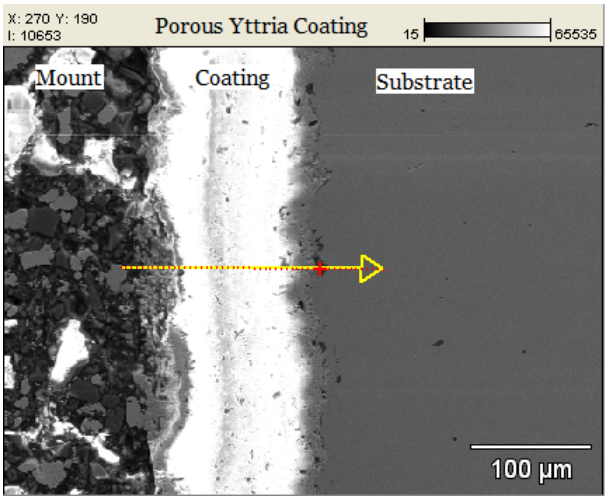

Figure 6.16: The coating was initially well adhered to the 416SS surface, with no noticeable cracking. The white streak is from charging of the non-conductive ceramic.

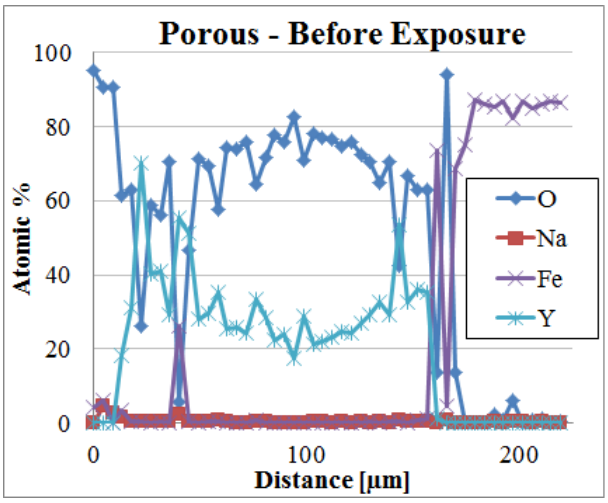

Figure 6.17: There was initially no measurable sodium within the Y_2O_3 coating. Oxygen and yttria concentrations were as expected. A zoomed-in plot of the sodium data is shown in figure 6.24.

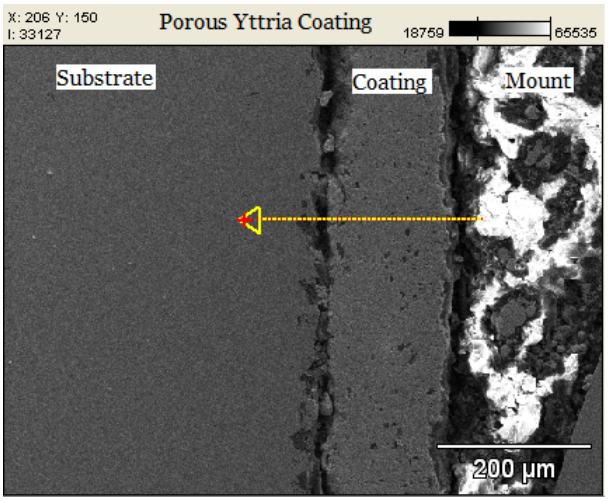

Figure 6.18: The porous coating is no longer well adhered to the surface. However, the integrity of the coating is intact.

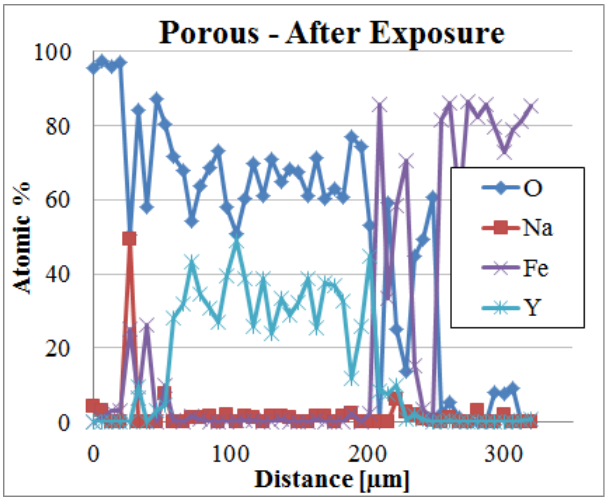

Figure 6.19: EDS line-scans showed that the coating remained intact, and further investigation would indicate very little sodium penetration through the substrate(figure 6.25).

The denser coatings did not survive well in liquid sodium. The dense samples experienced the same separation from the 416SS substrate, but also showed substantial fragmenting throughout the coating (see figure 6.22). EDS line-scans revealed that sodium penetrated directly through the coating (figure 6.23), whereas the more porous samples more effectively held sodium out.

Given that the porous samples survived better in liquid sodium than the dense coatings, appears that a mechanism other than selective leaching of oxygen from the coating into the sodium is taking place. It is expected that with increasing porosity (and surface area), the rate of oxygen leaching into the sodium would increase. However, the opposite effect was observed. Therefore, it is likely that the difference in thermal expansion between the 416SS substrate and the yttria coating was sufficient to stress the coating at elevated temperatures. A porous coating will adapt better to these stresses than a denser (and therefore more brittle) coating. The porosity allows room for the internal stresses to be dispersed, i.e. a greater ability to absorb stresses than with the dense coatings.

Once the dense coating began to crack under increased thermal stress, sodium was free to flow into pores and cracks within the coating, hence the deep sodium penetration observed

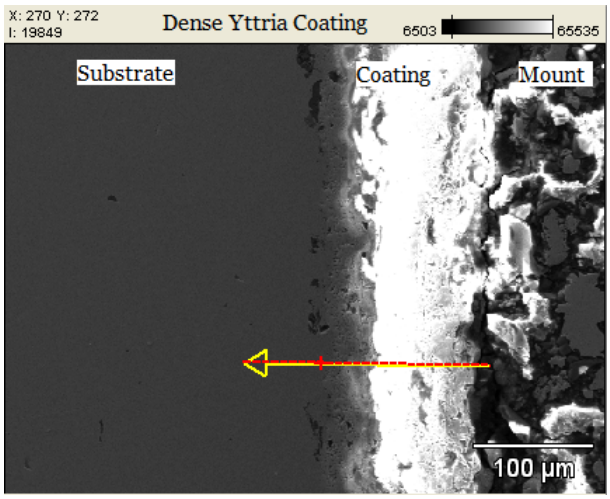

Figure 6.20: This figure shows the dense yttria coating closely adhered to the 416SS surface. The bright streak is from SEM charging.

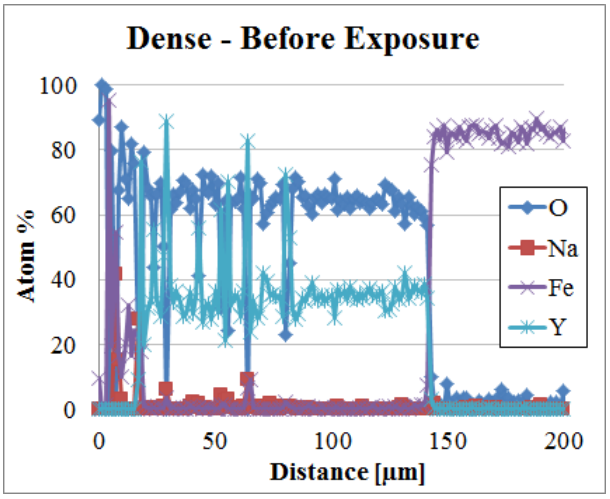

Figure 6.21: EDS line-scans of the pre-exposure samples showed no sodium presence within the ceramic or on the substrate surface. A zoomed-in plot of the sodium data is shown in figure 6.26.

in figure 6.23. An indicator of sodium attack on the yttria surface would be if oxygen concentration was decreased at the sample surface. This is not observed in figure 6.19, however. Because the sodium penetration in figure 6.23, it cannot be concluded whether the dense coating was experiencing significant attack at the surface. As described above, thermodynamic analysis suggests that the increased density would decrease the attack rate for this sample. A summary of the data from this experiment, including the change in porosity, is shown in table 6.5.

Table 6.5: Data from yttria coatings on 416SS substrates in liquid sodium for 200[hr] at 300[C]

Coating:	Initial Porosity	Final Porosity	Thickness gain	% Swelling
Dense yttria	0.97%	n/a	+84.57[μm]	60.0%
Porous yttria	1.81%	2.42%	+13.77[μm]	7.37%

The EDS scans shown in this section do not describe in detail the sodium penetration. A zoomed in version of each scan is shown in figures 6.24, 6.25, 6.26, and 6.27.

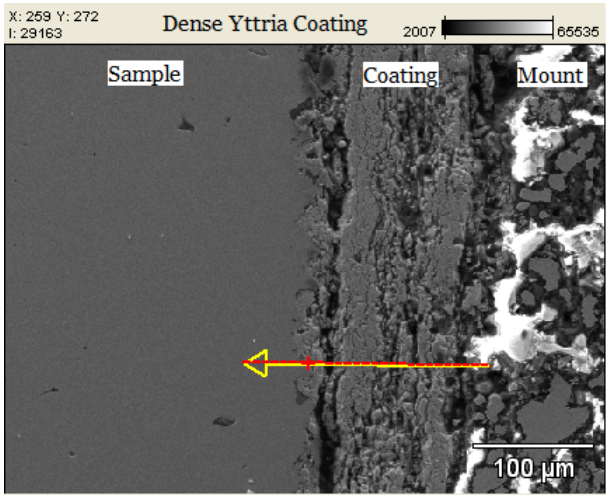

Figure 6.22: The dense coating was completely fragmented after 200[hr] exposure to 300[C] sodium.

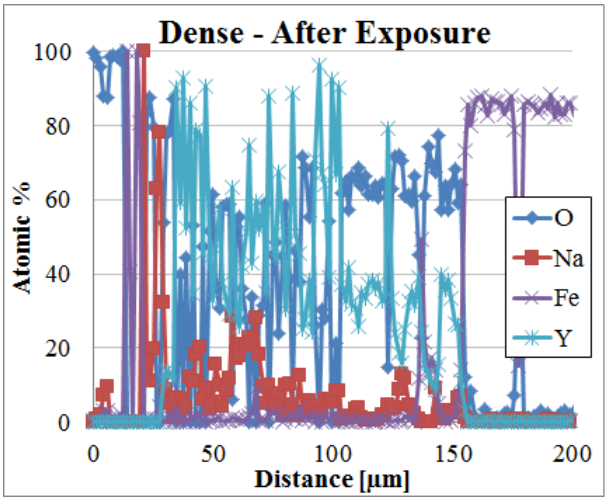

Figure 6.23: Sodium penetrated the coating all the way to the steel substrate as it corroded the Y_2O_3. A zoomed-in plot of the sodium data is shown in figure 6.27.

The main conclusion drawn from this experiment was that thermal spray coatings hold up at low temperatures in liquid sodium well enough to justify further investigation. Thermal spraying an electrolyte onto a sensor electrode is an attractive solution to the problem of engineering an oxygen sensor (the details of which are discussed in Appendix B). However, the stress from the substantial difference in CTE of 416 and yttria causes cracking and would cause the failure of a sensor. The following sections investigate the coating quality on MACOR and alumina, which have closer CTEs to yttria and YSZ.

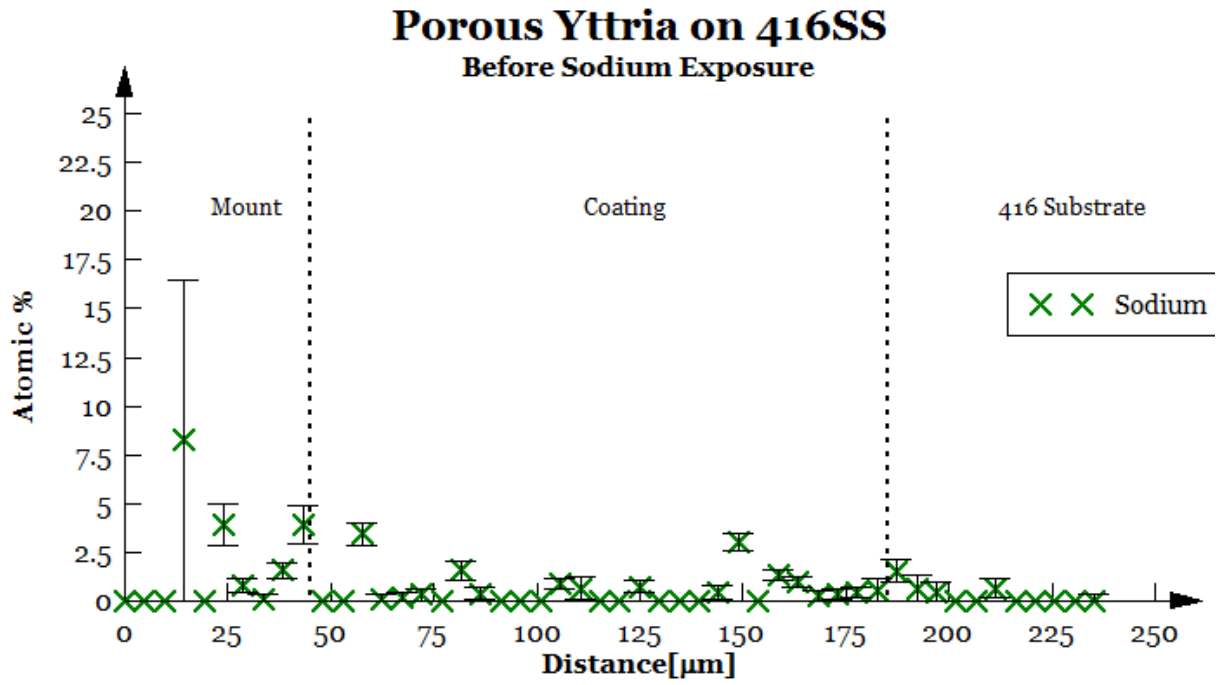

Figure 6.24: Very little sodium was detected throughout the porous yttria sample before sodium exposure. This is the same data from figure 6.17, but the sodium points have been isolated.

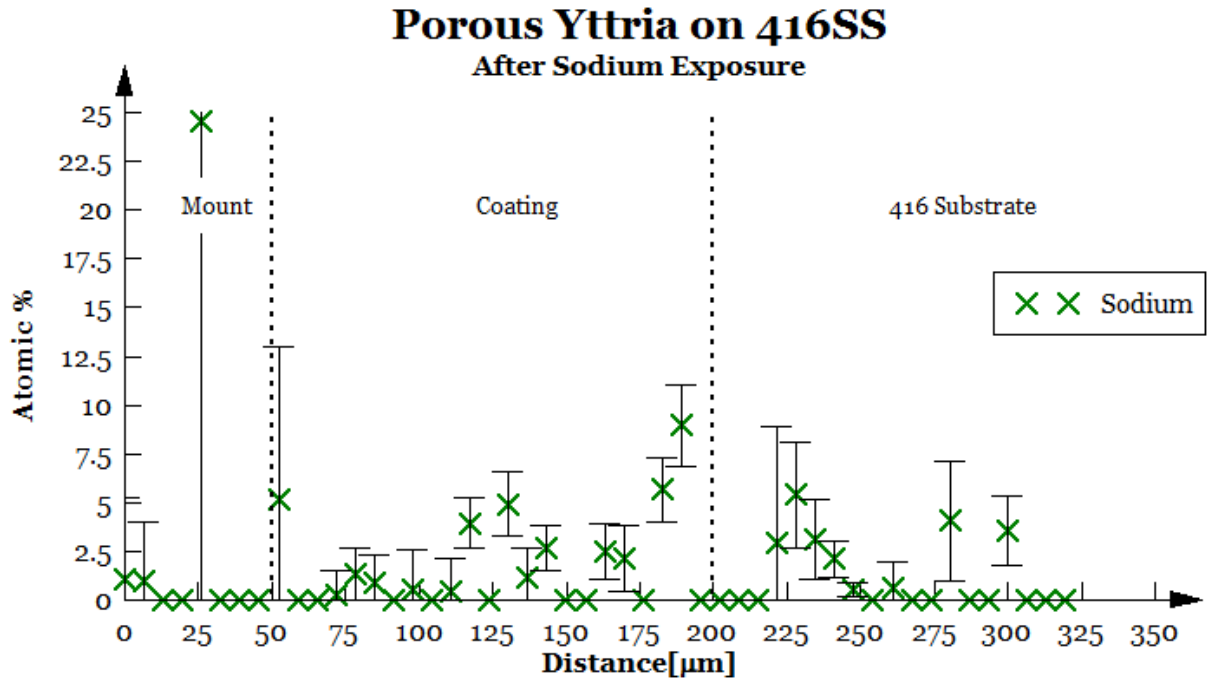

Figure 6.25: While the integretit of the coating appeared to be in tact from SEM images, this EDS scan shows slight penetration. This is the same data from figure 6.19, but the sodium points have been isolated.

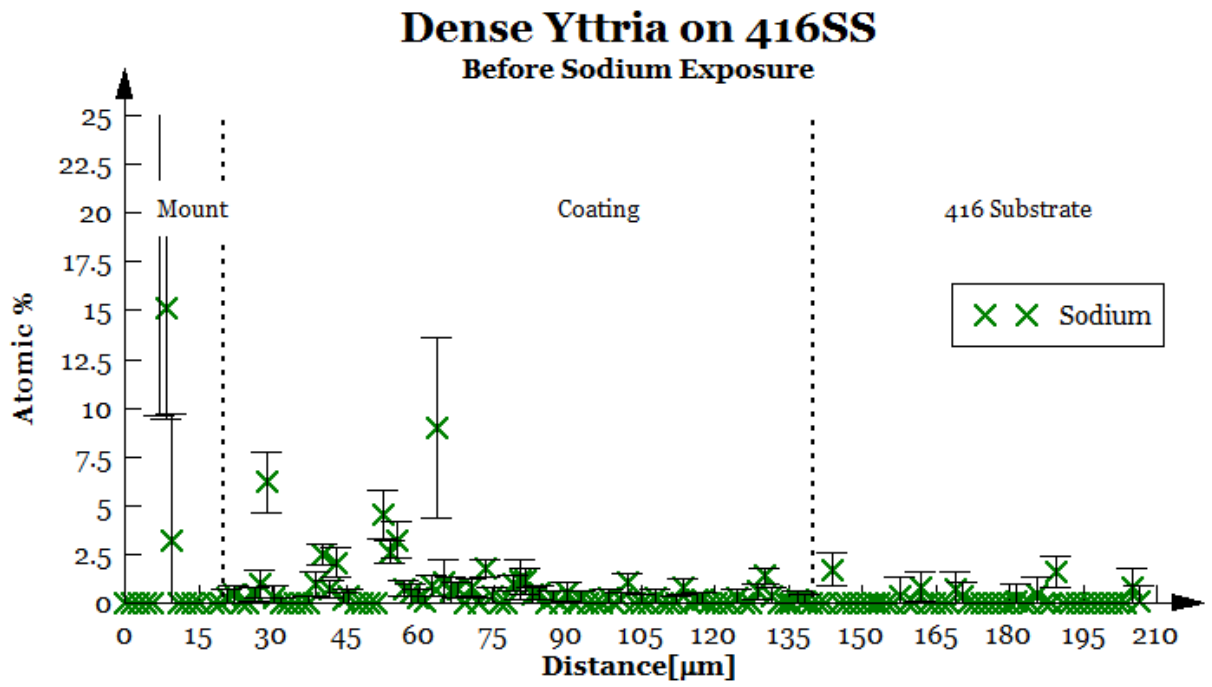

Figure 6.26: The dense yttria coating similarly showed very little initial sodium concentration, as expected. This is the same data from figure 6.21, but the sodium points have been isolated.

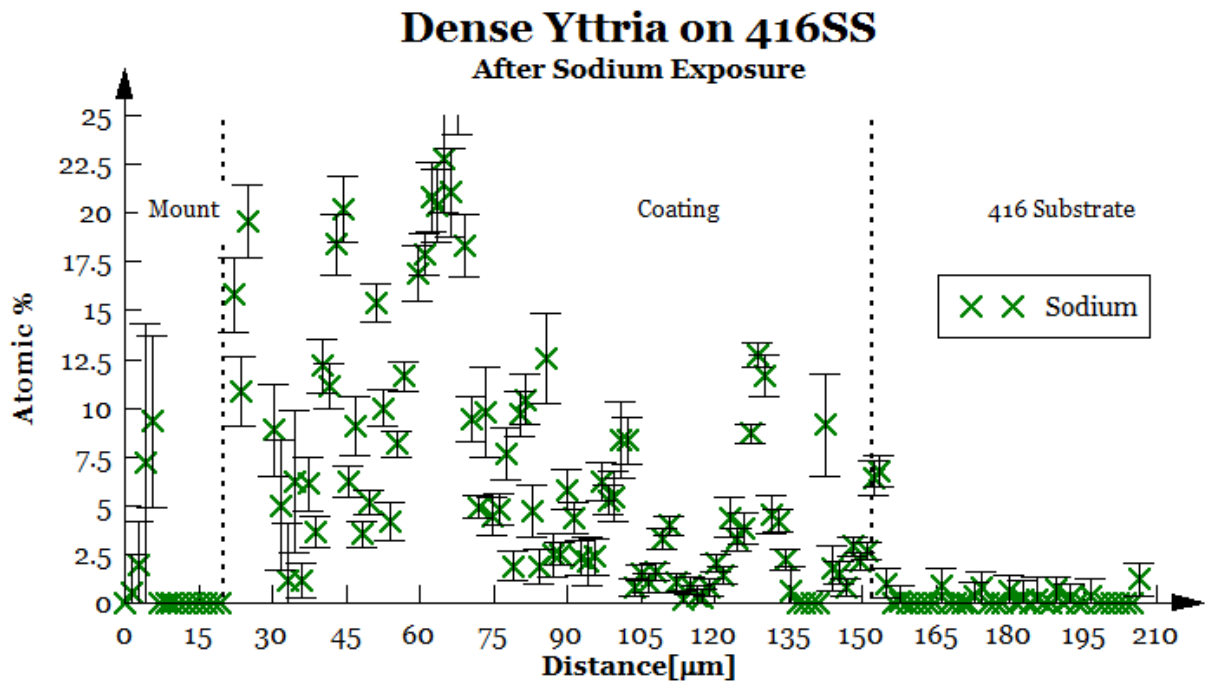

Figure 6.27: Once the dense coating cracked due to thermal stresses sodium freely penetrated the coating, as shown by this EDS line-scan. This is the same data from figure 6.23, but the sodium points have been shown exclusively to show how dramatic the sodium penetration was.

6.6.2 Thermal spray coatings on alumina

Dense and porous yttria coatings were also thermal sprayed onto alumina substrates. Since the CTE of alumina is very close to that of yttria (see table 6.4), one would expect lower stress at the coating interface, and therefore less cracking. This was observed in the SEM images of these samples (Figures 6.28, 6.29, 6.30, 6.31). No substantial sodium penetration was detected in these samples. Full-size plots of these lines-cans are available in Appendix D.

These samples were in liquid sodium for 200[hr] at 350[C]. The oxygen concentration of saturated liquid sodium at 350[C] is 288[wppm]. The coatings adhere better to alumina than they did to 416SS, as shown in table 6.6.

Table 6.6: Data from yttria coatings on alumina substrates in liquid sodium for 200[hr] at 350[C]

Coating:	Thickness gain	% Swelling
Dense yttria	$-7.02[\mu m]$	-4.67%
Porous yttria	$+7.01[\mu m]$	$+5.46\%$

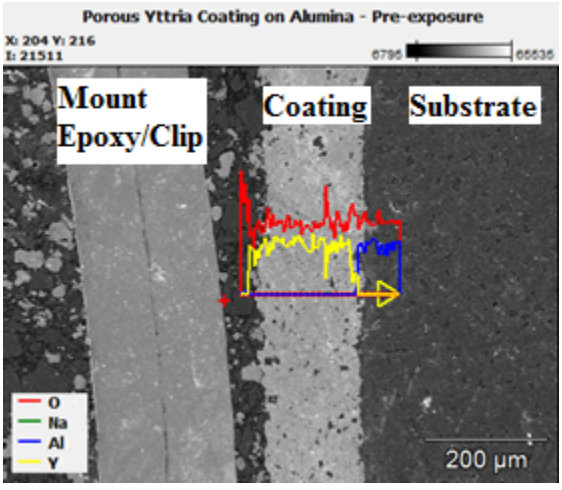

Figure 6.28: Porous yttria coating on alumina *before* liquid sodium exposure. No measurable sodium detected.

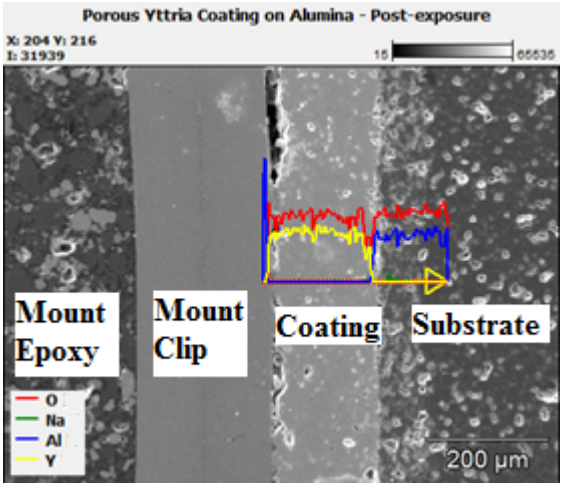

Figure 6.29: Porous yttria coating on alumina *after* exposure to 350[C] sodium for 200[hr]. No measurable sodium detected.

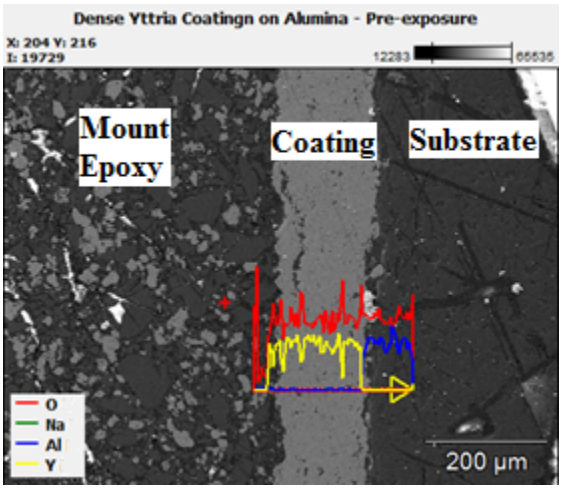

Figure 6.30: Dense yttria coating on alumina *before* liquid sodium exposure. No measurable sodium detected.

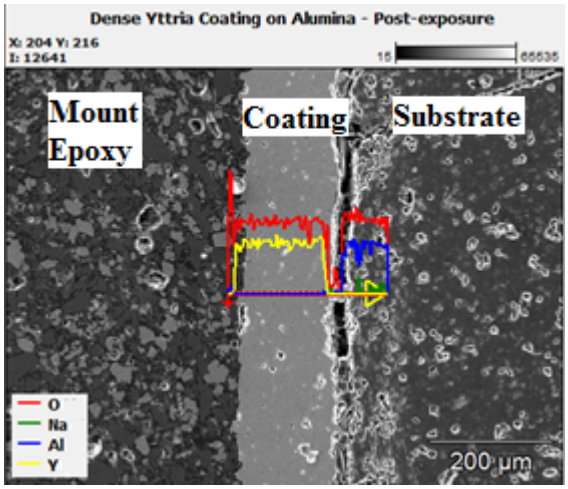

Figure 6.31: Dense yttria coating on alumina *after* exposure to 350[C] sodium for 200[hr]. No measurable sodium detected.

6.6.3 Thermal spray coatings on MACOR

Thermal spray quality on a machinable ceramic is of particular interest for oxygen sensor development since machining alumina is very difficult. Three different materials were sprayed onto MACOR substrates: 7% YSZ, 20% YSZ, and pure yttria. These coatings were each analyzed before and after exposure to 350[C] sodium for 25[hr]. These tests were of such short duration due to the extremely high oxygen concentration of the sodium, and the rapid formation of sodium zirconate. As discussed previously, exposing liquid sodium to a 2[wppm] gas for an extended period of time lead to the saturation of sodium with oxygen, and an oxide crust eventually formed over the surface.

An uncoated MACOR substrate was also tested at a high oxygen concentration to verify that the material could survive normal sensor operating temperatures. The bare substrate was submerged at 400[C] for 300[hr], and exhibited 23[g/m^2] loss and some discoloration. The thickness change of the coated samples was therefore assumed to be entirely due to the coating. Images are shown in figure 6.32 which show the coated samples before and after sodium exposure. The MACOR substrate experienced some discoloration, but had little damage. The YSZ coatings exhibited significant dissolution from the surface and edges.

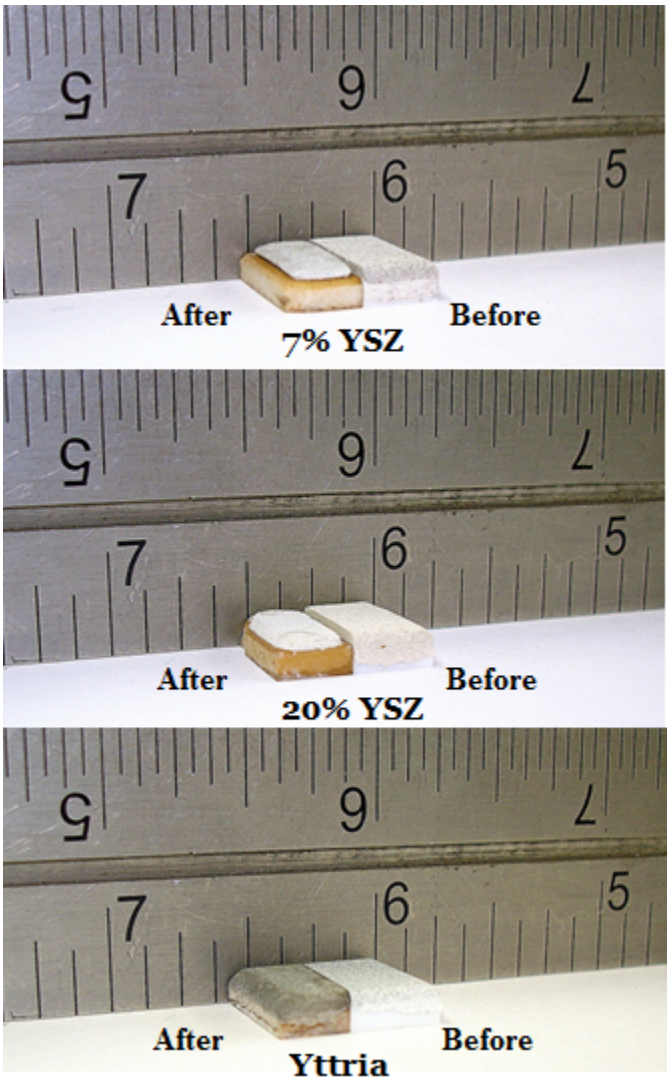

Figure 6.32: 7% YSZ, 20% YSZ, and pure yttria coated on MACOR substrates before (right) and after (left) exposure to 350[C] sodium for 25[hr]. Sodium attack appeared to be decreasing with increasing yttria concentration.

EDS line-scans of the cross-sections of these samples are shown in figures 6.33, 6.34, 6.35, and 6.36. However, the 7% YSZ sample had sufficiently separated from the MACOR substrate so it fell off when trying to cross-section the sample; no EDS data was acquired for this sample. The relative atomic percentages of each element are overlaid on each image and the legend defining the different color lines is displayed for each image. *More detailed and larger plots of these line-scans are available in Appendix D.*

Cross-sectioned images revealed that the 20% YSZ and the pure yttria coatings were still well adhered to the MACOR substrate in the middle of the sample (away from the edges). Most of the damage was due to zirconia dissolution into sodium via the process described in equation 6.3. The 20% YSZ coating saw very little sodium penetration (figure 6.36); however, the pure yttria coating experienced a substantial increase in porosity, and sodium was able to penetrate throughout the coating (the green line in figure 6.34). Yttria is thermodynamically more stable in sodium than YSZ, but due to the increased brittleness of yttria, a harder material than YSZ, it is more susceptible to thermal stresses. It is likely that the porosity developed in the yttria as a result of the differences in CTE between the MACOR and yttria. In contrast, YSZ, a less brittle material, was able to accommodate the thermal stress.

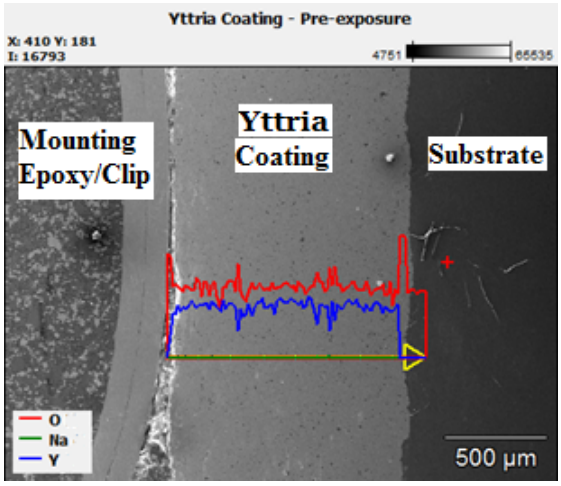

Figure 6.33: Yttria coating on MACOR *before* liquid sodium exposure. No detectable sodium in the coating.

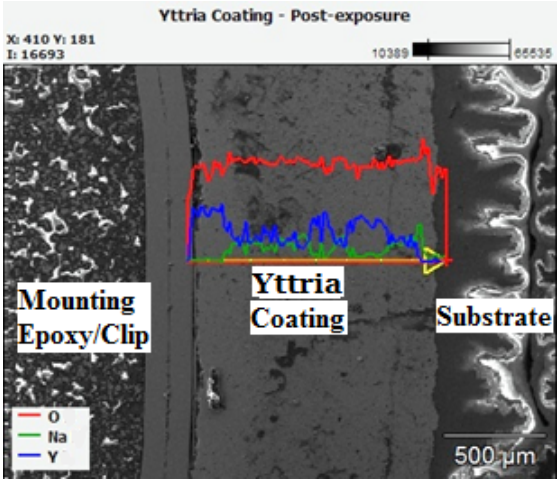

Figure 6.34: Yttria coating on MACOR *after* exposure to 350[C] sodium for 200[hr]. Sodium penetration throughout sample (green line).

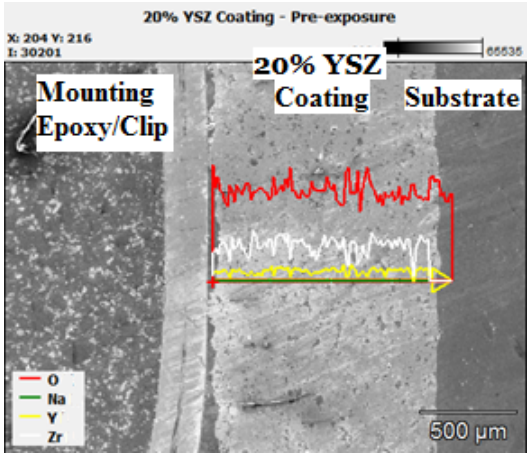

Figure 6.35: 20% YSZ coating on MACOR *before* liquid sodium exposure. No measurable sodium detected.

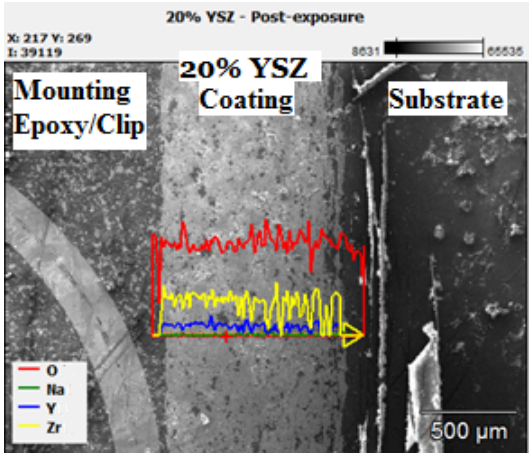

Figure 6.36: 20% YSZ coating on MACOR *after* exposure to 350[C] sodium for 200[hr]. No measurable sodium detected.

Coating thickness, although very uniform prior to sodium exposure, varied greatly after the tests. Table 6.7 summarizes the thickness results of these experiments. The standard deviation in each averaged measurement indicates how coarse the surfaces were after the tests. It may be noted that the 7% YSZ coating was the only one to experience a gain in thickness. This was not swelling of the coating, but rather the coating lifting from the surface of the MACOR substrate, as discussed previously in this section.

Table 6.7: Results of yttria and YSZ coatings on MACOR substrates in 350[C] sodium for 25[hr]

Coating:	Thickness change	Std. Dev. (σ)	% Thickness change
7% YSZ	$+192[\mu m]$	$\pm 19.1[\mu m]$	$+5.51\%$
20% YSZ	$-57.6[\mu m]$	$\pm 36.9[\mu m]$	-1.60%
Yttria	$-3.39[\mu m]$	$\pm 11.1[\mu m]$	-0.095%

These experiments have shown that increasing yttria concentration also increases resistance to sodium attack. However, increasing yttria concentration also increases the brittle-

ness of the ceramic, and thermal expansion stresses induced cracking, which allowed sodium penetration.

Because cracking was the cause of sodium penetration, coating thickness cannot be linked to sodium penetration at this time. Only when the cracking issue is resolved can longer duration tests indicate the effect of coating thickness. Sodium penetration must be stopped if the ceramic is to be used for oxygen sensor application. Finally, the attack rate for YSZ substrates is too high for sensor application in oxygen saturated sodium. Further tests need to be conducted at low oxygen concentration to determine whether or not the attack of YSZ would be reduced.

6.7 Summary of Chapter 6

This chapter has discussed a variety of ceramics and their behavior in liquid sodium. Magnesium oxide and beryllium oxide showed excellent resistance to sodium attack and MACOR performs well up to 400[C]. Since MACOR is a machinable ceramic with a coefficient of thermal expansion near that of YSZ, it could be an attractive material for many engineering purposes in liquid sodium. Sintered YSZ from Friatec survived much better in liquid sodium than McDanel YSZ, and both prevented sodium penetration into the electrolyte. Thus, either material is expected to function properly as an electrolyte for an electrochemical oxygen sensor, but likely only for a limited time.

The attack rate of thermal sprayed YSZ and yttria varied greatly depending on composition, density, and substrate material. Thermal sprays adhered best to substrates closest in CTE value. The alumina substrates saw the least separation between substrate and coating, while 416SS saw the most. High density yttria coatings experienced significantly higher cracking in sodium than more porous sprays. This is likely due to a reduced ability of the dense material to accommodate stresses caused by different thermal expansion between the substrate and coating. Increasing yttria concentration also increased the resistance to sodium

attack of thermal spray coating. The pure yttria coatings on MACOR substrates experienced little mass-loss, but EDS scans revealed significant cracking throughout the coating. This result is consistent with the aforementioned differential thermal expansion.

Similar ceramics sintered by different manufacturers were tested, both for YSZ and alumina, and these results showed significantly different resistance to sodium attack. Corrosion dependence on sintering recipe has been seen in past research[10]. Thus, for electrolyte development for liquid sodium, many different sintering recipes should be tested of a material before that material is discarded as a possible sensor electrolyte. This fact will be very important when investigating how to sinter a thermal sprayed electrolytes as discussed in Appendix B.

Notes on yttria doped thoria

YST was not tested in these experiments, however an extensive literature review was conducted to investigate past YST corrosion experiments in sodium. Numerous sources cited *no sodium attack* on sintered YST electrolytes[5, 7, 13, 14, 15, 16]. These researchers did not report mass-loss rates or provide SEM results, however they confirmed that YST was compatible with liquid sodium. However, YST ceramics were found to be susceptible to thermal shock during system start-up as a result of the low porosity and hardness of the material. Most importantly, desire to reduce dependence on radioactive actinides makes working with thoria expensive and impractical. Acquiring the material has proven to be very difficult throughout this research.

YSZ, in contrast, has been shown to experience significant sodium attack even at mild temperatures[9, 17]. The significant difference in sodium compatibility is discussed in terms of oxygen sensor technology in chapter 7.

Chapter 6 Bibliography

[1] R. N. Singh. Compatibility of ceramics with liquid na and li. Technical report, Argonne National Laboratory, Materials Science Division, April 1976.

[2] K. Natesan T.F. Kassner. Stability of mixed-oxide fuels in a sodium enviornment. Sodium technology quarterly report, Argonne National Laboratory, April, May, June 1970.

[3] M. H. Kamdar. Embrittlement by liquid metals. *Progress in Materials Science*, pages 349–65, 1973.

[4] J. T. A. Roberts W. D. Thohig and R. N. Singn. Proceedings of the 14th symposium on engineering aspects of magnetohydrodynamics. University of Tennessee Space Institute, April 1974. pp. IV.10.1-IV.10.3.

[5] J. Burda D. Jakeš, J. Král. Development of electrochemical oxygen meter for liquid sodium. Technical report, Nuclear Research Institute, 250 68 *Řež*, Chechoslovakia, July 1983.

[6] E.D. Wachsman et al. Lowering the temperature of solid oxide fuel cells. *Science*, 334(935), 2011. DOI:10.1126/science.1204090.

[7] O.J. Foust, editor. *Sodium-NaK Engineering Handbook*, volume 5. Liquid Metal Engineering Center, 1979.

[8] H. Steinmetz. Development of a continuous meter for oxyggen in sodium. Technical report, United Nuclear Corporation, White Plains, New York, January 1963.

[9] S.H. Shin et al., editor. *Development of Electrochemical Oxygen Sensor and Experimental System for Materials Compatibility Test for Ultra-long Cycle Fast Reactor*, Paris, France, March 2013. IAEA, Fast Reactor Conference - FR13. UNIST, Republic of Korea.

[10] et al. J.K. Fin. Interactions of certain refractory materials with sodium. Technical report, Argonne National Laboratory, 1976. Contract W-31-109-Eng-38.

[11] Roland Zils. Email correspondence, May 2013.

[12] D. Dumas J.C. Poignet N Adhoum, J. Bouteillon. Electrochemical isertion of sodium into graphite in molten sodium flouride at 1025[c]. *Electrochim. Acta.*, 2006. 5402-5406.

[13] R.G. Taylor and R. Thompson. Testing and performance of electrolytic oxygen meters for use in liquid sodium. *Journal of Nuclear Materials*, 1983.

[14] R.C. Asher et al. The harwell oxygen meters and harwell carbon meter. Technical report, British Nuclear Engergy Society, 1984.

[15] M.R. Hobdell and C.A. Smith. Electrochemical techniquies for monitoring dissolved carbon, hydrogen, and oxygen in liquid sodium. *Journal of Nuclear Materials*, (110):125–139, 1982. Berkeley Nuclear Laboratories, United Kingdom.

[16] R. Ganesan et al. Development of sensors for on-line monitoring of nonmetallic impurities in liquid sodium. *Journal of Nuclear Science and Technology*, 48(4):483–489, 2011. Indira Gandhi Centre for Atomic Research, India.

[17] J. Courouau et al., editor. *Corrosion by oxidation and carburization in liquid sodium at 550[C] of austenitic steels for sodium fast reactors*, Paris, France, March 2013. IAEA, Fast Reactor Conference - FR13. CEA Saclay, France.

Chapter 7

Electrochemical Oxygen Sensor - Results & Analysis

In this chapter the design and construction of a functioning yttria stabilized zirconia (YSZ) sensor are presented, along with performance analysis. Deviations between experimental data and theory were observed and it was determined that exactly quantifying these differences was unrealistic. Therefore a hypothesis testing approach was taken.

A series of hypotheses were tested in order to better understand oxygen sensor performance. These hypotheses were formed using both the results from these experiments as well as past results (discussed in Chapter 3). These hypotheses were constructed to be testable and to contribute evidence to otherwise qualitative arguments for the observed discrepancies between experiment and theory.

Chapter 7 Contents

Contents

7.1 Variables Used in this Chapter

Variable	Physical Meaning
$E_x = E_{\text{ex}}$	Experimental cell signal [V]
c	Dissolved oxygen concentration [ppm]
χ^2	Chi-squared value [-]
$E_{\text{theory}} = E_{\text{th}}$	Theoretical cell signal [V]
ΔE	Uncertainty in signal [V]
χ^2_{red}	Reduced chi-squared value [-]
ν	Number of degrees of freedom [-]
N	Number of measurements [-]
n	Number of fit parameters [-]
T	Temperature [K]
T_p	Plugging temperature [K]
F	Faraday constant $\left[\frac{C}{mol}\right]$
R	Gas constant $\left[\frac{J}{molK}\right]$
c_o	Dissolved oxygen concentration at saturation [ppm]
ΔG	Gibbs energy of formation [J/mol]
μ	Oxygen potential [J]
t_{ion}	Coefficient of ionic conductivity [-]
E^o_T	Standard electrode potential [V]
σ_{ion}	Electric conductivity from ions [S/m]
σ_{electron}	Electric conductivity from ions [S/m]

7.2 Oxygen Sensor Design

Commercially available yttria stabilized zirconia (YSZ) crucibles were chosen for the electrolyte of the sensor. The YSZ was manufactured by McDanel Advanced Ceramic Technologies, and was stabilized with 10.5 wt.% yttria, which should have an excellent oxygen diffusion coefficient (detailed theory on ionic conductivity is given in Appendix A).

The crucible was twelve inches long and 0.375 inches outer diameter, with an inside diameter of 0.25inches (0.625 inch thick walls). The electrolyte was secured into an eleven-inch 316SS tube using a zirconia based paste. The sensor was made this length to create a freeze seal before sodium could overflow into the reference electrode chamber. A first attempt with the zirconia paste was done with a six-inch crucible, and the hot sodium penetrated through the paste, and caused a leak. This likely occurred because the coefficients of thermal expansion (CTE) are so different between the 316 stainless steel sleeve, and the zirconia components (the CTE of 316SS is 2.5 times greater than that of zirconia). Thus, a longer sensor was made, and the thermal expansion at the cold end of the sensor was minimized. This design change fixed the leak problem. Figure 7.1 shows the sensor components described above.

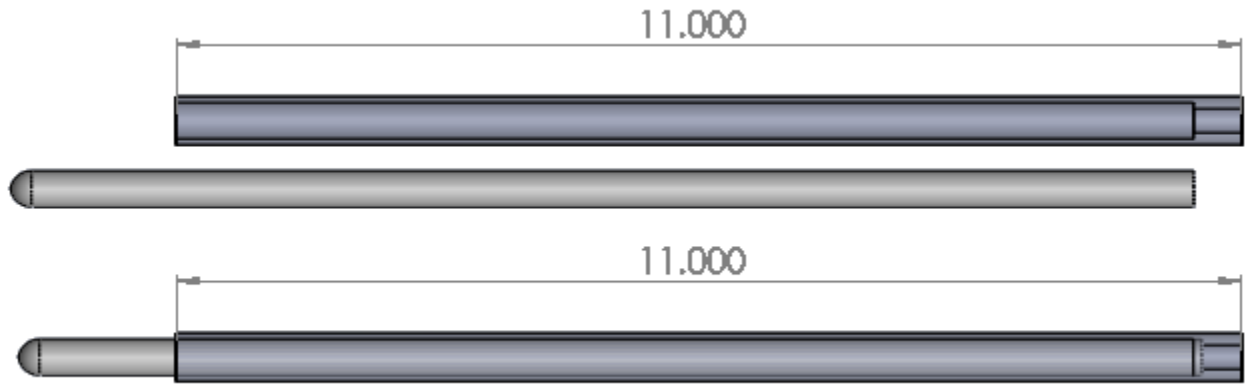

Figure 7.1: This figure shows the two main components of the prototype galvanic cell oxygen sensor which produced the data discussed in this chapter (units in inches).

Two different reference systems were tested, one was air interacting with copper as a catalyst, and the other was a metal-metal oxide. A -325 mesh ($44[\mu m]$) copper powder was used for both reference electrodes. The reference chamber was held at a constant oxygen concentration by either sealing the chamber with enough copper to fully equlibrate the gas in the chamber (a metal-metal oxide reference system), or by ensuring constant oxygen supply to the electrode. Past experiments have shown that copper gives more reproducible results than other reference electrode metals[1, 2]. The reference chamber was then sealed using a Swagelok^{TM}, rubber stopper, and silicone to ensure there would be no leakage of the cover gas (nitrogen). Figure 7.2 shows the actual sensor (prototype 2, P2) as assembled, before insertion into the sodium loop. Details on the operation theory for this reference system are discussed in Chapter 3.

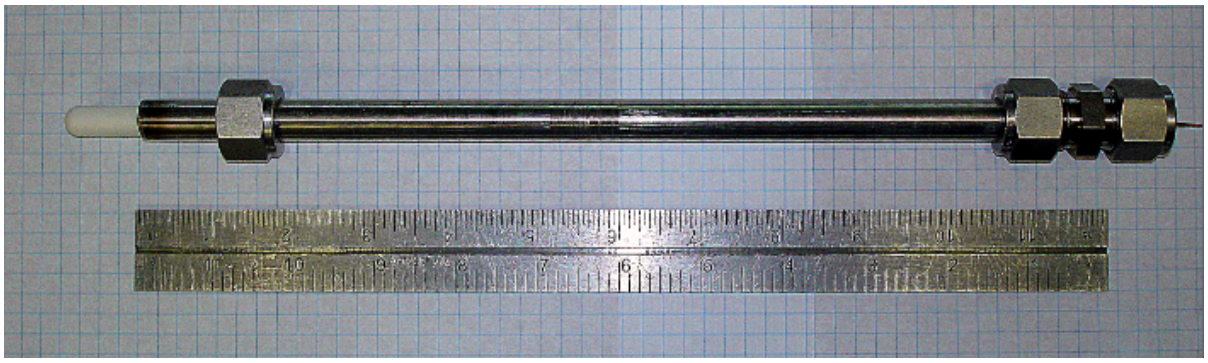

Figure 7.2: Prototype oxygen sensor 2 (P2) is shown. The YSZ crucible is epoxied in an eleven-inch stainless steel tube and a copper powder reference electrode is sealed within the probe tip.

7.3 Acquired Data & Fit to Theory

All oxygen measurements were taken with a plugging meter (as discussed in Chapter 5), and the cold trap was used to vary and control the oxygen concentration. The sensor voltage was averaged over the thirty seconds surrounding the plugging event, and the standard deviation of these measurements was calculated and used as the error in the voltage measurement. The relative magnitude of the error-bars in this data indicate how steady the sensor signal was.

The cold trap temperature was adjusted in order to control the oxygen concentration (as discussed in Chapter 5). The oxygen concentration was determined using the plugging meter rather than the cold trap so the user was not forced to wait for the system to reach equilibrium at each cold trap temperature. An example data set is shown in figure 7.3, for sensor P4, which used an air-reference electrode.

The raw data taken with sensor P4 is listed in figure 7.3. The expected sensor output, as calculated previously in this report, is also shown in figure 7.3. A least squares fit was conducted to the following functional form:

$$E_x(c) = A - B\ln(c) \tag{7.1}$$

$E_x(c)$ is the fit function, and the fit parameters A and B were determined individually for each sensor tested. The best fit curve was then plotted with the sensor raw data to visually inspect the quality of the fit. This fit is also shown in figure 7.3, and the equation for the best fit curve is shown in equation 7.2.

$$E_{P4}(c) = 1.496 - 0.0673\ln(c) \tag{7.2}$$

A chi-squared test was then conducted on the data set in order to quantitatively determine the quality of fit. The chi squared value of the fit was determined using equation 7.3.

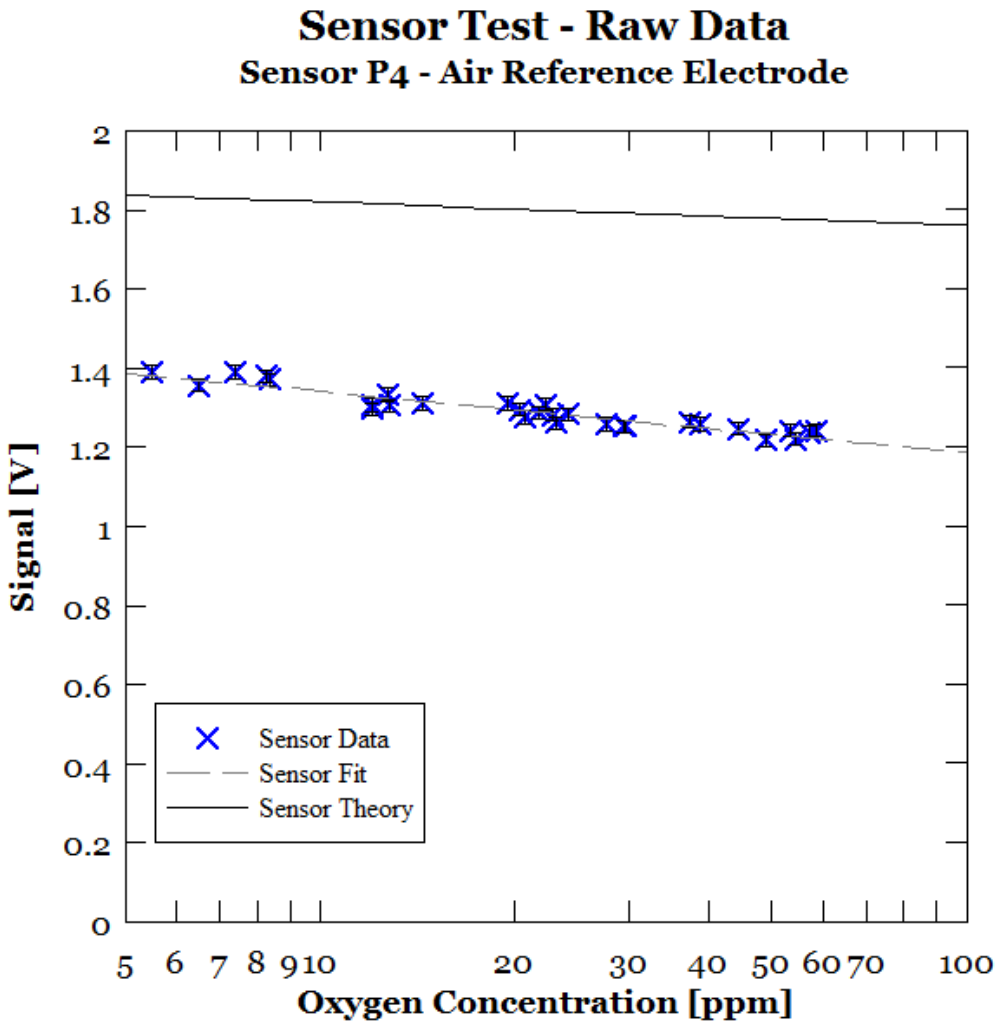

Figure 7.3: Data acquired with P4 is shown along with the resulting least-squares fit.

$$\chi^2 = \sum_{i=1}^{N} \frac{\left(E_x^i - E_{theory}^i\right)^2}{\Delta E^2} \tag{7.3}$$

In equation 7.3, N is the number of data points being fitted, E_x^i and E_{theory}^i are the experimental and theoretical voltages corresponding to each of the i measured oxygen concentrations, and ΔE is the estimated uncertainty in the voltage measurement. The chi-squared value by itself is arbitrary because it depends so heavily on the number of data points taken. However, the reduced chi-squared, χ^2_{red} can be calculated by dividing the chi-squared value by ν, the number of degrees of freedom.

$$\chi^2_{red} = \frac{\chi^2}{\nu} = \frac{1}{\nu}\sum_{i=1}^{N}\frac{\left(E^i_x - E^i_{theory}\right)^2}{\Delta E^2} \tag{7.4}$$

The number of degrees of freedom is the total number of data points minus the number of fit parameters, n. For fitting to the functional form in equation 7.1, $n = 2$.

$$\nu = N - n \tag{7.5}$$

The chi-squared value is a measure of the quality of fit where small values of χ^2 indicate a higher quality fit. However, it is clear that an overestimate of uncertainty in signal, ΔE, would similarly result in a small χ^2. By normalizing with the number of degrees of freedom, the χ^2_{red} is a good indicator of both the quality of fit and the error approximation. If $\chi^2_{red} \approx 1$, then the error in signal is optimally chosen for the least-squares fit through the acquired data. Once the reduced chi-squared value drops below one, then the fit is suspected of being *too good*, and the uncertainty is likely over-estimated. However, if the uncertainty has to be substantially larger than the experimenter would expect in order to drive the χ^2_{red} down to one, then the difference between experiment data and theory is too high, and the fit is not good. In this case, the source of experimental error needs to be investigated, or the mathematical form of the fit equation needs to be re-evaluated.

Continuing the example of sensor P4, if the uncertainty in signal strength is $\Delta E = \pm 16$[mV], then the chi-squared value for the least-squares fit of this data is $\chi^2(\text{P4}) = 29.7$. The reduced chi-squared is $\chi^2_{red} = 1.09$, indicating a quality fit if the uncertainty in signal seems reasonable. For the data shown in figure 7.3, a 14[mV] spread seems reasonable.

In order to calculate the error in each fit parameter, A and B, one must investigate the value of the chi-squared as a function of each fit parameter independently. Since A and B are fit-parameters and not physical measurements, the errors have to be determined using statistics. To begin, take a 'slice' of the chi-squared function in the slope-dimension (B). The resulting plot, shown in figure 7.4, shows a minimum at $B = 0.067$, which was the value

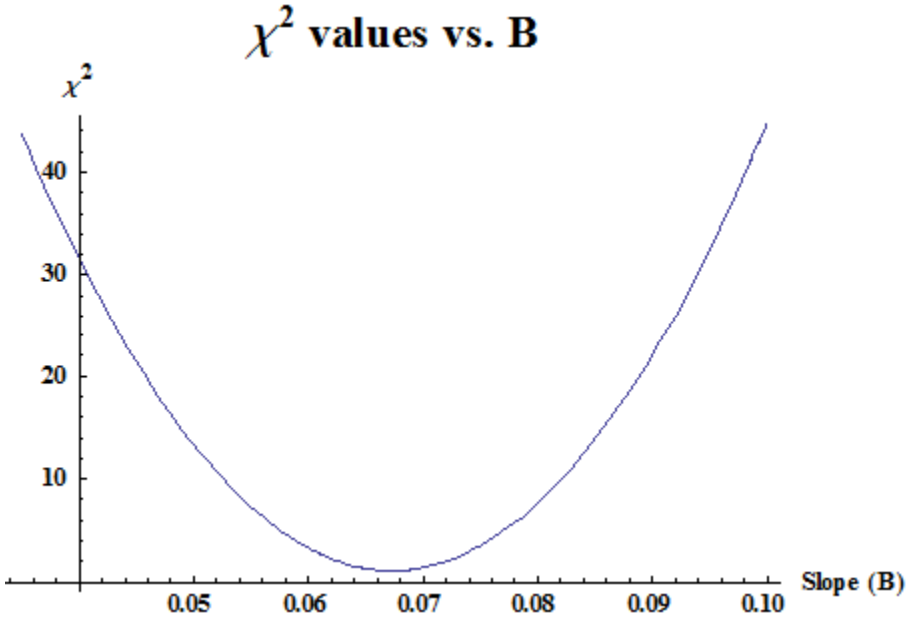

Figure 7.4: A slice of the chi-squared function in the direction of a fit parameter can be used to determine the spread (or error) in that fit parameter.

determined from the least-squares fit for this data.

One must then find the values of B which result in the chi-squared being increased by an amount corresponding to a one-sigma error (as determined from a chi-squared table). For two degrees of freedom, for a fit-parameter error of one sigma, that value is 2.3. *The range in values of B which result in an increase in chi-squared of* 2.3 *or less is the range of uncertainty for B.* In this example, $\chi^2 = 29.67$, and $\chi^2 + 2.30 = 31.97$, this range of χ^2 values allows the slope, B, to be in the range:

$$0.0404 \leq B \leq 0.0942 \tag{7.6}$$

Thus, the uncertainty in B is $\Delta B = \pm 0.0269$. The same analysis can be conducted on the y-intercept value A. For this analysis, the slope is kept constant, and a slice of the chi-squared curve is taken for different values of A. The result of this calculation is $\Delta A = 0.0663$.

Equation 7.2 can now be re-written including the associated uncertainties for a more

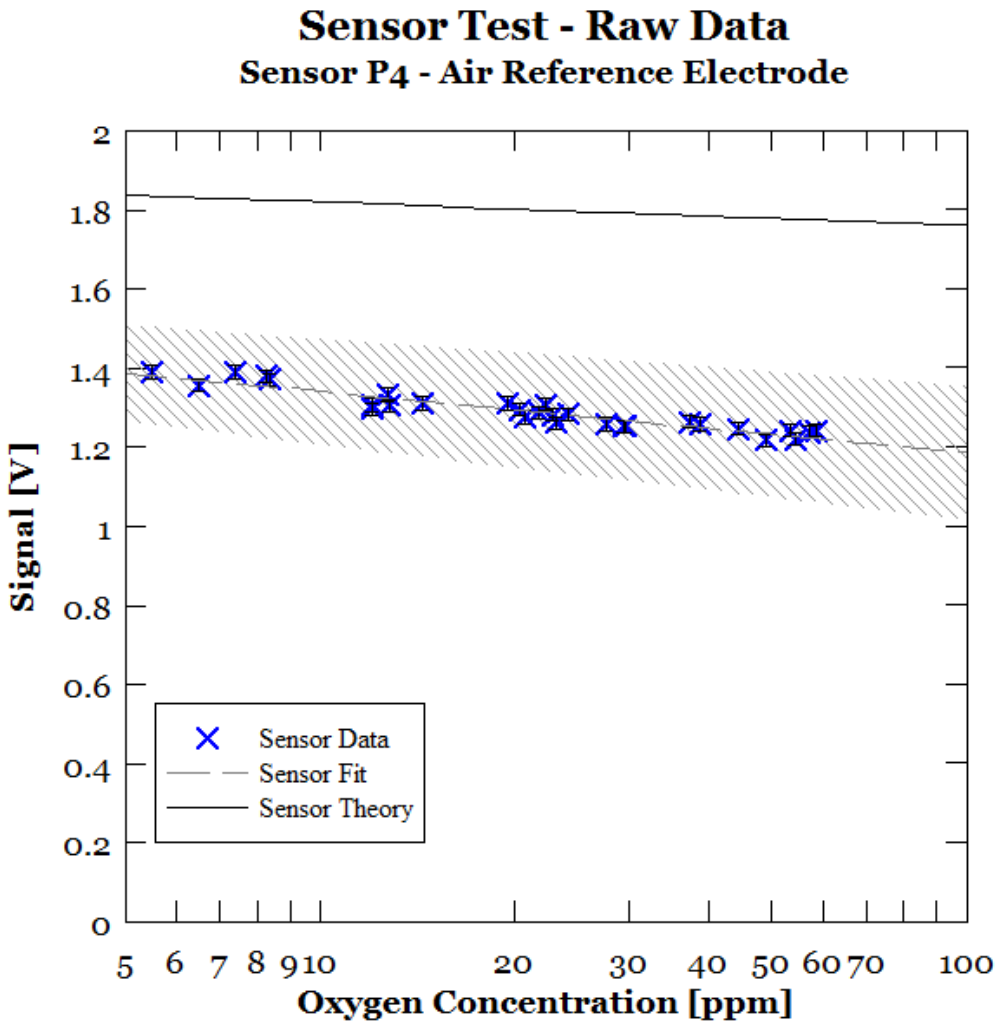

Figure 7.5: Results of the error analysis for sensor P4 shown with the raw data. Notice that all of the data points are easily within error.

complete representation of the acquired data:

$$E_{P4} = (1.496 \pm 0.0668) - (0.0673 \pm 0.0269)\ln(c) \tag{7.7}$$

This equation is shown graphically in figure 7.5. The dashed line is the result of the least-squares fit, and the shaded region represents the error in the fit.

This same analysis was conducted on multiple sensors, with both air and copper-copper oxide reference systems. The result of these tests are shown in figure 7.6. The fit of each

respective sensor curve is shown in figure 7.7, and the data for these fits are shown in table 7.1.

Table 7.1: The results of linear least-squares fits on YSZ oxygen sensors for copper and air reference electrodes.

Sensor	A	ΔA	B	ΔB
P2	0.979	± 0.101	-0.0470	± 0.0154
P3	1.172	± 0.0916	-0.0816	± 0.0126
P4	1.496	0.0358	-0.0673	± 0.0267
P5	1.618	0.0987	-0.117	± 0.0159
P6	1.819	0.179	-0.194	± 0.0298
P7	1.629	0.129	-0.122	± 0.0195

The oxygen sensors tested in this research followed the appropriate functional form of signal vs. oxygen concentration. However, as previously stated, it is clear that the sensor-to-sensor slope is inconsistent, and that the overall voltage is consistently low. Previous experiments with sensors using yttria stabilized thoria (YST) electrolytes have exhibited similar behavior, with voltage consistently under theory, and variability in sensor slope[1, 2, 3, 4, 5, 6]. Details on the conclusions drawn by these past experiments are described in Chapter 3.

Initial inspection suggests that oxygen sensors produced with YSZ electrolytes are generating appropriate signal-trends as a function of oxygen concentration. However, the aforementioned deviations from theory need to be explained. Since questions about the cause of oxygen sensor errors has been unanswered for decades, a series of testable hypotheses were constructed. These hypotheses were created such that answering them would contribute significant knowledge to the body of electrochemical oxygen sensor research. These hypotheses are proposed in section 7.3.1, and the testing and analysis of each hypothesis is described in

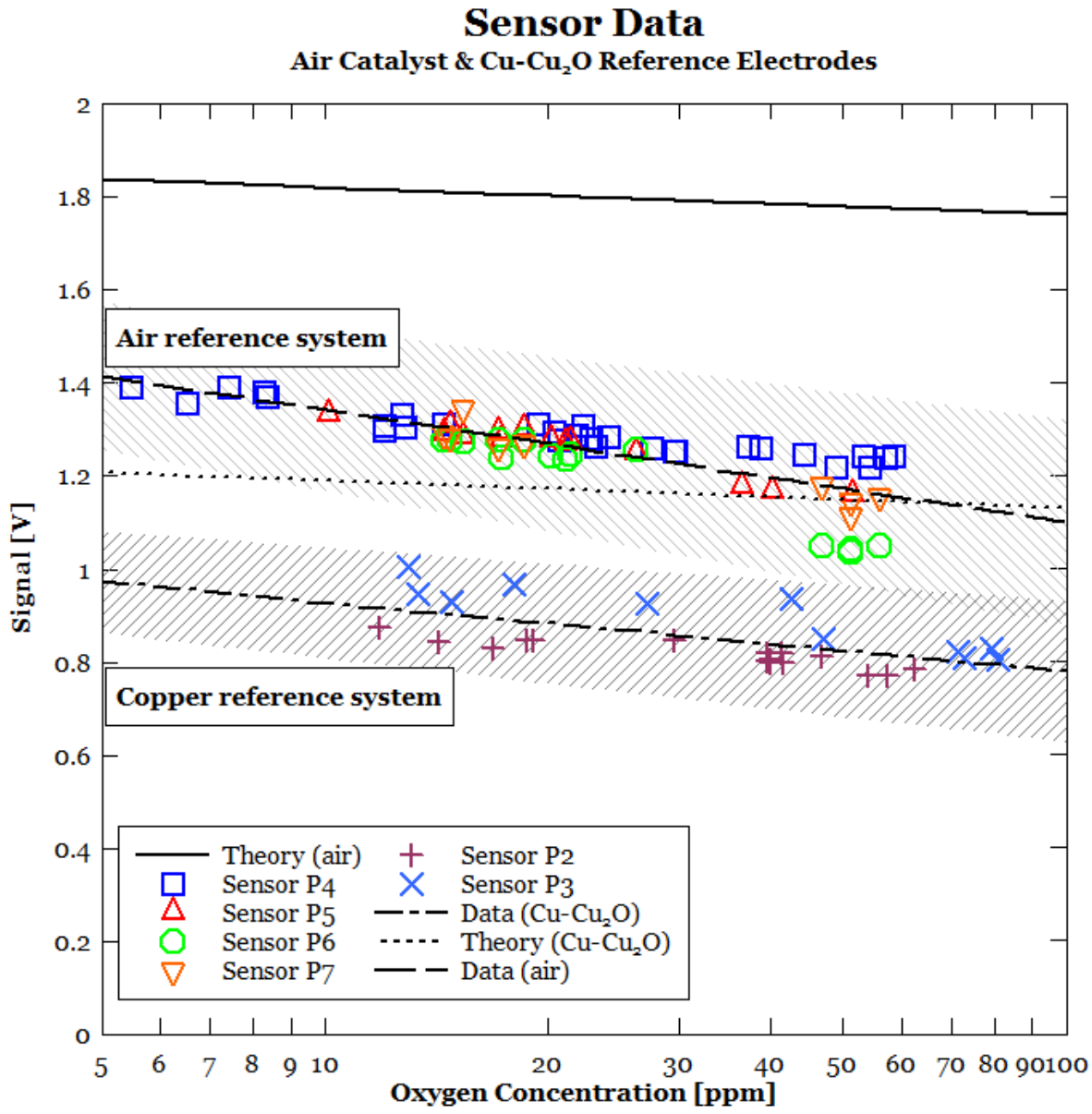

Figure 7.6: The data for various oxygen sensors shows a consistent trend which agrees with theory, but is significantly offset. Also, the sensor-to-sensor variation is substantial for both copper and air reference systems.

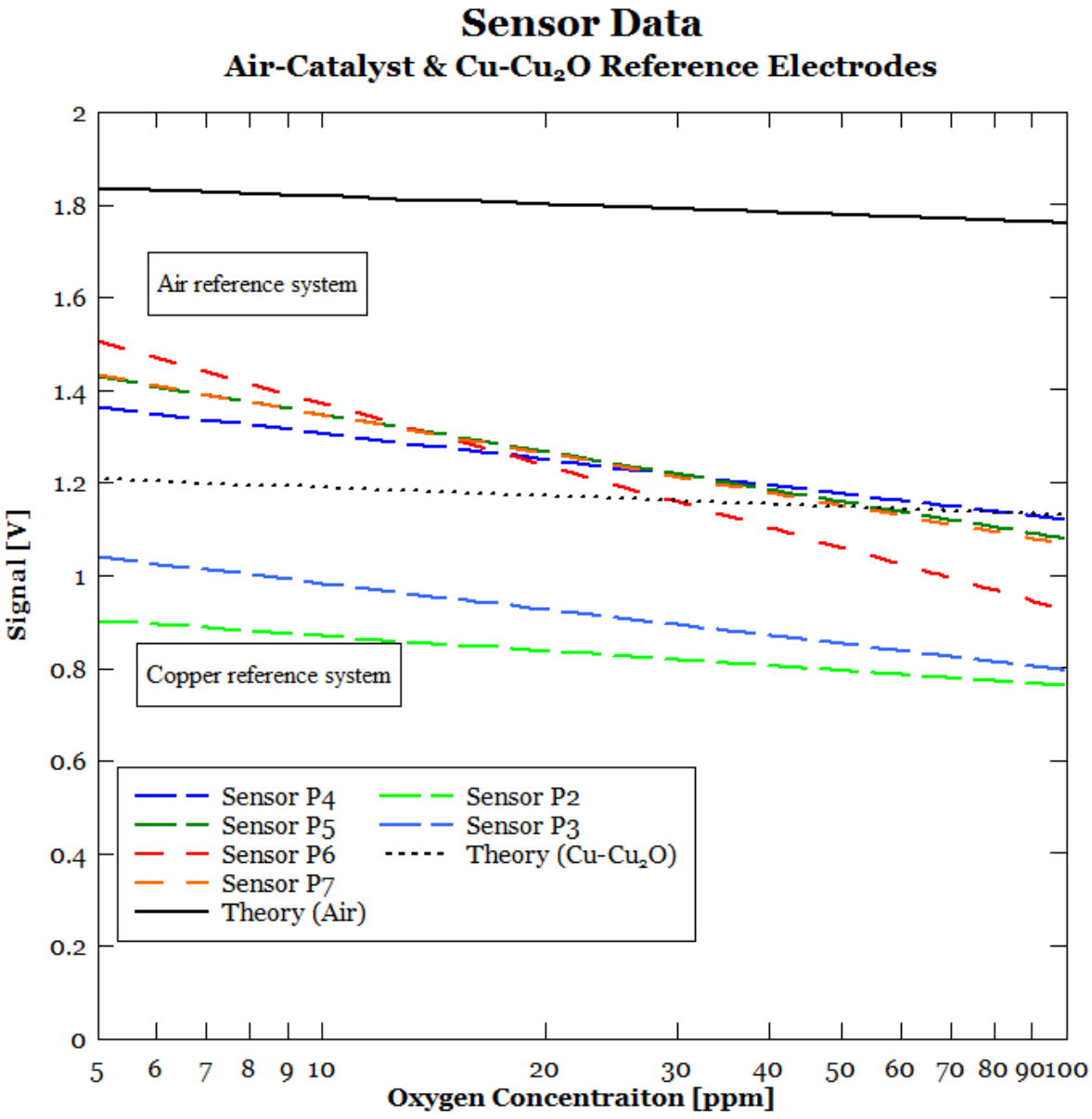

Figure 7.7: The individual data points are removed from this figure, and only the fits for each sensor are shown for clarity. The variability in slopes is clearly evident. Also, the signal is consistently below expectation.

historical research context in the following sections.

7.3.1 Proposed Hypotheses

The hypotheses outlined below were constructed in order to provide significant insight into observed discrepancies between oxygen sensor data and common theory. These are three unique tests, however, there is some overlap in the theory and proposed phenomena for each hypothesis. Thus, each hypothesis is discussed within its own section to minimize confusion. The goal of each hypothesis section is to explicitly discuss the cause and effect of a proposed mechanism, and investigate the likelihood that this effect is the primary contributor to signal error.

Hypothesis 1

Hypothesis 1 is that inaccuracies in solubility curves provide the primary contribution for the observed signal discrepancy. Errors in solubility data would cause both the error in slope as well as the low overall voltage.

Hypothesis 2

Hypothesis 2 is that sodium oxygen sensors are operated at a low temperatures which force non-equilibrium oxygen ion transport. Sensors operating out of equilibrium will not be governed by the common electrochemical theory developed in chapter 3. The low operating temperature is required to avoid the significant sodium attack that occurs at higher temperatures (as discussed in chapter 6).

The effect of corrosion on sensor signal will be discussed, but corrosion is not the focus of this hypothesis.

Hypothesis 3

Hypothesis 3 is that the YSZ electrolyte has a non-ideal coefficient of ionic conductivity in the temperature and partial pressure conditions seen in liquid sodium, and that this low coefficient of ionic conductivity is the cause of the low observed voltage.

7.4 Hypothesis 1

Hypothesis 1 is that inaccuracies in oxygen solubility curves, like the widely used Noden Correlation, are the primary cause for the error in sensor signal. This concept has been investigated in the past by Smith[2], and has been suspected in closing arguments by others[3].

It is shown in section 7.4.1 that changes in the solubility curve not only affect the theoretical magnitude of the signal, but also the slope. Acquired data will be fit to a new, hybrid solubility curve and that curve will be compared with a compilation of solubility data.

7.4.1 Background & Theory

As discussed in Chapter 3, oxygen solubility in sodium has been studied for decades, and a vast amount of data over a wide range of temperature has been acquired. See figure 7.8.

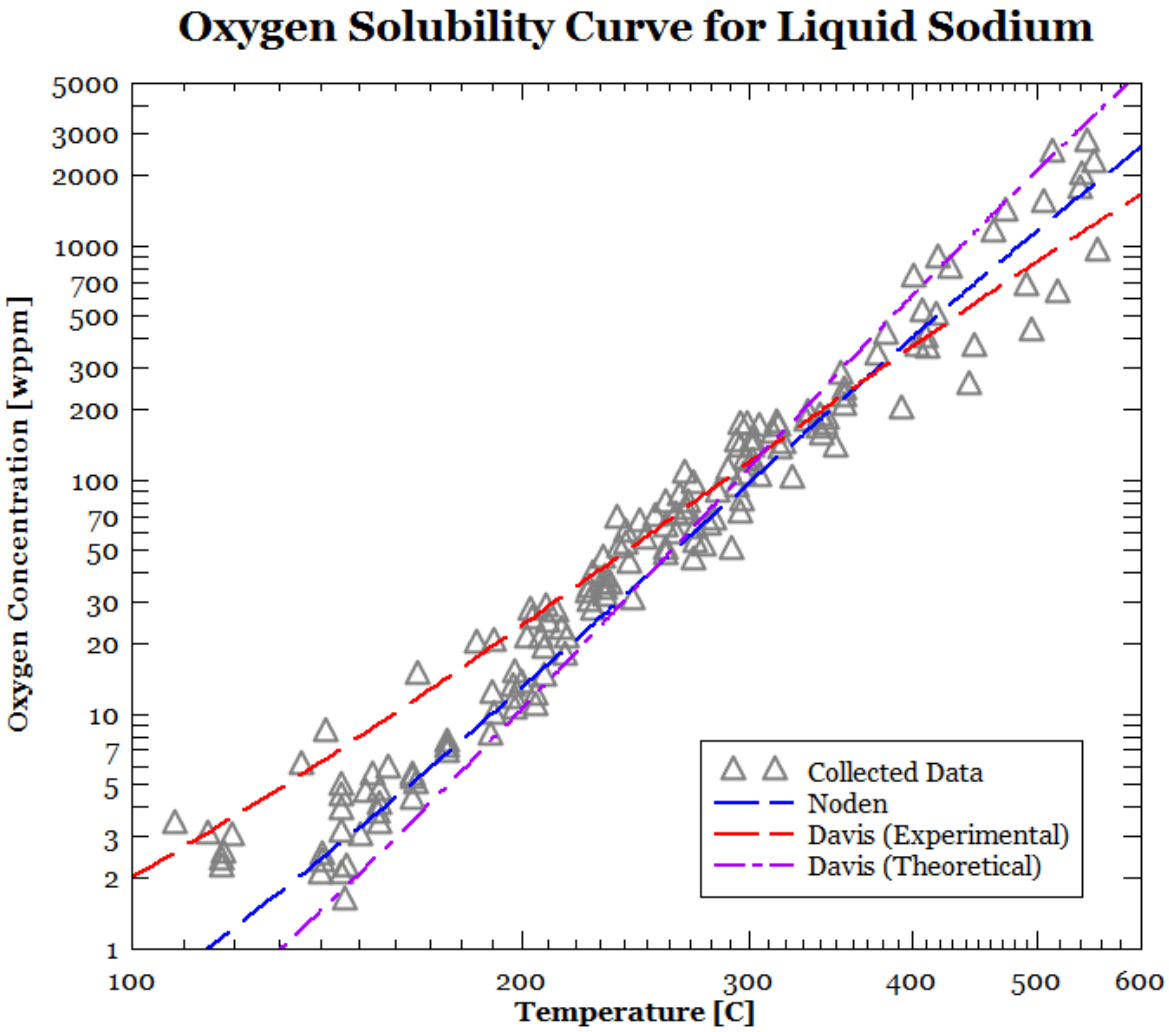

Figure 7.8: Oxygen solubility data assembled from many different experiments. Two common solubility curves are shown through the data, by Noden[7] and Smith[2]. Data from [8, 9, 10, 11, 12, 13, 14, 15, 16]

Solubility curve's effect on sensor signal

As derived in Chapter 3, the oxygen sensor output follows a Nernstian equation:

$$E(T,c) = E_o(T) - \frac{RT}{2F}\ln\left(\frac{c(T_p)}{c_o(T)}\right) \tag{7.8}$$

The sensor voltage, is listed in equation 7.8 as a function of operating temperature, T, and dissolved oxygen concentration, c. R is the universal gas constant, F is Faraday's constant, and $c_o(T)$ is the oxygen concentration at saturation temperature, T. The dissolved oxygen concentration is listed as a function of plugging temperature, T_p, since the plugging meter was used to determine the oxygen concentrations for these sensor measurements. $E_o(T)$ is the standard electrode potential, as defined in Chapter 3. Note that changing the solubility curve not only effects the $c_o(T)$ term, but also the $c(T_p)$ term since the oxygen concentration was calculated from temperature measurements. The solubility curve obeys the following functional form:

$$c(T) = \exp\left(A - \frac{B}{T}\right) \tag{7.9}$$

Substituting this function in for the respective concentrations in equation 7.8 results in a relationship for voltage in terms of operating temperature and plugging temperature.

$$E(T,c) = E_o(T) - \frac{RT}{2F}\left[\ln\left(\exp\left(A - \frac{B}{T_p}\right)\right) - \ln\left(\exp\left(A - \frac{B}{T}\right)\right)\right] \tag{7.10}$$

Sensor voltage can then be written in general, for any solubility curve. The following equation shows that the solubility curve depends on the fit coefficient, B, from equation 7.9.

$$E(T,c) = E_o(T) - \frac{RB}{2F}\left(\frac{T_p - T}{T_p}\right) \tag{7.11}$$

Studying the expected voltage for various values of B shows how a different solubility curve can affect not only the offset of the sensor voltage, but also the slope (see figure 7.9).

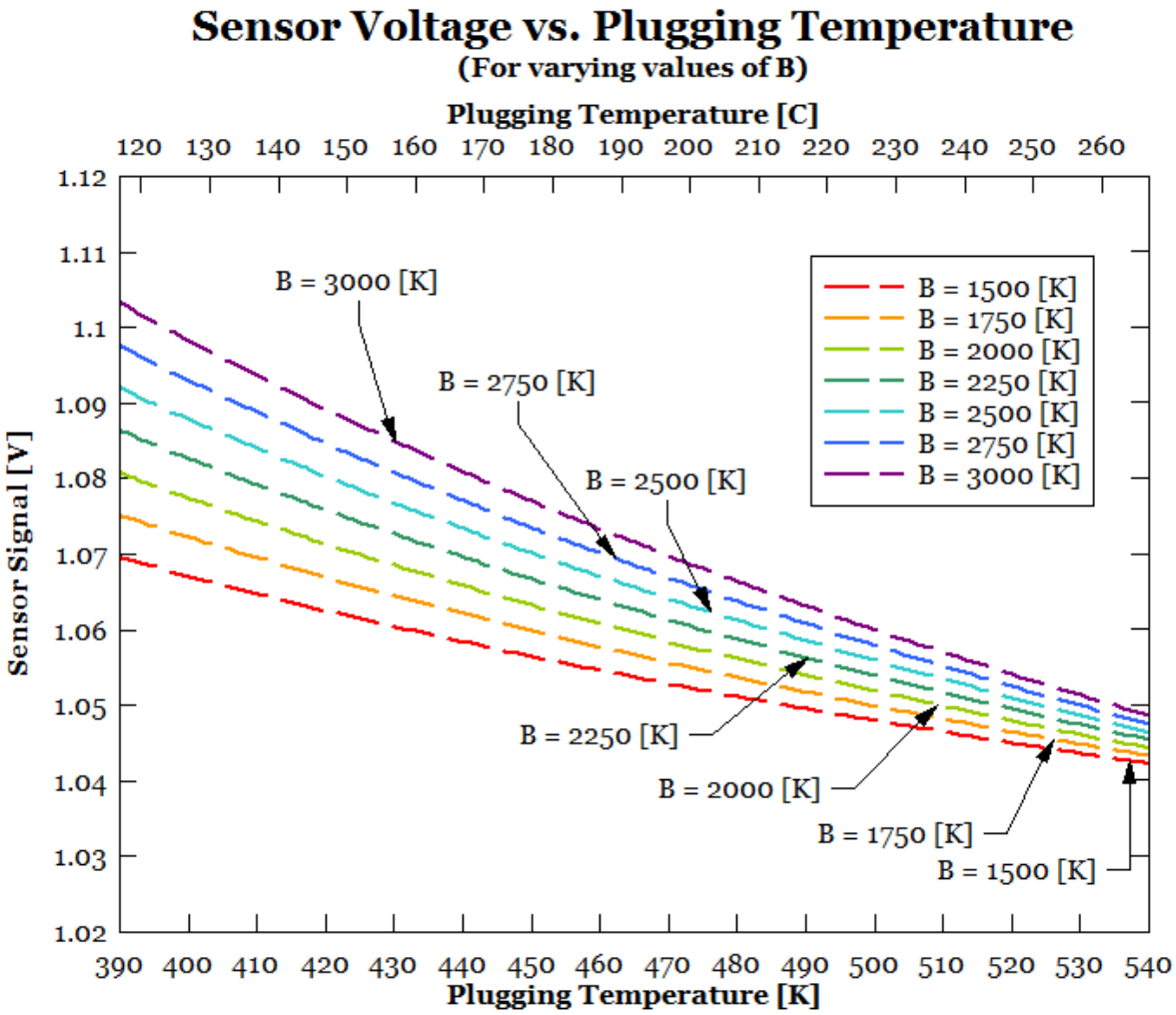

Figure 7.9: This figure shows the effect of different solubility curves on expected sensor signal.

Investigation of solubility curve modification for past YST data

Smith conducted his initial research using a solubility curve determined from combined data of Noden[10] and Rutkauskas[15]. This curve is shown in purple in figure7.8 and is listed as equation 7.12:

$$\log(c_o) = 6.967 - \frac{2809}{T} \tag{7.12}$$

Smith's sensors used YST electrolytes and liquid sodium as a reference electrode (the

benefits and problems with a sodium reference system are discussed in Chapter 3). These sensors exhibited the same problems as the YSZ sensors developed in this research, the acquired slope was off from theory, and the overall voltage was lower than expected in the measured range. This data is shown in figure 7.10.

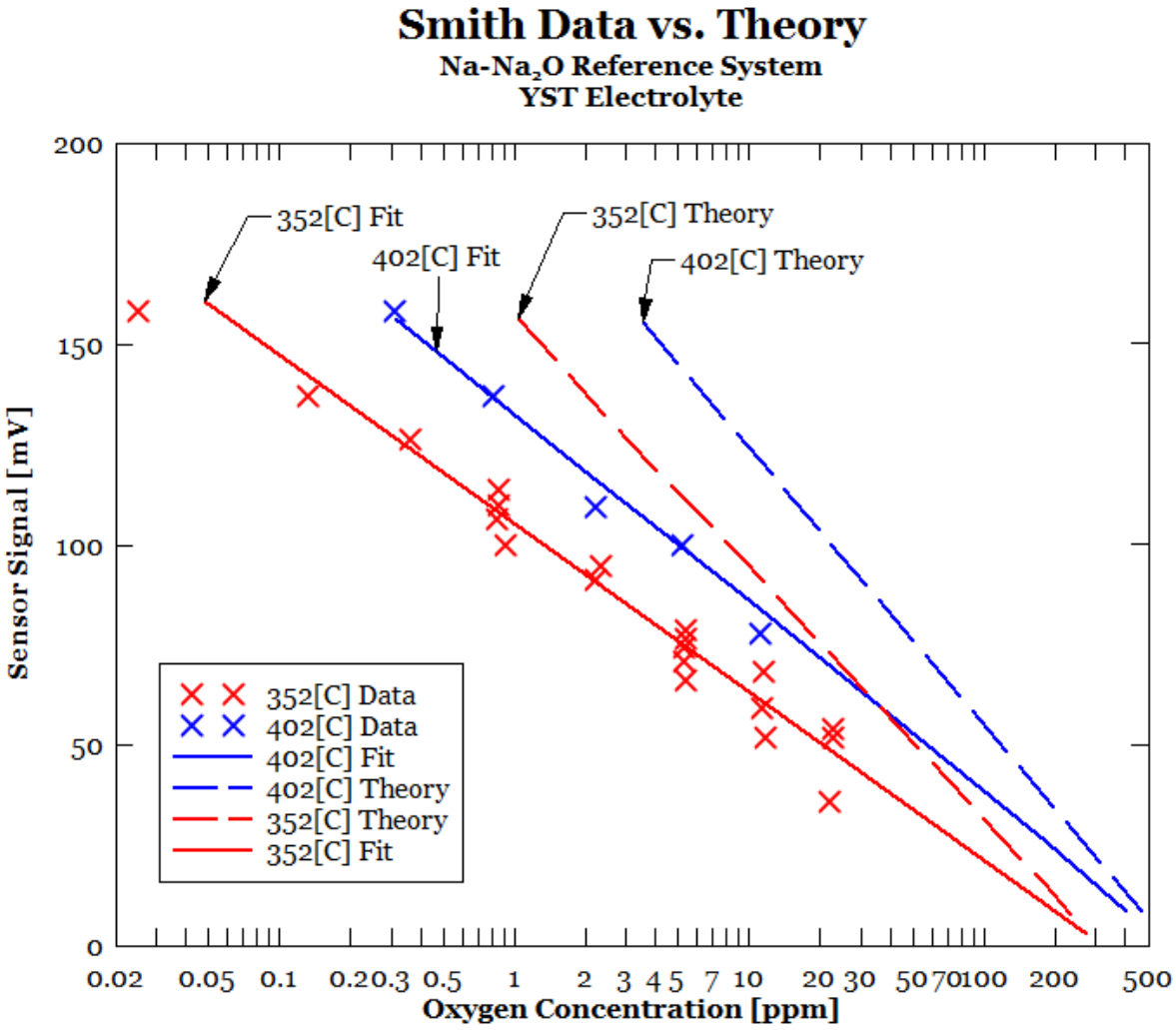

Figure 7.10: Smith's data consistently exhibited an error in slope between theory and experiment[2].

If Smith's acquired data is accurate and error is assumed to be entirely a result of an inaccurate solubility curve, then a new solubility curve can be determined from his sensor data. This operation was completed and the following experimental solubility curve was found:

$$\log(c_o) = 5.40 - \frac{1900}{T} \tag{7.13}$$

This curve is shown in figure 7.8 in red. Upon inspection of the experimental fit, it seems possible that solubility errors could produce the errors in these oxygen sensors.

Indeed, many past experiments produced curves that were close enough to theory so that errors in solubility curves could feasibly be the cause. However, These experiments were all conducted with thoria based electrolytes. Given that the data acquired at UW-Madison with zirconia-based electrolytes exhibited similar but more exaggerated results, this process must be re-investigated.

If it can be shown that the error in zirconia-based sensors cannot be explained by errors in solubility curves, then it is likely that other, more dominant sources of error exist as a result of using YSZ in place of YST.

7.4.2 Testing

The output from the YSZ sensors was assumed to be perfectly accurate for this test. If the data is accurate, and the only source of error is an inaccurate solubility curve, then an *experimentally perfect* solubility curve can be determined. This process was conducted to determine that the perfect solubility curve for sensor P4 is:

$$\log(c) = \left(10.97 - \frac{6277}{T}\right) \tag{7.14}$$

It should be again noted that in equation 7.11 the fit parameter, A, cancels out of the end voltage equation. Thus, when conducting a fit to that functional form, one cannot determine a value for A. So the optimum value for B was found, and that value was plugged into the functional form for the solubility curve (equation 7.9), and that equation was fit to the accumulated solubility data in order to find A. If this process was done correctly, then re-plotting equation 7.10 with the new fit parameters should produce a theoretical output

curve that goes perfectly through the sensor P4-data (see figure 7.11).

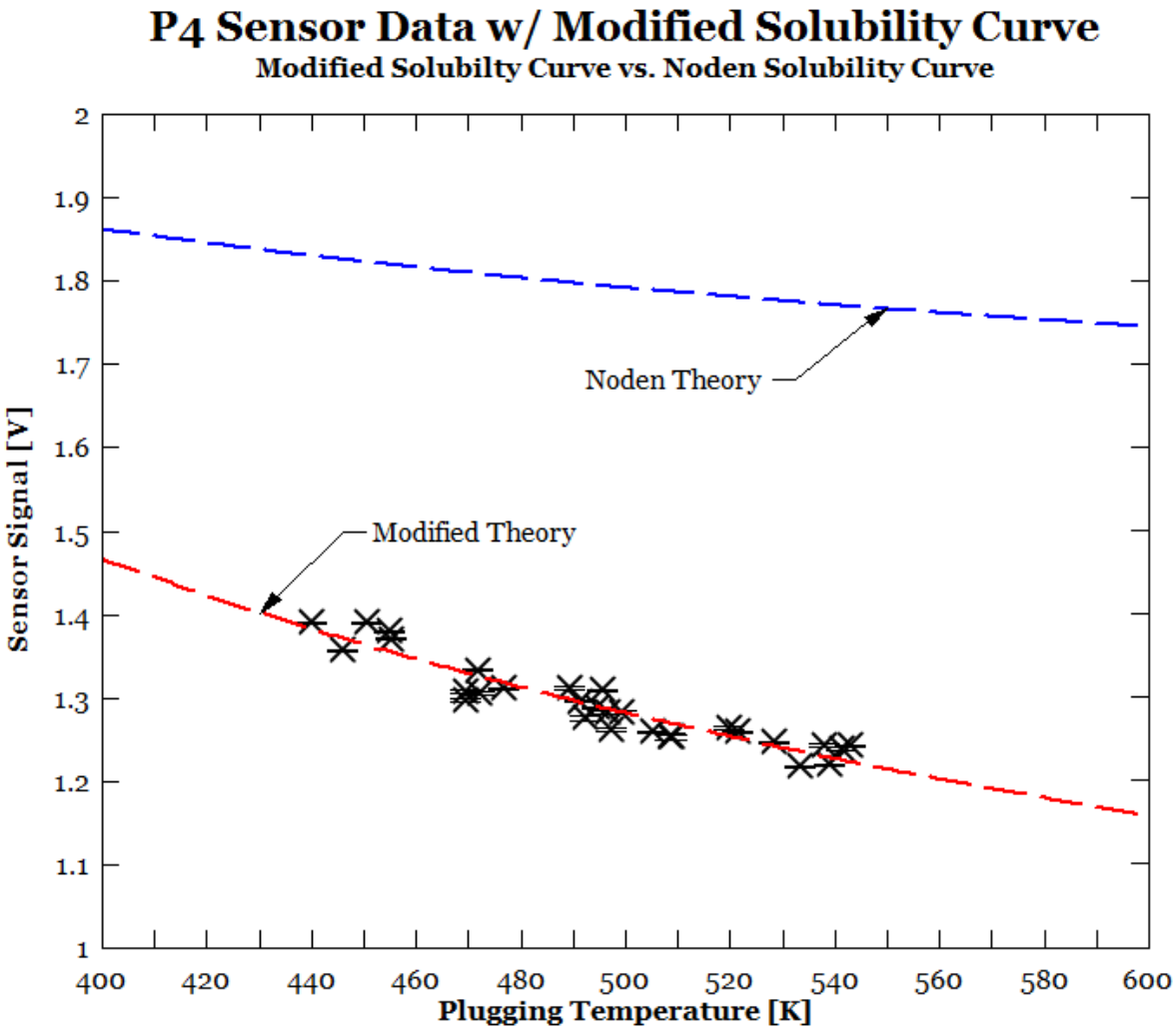

Figure 7.11: Modifiying the solubility curve generates a theoretical prediction which nicely agrees with theory. If the solubility curve which lead to this prediction appears to agree nicely with solubility data then errors in solubility data are likely a substantial contributor to sensor error.

The fact that the modified solubility curve accurately represents the acquired data shows that the mathematical process was conducted correctly. However, this is only a feasible possibility if the modified solubility curve overlays nicely on past data. The modified solubility curve written in equation 7.14 is plotted with the Noden and Smith curves in figure 7.12.

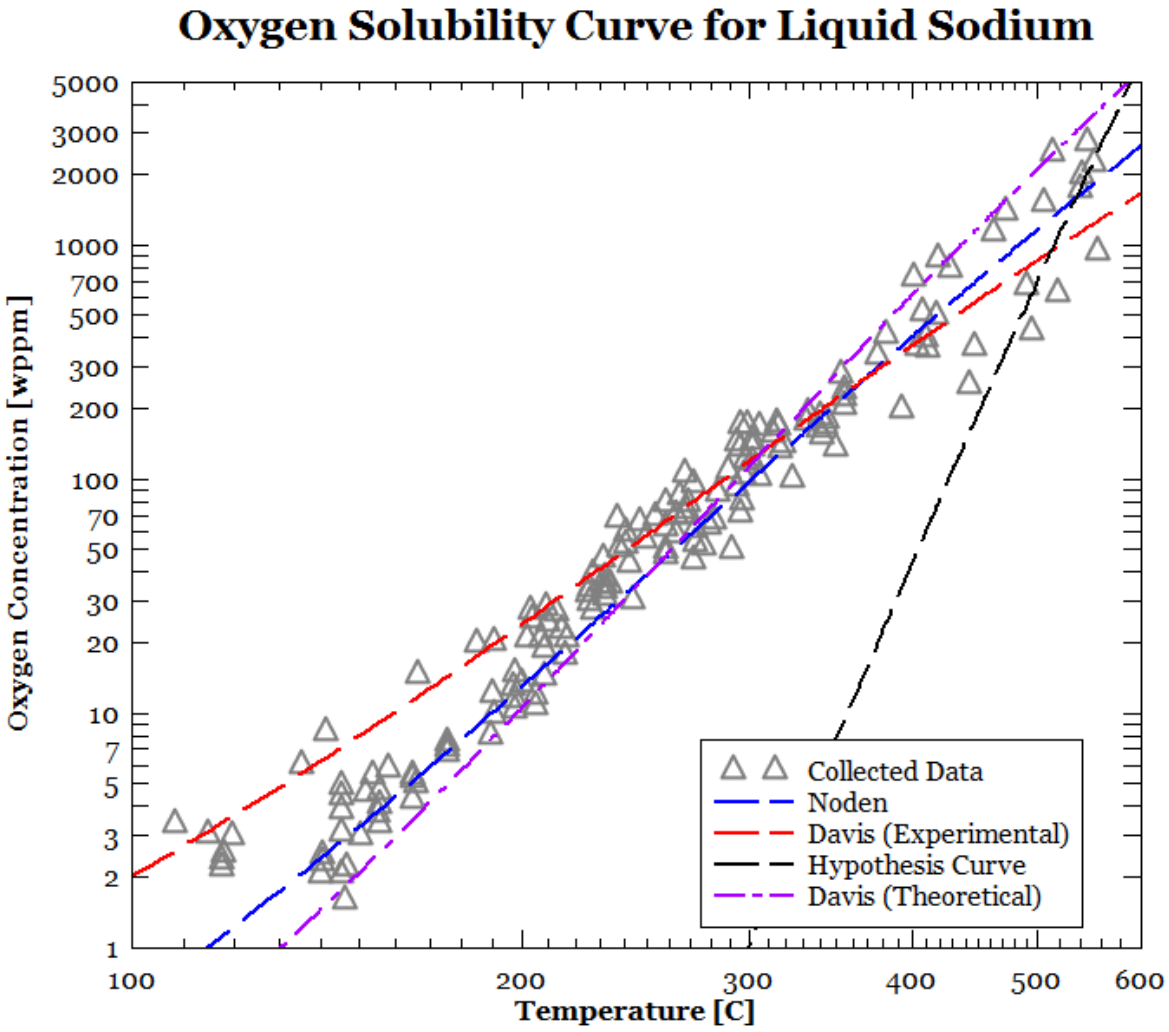

Figure 7.12: Plotting the solubility curve required to make electrochemical theory accurately predict YSZ oxygen sensor data clearly shows that this cannot be the primary source of error. The required curve is not close to overlaying the large body of solubility data.

7.4.3 Conclusion & Contributions of Hypothesis 1

While modifying the solubility curve to fit oxygen sensor data has appeared to be a feasible explanation in past research, doing so to explain errors in YSZ sensors has been shown to be highly improbable. The required change is too drastic, and the modified relationship no longer represents solubility data (as shown in figure 7.12).

The results of this hypothesis test support the conclusion that solubility error cannot be large enough to account for the YSZ signal discrepancy. While Smith's data provided no reason to doubt that solubility errors were the cause of inaccuracies in YST sensors, the tests outlined above suggest that another mechanism is likely the primary cause for YSZ.

A more conclusive study is to investigate Minushkin and Steinmetz's data, since the YSZ sensors tested in this research were very similar to their YST sensors. Both used similar input impedance data acquisition, and copper-reference systems. Figure 7.13 shows Minushkin's average sensor slopes on the same plot as Steinmetz; both experiments yielded similar results. Since Minushkin's data was consistently closer to theory than the YSZ sensors, it is suspected that the source of error is tethered to the electrolyte material, rather than solubility errors, which should affect both equally.

Hypothesis 1, which was that inaccuracies in oxygen solubility curves are the primary cause for the error in sensor signal has been shown to be *false*. Data taken with YSZ electrolytes suggests that another, more substantial source of error is introduced along with the new electrolyte material. The required change to commonly accepted solubility curves has been shown to be too drastic to account for the new data. In addition, since effects on sensor performance from changes in solubility curves should be invariant to changes in electrolyte materials, the large difference between the YSZ sensors in this research and previous YST sensors suggests an electrolyte-dependent mechanism is present.

While the result of this hypothesis test was a 'no', the contribution is still significant. It has been shown that changing the electrolyte significantly changes sensor slope, and by demonstrating this fact, it has also been shown that solubility errors are likely not the primary

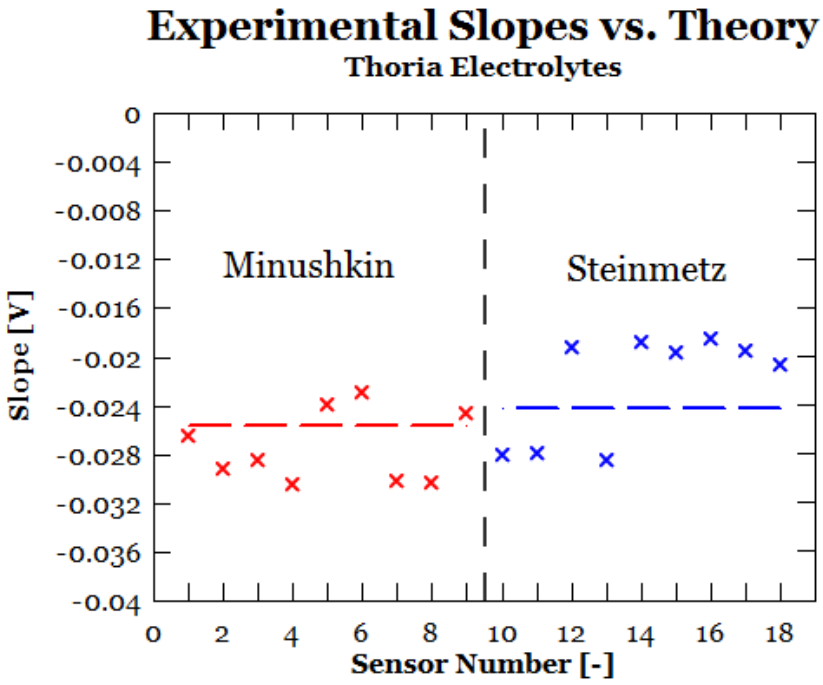

Figure 7.13: Steinmetz and Minushkin tested similar sensors to those used in this research, with the only difference being YST rather than YSZ electrolytes[3, 1]. Both slopes were closer to theory than the YSZ data.

cause of error in the YSZ sensor type. It can now be safely assumed that some electrolyte or electrolyte-electrode effect is the primary cause of signal error. This conclusion leads logically to hypothesis 2.

7.5 Hypothesis 2

Hypothesis 2 was that the difference between experimental and theoretical slope was primarily attributed to the sensor operating out of equilibrium due to low operating temperature, which prevent the electrochemical reaction from accessing bulk yttria stabilized zirconia (YSZ). Corrosion experiments and past oxygen sensor experiments have shown that sodium attack of the electrolyte material is too severe at temperatures above 400[C] for reliable operation, so oxygen sensor experiments in liquid sodium have mostly been conducted at or below this temperature[1, 2, 3]. Experimental data acquired during this research is shown

in figure 7.14. This figure shows the variability in the slopes of these sensors. The error bars on each slope show a statistically significant difference between experiment and theory. Table 7.2 shows the numeric values for each slope and respective uncertainty.

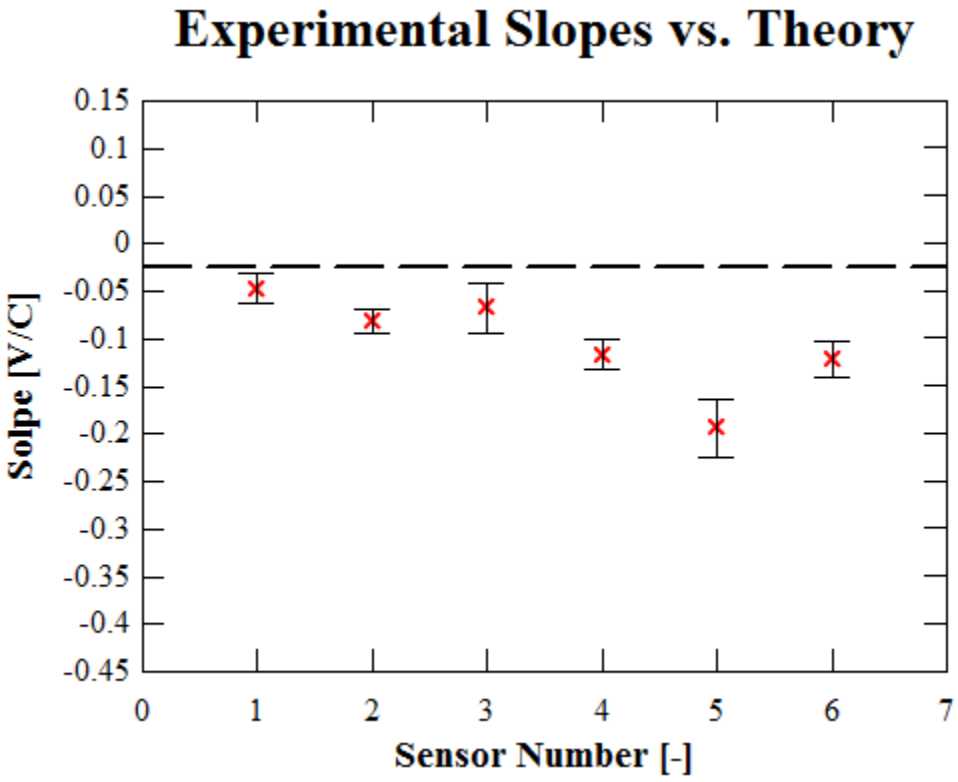

Figure 7.14: The experimental slope differs from theory with substantial variability. Hypothesis 2 is that the corrosion-limited low operating temperature of the YSZ electrolyte is the primary cause of this deviation.

It is shown in section 7.5.1 that the operating temperature (which is dictated by corrosion complications) and electronic current results in the sensor being governed by non-bulk thermodynamics. All oxygen sensor theory developed in Chapter 3 is based on a steady-state thermodynamic scenario. Since these oxygen sensors are operating at a temperature and current which limits oxygen transport to surface ions, the oxygen from the bulk YSZ has no effect on sensor signal. The kinetics of this problem are discussed below.

Experiments conducted to investigate this problem are described in section 7.5.2, and the results of these tests are discussed in section 7.5.3.

Table 7.2: Experimental slopes of oxygen sensors compared to theory. When considering the uncertainties of each slope, there is a statistically significant difference between theory and experiment.

Sensor	Slope [V/C]	Uncertainty [V/C]
Theory	-0.0256	—
P2	-0.0470	± 0.0154
P3	-0.0816	± 0.0126
P4	-0.0673	± 0.0267
P5	-0.117	± 0.0159
P6	-0.194	± 0.0298
P7	-0.122	± 0.0195

7.5.1 Background & Theory

A hand-calculation reveals that the signal generated by an electrochemical oxygen sensor is determined not from oxygen ions in the bulk-YSZ, but by ions only on the surface of the electrolyte. For example, if the sensor generates a 1[V] signal, and the high-impedance multimeter (or electrometer) limits the current to 0.1[nA] (which is an *upper-limit approximation*), then the flux of ions-per-second transporting through the YSZ is 3.12×10^8[ions/s]. This translates to 2.70×10^{13}[ions/day] being transported through the electrolyte.

This ion-flux will be compared to the number of oxygen atoms at the outermost layer of the probe. The probe is a 0.375 inches ([in]) diameter cylinder which is 0.5[in] long. The surface area of the probe is then the sum of the outer cylinder-wall, and the hemispherical tip: $A = 0.8099[\text{in}^2] = 0.0005225[\text{m}^2]$. This surface area estimate does not include roughness, which would increase the surface area by at least one or two orders of magnitude. Thus, $5.225 \times 10^{-4}[\text{m}^2]$ is a *lower-limit approximation* of the surface area.

A rough estimate of the number of oxygen ions per unit-surface-area is $\approx 1[\text{ion}/\text{Å}^2]$ (it will

be shown that even if this approximation is off by a couple orders of magnitude, the conclusion of this calculation would not change). This surface-density translates to $\approx 1 \times 10^{20}$[ions/m^2]. Thus, a lower estimate for the number of oxygen ions on the surface of the YSZ probe is 5.225×10^{16}[ions]. Since the sensor is transporting a maximum of 2.70×10^{13}[ions/day], the sensor will not transfer all of the surface atoms throughout the course of many days testing. This conservative estimate suggests that the sensor would have to operate continuously for ≈ 2000 days before oxygen ions from within the electrolyte could be accessed.

Thus, surface conditions play a vital role in determining the expected sensor output. The theory derived in Chapter 3 assumed bulk-YSZ interaction, which is not necessarily applicable.

Effects of non-bulk thermodynamics

Figure 7.15 is a two-sided portrayal of the oxygen-ion transport in the electrochemical oxygen sensor. The sensor is referred to as two different half-cells for this analysis. If the sensor was transporting oxygen from the bulk-YSZ and not strictly from the surface, the two halves of figure 7.15 would operate as a single unit, with steady-state transport across the electrolyte.

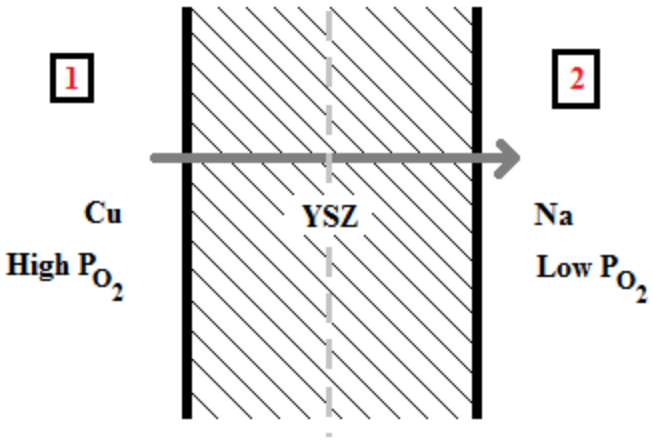

Figure 7.15: The electrochemical oxygen sensor is divided into two half-cells for this analysis.

Side 1 of the oxygen sensor is defined as the reference-electrode side, which is at a higher relative oxygen partial pressure (p_{O_2}) than that of the sodium side (side 2). The reactions

at side 1 and side 2 are shown in equations 7.15 and 7.16, respectively.

$$(\mathrm{YSZ} - V_o) + \mathrm{Cu_2O} + 2e^- \leftrightarrow \left(\mathrm{YSZ} - \mathrm{O}^{2-}\right) + 2\mathrm{Cu} \tag{7.15}$$

$$\left(\mathrm{YSZ} - \mathrm{O}^{2-}\right) + 2\mathrm{Na} \leftrightarrow (\mathrm{YSZ} - V_o) + \mathrm{Na_2O} + 2e^- \tag{7.16}$$

The above equations show the electrochemical oxidations of copper and sodium, respectively. The exchange of an oxygen ion for a vacancy and electron pair produces a current due to the net-flow of charge from one cell to the other. These electrochemical reactions move forward and backward according to their respective Gibbs energies of reaction, ΔG_1 and ΔG_2. For the following calculations the Gibbs energy of reaction for each element in equations 7.15 and 7.16 will be denoted simply as the species itself (dropping the ΔG in front of each term). The change in Gibbs energy for each half-cell reaction is given as equations 7.17 and 7.18.

$$\Delta G_1 = \left(\mathrm{YSZ} - \mathrm{O}^{2-}\right)_1 + 2\mathrm{Cu} - 2e^- - (\mathrm{YSZ} - V_o)_1 - \mathrm{Cu_2O} \tag{7.17}$$

$$\Delta G_2 = (\mathrm{YSZ} - V_o)_2 + \mathrm{Na_2O} - \left(\mathrm{YSZ} - \mathrm{O}^{2-}\right)_2 - 2\mathrm{Na} + 2e^- \tag{7.18}$$

If each side of the cell is accessing bulk YSZ, then the YSZ-vacancy and YSZ-ion exchange will be identical on both sides of the cell. Indeed, in this bulk-thermodynamic scenario:

$$\left(\mathrm{YSZ} - \mathrm{O}^{2-}\right)_1 = \left(\mathrm{YSZ} - \mathrm{O}^{2-}\right)_2$$

$$(\mathrm{YSZ} - V_o)_1 = (\mathrm{YSZ} - V_o)_2$$

The resulting total change in Gibbs energy is $\Delta G_{\mathrm{total}}$:

$$\Delta G_{\mathrm{total}} = \Delta G_1 + \Delta G_2 = 2\mathrm{Cu} + \mathrm{Na_2O} - \mathrm{Cu_2O} - 2\mathrm{Na} \tag{7.19}$$

In the event of bulk-YSZ thermodynamics, then equation 7.19 is true, and the theory

developed in Chapter 3 is accurate. However, given the surface analysis previously shown, the ability of YSZ to exchange ions and vacancies may not be uniform on both sides of the electrolyte, and these terms would not cancel out of the total change in Gibbs energy.

$$\Delta G'_{\text{total}} = \Delta G_{\text{total}} + \left[\left(\text{YSZ} - \text{O}^{2-}\right)_1 - \left(\text{YSZ} - \text{O}^{2-}\right)_2\right] + \left[(\text{YSZ} - V_o)_2 - (\text{YSZ} - V_o)_1\right] \quad (7.20)$$

$$\left(\text{YSZ} - \text{O}^{2-}\right)_1 \neq \left(\text{YSZ} - \text{O}^{2-}\right)_2$$

$$(\text{YSZ} - V_o)_1 \neq (\text{YSZ} - V_o)_2$$

Upon inspection of equation 7.20, it is clear that the contribution to sensor signal for the actual sensor is simply the theoretical output of a bulk-thermodynamic system, plus the difference between the vacancy-ion transport of the respective sides of the sensor. Since one side of the sensor is subjected to a hostile liquid sodium environment and the other is not, then it seems likely that the exchange-ability of YSZ would be different between the two sides.

First, consider the oxygen-ion exchange with the YSZ: $\left[\left(\text{YSZ} - \text{O}^{2-}\right)_1 - \left(\text{YSZ} - \text{O}^{2-}\right)_2\right]$. If the oxygen on the sodium side is **stabilized**, then $\left(\text{YSZ} - \text{O}^{2-}\right)_2$ becomes more positive, pushing this net contribution negative. This negative addition to ΔG_{total}, which is already negative, makes $\Delta G'_{\text{total}}$ more negative. This drives the voltage ($V'_{\text{total}} = -\Delta G'_{\text{total}}/2F$) more positive, so the **voltage goes up** as the oxygen becomes more stabilized on the sodium side.

If the oxygen on the sodium side is **destabilized**, then $\left(\text{YSZ} - \text{O}^{2-}\right)_2$ becomes less positive, and the net contribution of the oxygen-YSZ term becomes a positive contribution to the negative ΔG_{total}, so the $\Delta G'_{\text{total}}$ becomes less negative. The sensor voltage, accordingly, **decreases** as the oxygen becomes destabilized. The result of this analysis is shown in figure 7.16.

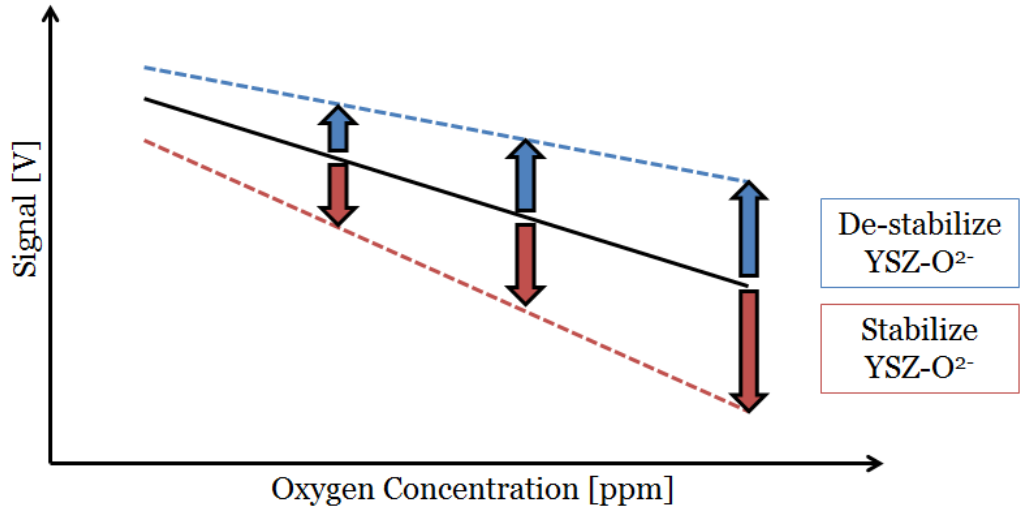

Figure 7.16: If the oxygen in YSZ on the sodium side is stabilized, then the oxygen transport will be inhibited, and the above analysis shows that the signal will be pushed down. The opposite effect is true if the oxygen is destabilized.

7.5.2 Testing

Unfortunately, quantifying non-bulk thermodynamics is extremely difficult due to the inconsistency of these effects. It is for this reason that hypothesis 2 was formed. Since it is unrealistic to model the effects of non-bulk thermodynamics and compare the results to experiments, a specific hypothesis was formed which could be tested. This hypothesis was that the sensor was operating in a regime which required transport of oxygen from the surface rather than through the bulk electrolyte, and that as a result, bulk thermodynamics do not accurately predict the sensor output.

This hypothesis could be tested by removing the corrosion limitation and operating these sensors at high temperature. These sensors were modified to be tested in tin-tin oxide (Sn-SnO_2). A 0.016" tungsten wire was used to connect the tin electrode to an electrometer (liquid tin dissolves copper so another material had to be used for the wire). Copper was still used for the other electrode, just as it was in the liquid sodium system. Both chambers were then sealed to ensure that each chamber would equilibrate with their environment. In these experiments, both sides of the sensor became reference electrodes, with oxygen concentrations

dictated by the temperature of the cell. Since the respective metals could control their own oxygen environments, the cell would generate a voltage strictly as a function of temperature, and not as a function of both temperature and dissolved oxygen concentration, as in sodium.

Tin was chosen as the test metal because it is compatible with YSZ, so there should be no corrosion, and it has been used to control oxygen pressure in past experiments[17]. Other metals which have been similarly used are copper, palladium, bismuth, and indium[18, 19, 20, 21]. Usually the reference chambers contain enough oxygen to oxidize on their own, so no additional oxygen is needed[22]. A schematic of this sensor test is shown in figure 7.17.

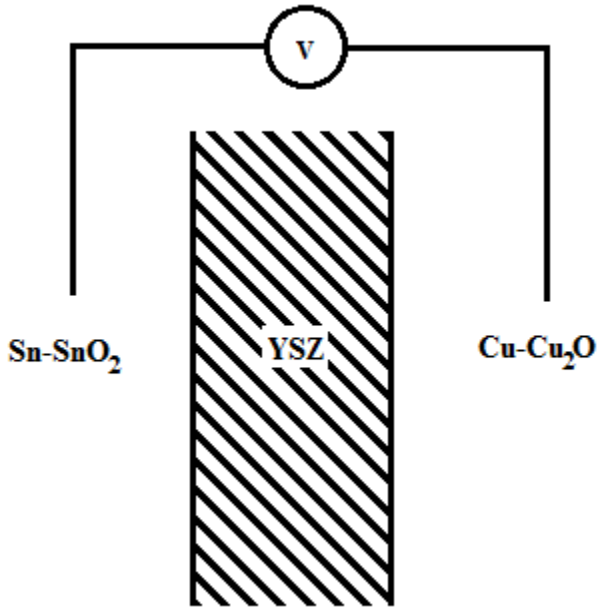

Figure 7.17: Sn-SnO_2 and Cu-Cu_2O are the two reference electrodes for this hypothesis test. Each electrode is sealed, and the oxygen pressures are controlled by temperature.

The Gibbs energies of formation of the involved reactions must be acquired as a function of temperature. The dominant reactions on either side of the sensor are:

$$\frac{1}{2}\mathrm{Sn(l)} + \mathrm{O^{2-}} \leftrightarrow \frac{1}{2}\mathrm{SnO_2(s)} + 2e^- \tag{7.21}$$

$$\mathrm{Cu_2O(s)} + 2e^- \leftrightarrow \mathrm{O^{2-}} + 2\mathrm{Cu(s)} \tag{7.22}$$

The Gibbs energies as a function of temperature were calculated using HSC Chemistry-7 software (made by Outec Research Oy) and confirmed using literature[19]. These values were used to determine the expected sensor voltage as a function of temperature using $V = -\Delta G(T)/2F$. The result of this calculation is shown in figure 7.18.

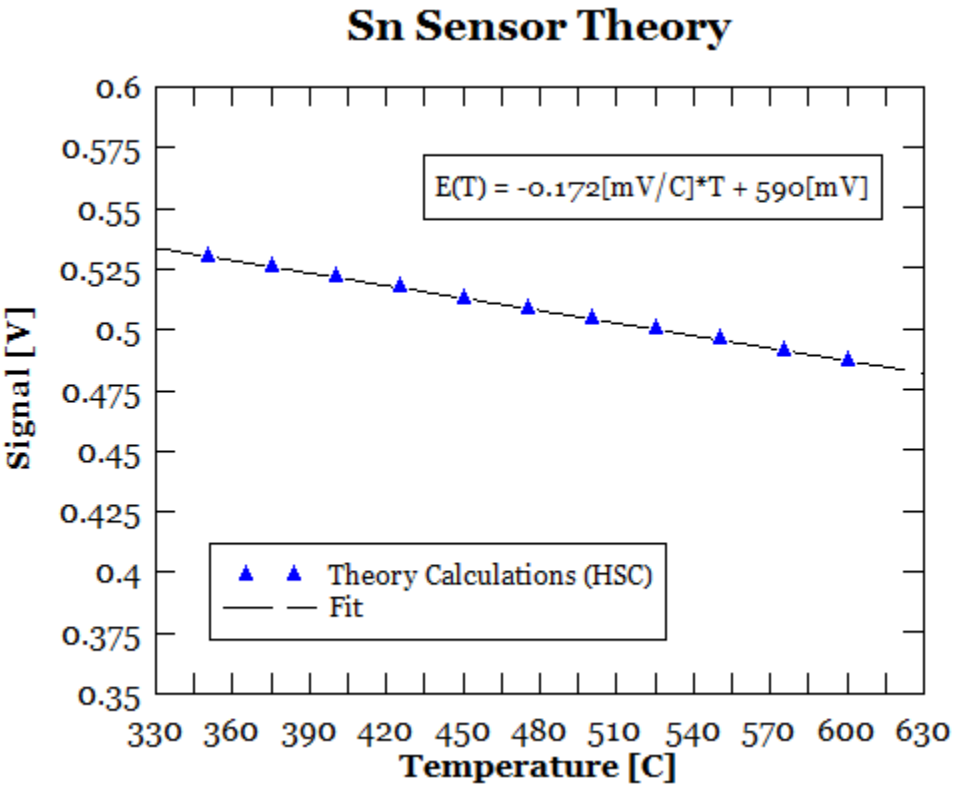

Figure 7.18: Expected sensor signal from a Sn-SnO_2 - Cu-Cu_2O electrochemical cell.

The experimental slope should be -0.172[mV/C] in regimes where the sensor is experiencing bulk thermodynamics. The oxygen sensors in sodium have shown increased slope in their operating regimes, but no oxygen sensor data has been taken in liquid sodium at elevated temperatures (because of the corrosion issues discussed above). The hypothesis under investigation is that, at elevated temperatures the sensor will start to converge to theoretical slope. Figure 7.19 shows data taken with Sn-SnO_2 at a range of temperatures.

In figure 7.19, the theoretical slope is overlaid on the same plot as the sensor data, showing that, at temperatures above 550[C], the data converges with theory.

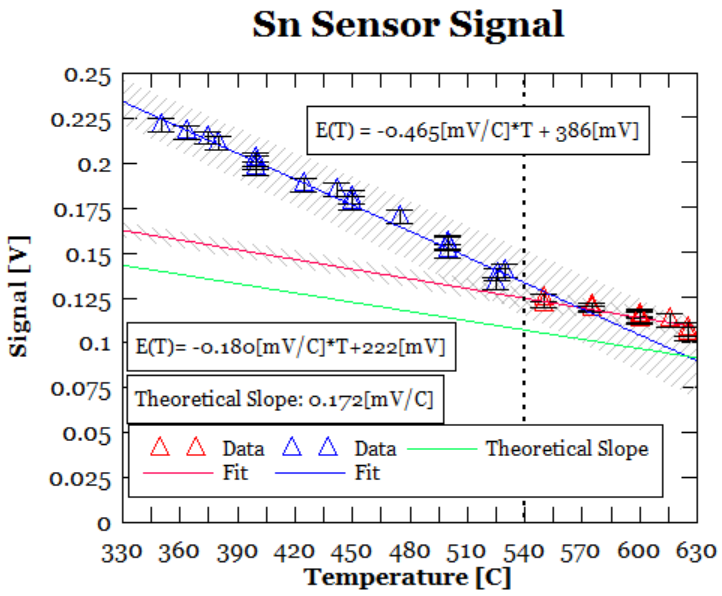

Figure 7.19: Data acquired from several experiments with the tin sensor. There are six data points in red (they are close together and hard to distinguish), which highlight the data taken above 540[C]. There appears to be a significant physical event that occurs above this temperature which results in the bend in acquired data.

7.5.3 Conclusion & Contributions of Hypothesis 2

When operating the oxygen sensors at low temperature, whether in a corroding environment or not, the generated slope is too steep. The fact that these oxygen sensors converge with theoretical slopes at high temperatures supports hypothesis 2. Hypothesis 2 was that the oxygen sensor was generating a different slope from theory as a result of operating with non-bulk YSZ. Since the current and corrosion-limited operating temperature of these sensors dictates that only surface oxygen ions will be sampled, commonly used electrochemical theory is not accurate.

This hypothesis helps explain why past oxygen sensor work in sodium, even with YST electrolytes, produced inconsistent slopes, and usually steeper than theory (due to the stabilization/destabilization of YSZ oxygen ions discussed in section 7.5.1).

Temperature limitations of ionic conductivity have been studied for solid oxide fuel cells(SOFC)[23], but SOFCs operate at maximum current, transferring as much charge as

possible. In contrast, oxygen sensors are operated in current-limiting environments, which prevents bulk oxygen from being transported.

An explanation for why the sensors generate a steeper temperature dependence than thermodynamic theory comes from the kinetics of how surface ions are removed. At elevated temperatures, the least stable adatoms are removed first. As temperature is increased, the signal contribution becomes less and less significant, driving the signal down faster than expected (which explains the steeper slope observed in each sensor test). This process continues until the sensor nears an equilibrium temperature at which the cell begins to behave closer to bulk transport. The vacancy side of the oxygen sensor reacts slightly different to low temperature. Oxygen ions will always fill equilibrium vacancies first. Only when the lower energy vacancies are filled will the sensor voltage begin to shift due to higher energy vacancies being filled. Thus, the result of the sensor signal to low temperature is to shift the slope more negative until some higher temperature when the sensor begins to behave according to theory. A schematic of this mechanism is shown in figure 7.20.

The mechanism proposed above for the cause of a steeper slope would tend to shift the sensor signal up as well. Many possible over-potentials likely exist in the sensor which would shift the overall voltage back down without affecting the slope. Indeed, most real-world effects that electrochemical cells endure shift the voltage in this way, like impurities in the ceramic depleting the ionic conductivity, current leakage through the data acquisition system, or corrosion layer buildup on the outer electrolyte wall.

A non-equilibrium mechanism which explains why the oxygen gradient is steeper than expected has not yet been determined. However, the molten tin experiments have provided substantial evidence that non-equilibrium effects are the cause for the sensor slope deviations. Research is still ongoing into a possible oxygen-dependent mechanism.

An interesting comparison is the different experiments relative error from their expected results. Figure 7.21 shows the two different types of liquid sodium oxygen sensor in comparison to the low temperature liquid tin sensor (the high temperature data will be discussed

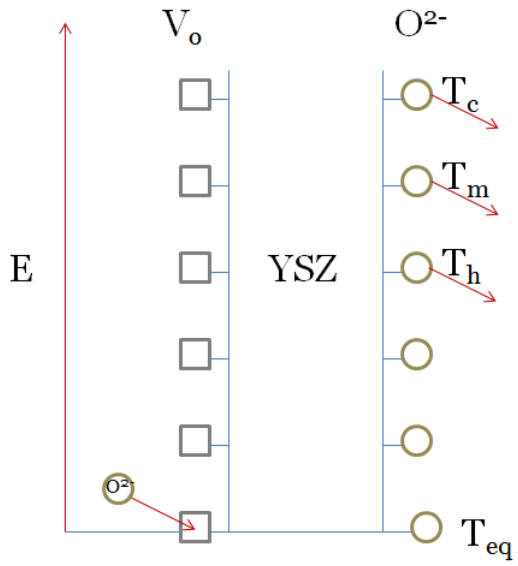

Figure 7.20: It is hypothesized that as temperature is increased, the least stable adatoms are lost first. As temperature is further increased, the more stable oxygen ions, closer to bulk-thermodynamics, become mobile. In contrast, oxygen ions will always fill the lowest-energy vacancies first. So shifting from equilibrium has little effect on the vacancy side of the sensor.

next). The acquired signal is plotted on the y-axis as a function of the theoretical signal on the x-axis.

The most noteworthy characteristic of figure 7.21 is that all three experiments produced the same slope (within error), but did not fall on the same line. This suggests that the slope-contributions are caused by the same mechanism, but the over-potentials are different. The oxygen pressures are substantially different between the three sensors, as well as the material interface at the electrolyte, so different over-potentials are very likely. The fact that the slopes are the same further supports hypothesis 2. Since only the low-temperature tin data is shown ($T < 550$[C]), the identical slopes suggest that the same mechanism is responsible for all three effects.

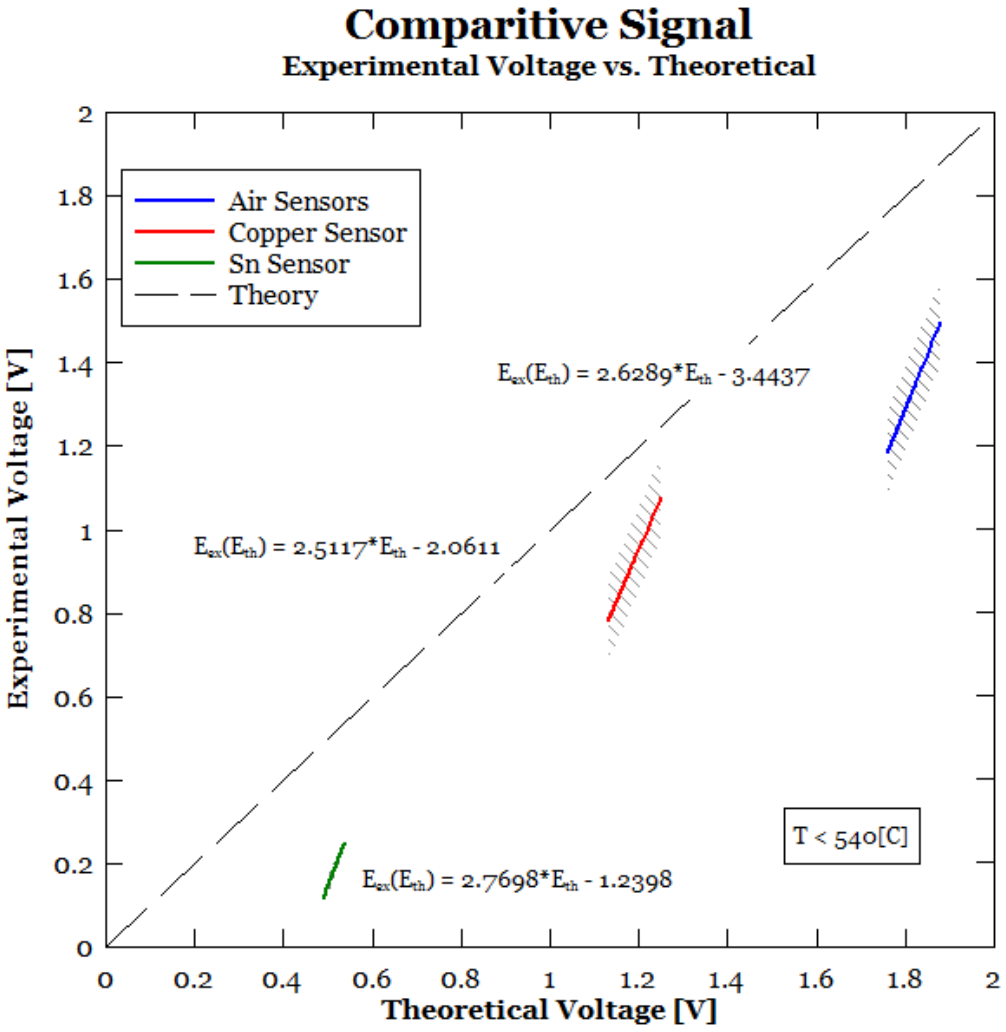

Figure 7.21: Experimental signal compared to theoretical signal for three different types of sensors. The error in corrosive sodium environments is substantially higher than in a non-corrosive environments (the error is shown for the tin data, but is very small). The dominant source of sensor-variability appears to be corrosion.

In contrast, when the tin sensor was operated at a higher temperature the slope shifted into agreement with theory, as shown in figure 7.19. These two different zones of the tin sensor data set are shown in figure 7.22 in a similar comparison as to figure 7.21.

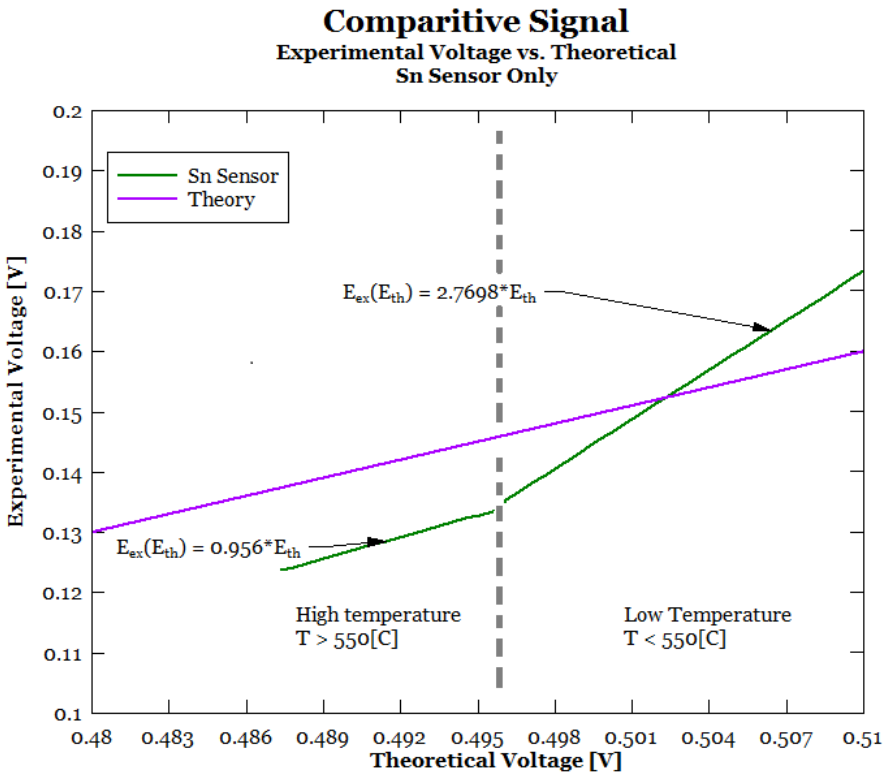

Figure 7.22: Experimental signal compared to theoretical signal for the high temperature tin data. The two different fits are shown, above and below 550[C]. Only the experiments which exceeded 550[C] generated a slope that agreed with theoretical predictions.

Figure 7.22 further verifies hypothesis 2. Increasing the temperature of the cell enables theoretical slope to be achieved. All data at low temperature generates a slope that is ≈ 2.7 times as steep as expected.

The second noteworthy aspect of figure 7.21 is the difference between the signal-errors of the sensors. Both types of sensors in sodium (air and copper reference electrodes) produced substantially larger error than the tin sensor, even though the temperature ranges of these experiments overlap. This suggests that the cause of variability is not a low operating temperature, but rather is the corrosive sodium environment. Without the presence of

sodium corrosion, the tin sensor appears to produce much more steady results. The chaotic process of sodium-zirconate production, dissolution, and oxygen leaving the surface of YSZ likely destabilizes the sensor signals. This observation is consistent with the fact that previous YST experiments yielded more consistent experimental slopes (shown above as well as in Chapter 3). This improved consistency is because YST is more stable in liquid sodium than YSZ, as discussed in Chapter 6.

While the effect of surface thermodynamics is difficult to quantify and accurately model, this hypothesis test does help explain long-standing inaccuracies and inconsistencies in liquid sodium oxygen sensor technology. Past sodium-sensor work has been limited to 300-400[C] and usually thoria electrolytes because of corrosion issues. Experimentalists have commonly theorized that experiment inaccuracies may be attributed to electronic conductivity (and therefore current-leakage) in the YSZ or inaccuracies in solubility curves for liquid sodium; but higher operating temperature in sodium has had little investigation because of increased sodium attack and decreased lifetime. This experiment has shown that the temperature-limitation is a substantial cause for signal disparity by eliminating corrosion, increasing sensor temperature, and observing the slope approach theory. While this conclusion does not *solve* the problem (indeed, sodium will always attack the YSZ at increasing rates with increasing temperatures), it does provide evidence in support of an explanation for a substantial cause of sensor error.

7.6 Hypothesis 3

Hypothesis 3 is that the coefficient of ionic conductivity deviates sufficiently from unity to cause the observed voltage offset seen with the YSZ sensors. The following sections investigate the effect of t_{ion} on sensor signal, and compare the acquired data to these effects. In addition, past YST sensor data will also be used to investigate this hypothesis.

7.6.1 Background & Theory

The explanation of slope provided above has not explained why thoria sensors produced signals closer to theory than zirconia sensors (as shown in figure 7.13). As discussed in chapter 3, YST is a better ionic conductor at low oxygen pressure and temperature than YSZ. In addition, YST is more stable at low oxygen pressure, only losing 0.05% of its oxygen, in comparison to 0.6% oxygen loss in YSZ at identical conditions[24, 25]. While data is not available at extreme conditions seen in liquid sodium systems, higher pressure and lower temperature behavior of the electrolytes will be extrapolated to sodium conditions and discussed in figure 7.23.

In chapter 3 the expected oxygen sensor voltage was derived from the following equation:

$$E = \frac{1}{2F}\int_{\mu_R}^{\mu_L} t_{ion}\, d\mu \tag{7.23}$$

μ_L and μ_R referred to the different oxygen potentials on either side of the electrolyte, and F is the Faraday constant. The coefficient of ionic conductivity was assumed to be unity (in other words, the electrolyte is assumed to be a perfect ionic conductor), at which point the expected sensor voltage follows the Nernst equation.

$$E = E_T^o(T) - \frac{RT}{2F}\ln\left(\frac{c}{c_o}\right) \tag{7.24}$$

However, in conditions which induce electronic conduction ($\sigma_{\text{electron}} \neq 0$) the electrolyte will behave as only a partial ionic conductor:

$$t_{ion} = \frac{\sigma_{\text{ion}}}{\sigma_{\text{ion}} + \sigma_{\text{electron}}} < 1 \tag{7.25}$$

In cases where t_{ion} is not unity, equation 7.23 becomes much more difficult to solve. However, if t_{ion} is constant over the range of oxygen potential between μ_L and μ_R, then the integral can be solved as:

$$E = t_{\text{ion}} E_T^o(T) - t_{\text{ion}} \frac{RT}{2F} \ln\left(\frac{c}{c_o}\right) \tag{7.26}$$

Since the coefficient of ionic conductivity is always less than one, the factor in front of equation 7.26 will offset the overall voltage down. Indeed, all sensor signals both in thoria and zirconia electrolytes gave sensor voltages that were less than theory.

Studies on the ionic conductivity of both zirconia and thoria electrolytes have been conducted, and the oxygen pressures and temperatures at which these electrolytes behave as pure ionic conductors has been tabulated in limited conditions, as discussed above and in chapter 3. Data has been acquired from various sources and consolidated into one plot, shown in figure 7.23[24, 25, 26]. The individual colored lines represent the range of oxygen pressure and temperature which result in a coefficient of ionic conductivity of ≈ 0.99. Deviating in any direction from that line results in inducing electrical conductivity (the effects of changing oxygen pressure on a solid electrolyte were discussed in chapter 3) and a reduced overall t_{ion}. Note that the data presented in figure 7.23 was taken only for temperatures above 800[C]. The data had to be extrapolated to sodium conditions, so the dotted lines are approximations.

The top line of the shaded region in figure 7.23 is a rough description of the oxygen pressure in saturated sodium. Sodium systems are maintained well below this pressure, which is why the shaded region extends infinitely downward.

Even considering inherent error in extrapolating the data in figure 7.23 to low temperature and pressure, it is likely that thoria-based electrolytes are better ionic conductors at sodium conditions than zirconia sensors. Hypothesis 3 was therefore formed that the greater voltage offset observed with past oxygen sensor research from the current work was the result of poorer ionic conductivity with the YSZ electrolyte than the YST electrolyte.

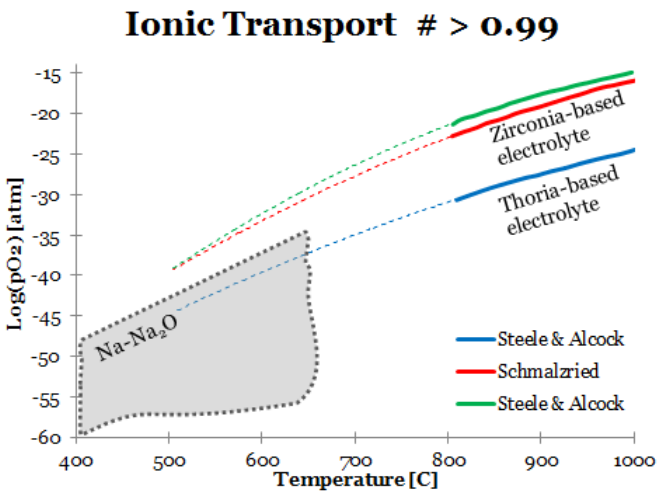

Figure 7.23: The conditions for which YSZ and YST have shown ideal ionic conductivity ($t_{ion} > 0.99$) are shown as the respective colored lines. This data extrapolated to the low-oxygen pressure zone more appropriate for liquid sodium suggests that YST is a better ionic conductor than YSZ[24, 25, 26].

7.6.2 Testing

This hypothesis did not require any additional experiments, but rather a comparison of collected data from YST and YSZ sensors. It should be noted that if while t_{ion} may be shifting the sensor signal down by deviating away from unity, the coefficient must be constant for each sensor, or the $\ln c$ vs. E plots would not be linear (figure 7.7 and figures 3.6-3.8).

In order to test this hypothesis, the assumption was made that the only error in the sensor output was a deviation from $t_{\text{ion}} \approx 1$. The required t_{ion} for each sensor was then calculated using the intercept value from the fit equation (A in equation 7.9). In this scenario, the YST sensors from past research would have required ionic conductivity numbers in the range: $0.82 \leq t_{\text{ion}} \leq 0.98$ [1, 2, 3, 27, 28, 29]. The YSZ sensors tested for this research were slightly farther from theoretical predictions, suggesting t_{ion} values between $0.78 \leq t_{\text{ion}} \leq 0.94$.

The respective ionic conductivity numbers, averaged from past YST sensor experiments are shown side-by-side with the YSZ experiments from this research in figure 7.24. The average values for t_{ion} of the YSZ and YST sensors are 0.869 and 0.912 respectively. However, as seen in the figure, there is considerable variation from sensor-to-sensor.

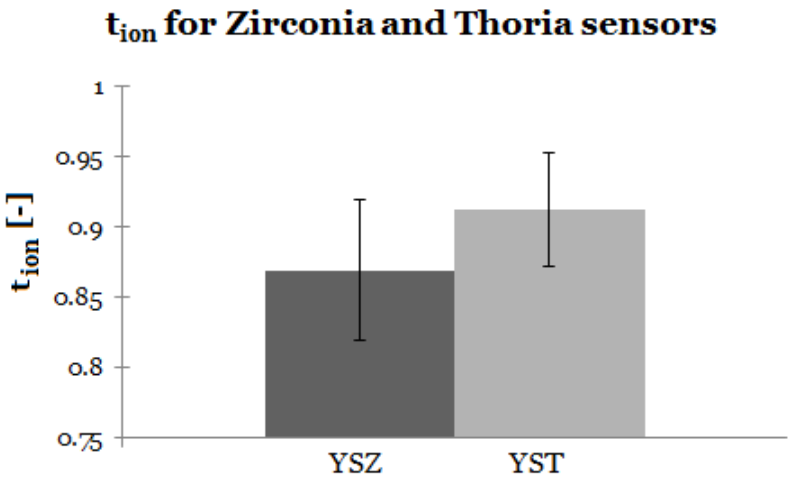

Figure 7.24: The average coefficient of ionic conductivity is shown for YSZ and YST sensors. Notice the YSZ average is slightly lower than then YST, however, the results are nearly within error of each-other.

The uncertainty in the YST sensors was slightly better than for the YSZ probes, a result of increased corrosion on the latter material as discussed in hypothesis 2. The YSZ data is just outside the experimental error of the YST sensors. Even with some t_{ion} data points overlapping, it appears as though the YST sensors require a lower ionic conductivity number than the YSZ sensors.

7.6.3 Conclusion & Contributions of Hypothesis 3

Hypothesis 1 investigated a possible primary source of error in both the voltage offset as well as slope error of the sensors, and was dis-proven. Hypothesis 2 provides a convincing argument for the primary cause of error in slope, as well as the increased sensor variability. Thus far, no explanation of the offset voltage has been presented. Hypothesis 3 was tested in effort to contribute insight into this deviation.

Hypothesis 3 claimed that the offset error in oxygen sensor voltage was primarily caused by the coefficient of ionic conductivity deviating from unity in the YSZ sensors. Evidence was found which shows that thoria sensors are better *ionic* conductors at sodium conditions

than YSZ. Furthermore, YSZ and YST sensors were compared in terms of deviations from theory in the overall voltage. The data suggests that the YST sensors have a higher t_{ion} than the YSZ sensors, which is in agreement with figure 7.23. Moreover, the range of t_{ion} values is not far from those suggested by Minushkin as being probable[3, 28].

There is considerable variability in sensor-to-sensor t_{ion}, as shown by the error bars in figure 7.24. This uncertainty is a result of the overlap of some of the YSZ and YST t_{ion} data. Accordingly, while the data presented suggests that hypothesis 3 is true, more data must be taken to reduce the error bars in figure 7.24 before this cause can be conclusively accepted.

Even though this hypothesis has not been conclusively accepted, data has been added to fortify the suggestion that t_{ion} deviations are responsible for significant sensor error. The extrapolation of data shown in figure 7.24 is also a unique contribution to the sodium oxygen sensor field, and suggests strongly that YST is a better material for an electrolyte not only for the improved resistance to sodium attack, as discussed in chapter 6, but also for improved ionic transport in liquid sodium conditions. YSZ, while it is an excellent ionic conductor at high temperature and oxygen pressures commonly seen in solid oxide fuel cells, is not ideal for low oxygen pressure and temperature.

7.7 Summary of Chapter 7

In this chapter the results of YSZ-based oxygen sensor tests in liquid sodium have been presented. The oxygen sensors produced a signal that varied with oxygen concentration as theory predicted. However, the sensors response to changes in oxygen concentration were too high and the overall voltage was lower than theory suggests. Furthermore, the calibration curves varied from sensor-to-sensor. While these results were not unique compared to past oxygen sensor tests with YST electrolytes, the effects were of higher magnitude. Arguments were made in this research as well as in past work (see chapter 3) that quantifying these errors was not realistic.

A series of hypotheses were proposed in order to narrow the range of unknowns surrounding electrochemical oxygen sensor signals. These hypotheses were carefully constructed to be answerable and contribute substantial knowledge to the body of sensor work already in literature regardless of the outcome of the hypotheses. Below is a tabulated list of conclusions from this study.

- It has been shown that solubility error cannot be the primary explanation for the YSZ sensor's deviation from theory (figure 7.12).

- The fact that otherwise identical sensors produced significantly different data when YSZ electrolytes were used instead of YST suggests that the primary cause of discrepancy in the YSZ sensors is due to the electrolyte material (figure 7.13 and figure 7.14).

- It has been shown that operating the oxygen sensors at high temperature causes the sensor slope to approach theory, suggesting that the sensors are operating out of equilibrium in liquid sodium conditions (figure 7.22).

  Mathematical half-cell model of the effects of non-equilibrium operation has been developed, and a possible mechanism for the temperature-slope effect has been presented. However, a mechanism for the oxygen concentration-slope effect has not been suggested.

  Not finding a mechanism responsible for the oxygen-slope problem does not disprove its existence. The data presented is compelling evidence that the sensors are operating out of equilibrium and, therefore, conventional electrochemical theory is not the sole governing model for oxygen sensors in sodium.

- It has been shown that, at low temperature, all the sensors are likely enduring the same physical mechanism for error (figure 7.21). Data suggests that this mechanism becomes less dominant at high temperature when the slope of the sensor approaches theory.

- The increased uncertainty in YSZ sensors compared to YST sensors has been linked to more aggressive sodium attack of the zirconia-based electrolyte compared to thoria (figure 7.21).

- Evidence has been presented which *suggests* that the coefficient of ionic conductivity, t_{ion}, is closer to unity for YST than YSZ in sodium conditions (figure 7.23). This evidence is supported by experimental comparison of YST data to YSZ (figure 7.24). The error bars of the data supporting this hypothesis are statistically significant, so it is concluded that the presented data *supports* but does not *prove* the statement that t_{ion} is responsible for the thoria-based electrolytes producing more accurate signals than the zirconia-based electrolytes.

Chapter 7 Bibliography

[1] H. Steinmetz. Development of a continuous meter for oxyggen in sodium. Technical report, United Nuclear Corporation, White Plains, New York, January 1963.

[2] D.L. Smith. Monitoring and measurement of oxygen concentrations in liquid sodium. Technical report, International Conference on Liquid Metal Technology in Energy Production, 1976.

[3] B. Minushkin & M. Kolodney. Development of a continuous electrochemical meter for oxygen in sodium. Technical report, United Nuclear Corporation, 1967.

[4] M.R. Hobdell and C.A. Smith. Electrochemical techniquies for monitoring dissolved carbon, hydrogen, and oxygen in liquid sodium. *Journal of Nuclear Materials*, (110):125–139, 1982. Berkeley Nuclear Laboratories, United Kingdom.

[5] R.G. Taylor and R. Thompson. Testing and performance of electrolytic oxygen meters for use in liquid sodium. *Journal of Nuclear Materials*, 1983.

[6] R.C. Asher et al. The harwell oxygen meters and harwell carbon meter. Technical report, British Nuclear Engergy Society, 1984.

[7] J. D. Noden. A general equation for the solubility of oxygen in liquid sodium. *Journal of the British Nuclear Energy Society*, 12(1):57–62, 1973.

[8] S.L. Walters. Effect of adding oxygen to sodium flowing in a stainless-steel system. Technical Report NP-1955, Mining Safety Appliances, 1950.

[9] A.D. Bogard and D.D. Williams. Solubility of sodium monoxide and sodium hydroxide in metallic sodium. Technical Report NRL-3865, Naval Research Laboratory, 1951.

[10] J.D. Noden and K.Q. Bagley. Solubility of oxygen in sodium and nak alloy. Technical Note 80, United Kingdom Atomic Energy Association (UKAEA), 1954.

[11] W. Jahns and G. Weidmann. The determination of low oxygen concentrations in sodium. Technical Report 1:189-190, Nucleonick, 1959.

[12] K.S. Bergstresser et al. Determination of trace amounts of oxygen added to metallic sodium. Technical Report LA-3343, Los Alamos Scientific Laboratory, 1965.

[13] S. Dorner. Solubility of oxygen in sodium. Technical Report EURFNR-179P, English Translation of Projekt Schneller Bruter Report, 1966.

[14] R.C. Andrews and K.R. Barker. Effect of high temperature sodium on the mechanical properties of candidate alloys for the lmfbr program. Technical Report MSA R67-207, Mining Safety Appliances, 1967.

[15] V.J. Rutkauskas. Determination of the solubility of oxygen in sodium by vacuum distillation. Technical report, Los Alamos Scientific Laboratory, July 1968.

[16] J.R. Humphreys. Argonne national laboratory reactor development program progress reports. Technical Report ANL-7518 & ANL-7460, Argonne National Laboratory, 1968.

[17] J. Burda M. Fresl D. Jakes, J. Kral. Development of electrochemical oxygen meter for liquid sodium. In *Solid State Ionics 13*, pages 165–173, North-Holland, Amsterdam, 1984. Nuclear Research Institute, Czechoslovakia.

[18] N. Li J. Zhang. Review of the studies on fundamental issues in lbe corrosion. *Journal of Nuclear Materials*, 373:351–77, 2008.

[19] G.M. Kale R. Kurchania. Oxygen potential in molten tin and gibbs energy of formation of sno2 employing an oxygen sensor. *Journal of Material Research*, 15:1576–82, 2000.

[20] G.M. Kale. Oxygen potentials in ni + nio and ni + cr2o3 + nicr2o4 systems. *Metallurgical and Material Transactions B*, 25B:373–8, 1994.

[21] H. Taimatsu H. Kaneko, T. Okamura. Characterization of zirconia oxygen sensors with a molten internal reference for low-temperature operation. *Sensor Actuators B*, 93:205–8, 2003.

[22] R.A. Rapp T.A. Ramanarayanan. The diffusivity of oxygen in solid nickel. *Metallurgical Transactions*, pages 3239–46, 1972.

[23] E.D. Wachsman et al. Lowering the temperature of solid oxide fuel cells. *Science*, 334(935), 2011. DOI:10.1126/science.1204090.

[24] H. Schmalzried. Uber zirkondioxyd als elektrolyt fur elektrochemische utersuchungen bei hoheren temperaturen. *Zeitschreift fur Electrochemie*, (66:572), 1962.

[25] R.A. Rapp. Personal communication. Technical report, Ohio State University, May 1964.

[26] B.C.H. Steele and C.B. Alcock. Factors influencing the performance of solid electrolytes in high temperature thermodynamic measurements. In *AIME Annual Meeting*, New York City, February 1964.

[27] B. Minushkin. The liquid metal oxygen meter. Technical report, United Nuclear Corporation, White Plains, New York, 1965. p.272-273.

[28] J. McKee B. Minushkin, editor. *Development of Electrochemical Methods for Oxygen Monitoring and Removal in Sodium*. United Nuclear Corporation, April 1965.

[29] O.J. Foust, editor. *Sodium-NaK Engineering Handbook*, volume 5. Liquid Metal Engineering Center, 1979.

Chapter 8

Conclusions, Contributions, and Recommendations

This report details the design and construction of two liquid sodium test facilities at UW-Madison. This report specifically describes research pertaining to dissolved oxygen measurements using an electrochemical oxygen sensor. Yttria stabilized zirconia (YSZ) was the primary material of investigation to replace yttria stabilized thoria (YST) as the electrolyte for oxygen sensors.

The YSZ oxygen sensors produced a signal that varied with oxygen concentration in agreement with the theoretical functional form, but with considerable variability in slope and voltage offset from sensor-to-sensor. Conclusions from this research, including contributions to the field of electrochemical oxygen sensors are presented. Suggestions for future research are included in this chapter as well.

Chapter 8 Contents

Contents

8.1 Experiment Facilities Improvements

As discussed in chapter 6, the corrosion experiments conducted thus far at UW-Madison all occurred in oxygen saturated sodium. This process is unavoidable in a sodium bath open to glovebox atmosphere. However, a sealable crucible attached to a small cold trap would enable precise oxygen control. Given the successful agreement between cold trap and plugging meter achieved in chapter 5, no additional instrumentation in this crucible would be necessary to know oxygen concentration.

This addition would allow the ceramic corrosion tests to be conducted with temperature and oxygen concentration decoupled. This would enable static corrosion testing at loop (ie. reactor) conditions.

8.2 Electrolyte Materials

Yttria stabilized zirconia (YSZ) is less resistant to sodium attack than yttria doped thoria (YST). This was shown through literature review and experiments discussed in chapter 6. While this fact is not new information, the measured corrosion rates help quantify the limiting factor in YSZ-based oxygen sensors. The presented data indicates the importance of the sintering process, as two different manufacturers produced YSZ with the same dopant concentration and yet the corrosion results were significantly different (Friatec was much more compatible than McDanel). Furthermore, the existence of porosity can allow sodium penetration into the ceramic which would cause a short in the electronic circuit of the sensor, however, too little porosity can result in the ceramic cracking under thermal stress.

Materials that appear compatible with liquid sodium appear to include BeO, MgO, and Al_2O_3. However, as demonstrated with alumina bisque and full-sintered alumina, there is a significant difference between the corrosion resistance of full-sintered materials and partially sintered. These three materials do not allow ionic conduction but could increase the lifetime of an electrolyte if added in small quantities.

8.2.1 Potential Future Work in Electrolyte Materials

Sintering recipes

A detailed test matrix of various sintering recipes of an otherwise identical YSZ electrolyte would be a valuable publication to this field. Since it has been repeatedly found that similar materials from different manufacturers produce significantly different corrosion results in sodium, it would be beneficial to attempt to isolate the cause of these differences. Friatec AG may be interested in experimenting with different sintering techniques, so a partnership in this research is possible. The sodium research group at CEA-Saclay is headed by Dr. Jean-Louis Courouau, and they are producing several different blends of YSZ for sodium testing. Exchange and samples and data has already been established, and a healthy relationship with this research group could yield impressive combined results.

Sintered YSZ of various yttria concentraitons

Given that preliminary results of thermal sprayed ceramics indicate increasing resistance to sodium attack with increasing yttria concentration, a similar study with full-sintered ceramics would be valuable. At the time of this research, a company that offered various yttria concentrations of full-sintered YSZ was not found. However, if Friatec AG or the ceramics group at CEA-Saclay became interested in getting involved with this research, then this test matrix could be conducted.

Sintering thermal sprayed YSZ

Thermal sprayed ceramics have also shown potential for use in sodium. Indeed, prototype oxygen sensors using this technology were designed and tested in this research, and the results are available in Appendix B. These electrolytes allowed slow penetration of sodium until the sensor completely shorted out. However, the electrochemical cell did generate a signal until complete failure. If the density of the thermal spray could be increased via sintering then

these sensors could possibly function properly in sodium. This experiment requires that a range of sintering techniques be tested.

8.3 Electrochemical Oxygen Sensors

The oxygen sensors tested in this research used YSZ electrolytes, whereas a vast majority of past success was achieved using YST. The YSZ sensors achieved a signal that responded as expected to changes in oxygen, but with a different slope and overall voltage. The results were similar to YST data, but more exaggerated. The sensor-to-sensor variability was substantially higher, and the responsiveness to changes in oxygen concentration was higher. The ensuing hypothesis tests yielded an improved understanding of errors in electrochemical oxygen sensors in sodium. Those results were discussed in detail in chapter 7, but are re-summarized below. The following list of results was taken from section 7.7.

- It has been shown that solubility error cannot be the primary explanation for the YSZ sensor's deviation from theory (figure 7.12).

- The fact that otherwise identical sensors produced significantly different data when YSZ electrolytes were used instead of YST suggests that the primary cause of discrepancy in the YSZ sensors is due to the electrolyte material (figure 7.13 and figure 7.14).

- It has been shown that operating the oxygen sensors at high temperature causes the sensor slope to approach theory, suggesting that the sensors are operating out of equilibrium in liquid sodium conditions (figure 7.22).

  Mathematical half-cell model of the effects of non-equilibrium operation has been developed, and a possible mechanism for the temperature-slope effect has been presented. However, a mechanism for the oxygen concentration-slope effect has not been suggested.

Not finding a mechanism responsible for the oxygen-slope problem does not disprove its existence. The data presented is compelling evidence that the sensors are operating out of equilibrium and, therefore, conventional electrochemical theory is not the sole governing model for oxygen sensors in sodium.

- It has been shown that, at low temperature, all the sensors are likely enduring the same physical mechanism for error (figure 7.21). Data suggests that this mechanism becomes less dominant at high temperature when the slope of the sensor approaches theory.

- The increased uncertainty in YSZ sensors compared to YST sensors has been linked to more aggressive sodium attack of the zirconia-based electrolyte compared to thoria (figure 7.21).

- Evidence has been presented which *suggests* that the coefficient of ionic conductivity, t_{ion}, is closer to unity for YST than YSZ in sodium conditions (figure 7.23). This evidence is supported by experimental comparison of YST data to YSZ (figure 7.24). The error bars of the data supporting this hypothesis are statistically significant, so it is concluded that the presented data *supports* but does not *prove* the statement that t_{ion} is responsible for the thoria-based electrolytes producing more accurate signals than the zirconia-based electrolytes.

8.3.1 Potential Future Work on Electrochamical Oxygen Sensors

Varying Yttria Concentration in Sintered YSZ

Increasing yttria concentration can increase the resistance of YSZ to sodium attack, however, the increase in Y_2O_3 will inhibit ionic conductivity (see Appendix A). It would be beneficial to study oxygen sensor signal with increasing Y_2O_3 in conjunction with the research suggested in section 8.2.1. This combination of data would enable the user to optimize a dopant yttria concentration. This parameter was not a variable in the sensors tested in this research.

Sensors with Thermal Sprayed Electrolytes

Thermal sprayed electrolytes were briefly investigated in this research, and these result are shown in Appendix B. However, the sodium penetration through the high-porosity electrolyte must be eliminated for a functioning sensor. In addition to the corrosion experiments discussed in section 8.2.1, the application of these ceramics to electrochemical cell technology must be tested. These coatings can be tested in similar experiments to those described in chapter 7, but the addition of thermal spray sensor data will be valuable to the oxygen sensor field.

8.4 Summary

All future work should be conducted while thinking about its implications on the oxygen sensor results achieved to date. If future research with YSZ successfully reduces sodium attack on the electrolyte, then the nose/uncertainty should improve. Furthermore, improved corrosion resistance could result in a higher operating temperature which would allow the sensors to operate closer to (or at) equilibrium. In this case, the sensor-to-sensor consistency and predictability of slope should improve. If these achievements are made using cost effective electrolytes (like a thermal sprayed YSZ), then the relative improvement over previous YST sensors becomes more attainable. As the current results indicate, YSZ is not likely a good replacement for YST in sodium, even if YSZ is significantly cheaper.

Development of a YST sensor is valuable from a commercial product standpoint, but *research* on these sensors is a different problem altogether. As discussed in chapters 3 and 7, the dominant problems with YST sensors are different from those of the YSZ sensors. If one desires to produce a reliable sensor in sodium, at this point in time, YST is a better electrolyte. However, if a cost effective alternative electrolyte to the actinide thorium is desired for an electrochemical oxygen sensor in sodium, then the research described in this report provides significant groundwork for YSZ. A deeper understanding on electrochemical

oxygen sensor theory has been presented, and several prominent causes of YSZ sensor error have been characterized.

8.5 Past and Future Publications from this Research

8.5.1 Past Publications

- *Corrosion of Thermal Sprayed Coatings in Liquid Sodium for the Development of an Electrochemical Oxygen Sensor*, B.K. Nollet, M.G. Hvasta, M.H. Anderson, NURETH15-345, Pisa, Italy, May 12-15,2013

- *Development of Electrochemical Oxygen Sensors for Liquid Sodium*, B.K. Nollet, M.G. Hvasta, M.H. Anderson, CN-199-317, IAEA FR13, Paris, France, March 4-7, 2013

- *Analysis & Methodology for Measuring Oxygen Concentration in Liquid Sodiium with a Plugging Meter*, B.K. Nollet, M.G. Hvasta, M.H. Anderson, ICAPP-12020, ICAPP'12, Chicago, USA, June 24-28, 2012

- *Preliminary Results from the UW-Madison Sodium Corrosion Testing Facility*, M.G. Hvasta, B.K. Nollet, M.H. Anderson, NURETH15-379, Pisa, Italy, May 12-15,2013

- *Design & Development of a High-Temperature Sodium Compatibility Testing Facility*, M.G. Hvasta, B.K. Nollet, M.H. Anderson, ICAPP-12017, ICAPP'12, Chicago, USA, June 24-28, 2012

8.5.2 Intended Future Publications

- *Development of an Electrochemical Oxygen Sensor for Liquid Sodium Using a YSZ Electrolyte*

  Intended Journal: Journal of The Electrochemical Society

- *Ceramic Corrosion in Liquid Sodium - Solid Electrolytes & Refractory Materials*
  Intended Journal: Journal of Nuclear Materials

- *Design of an Electrochemical Oxygen Sensor with a Thermal Spray Electrolyte*
  Intended Journal: ANS Nuclear Technology

- *Liquid Sodium Corrosion & Instrument Testing Facilities at UW-Madison*
  Intended Journal: ANS Nuclear Technology

Part III

Appendices

Appendix A

Ionic Transport and Signal Loss

This appendix discusses the details involved in oxygen ion transport across an electrolyte. It is of particular interest to investigate the effect of increasing yttria concentration on ionic conductivity since it was shown in chapter 6 that increasing yttria also increases the corrosion resistance of YSZ. This study begins by re-examining the Nernst equation which governs the electrochemical oxygen sensor:

$$E = E_o - \frac{RT}{2F} \ln\left(\frac{c}{c_o}\right) \tag{A.1}$$

The derivation and numeric details of equation A.1 are given in chapter 2. The magnitude of voltage expected from an oxygen sensor was shown to be over 1[V]. A useful sensor must produce a significant change in signal when oxygen concentration is changed even a small amount. Figure A.1 shows the magnitude of voltage change for an *increase* in oxygen concentration of 5[ppm]. This plot is shown as a function of initial concentration. For example, a change in concentration from 40[ppm] to 45[ppm] is shown at the 40[ppm] point on the x-axis of figure A.1.

As clearly seen in figure A.1, the change in signal magnitude increases as small concentrations of oxygen are approached. This is a result of the logarithmic behavior of electrochemical potential. Furthermore, the magnitude of this voltage change increases with increasing

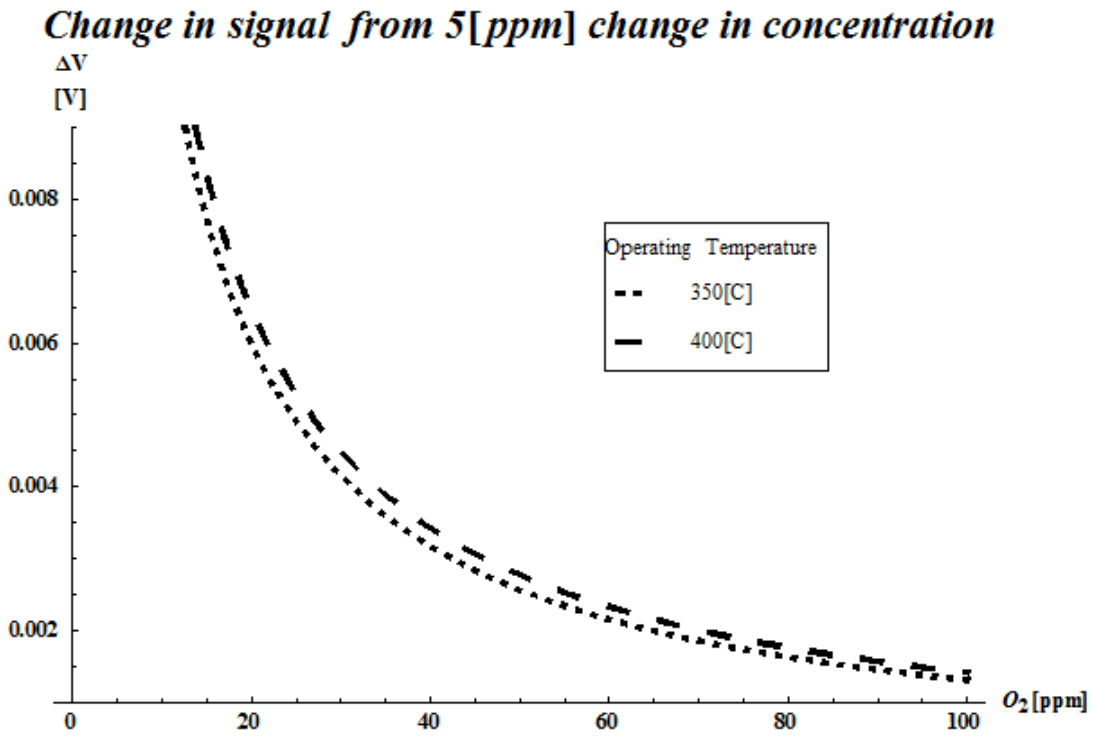

Figure A.1: This plot shows the change in cell voltage given an *increase* in dissolved oxygen concentration of 5[ppm]. This voltage increase is plotted as a function of *initial dissolved oxygen concentration*. For example, the 20[ppm] location on the x-axis shows the voltage change for a concentration increase from 20 to 25[ppm].

temperature, which implies that higher cell temperature results in easier detection.

Instruments used to read the oxygen sensor must have adequate resolution to measure a milivolt change on a $\approx$ 2[V] signal. As long as this requirement can be met, the cell performance predicted above should be sufficient for low oxygen concentrations.

All of the general theory mentioned above assumes an electrochemical equilibrium has been met. In addition, there is no accounting for losses due to charges moving through the imperfect ionic conductor, and no mention of the geometry of the sensor. A more detailed look at the specific loss mechanisms follows in this report to assess whether the above theory is sufficient to describe the electrochemical oxygen sensor.

Underlying Chemistry of the Electrochemical Oxygen Sensor

The operation of a galvanic cell oxygen sensor requires a difference in oxygen concentration across a solid electrolyte. For the air-catalyst sensor, air ($\approx 20\%$ oxygen) is supplied to one side of the electrolyte, while liquid sodium with oxygen dissolved in solution contacts the other side. The oxygen gas (O_2) is not free to move through the electrolyte in molecular form, so a porous catalyst (usually platinum) is attached at the electrolyte-air interface. The porous structure of the platinum catalyst provides vacancies within which molecular oxygen can break into oxygen ions, and borrow electrons from the platinum (from now on referred to as the reference electrode). This process can be seen in the following equation (A.2):

$$O_2 + 4e^- \rightarrow 2O^{2-} \tag{A.2}$$

These newly created oxygen ions are now free to traverse the ionic conductor (electrolyte). They will be driven across by diffusion of high oxygen concentration (air) to low concentration (in sodium). Upon reaching the electrolyte-sodium interface, the sodium atoms will shed an electron and ionically bond with the newly arrived oxygen ions.

$$Na \rightarrow Na^+ + e^- \tag{A.3}$$

$$2Na^+ + O^{2-} \rightarrow Na_2O \tag{A.4}$$

The liberated electrons allow an electronic current to flow through the sodium and adjoining stainless steel walls (this metal-metal combination is used as the second electrode) for the system. A high impedance voltmeter then completes the circuit when connected between the platinum wire and the liquid sodium. The signal generated on the multimeter should resemble the Nernst equation described above (equation A.1).

Platinum, as mentioned above, is an excellent catalyst for this system. Platinum provides locations for the oxygen molecules to dissociate into ions, and deposit electrons. Indeed,

when investigating trends in oxygen reduction activity, platinum has the highest activity[1]. However, platinum is by no means the only metal capable of acting as a catalyst for these sensors. The automotive industry, for example, frequently uses palladium as a cheaper substitute. Upon inspection of figure A.2, it is clear that many other metals could be used if platinum was thought to be too expensive.

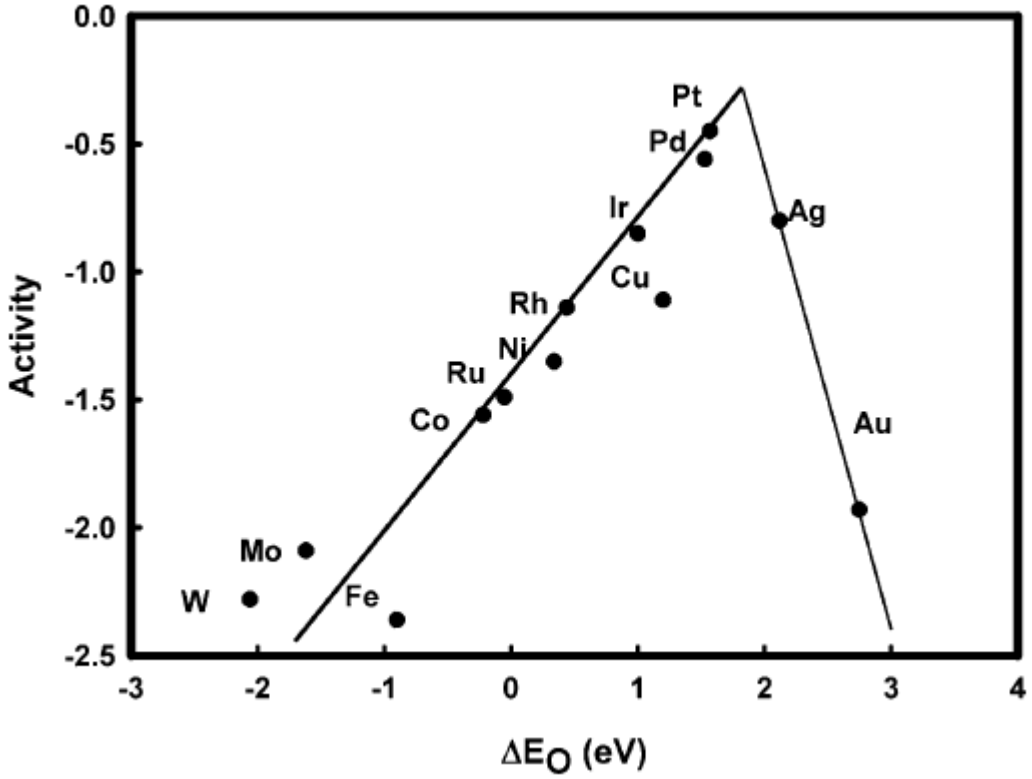

Figure A.2: This figure shows the catalytic ability of various metals (in terms of oxygen reduction activity) as a function of oxygen binding energy[1].

The metal-metal oxide reference electrode does not require a catalyst. Rather, the ratio of metal to metal oxide will remain in equilibrium with the available oxygen in the cover gas as long as the cover gas is sealed (no leaking). Thus, the oxygen concentration on the reference side of this sensor is maintained at a constant value. The magnitude of this partial pressure can be looked up on an Ellingham diagram. As long as this partial pressure is still higher than that of liquid sodium, oxygen ions will continue to move in to the sodium through the electrolyte, and the reaction will be the same as for the air-catalyst sensor.

As will be discussed in the following sections, the electrical current (and therefore, oxygen diffusion rate into sodium) is limited by the cumulative circuit resistance. The single largest resistor in the system is the multimeter, which limits the oxygen flux to such a small rate that any change in oxygen potential in sodium due to this effect can be neglected.

Equivalent Electronic Circuit - Construction

Nowhere in the theory described above does the geometry of the sensor come into play. The composition, thickness, and density are all ignored with the assumption that the electrolyte is a good ionic conductor. However, in searching for an electrolyte with improved lifetime and performance in liquid sodium, it is essential to understand the mechanism for ionic conduction, and understand the limiting factors to good ionic conduction.

This oxygen sensor will be analyzed as an electrical RC circuit to assess the signal losses at various places in the sensor circuit. All interfaces of two materials will be described as a resistor and capacitor in parallel, and every medium which must be traversed by a charged particle will be described as a resistor. At interfaces, charged particles either cross from one material to the other, losing some potential, or they get bound up and collect at the interface, acting as a capacitor. This analysis follows the transfer of charge all the way around the sensor, and the current as well as the IR losses within the cell will be analyzed.

Figure A.3 shows the chemical processes occurring throughout the sensor. Oxygen molecules present in air dissociate into oxygen ions in the platinum catalyst on the electrolyte circuit. These ions steal electrons from the platinum wire connecting to the volt-meter. These newly created oxygen ions can then traverse the electrolyte vacancies to the liquid sodium which is at a much lower oxygen partial pressure. Once at the sodium-electrolyte interface, sodium will readily shed an electron to briefly become a sodium ion, which can then form Na_2O. The newly liberated electrons are then free to transfer their charge across the sodium, and into the steel, which is connected as the return electrode back to the volt-meter. Schematically in figure A.3, this is shown as the electrons moving back to the voltmeter, and the circuit is complete.

To analyze signal losses within the sensor, as discussed above, the sensor is described as an electric circuit (figure A.4). This circuit is constructed by following the transfer of charge around the entire sensor loop. This figure is meant to be inspected in parallel with figure A.3.

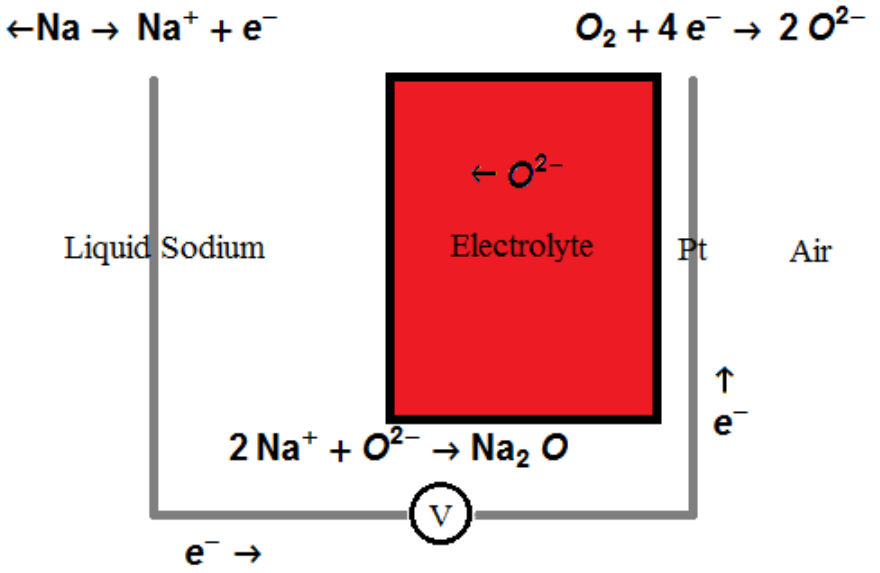

Figure A.3: This figure shows the basic layout of the elctrochemical cell including the chemical processes taking place which complete the circuit. Even though oxygen is being pumped into the system, the current is so small that the effect on potential is negligible.

The driving potential for the circuit is provided by the electrochemical potential difference between oxygen in sodium and oxygen in the reference electrode (in this case, air). This potential is sometimes referred to as the 'Nernstian Potential'. In a perfect system, this is the voltage one would expect to measure, as discussed above. Each chemical process described in figure A.3 will be analyzed, however. The following section discusses each loss mechanism shown in the equivalent circuit (figure A.4).

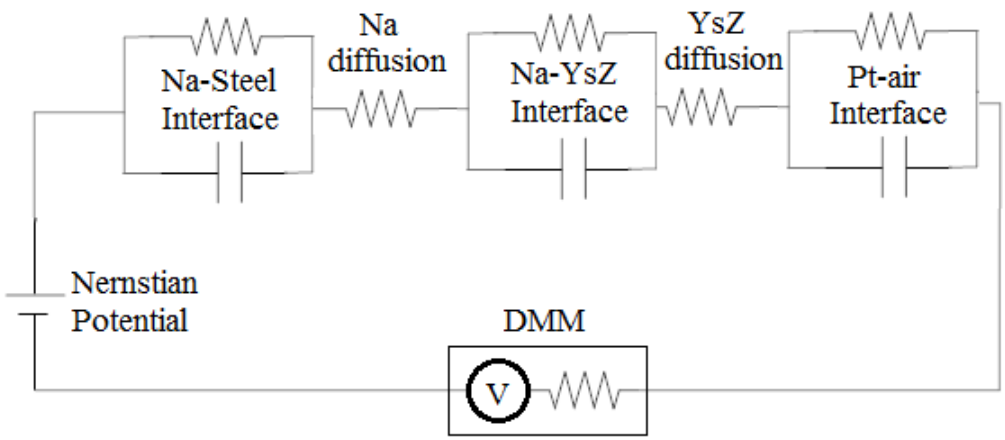

Figure A.4: This figure is the equivalent circuit which describes the voltage drops across the cell. The elctrolyte material for this analysis is yttria stabilized zirconia (YsZ).

Equivalent Electronic Circuit - Loss Mechanisms

If any of the following loss mechanisms are responsible for losses in the millivolt range, then the losses are on order with the signal generated according to figure A.1. The following pages of this section present research and data that argue that these losses won't significantly affect sensor performance.

The first interaction to discuss is the interaction at the platinum-air interface. In order for the platinum to act as a catalyst for this sensor it must be a porous structure, and have high catalytic activity. The catalytic process for a hot system should be of negligible resistance[2]. If a metal of lesser catalytic ability (figure A.2), this may not be true. However, for a platinum catalyst, which has been optimized for high current densities seen in solid oxide fuel cells, signal loss at this interface should be negligible for the small currents seen in an oxygen sensor.

The other two interface reactions, Na-YsZ and Na-Steel can be assumed zero for different reasons. First, the Na-Steel interface features two metals at high temperature in excellent electrical contact (one of them is a liquid). This interaction only needs to allow the transfer of charge between these two hot metals, an occurrence that intuitively should happen easily.

The third interface, Na-YsZ relies on oxygen being dissolved into hot molten sodium. The formation of sodium oxide between 400-600[C] occurs according to the following reaction:

$$4Na + O_2 \rightarrow 2Na_2O \tag{A.5}$$

This reaction occurs with a $\Delta G = -590$[kJ] or less within this temperature range. Since the Gibbs energy is negative, this reaction will occur spontaneously so long as the involved components are present. Thus, signal losses across all three interface reactions can be neglected for this sensor design.

Now the resistance network in figure A.4 is reduced to two diffusion problems and the digital multi-meter (DMM). As sodium atoms shed charge in favor of joining with oxygen ions to make Na_2O, the free electrons (or more accurately, their charge) must diffuse across the liquid metal to the wall, or other electrode. Again, since sodium is a metal with good electrical conductivity, this resistance should be far smaller than the millivolt signal expected from a change in oxygen concentration.

The final resistor shown in figure A.4 is the signal loss due to diffusion of oxygen ions across the yttria-stabilized zirconia electrolyte. This loss warrants a closer look into the mechanics of the interaction, as well as the composition and the geometry of the electrolyte. This problem will be approached from the fundamentals of diffusion in effort to understand the process and its limitations.

To begin, the coefficient of ionic conductivity is defined as κ [3]:

$$\kappa = F^2 \left(z_+^2 \mu_+ c_+ + z_-^2 \mu_- c_- \right) \tag{A.6}$$

This all-inclusive definition of κ can quickly be simplified with the assumption that the large positive charge carriers are immobile compared to the negative charge carriers. With this assumption, equation A.6 becomes:

$$\kappa = F^2 \left(z_-^2 \mu_- c_- \right) \tag{A.7}$$

F is the well known Faraday constant: $F = 96,485 \left[\frac{C}{mol}\right]$, z is the charge quantity, and, for oxygen ions, is $z = -2[-]$. μ is the mobility, which describes how freely ions move around. c is the defined as the concentration of vacancies in the YsZ, and should have units of $\left[\frac{mol}{cm^3}\right]$. This should be the same as the concentration of Y^{3+} ions doped into the zirconia to form YsZ. Typically, there are 4 yttrium atoms per unit cell, and the cell volume can be approximated using a lattice constant, $a \approx 5 \times 10^{-}8[\text{cm}]$. Avogadro's number ($N$) is then used to make the units correct:

$$c = \frac{4[atoms]}{a^3 \left[cm^3\right] N \left[\frac{atoms}{mol}\right]} \approx 0.532 \left[\frac{mol}{cm^3}\right] \tag{A.8}$$

Now with F, z, and c defined, only the mobility, μ needs to be determined so one can determine the ionic conductivity of the YsZ. The mobility should result in a term with units: $\left[\frac{cm^2 mol}{Js}\right]$. To begin, the mobility is related to the more commonly found diffusion coefficient, D, by the Einstein Relationship[4]:

$$D = \frac{\mu \; k_B \; T}{z} \tag{A.9}$$

z, the charge number, has already been discussed above. D has been documented in literature for various temperatures and concentrations of yttria in YsZ[5]. In place of Boltzmann's constant which is on a per atom basis, the universal gas constant, $\mathcal{R} = 8.31 \left[\frac{J}{molK}\right]$ will be used. Solving equation A.9 for μ, the following relationship betwen temperature, diffusion coefficent, and mobility is obtained:

$$\mu = \frac{zD}{\mathcal{R} \; T} \tag{A.10}$$

Now each term in equation A.7 has been described with exception of temperature and

diffusion coefficient (note that the diffusion coefficient is also a function of temperature). Sample values of the diffusion coefficient for different temperatures and yttria concentrations are given in figureA.5 [5].

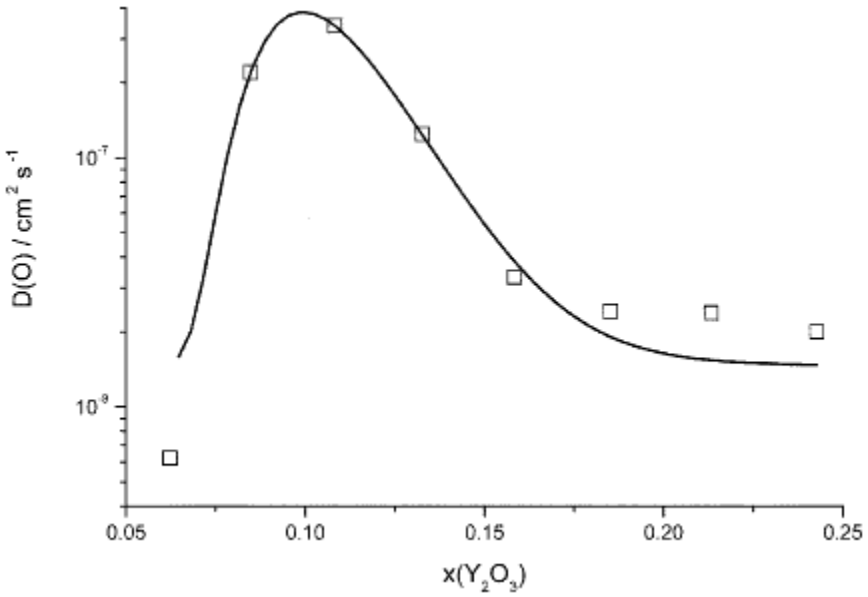

Figure A.5: This figure shows that the diffusion coeffient of oxygen in YsZ depends greatly on yttria concentration in the electrolyte. Temperature: 700[C][5].

Further inspection of figure A.5 reveals a suggested peak in diffusion coefficient around ten percent yttria. As yttrium ions are introduced into the zirconia, the yttrium ions(3+) replace zirconium ions (4+). An oxygen vacancy is therefore needed for every two yttrium ions in order to conserve charge. By using these vacancies the oxygen ions can jump their way through the ceramic. This is why there is initially an increase in diffusivity with an increase in yttria, because the availability of vacancies increases as well. However, it makes sense that, for a high enough yttria concentration, the vacancies will begin to interact with one-another, and the overall availability of vacant sites for oxygen ions to occupy diminishes[5], causing the drop in diffusion coefficient seen in figure A.5. The deminishing diffusivity is not a result of the presenece of vacancy clusters, rather the conductivity drops off because as the vacancies move together, they are no longer interconnected, and the ions can not traverse

the entire lattice.

The temperature dependence of the diffusion coefficient is substantial as well. Note that the data presented in figure A.5 is at a much higher temperature than the oxygen sensors need to operate. Figure A.6 shows how important temperature is to oxygen diffusivity; the diffusion coefficient drops nearly two orders of magnitude as temperature decreases from 700[C] to 400[C].

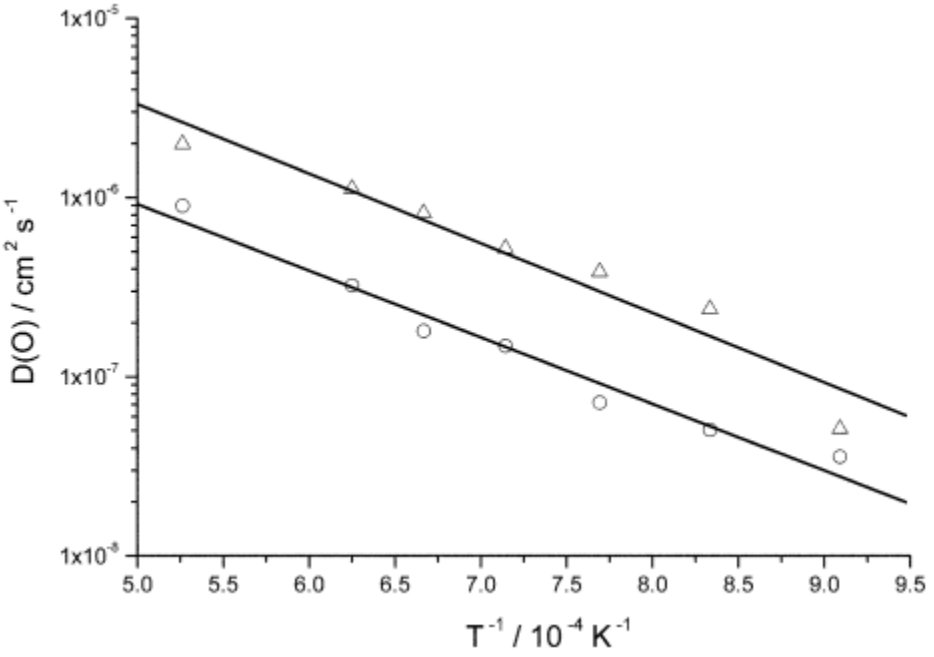

Figure A.6: This figure shows that the oxygen diffusivity in yttria-stabilized zirconia varies greatly with temperature. This figure, along with figureA.5 summarize the effect of both yttria concentration and temperature on the diffusion of oxygen in YsZ[5]. 8% YsZ = triangles, 24% YsZ = circles.

The above derivations and assumptions are enough to move onto estimating the electrical resistance due to these chemical processes. To move forward, the geometry of the sensor must be constructed. The sensor will be cylindrical, with inner and outer radii: r_i and r_o respectively, and height, H.

The electrolyte, YsZ in this example, is between the two concentric, cylindrical electrodes. The equation describing the resistance between the two electrodes is given by the following

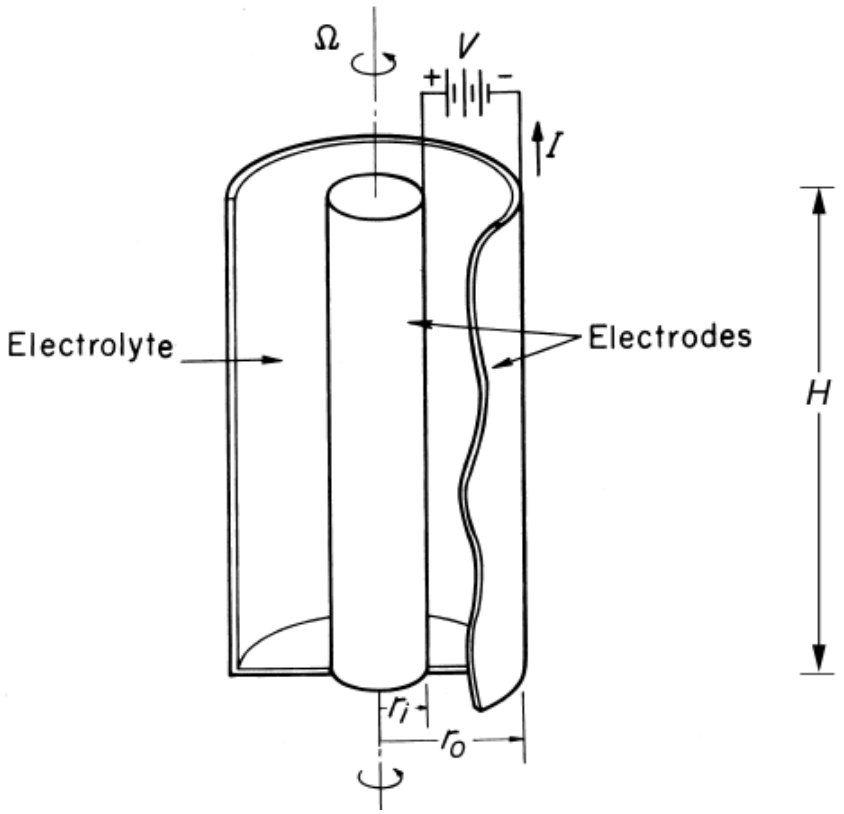

Figure A.7: This figure is taken from *Electrochemical Systems*. It shows the geometry of the sensor being discussed in this section[3].

equation[3]:

$$R = \frac{\ln \frac{r_o}{r_i}}{2\pi H \kappa} \tag{A.11}$$

Since most oxygen sensor work deals with electrolyte thickness rather than inner and outer diameters, equation A.11 will be modified accordingly with Δx, the electrolyte thickness:

$$R = \frac{\ln \frac{r_i + \Delta x}{r_i}}{2\pi H \kappa} \tag{A.12}$$

Using equation A.12, the resistance due to oxygen ions traversing the electrolyte can be calculated as a function of both electrolyte thickness and temperature (see figure A.8).

The resistance calculated and displayed in figure A.8 is between 0.1[Ω] and 0.6[Ω]. As

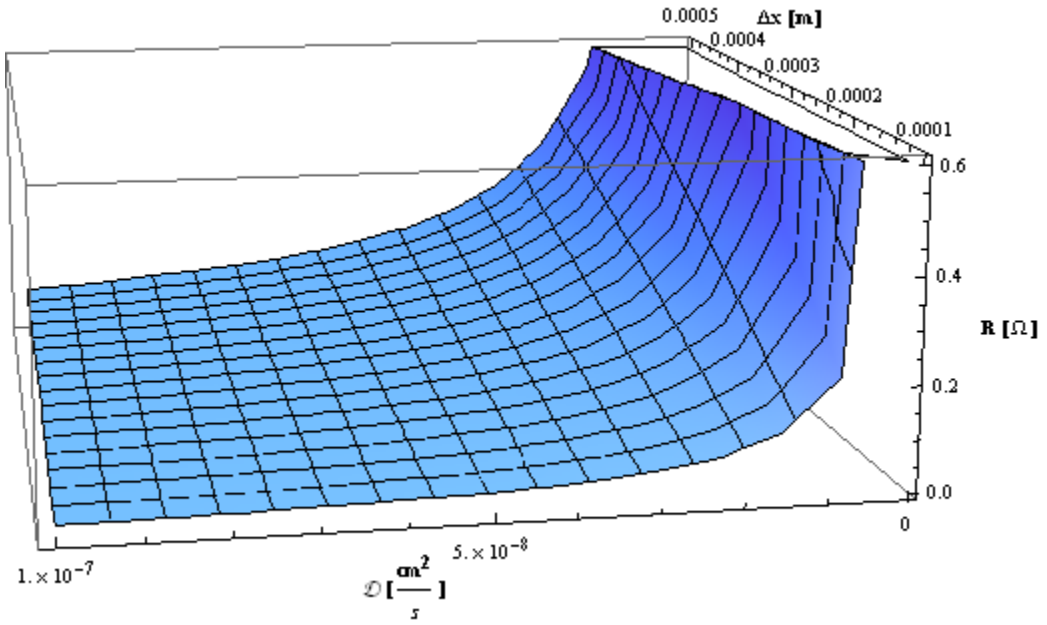

Figure A.8: This figure shows the theoretical electrical resistance due to oxygen ions diffusing across a YsZ membrane of thickness Δx at temperature, T.

electrolyte thickness increases, so too does the resistance. In addition, the developed theory shows an increase in resistance as the diffusion coefficient decreases. This trend makes sense since the diffusion coefficient describes how easily the oxygen can move across the membrane. Restriction to this flow translates to a restriction of electrical current.

The most important quantity, however, is not resistance. One needs to know the voltage drop that will occur across this resistor, which is related to resistance via the electric current. To assess the current across this electrolyte, the entire circuit must be solved. Indeed, nearly all the resistors in figure A.4 have been accounted for; the remaining resistor is within the volt-meter. Since a typical multimeter has an internal impedance in excess of a mega-ohm, this resistor dominates all those previously mentioned.

A hand calculated approximation assuming a mega-ohm resistance and a 2[V] electrochemical potential difference yields a current of $\approx 10^{-10}$[A]. This current across resistances under an ohm results in a signal loss of less than a nanovolt. As an example, figure A.9 shows

the signal loss across a YsZ electrolyte with a modest diffusion coefficient $D = 10^{-9}\left[\frac{cm^2}{s}\right]$ over a range of thicknesses: $250[\mu m] < \Delta x < 1500[\mu m]$ at temperature 400[C].

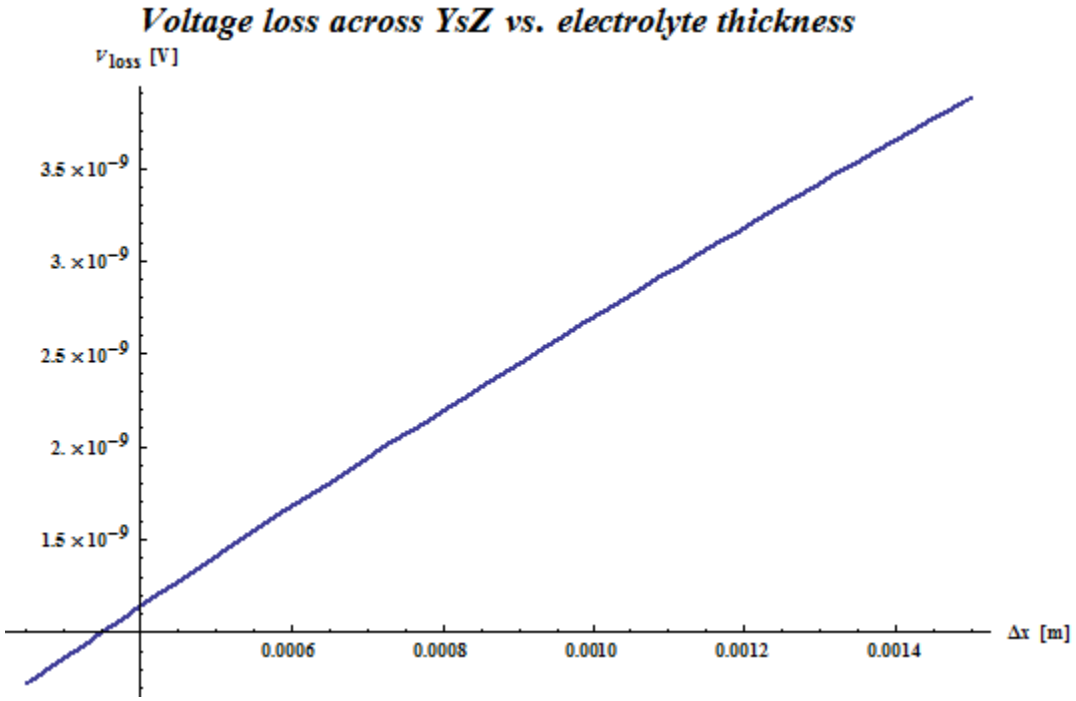

Figure A.9: This figure shows theoretical signal loss across a YsZ ionic conducting membrane as a function of thickness. Temperature for this plot is 400[C].

This result suggests that a probe with a thick electrolyte (in excess of $1000[\mu m]$ will still produce an accurate signal. Recalling from figure A.1 even a modest change in oxygen concentration produces millivolt changes in sensor output, so the losses due to electrolyte diffusion are six orders of magnitude less, and can be considered negligible.

If increasing thickness or changing the yttria concentration improves electrolyte resistance to corrosion, then the above analysis suggests that these parameters can be varied without significant effect on sensor performance. This conclusion is critical when trying to optimize a sensor for lifetime and performance.

Appendix B

Thermal Spray Sensor Design & Preliminary Testing

B.1 TS Sensor Design

MACOR crucibles were manufactured with a hole in the bottom. This hole was then filled with thermal spray coatings of varying thicknesses. A sensor was then made using these ceramic pieces as the electrolyte. The MACOR crucible was loaded into the bottom of a 316SS tube, and sealed by crushing a graphite gasket. A schematic of this assembly is shown in figure B.1.

The parts used in a sensor assembly are shown in figure B.2, and a view of the probe tip after exposure to sodium is shown in figure B.3.

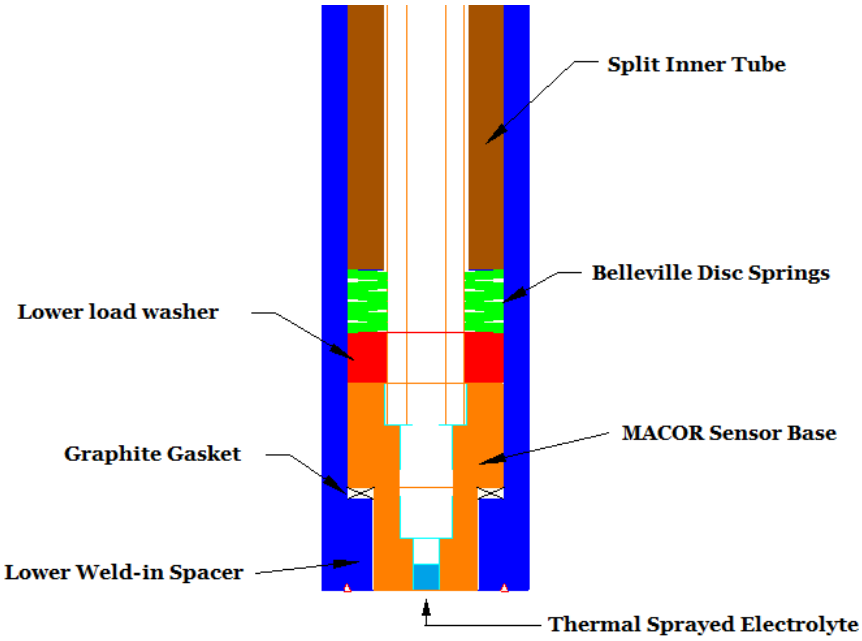

Figure B.1: The MACOR crucible has a thermal sprayed bottom and is loaded into a 316SS tube. The seal is made by top-loading the assembly with pressure to crush a graphite washer.

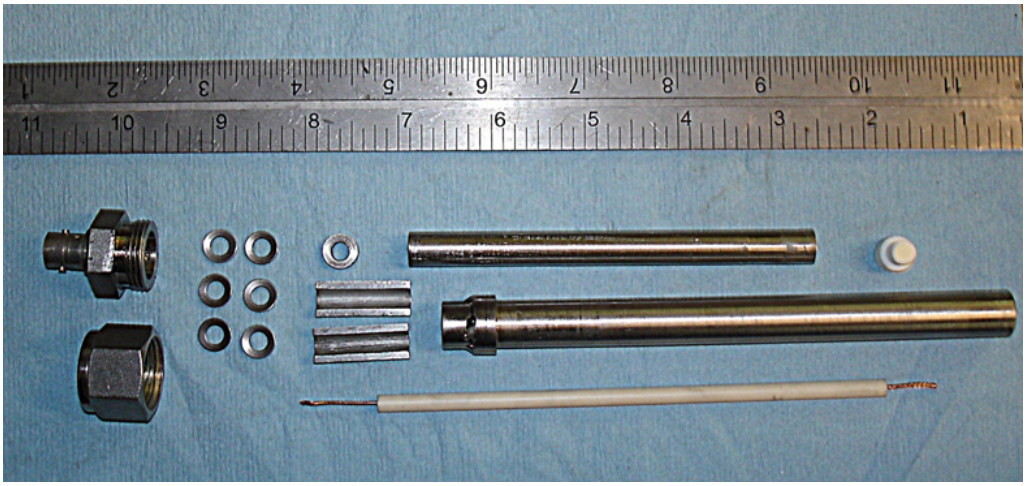

Figure B.2: These parts are assembled to make each thermal spray oxygen sensor.

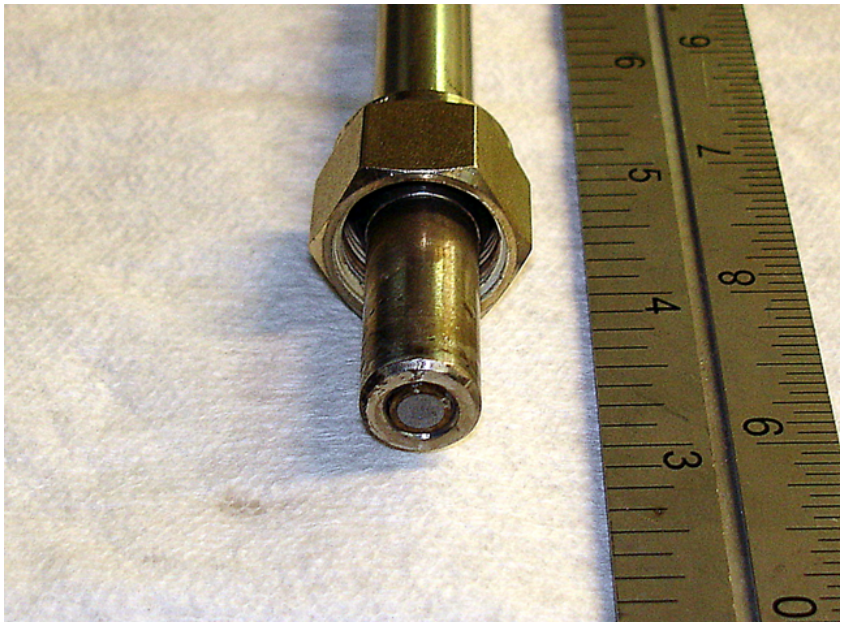

Figure B.3: The TS oxygen sensor probe tip after sodium exposure. This probe had shorted out in sodium after 19[hr] in sodium. The probe tip is visually still in tact, which means sodium migrated through the ceramic.

B.2 TS Sensor Tests & Results

The TS sensor did not produce meaningful data during testing. The voltage did not change with oxygen concentration, but continued to climb until it plateaued around 1.9[V]. This data is shown in figure B.4. After 19[hr] in sodium, the voltage dropped to zero volts, and the sensor was permanently shorted out.

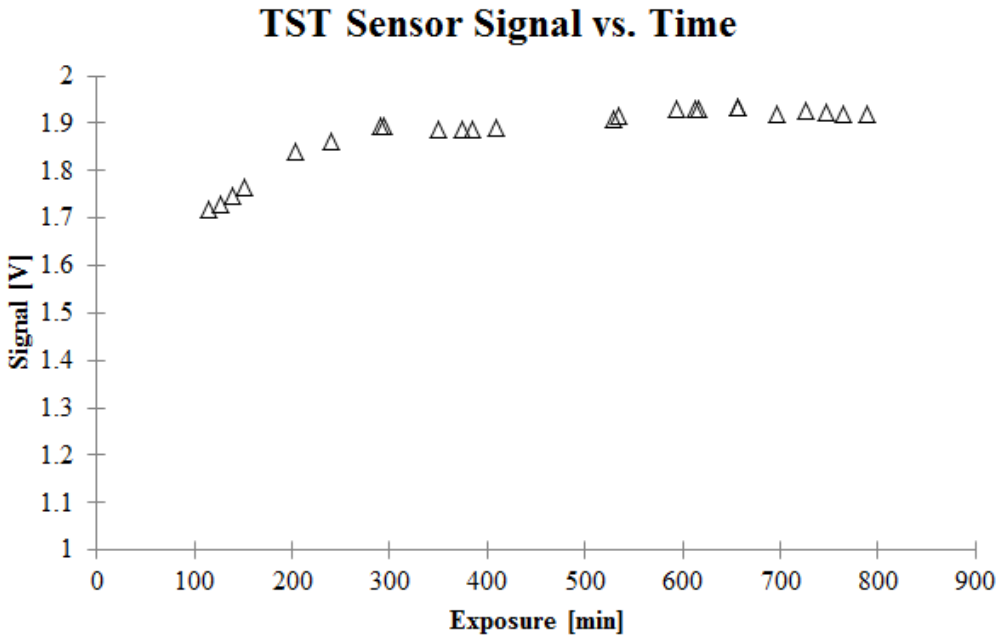

Figure B.4: The TS oxygen sensor produced a signal which slowly climbed to a plateau of $\approx$ 1.9[V]. The signal remained near this value until the sensor failed after 19[hr] of sodium exposure.

Once the TS sensor had failed, it was cross-sectioned and the exposed electrolyte was diagnosed with an EDS map. The cross-sectioned image is shown in figure B.5. While cutting the sensor, substantial sodium deposits were found inside the reference cell, embedded with the copper. This suggested that sodium had penetrated either by going around the MACOR and leaking through the graphite seals, or directly through the electrolyte.

EDS-mapping of the cross-section of the sensor would reveal that sodium had, in fact, penetrated directly through the electrolyte. Detailed images of all possible leak points were

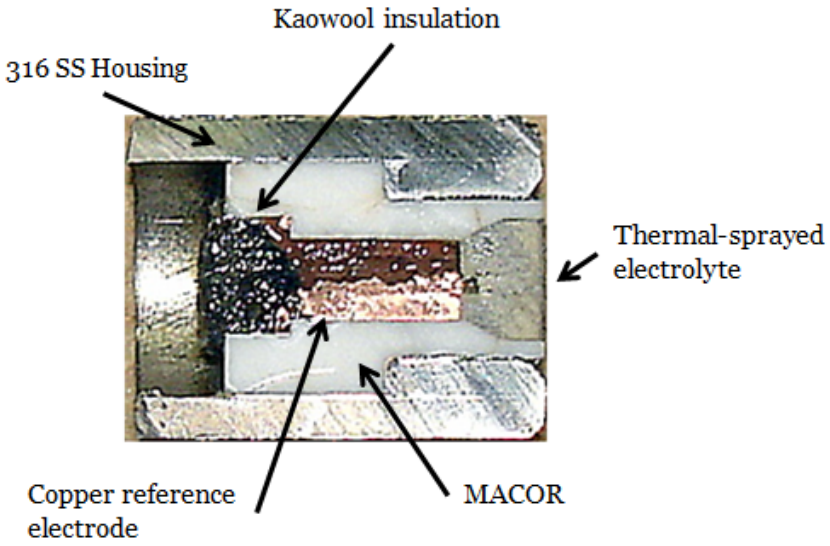

Figure B.5: A cross-section of the TS sensor tip is shown. The key components are identified.

taken and sodium was only found through the thermal spray (see figure B.6) . The inherent porosity of the TS electrolyte proved to be sufficient to allow sodium penetration. This is consistent with the results seen in chapter 6.

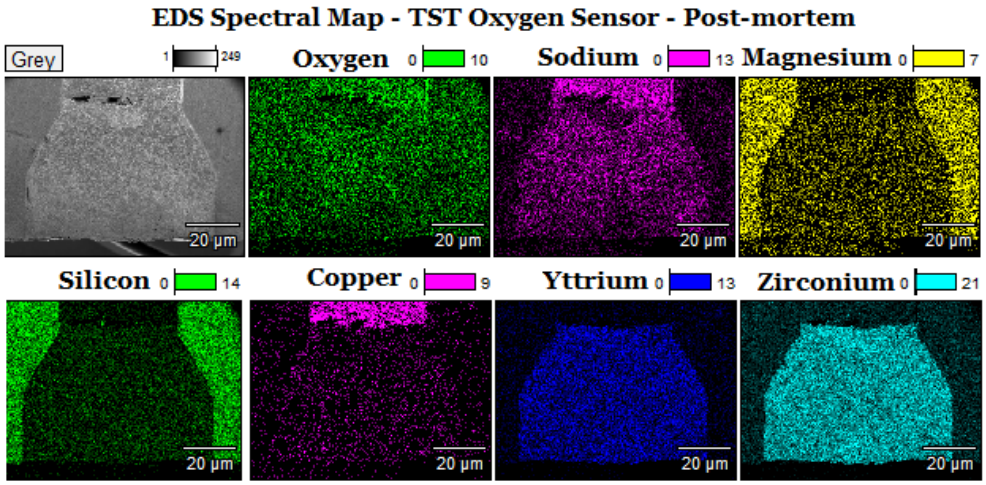

Figure B.6: Sodium penetrated through the porous thermal spray ceramic and into the reference chamber. This short-circuited the sensor and drove the voltage to zero.

An annotated larger view of the scanned cross-section is shown in figure B.7.

If the density of thermal spray coatings can be increased to the extent where sodium can

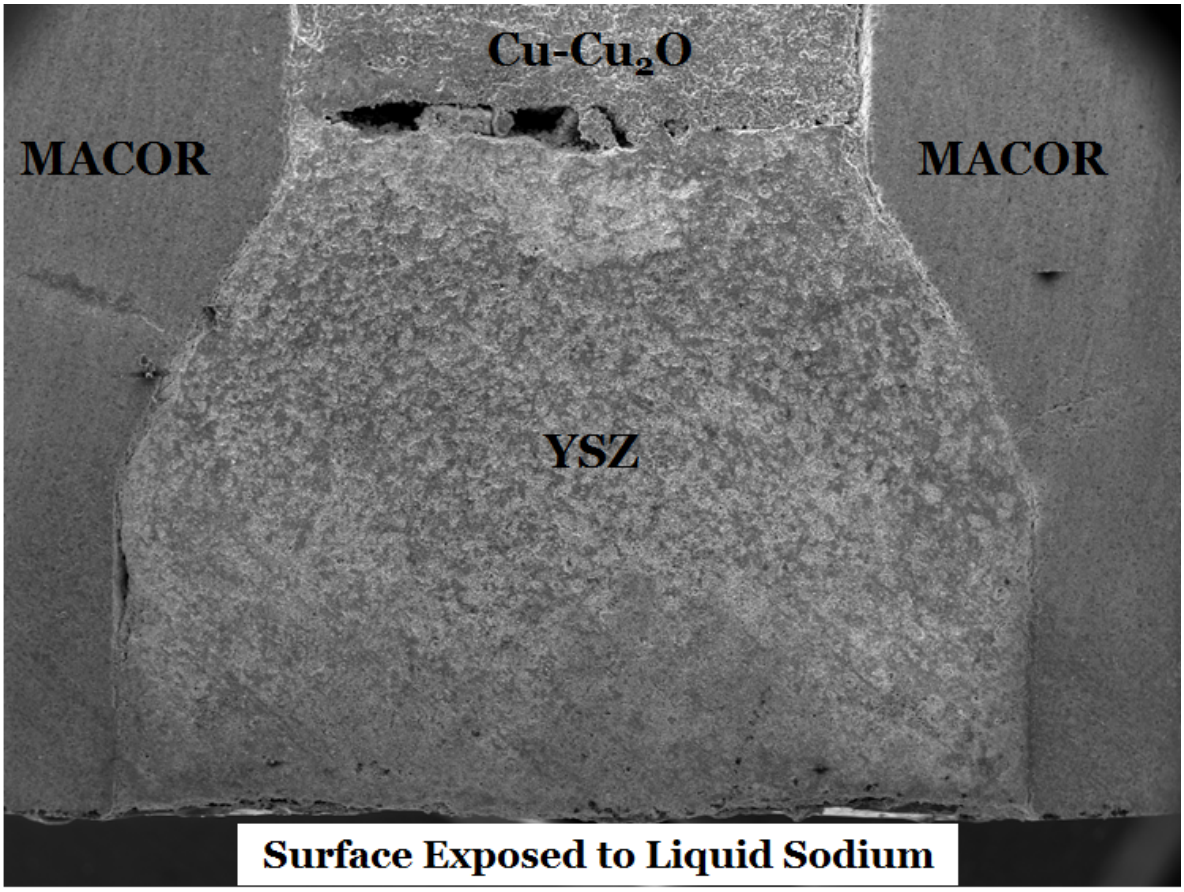

Figure B.7: The cross-section of the sensor after sodium exposure. Sodium penetrated through the ceramic into the reference chamber, electronically connecting the reference and sodium electrodes.

no longer penetrate the surface, then they could be used as electrolytes in a dissolved oxygen sensor. These TS sensors generated a strong voltage, indicating a substantial potential difference on either side of the electrolyte. However, the continuous ingress of sodium must be stopped before a meaningful signal can be acquired.

Possible ways to improve the electrolyte density include changing the standoff distance when spraying, sintering the electrolyte after spraying, or laser densification.

Appendix C

MACOR Composition

Table C.1: Chemical composition of MACOR machinable ceramic

% Composition	Material Name	Chemical Formula
46	silica	SiO_2
17	magnesium oxide	MgO
16	alumina	Al_2O_3
10	potassium oxide	K_2O
7	boron oxide	B_2O_3
4	flourine	F

Appendix D

Additional EDS Scans

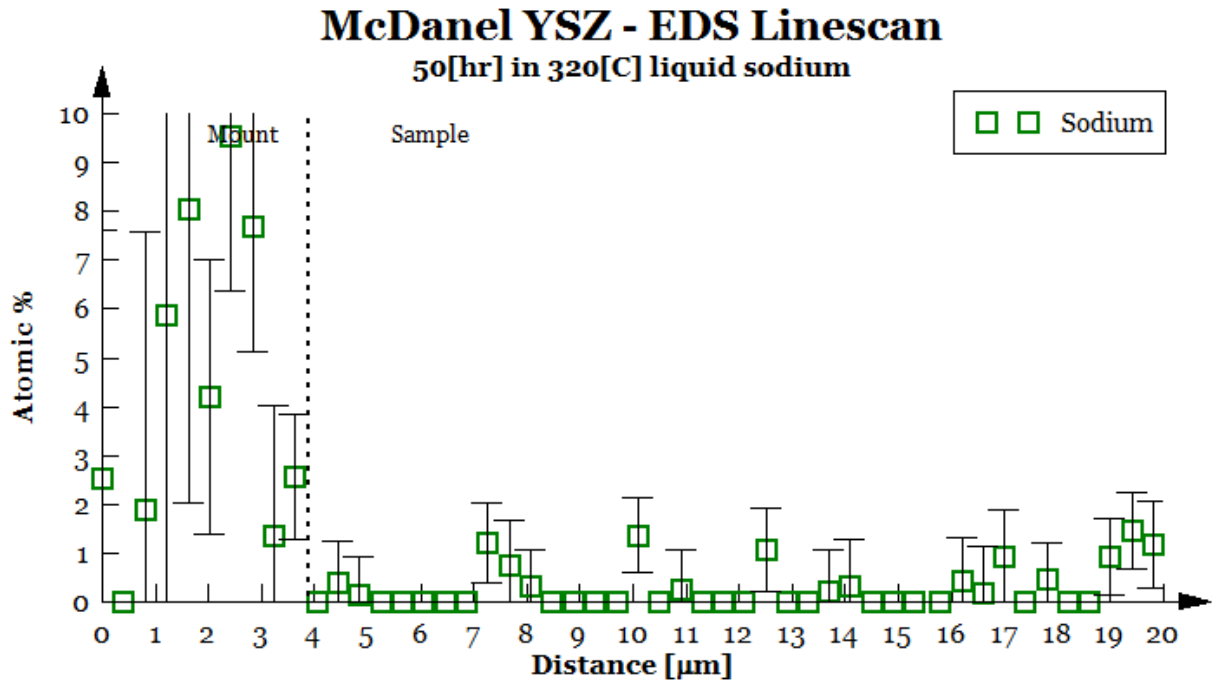

Figure D.1: This zoomed-in version of figure 6.5 shows specifically the sodium concentrations of the linescan into the McDanel YSZ sample. Very little sodium penetration was detected.

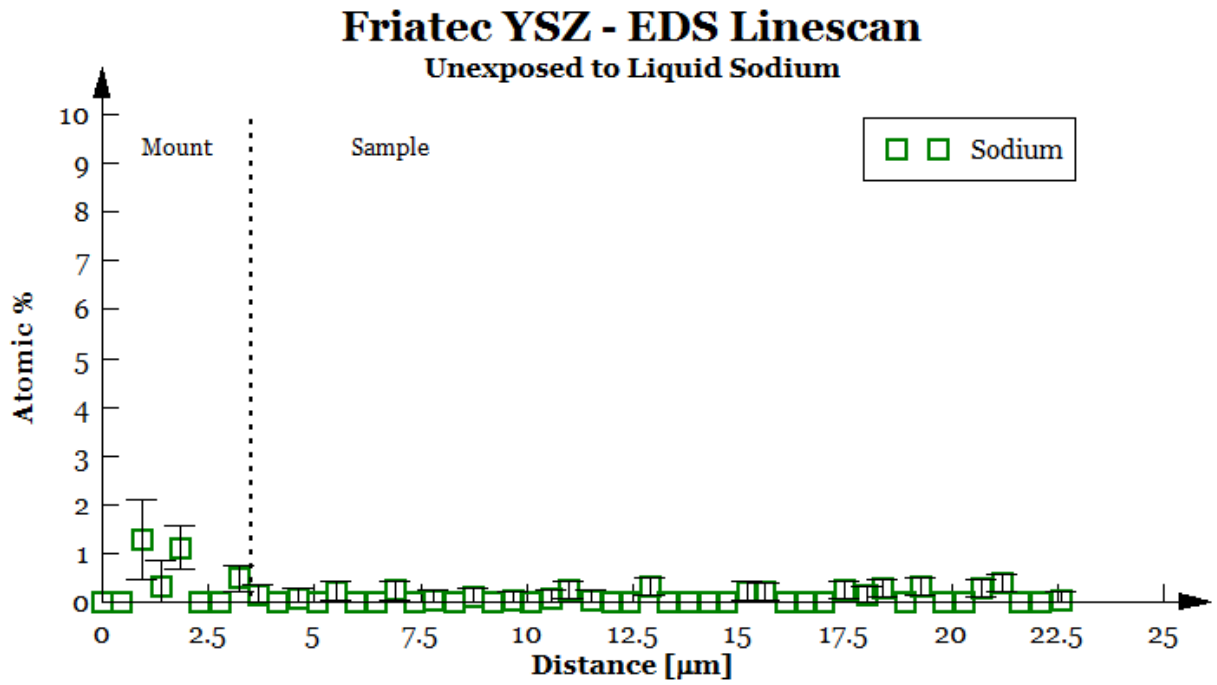

Figure D.2: Focusing on the sodiium concentration through the Friatec YSZ shows that very little sodium was present before sodium exposure.

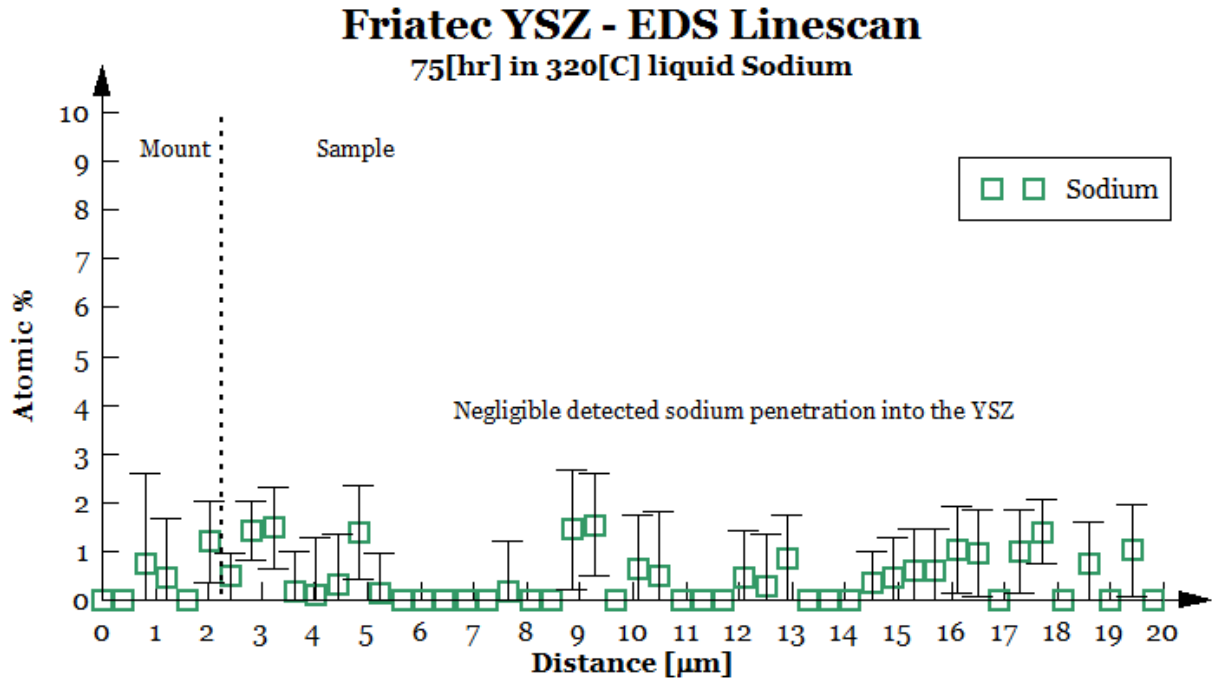

Figure D.3: Very little change in internal sodium concentraiton was detected after sodium exposure. This is a zoomed-in version of figure 6.7 which specifically focuses on sodium.

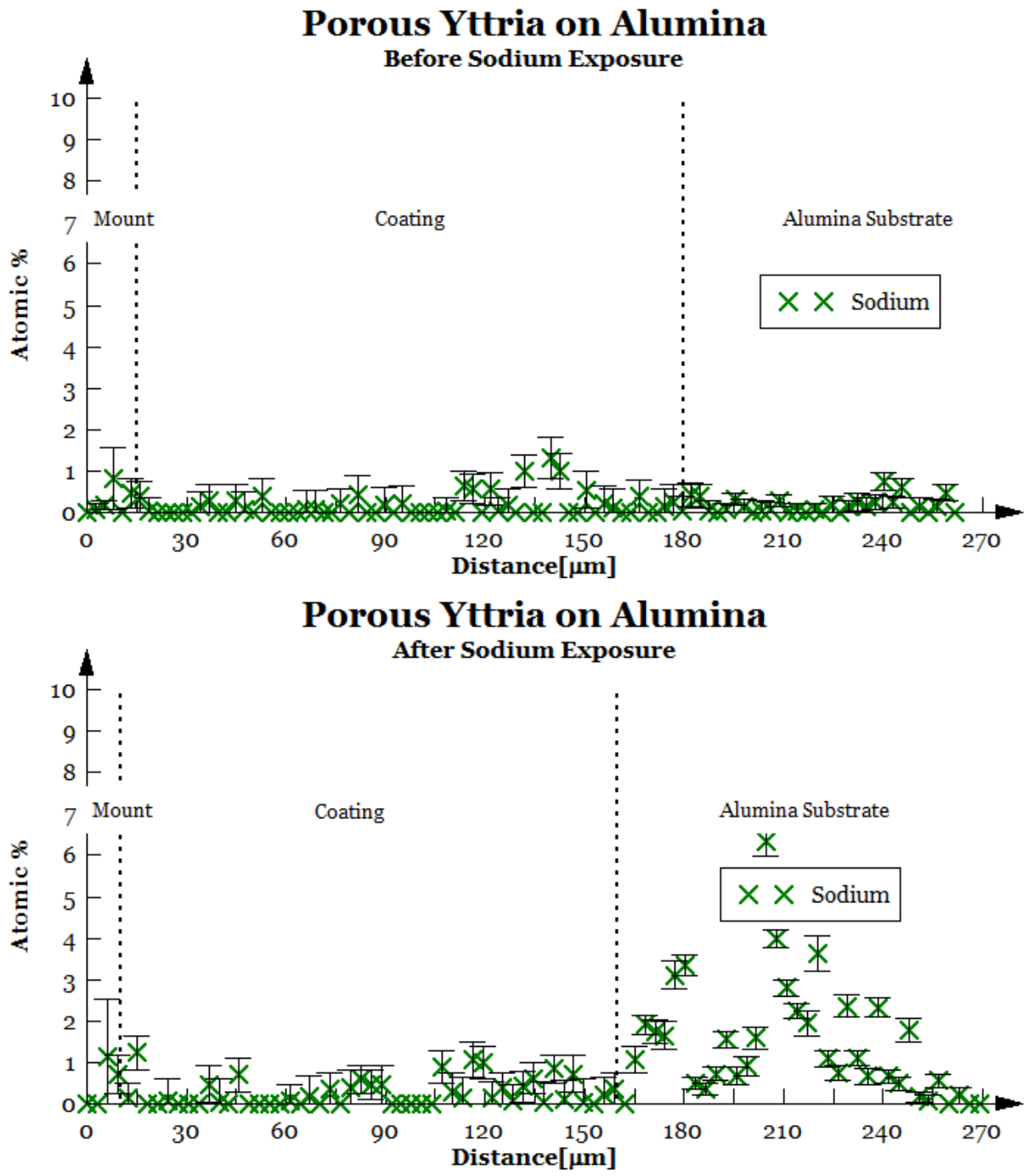

Figure D.4: Very little measurable sodium was initially found in the porous yttria coating. However, after sodium exposure substantial sodium as found in the alumina substrate. The coating integrity was intact, so the sodium likely came from the edges of the sample when the coating began to separate.

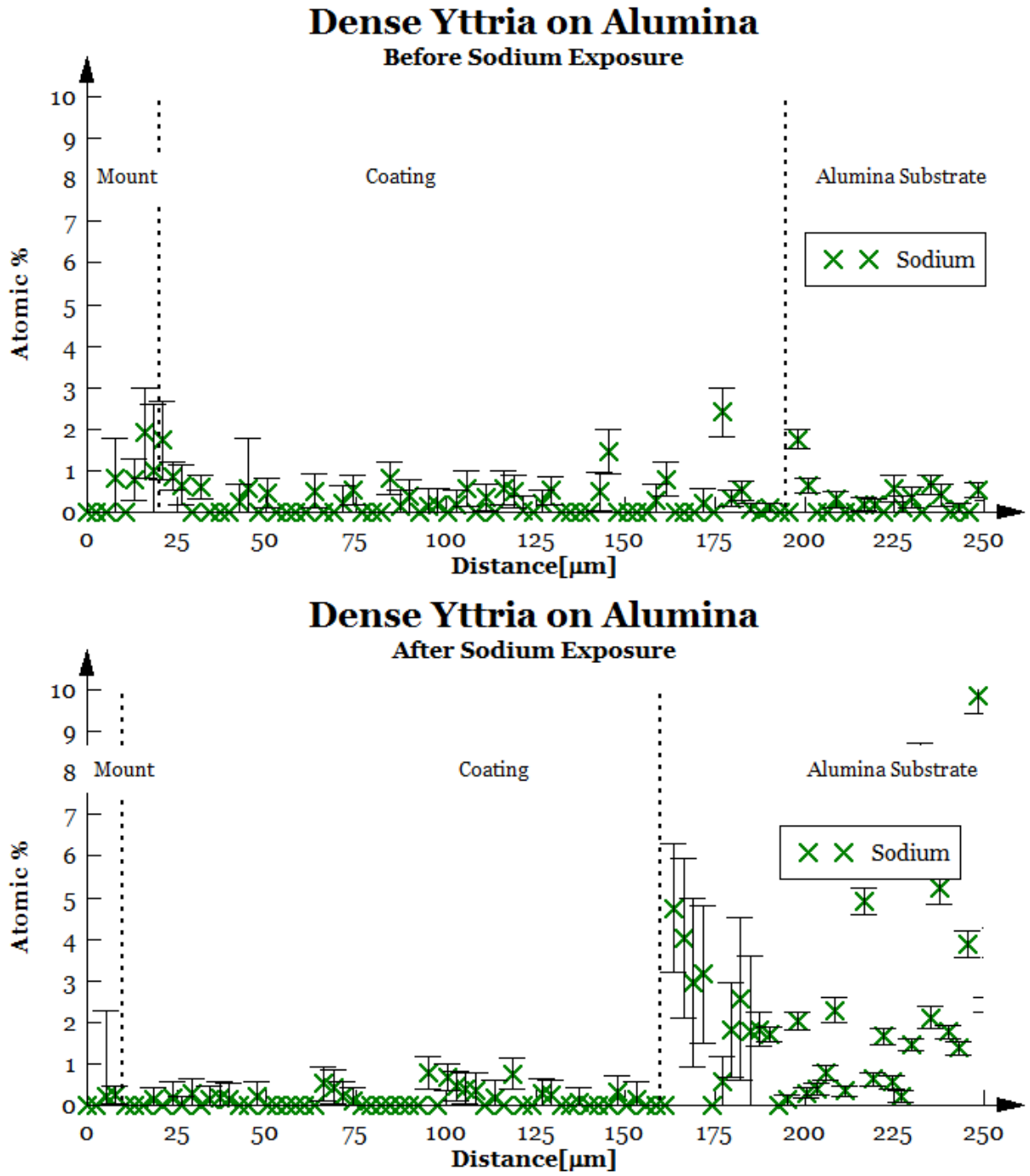

Figure D.5: The dense yttria coating resisted sodium penetration, however, significany sodium concentrations were found in the alumina substrate. It is expected that, like with the porous coating, a thermal expansion-induced gap allowed sodium to infiltrate.

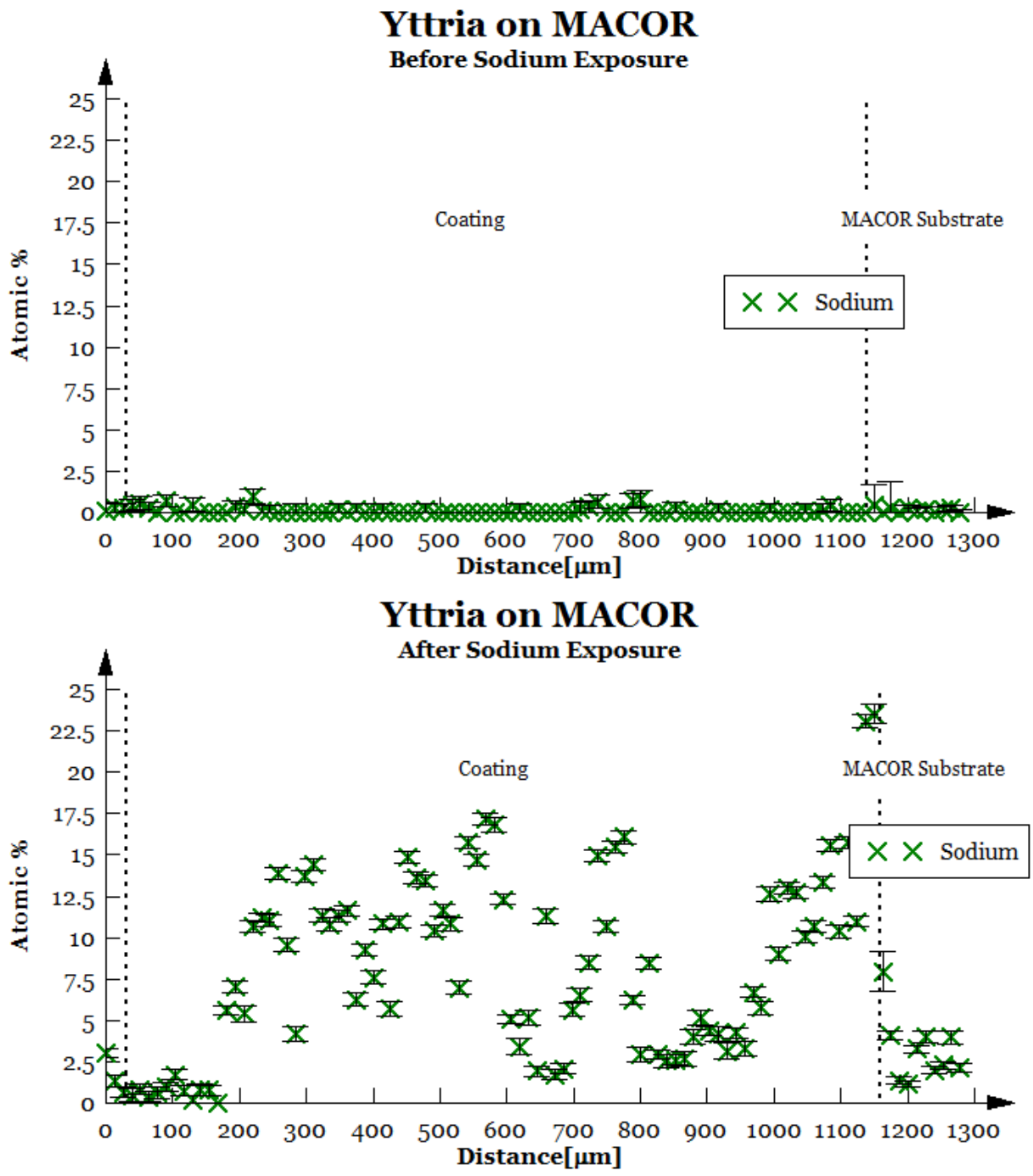

Figure D.6: Yttria coatings on MACOR experienced significant cracking and consequent sodium penetration. The higher difference in CTE between MACOR and yttria as compared to alumina and yttria is likely the cause for this increased cracking (as compared to figure D.4 and D.5).

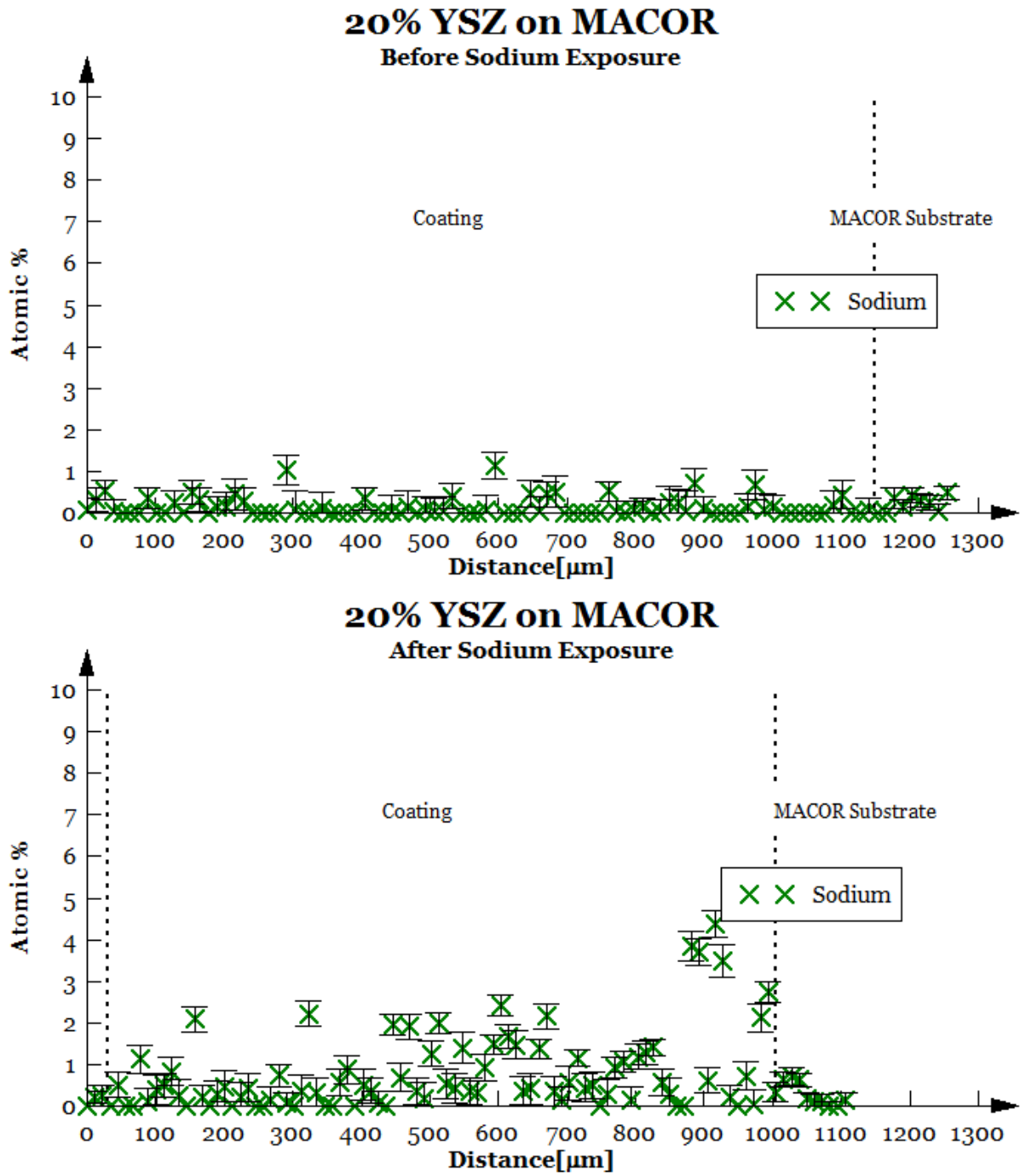

Figure D.7: 20% YSZ proved more damage resistant than yttria on MACOR. This is explained by the less-brittle structure of YSZ compared to yttria.

Chapter D Bibliography

[1] J.K. Norskov. Origin of the overpotential for oxygen reduction at a fuel-cell cathode. *Physical Chemistry Journal*, September 2004.

[2] Amrita Saigal. Fabrication of low temperature solid oxide fuel cells with ultra-thin yttria-stabilized zirconia electrolytes. Technical report, Massachusets Institute of Technology, 2007.

[3] Karen E. Thomas-Alyea John Newman. *Electrochemical Systems*. John Wiley & Sons, Inc., 3 edition, 2004.

[4] Sarina Bromberg Ken A. Dill. *Molecular Driving Forces - Statistical Thermodynamics in Chemistry and Biology*. Garland Science, 2003.

[5] Gunter Borchardt Robert A. Jackson Martin Kilo, Christos Argirusis. Oxygen diffusion in yttria stabilized zirconia - experimental results and molecular dynamics calculations. In *International Bunsen Discussion Meeting*, volume 78, October 2002.